Numerical Modelling of Braiding Processes in Gravel-Bed Rivers

Bishnu Raj Baral

School of Geography

Queen Mary University of London

Thesis submitted in partial fulfilment of the requirements of the Degree of Doctor of Philosophy (PhD)

November 2017

United Kingdom, London

PhD Thesis on

Numerical Modelling of Braiding Processes in Gravel-Bed Rivers

By

Bishnu Raj Baral

Primary University

School of Geography,
Queen Mary University of London,
United Kingdom

Secondary University

Department of Civil, Environmental and Mechanical Engineering,
University of Trento, Italy

Supervisors

Prof. James Brasington (Queen Mary University of London, UK)
Dr. Alexander J. Henshaw (Queen Mary University of London, UK)
Dr. Walter Bertoldi (University of Trento, Italy)

Dedicated to the memory of my late parents, Dada Ram Baral and Bishnu Maya Baral

Statement of Originality

I, **Bishnu Raj Baral**, confirm that the research included within this thesis is my own work or that where it has been carried out in collaboration with, or supported by others, that this is duly acknowledged below, and my contribution indicated. Previously published material is also acknowledged below.

I attest that I have exercised reasonable care to ensure that the work is original and does not to the best of my knowledge break any UK law, infringe any third party's copyright or other Intellectual Property Right, or contain any confidential material.

I accept that the College has the right to use plagiarism detection software to check the electronic version of the thesis. I confirm that this thesis has not been previously submitted for the award of a degree by this or any other university.

The copyright of this thesis rests with the author and no quotation from it or information derived from it may be published without the prior written consent of the author.

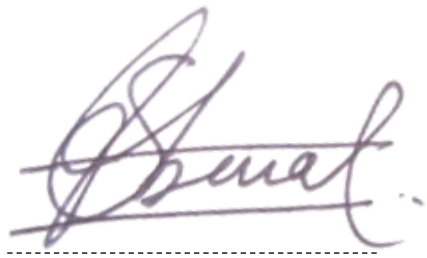

Bishnu Raj Baral

29 November 2017

London

PhD in River Science

Research for this thesis was conducted within the framework of SMART (Science for MAnagement of Rivers and their Tidal systems), which is an Erasmus Mundus Joint Doctoral Programme (EMJD).

EMJDs aims to foster cooperation between higher education institutions and academic staff in Europe and third countries with a view to creating centres of excellence and providing a highly skilled 21st century workforce enabled to lead social, cultural and economic developments. All EMJDs involve mandatory mobility between the universities in the consortia and lead to the award of recognised joint, double or multiple degrees.

The SMART programme represents a collaboration among The University of Trento, Queen Mary University of London, and Freie University Berlin. Each doctoral student within the SMART programme has conformed to the following during their 3 years of study:

(i) Supervision by a minimum of two supervisors in two institutions (their primary and secondary institutions).

(ii) Study for a minimum period of 6 months at their secondary institution

(iii) Successful completion of a minimum of 30 ECTS of taught courses

(iv) Collaboration with an associate partner to develop a particular component / application of their research that is of mutual interest.

(v) Submission of a thesis within 3 years of commencing the programme.

Abstract

Gravel-bed braided rivers are distinctive natural environments that provide a wide range of key environmental, economic and recreational services. There is, however, a growing concern that over the twentieth century, an increasing number of braided rivers have metamorphosed into wandering or single thread channels, representing a loss of key habitats, geodiversity and amenity. While in some situations, shifts in channel pattern may be unambiguously linked to abrupt changes in flow or sediment supply, the lack of a theoretical basis underpinning the development and maintenance of braiding makes identification of the cause and effect of channel metamorphosis hazardous. A growing body of research has suggested that the transition between channel patterns may depend on the poorly understood interaction between the flow regime, sediment supply and vegetation colonisation. Such interactions are governed by critical thresholds, due to changes in flow resistance and bank strength associated with the distribution, form and intensity of vegetation colonisation. Subtle changes in flow or sediment supply that promote vegetation growth or indeed remove it through inundation or attrition. This can lead to complex non-linear shifts in the balance of forces that govern sediment transport and bedform morphodynamics, ultimately resulting in one-way changes in channel morphology. There is, therefore, a critical need to develop a quantitative understanding of these feedbacks in order to design sustainable river management programmes that seek to optimize the ecological and socio-economic benefits these rivers offer.

During the last three decades, significant advances in the understanding of the morphodynamics of braided rivers have been made through a combination of field and physical experimentation. More recently, the emerging field of numerical modelling has created a new avenue to investigate the processes that govern channel

dynamics. While this methodology offers significant promise through the construction of virtual experiments that examine the spectrum of drivers and responses of river systems, such models require careful and critical evaluation before they can be used to guide management practice. The wider goal of this research is to explore the application of a numerical modelling to investigate the feedbacks associated with the development and maintenance of braiding. Specifically, the state-of-the-art numerical model, BASEMENT, was used to examine channel responses to steady, and unsteady flow regimes, with and without the representation of vegetation. The research focuses on four main contributions:

1. The development of a systematic framework to quantify the evolving form and processes of braided rivers that can be used as part of a comprehensive approach to model validation.
2. Simulation of braiding development and maintenance using BASEMENT under steady flow conditions. Model simulations based on the natural prototype of the braided River Feshie were used to examine the sensitivity of emergent channel morphologies to the model parameterisation, focusing in particular on the representation of bank erosion and gravity-driven sediment transport. A novel multi-metric framework for model validation is presented and the results demonstrate the critical importance of lateral bank migration processes in order to maintain braided morphologies under steady flow.
3. A critical evaluation of the simulation of braiding under different form of steady and unsteady flow regimes is presented. These experiments investigate how the morphodynamics of braiding vary under energetically-normalised flow regimes characterized by differences in hydrograph form (peak discharge and duration). This experiment provides a novel insight into the role of flow variation in the maintenance of braiding.

4. Finally, the feedback between flow regimes, sediment transport and vegetation growth are examined using a novel model of vegetation colonisation and die-back. Four scenarios are presented, a no-vegetation model, one based on low growth rate, one based on an intermediate growth rate, and finally a high growth rate parameterisation. These simulations provide a clear insight into the non-linear processes driving channel evolution and demonstrate how subtle changes in the balance between flow frequency and vegetation growth can lead to divergent channel patterns.

In summary, this thesis aims to advance our understanding of the morphodynamics of braided rivers and the role numerical models may have in helping to interrogate their behaviour and governing controls. It is hoped that this work may contribute, albeit in a small way, to advancing the science that promotes the sustainability of these fascinating and valuable environments.

Key Words: Braided Rivers, Numerical Modelling, BASEMENT, Unsteady Flow, Vegetation

Acknowledgements

I wish to thank, first and foremost, my supervisor Prof. James Brasington, for his enthusiastic guidance, motivation and support throughout the research. I am deeply indebted to his prompt reviews and feedback. I would also like to express my gratitude to my two co-supervisors Dr. Alex Henshaw (QMUL) and Dr. Walter Bertoldi (UNITN) for their continuous support, encouragement and valuable feedback on this research.

I am thankful to Dr. Annunziato Siviglia (ETH Zürich) for providing the numerical code to model vegetation dynamic that was not available in the freeware version of the BASEMENT numerical model. I am also thankful to Dr. Umesh Singh and Dr. Marco Redolfi for sharing their ideas about the use of MATLAB program which was one of the tools most necessary to analyse the vast data set. I am largely indebted to Michelle Day (QMUL) for her generous management support to make uninterrupted use of two High–Performance Computing Machine for a complete year at the Geo-spatial laboratory in QMUL. I am also thankful to Dr. Simone Zen and Federico Monegaglia for their facilitation to make use of the Trento server for some part of the simulation.

Without a doubt, I must acknowledge the Erasmus Mundus Joint Doctoral Programme (EMJD), European Commission for granting full scholarship to conduct the research. I am also thankful to Marina Rogato (UNITN), Aureliano Cerreti (UNITN), Ina Severin (IGB-Berlin), Jennifer Murray (QMUL), Anna Dulic-Sills (QMUL), Shazia Sadiq (QMUL), and Helen Mclurg (QMUL) for their generous management support. My gratitude also extends to all colleagues within the SMART and QMUL research degree program for sharing knowledge and moments with each other.

Finally, I would like to express my gratitude to all of my family members, particularly my wife and daughter for their unconditional love and support in each step of my PhD life.

Attribution Page

First of all, I am largely indebted to the developer of the BASEMENT numerical model (*http://www.basement.ethz.ch*) for developing such a powerful freeware software, which facilitated to develop some insights into form and behavior of braided rivers. I would like to thank the developer of the freeware QGIS software (*http://www.qgis.org/en*), which helped to prepare grid for the numerical simulation.

I would like to thank QMUL IT for a providing license for the GIS software (*http://desktop.arcgis.com*), which was useful to analyse some data. I am also indebted to the Scottish Environment Protection Agency (SEPA) (*https://www.sepa.org.uk*) for providing the long-term flow series data measured at Feshie Bridge that was important for this study. I would like to thank QMUL IT for providing a license for MATLAB (*https://uk.mathworks.com*) software, which was one of the tools most necessary to analyse the vast data presented in the research. I also want to thank different MATLAB user's platforms where I got chance to learn about developing codes and sharing knowledge with others. I am thankful to the developer of Paraview software (*https://www.paraview.org*), which helped to post process some of the output data of the BASEMENT simulation.

Lastly, I am thankful to Google Scholar (*https://scholar.google.co.uk*) for developing such an outstanding platform to search and manage scholarly literatures. I am grateful to all the scientific communities for their stimulating innovations and publications related to this research.

Table of Contents

List of Figures

List of Tables

List of Abbreviations

ABI	Active Braiding Index
aDcp	acoustic Doppler current profiler
AHG	At - a station Hydraulic Geometry
BASEMENT	Basic Simulation Environment for Computation of Environmental flow and Natural Hazard Simulation
BSS	Brier Skill Score
CAESAR	Cellular Automaton Evolutionary Slope And River
CFL	Courant-Friedrich-Levy
DEM	Digital Elevation Model
DHI	Danish Hydraulic Institute
DoD	DEM of Differencing
EMJD	Erasmus Mundus Joint Doctoral Programme
FDC	Flow Duration Curve
GPS	Global Positioning System
GNSS	Global Navigation Satellite System
HSTAR	Hydrodynamics and Sediment Transport in Alluvial Rivers model
HLL	Harten, Lax, and van Leer
HLLC	Harten-Lax-van Leer-contact
HPC	High-Performance Computing
IOUP	Upstream Morphodynamic Boundary in BASEMENT MODEL
IODOWM	Downstream Morphodynamic Boundary in BASEMENT MODEL
iRIC	International River Interface Cooperative
LCB	Link Length
MAAH	Mean Annul Active Hour
MBL	Mean Bed Level
MAME	Mean Annual Maximum Energy
MSESS	Mean-Squared Error Skill Score
MORFAC	Morphological Acceleration Factor
MP	Murray and Paola
MPM	Meyer-Peter and Müller
NES	Nash Efficiency Statistic
NZ	New Zealand
PBM	Physics Based Models
QMUL	Queen Mary University of London
RCM	Reduced Complexity Models
SEPA	Scottish Environment Protection Agency
SMART	Science for MAnagement of Rivers and their Tidal systems
SSSI	Sites of Specific Scientific Interest
SWE	Shallow Water Equations
SWW	Shallow Water Wave
TLS	Terrestrial Lesser Scanning
TBI	Total Braiding Index

UK	United Kingdom
UNITN	University of Trento
1D	One-Dimensional
2D	Two-Dimensional
2D	Three-Dimensional
4D	Four-Dimensional
2DH	Two-Dimensional Depth-Averaged

Chapter 1: Thesis Introduction

Chapter Summary

This chapter firstly introduces wider aim of the thesis and explores the available research methodologies. Secondly, it establishes scope of the BASEMENT numerical model and data from the river Feshie in the context of this thesis. Thirdly, four specific research questions are posed, and structure of the whole thesis is presented.

1.1 Rationale for the Thesis

Gravel-bed braided rivers are characterized by high energy, branching channel networks that bifurcate and re-join around mid-channels bars. They are found in a variety of physiographic settings, but most commonly in proglacial settings, glaciated valleys and piedmonts (Figure 1.1), associated with high rates of sediment supply and unconfined or erodible boundaries (Ashmore, 2013). A key characteristic of these rivers is that they are capable of transporting sediment across a wide range of flows, which leads to high rates of bed turnover and the production of a spatially and temporally diverse mosaic of habitats (Tockner et al., 2006). In addition to their high ecological value, braided rivers also represent a ready source of easily available aggregate that is economically prized (Surian, 2006). Furthermore, the sedimentary deposits of braided rivers represent key aquifers and reservoirs for the petroleum industry (Miall, 1977, 2013).

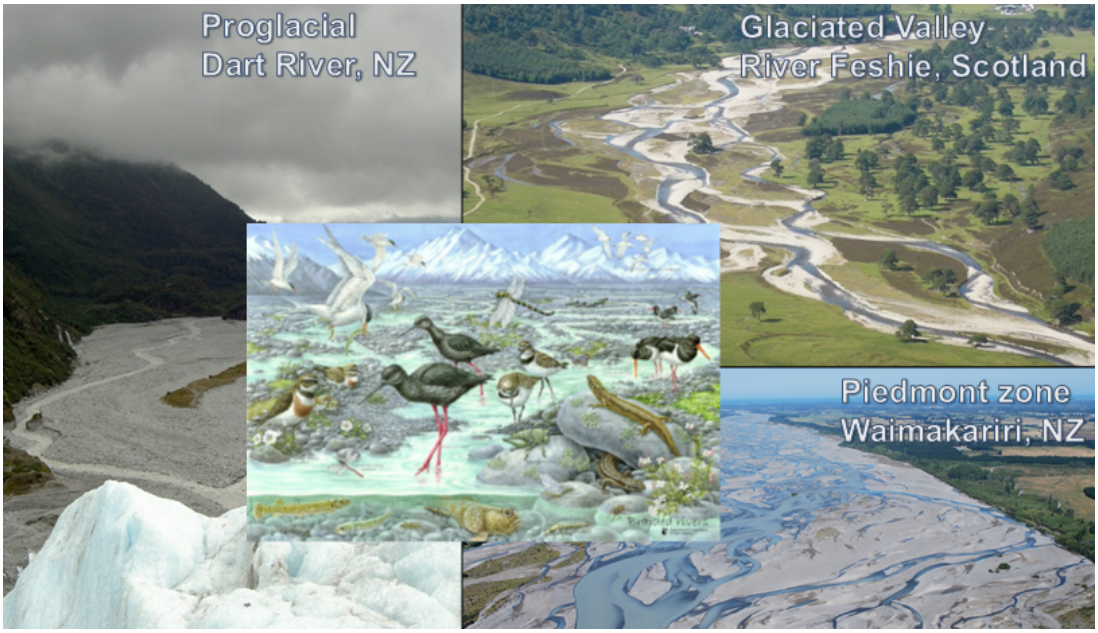

Figure 1.1 Example of braided rivers (not to scale). Photo Courtesy: Prof. James Brasington. The middle sketch is the artwork by Simone End adopted from O'donnell et al. (2016), illustrating the rich biodiversity that braided rivers support.

Given the multiple and sometimes competing resources and ecosystem services offered by these dynamic rivers, there has been long-standing interest in

understanding the factors controlling the emergence and maintenance of this distinctive channel pattern. However, the emphasis on equilibrium states may be largely theoretical, as there is a growing understanding that braided rivers are highly sensitive to changes in their flow regime and the available sediment supply (Ferguson, 1993; Piégay et al., 2009). Adjustments to these governing boundary conditions can lead to rapid changes in channel form associated with narrowing, widening and degradation (Liébault and Piégay, 2002). Ultimately, such changes may lead to metamorphosis of the channel pattern, from a braided planform to wandering or single thread meandering morphology, or the reverse trajectory under contrary environmental forcing (Ferguson, 1993; Richards et al., 2002; Caruso, 2006b).

While the geographic context for braiding is broadly well-established, the physical controls that lead to this channel pattern have been a long source of debate and remain contested (Ashmore, 1991; Church, 2006; Ashmore, 2013; Church and Ferguson, 2015). Historically, in addition to high sediment influx and erodible boundaries, the development and maintenance of braiding was considered to be dependent on a strongly varied or flashy discharge regime (Doeglas, 1962; Miall, 1977). However, the emergence of braided planform under steady flows in laboratory experiments (e.g., Ashmore, 1991; Bertoldi et al., 2009b; Redolfi et al., 2016a), has cast doubt on the necessity of this condition, which may instead be a confounding variable associated with high rates of sediment supply and glacial discharge. The search for a strong theoretical understanding of braiding has a long tradition. Leopold and Wolman (1957) argued for causal link between valley slope and formative discharge, an approach that led to a range of empirical relationships between bankfull discharge, reach averaged slope, sediment calibre and bank vegetation to distinguish channel patterns (e.g.,Henderson, 1963; Schumm and Khan, 1972; Van Den Berg, 1995; Millar, 2000; Eaton et al., 2010). Identifying an empirical threshold condition for braiding has however remained an elusive difficult task, due to the difficulties in

defining channel patterns that vary across a continuum of forms. The search for empirical discriminatory relationships are arguably ultimately confounded by different approaches to the classification of channel patterns, coupled with characteristically small data sets and a lack of consistent definitions of relevant variables (Ashmore, 2013).

An alternative theoretical approach for understanding the conditions for braiding has been pursued through the development of numerical stability analysis that seeks to understand the flow-bed interaction and role of bars in the formation of braiding (e.g., Engelund and Skovgaard, 1973; Parker, 1976; Fredsøe, 1978; Crosato and Mosselman, 2009; Kleinhans and Van Den Berg, 2011). This approach has led to the recognition of the initial width-depth ratio as a key predictor to delimit braiding (e.g., Crosato and Mosselman, 2009). However, the dynamism of fully developed braiding leads to the frequent breakdown of bars and channels, giving rise to morphologies that have a wide range of wavelengths that are poorly predicted by stability theories (Sapozhnikov et al., 1998; Gran and Paola, 2001; Schuurman et al., 2013; Garcia Lugo et al., 2015). While prediction of equilibrium channel forms is complicated, such stability analysis has indicated that braiding may actually be the default channel planform systems with high width-depth ratios, and that the maintenance of braided planforms only occurs for systems that have high sediment influx and are threshold-limited (Paola, 2001; Ashmore, 2013).

In addition to empirical and theoretical analysis, experimental analysis of the physical controls on braiding has been pursued through both laboratory (e.g., Hong and Davies, 1979; Ashmore, 1991; Bertoldi et al., 2009b) and numerical modelling (e.g.,Murray and Paola, 1994; Enggrob and Tjerry, 1999; Nicholas, 2013; Schuurman et al., 2013; Sun et al., 2015; Singh et al., 2017). Both these physical and numerical simulations have collectively concluded that braided channel networks can develop and continue to evolve dynamically under steady formative discharge in a relatively

unconstrained setting. There is, therefore, a broad consensus now that such discharge variability is not required for development and maintenance of braiding channel patterns (Bristow and Best, 1993; Ashmore, 2013). What remains less clear, however, is whether the characteristics of braided morphologies are sensitive to flow variability.

It is clear that braided rivers change their planform radically with changes in discharge (Mosley, 1983; Egozi and Ashmore, 2009). Moreover, the inheritance of varying morphological conditions will, in turn, affect the pattern of adjustment that ensues from different stage conditions (Bristow and Best, 1993). Qualitatively, we would expect rising stages to be associated with high-intensity erosional processes, leading to channel scouring and bar trimming (Bristow and Best, 1993). By contrast, during falling stages, rapid sedimentation is likely to promote flow divergence and sculpting of top bar morphologies under fast, steep, shallow flows (Bristow and Best, 1993). In terms of the broad pattern of morphological response to variations in flow, three characteristic modes of channel adjustment have been recognized from field observations (Surian et al., 2009a; Bertoldi et al., 2010; Ashmore, 2013). During low-magnitude formative floods, when discharge is limited to only a few anabranches, erosion and deposition are concentrated within the channel thalweg, outer-bank bends and confluences leaving the elevated bars undisturbed. During intermediate-magnitude floods, when braiding intensity peaks, many channels and bars are partially submerged and there is the frequent exchange of sediment between channel bifurcations and rapid rates of lateral bank erosion. At very high formative discharges, the entire braidplain may become inundated, resulting in a transient loss of apparent braiding intensity. Such conditions are associated with major reorganization of channel bifurcations, with chute cut-offs leading to frequent avulsions creating both local and far-field effects on the network structure. Formalizing this conceptual understanding of the role of discharge on the morphodynamics of braiding is

complicated by the difficulty of observing rivers in flood, so that our empirical insights are inevitably gleamed by examining channel structure before and after events, but rarely during. Moreover, scaling physical models to fully account for the effects of variable discharge is complicated by the difficulty of representing sediment mixtures and the need to establish and maintain relationships between discharge and sediment influx. As such, there is an urgent need to evaluate alternative methods to understand these interactions and the emergent morphological responses.

In recent years, the role of discharge variability has gained further interest due to the interaction such variability will have on the pattern of vegetation colonisation and development (Hickin, 1984; Osterkamp, 1998; Millar, 2000; Gran and Paola, 2001; Gurnell et al., 2001; Tal et al., 2004; Jang and Shimizu, 2007; Eaton et al., 2010; Tal and Paola, 2010; Crosato and Saleh, 2011; Welber et al., 2012; Nicholas, 2013; Welber et al., 2013; Surian et al., 2015). The colonisation of bars by vegetation is associated with significant increases in the bed/bank strength and flow resistance, which together increase the required force for erosion, while simultaneously promoting sedimentation (Hickin, 1984). Studies exploring effects of the bank vegetation on channel pattern have consequently identified the reduced rates of lateral channel mobility, which promote transformation of the channel pattern from braiding to single thread sinuous forms through increased bar height and lower width-depth ratio as the channel network incises (Millar, 2000; Jang and Shimizu, 2007; Eaton et al., 2010; Crosato and Saleh, 2011; Nicholas, 2013). Conversely, the removal of vegetation has been likely to promote the re-establishment of braiding (Hicks et al., 2007). Laboratory simulations have also been used to explore the effects of bar colonisation on the morphodynamic evolution of braided rivers at formative steady discharge (Gran and Paola, 2001; Tal et al., 2004). These studies show that vegetation restrains bar mobility and promotes incision, so that the active width contracts into only a few bifurcating channels. Over the longer-term, vegetation

colonisation is associated with increasing channel depth, increased bar height, a decrease in width : depth ratio, a decrease in the channel mobility and a decrease in braiding intensity (Gran and Paola, 2001; Tal et al., 2004). More recently, Tal and Paola (2010) studied the morphodynamic evolution that takes place during vegetation colonisation under an unsteady flow regime. This pinpointed the importance of flow variation as a pre-requisite to allow vegetation to colonize bar surfaces and then subsequently drive metamorphosis of the planform by the associated incisional morphodynamics described above. Specifically, they observed that bar colonisation was dependent on the dispersal of vegetation propagules (here, alfalfa seeds) on to bar tops. During periods of low flow, these dispersed propagules lead to colonisation of the emergent bars and acted to trap further seeds during subsequent high flows. Plants that survived successive high flow periods then continued to grow facilitating further deposition and seedling growth, ultimately creating stable islands. These islands coalesced through time forming a continuous floodplain dissected by palaeochannels. Colonisation of vegetation continued until a new stable channel width and dynamic steady state was established.

Beyond the laboratory, there are numerous examples of rivers that have undergone channel metamorphosis, changing their form from a highly braided state to less active or even incised single thread channels. In many cases, anthropogenic stresses, through either flow regulation, the introduction of aggressive non-native species, or sediment trapping have been identified as key precursors driving the responses (Piégay et al., 2009;e.g., Ubaye River, Ain River, Fier River, Arve River, and Upper Rhône in France; Waitaki River in New Zealand; Platte River in USA). Similar trends of change have also been reported in Italy, Austria and Japan (see Surian and Rinaldi, 2003; Tockner et al., 2006; Gurnell et al., 2009). Conversely, in some cases, shifting form from single thread to a highly active braiding state has also been reported, following human activities such as pastoral farming, clearing of the natural forest, and

related excessive sediment supply (Piégay et al., 2009; e.g., Waiapu and the Waiapoa from New Zealand). It is, however, increasingly clear that the sensitivity of these feedback processes could potentially drive instability in channel pattern from subtler and less readily identifiable causes. For example, changes in the inter arrival frequency of floods may promote bar top vegetation colonisation, that should reach a sufficient state of maturity, raising the critical entrainment threshold for erosion so that the next major floods are incompetent and the channel inevitably becomes to incise (Richards et al., 2002).

The impact of vegetation colonisation on the ecosystem services offered by channels is complex. For example, vegetation may be introduced to control bank or bend erosion (Beeson and Doyle, 1995), although a significant reduction in channel width (Liébault and Piégay, 2002) may reduce channel capacity leading to flooding (Eschner, 1983). Vegetation helps to trap fine sediment, which in the long-term may have a tendency to facilitate bed armouring that degrades in-stream habitat (Kondolf et al., 1993). Significant change on the bar and channel pattern may also degrade the habitat for key migratory, ground-nesting birds (Tal et al., 2004; O'donnell et al., 2016). To alleviate such problems, river management programmes often consider strategies such as vegetation removal (Tal et al., 2004; Piégay et al., 2009) and allocation of sufficient discharge on the main stream to avoid excessive vegetation establishment (Biggs et al., 2008). Such actions are, however, often based on trial and error, given the lack of a clear theory governing the potential long-term geomorphic trajectory. There is, therefore, an urgent need to develop robust quantitative insights into the interaction of flow regimes, sediment transport and vegetation growth, in order to provide a strong science base for management strategies. This thesis aims to support this wider goal.

1.2 Research Methodologies

Having identified the context for this thesis, this section examines the available approaches and research methods that could be adopted. There are three commonly used methodologies to interrogate the behaviour of river systems: physical modelling using flume-based experiments; field observations and experiments in natural rivers; and numerical modelling of the conceptual or physical driving processes. The relative merits of these approaches and their potential synergies are discussed briefly below.

1.2.1 Flume Based Approach

Physical models, also termed as hardware models, typically take the form of flume-based experiments that seek to represent a scaled model of a given natural prototype. Scaling relationships are typically based on the concept of similarity comparing Froude number and shear stress and prescribed relationships between slope and sediment size to parameterize sediment mobility (Parker, 1979; Kleinhans, 2010). Physical models of braiding have been a cornerstone of our current perceptual understanding, providing a ready means to create a closed system in which it becomes possible to examine the response of channel morphology to key allogenic controls (e.g., Leopold and Wolman, 1957; Ashmore, 1982, 1991). Flume models have provided critical insights into the mechanisms of bedload transport/transfer (Ashmore, 1987, 1988; Young and Davies, 1990; Warburton, 1996; Bertoldi et al., 2009a), planform dynamics (Bertoldi et al., 2009b); the effects of altered sediment and discharge supply (Germanoski and Schumm, 1993; Madej et al., 2009); changing of channel forming discharge (Egozi and Ashmore, 2009), and controls on bed form and grain mobility path (Kasprak et al., 2015).

More recently, as described above, laboratory experiments have also been instrumental to understand the role of vegetation on braided river morphodynamics (e.g., Gran and Paola, 2001; Tal et al., 2004; Coulthard, 2005; Jang and Shimizu,

2007; Tal and Paola, 2010; Welber et al., 2013). However, while physical models have provided valuable insights, they suffer from the difficulty of reconciling widely contrasting physical scales. Particularly problematic in this regard, are the representation of highly heterogeneous sediment mixtures (fundamental to understand bed armouring and shear stress partitioning) and flexible vegetation. Moreover, physical models require the maintenance of expensive laboratory facilities and long run-times (to avoid capturing transient responses) that preclude comprehensive exploration of the system's parameter space.

1.2.2 Field Studies and Remote Sensing

Insights into braiding processes and the morphological structure and kinematics of braided rivers have long been the subject of detailed empirical studies of natural river systems. In this context, gravel-bed braided rivers pose a major challenge, due to their high width, shallow topography (high width-depth ratio) and typically fast, shallow flows that transport sediments across a wide range of flows (Williams et al., 2014).

Historically, therefore, studies of braided rivers have tended to focus on the analysis of changing channel form through time. Traditionally, this was pursued through a combination of planform mapping (from aerial photography and satellite imagery) and repeat surveys of monumented cross-sections (Sanyal, 1980; Mosley, 1982; Ferguson et al., 1992; Warburton et al., 1993; Bertoldi et al., 2010). The use of repeat observations of channel morphology enables what (Church, 2006) describes as the 'inverse approach' to link river form and the sediment fluxes that drive it. In this, observations (estimates) of volumetric change through time can be coupled with either assumed or known rates of sediment influx or efflux to derive a sediment budget for a reach, that accounts for the storage and transfer of bed material fluxes longitudinally (Brasington et al., 2000). Recently, this approach has also been used to provide insights into evolutionary trajectory of rivers (in response to a range of disturbances or perturbations associated with varying discharge, sediment supply/calibre,

vegetation and anthropogenic interventions). These approaches use a combination of geospatial and cross-sectional data to reconstruct the morphological trajectory which is then used to identify the linkage between the nature of adjustment and the associated controls and an attempt to help forecast possible future states/trajectories (e.g., Fryirs et al., 2012; Ziliani and Surian, 2012; Brierley and Fryirs, 2013; Brierley and Fryirs, 2016; Scorpio et al., 2018). Clearly, while a powerful tool to interrogate the pattern of channel adjustment and link this to the forcing controls, this approach is limited by coarse spatial and temporal resolution of the observations available (Ferguson et al., 1992; Brasington et al., 2000; Lane et al., 2003). Recent developments in remote sensing and geomatics, in particular the advent of airborne and terrestrial lidar, softcopy and structure-from-motion photogrammetry, however, offer new pathways to understanding channel morphodynamics (Vericat et al., 2017). These new technologies enable dense 3D reconstructions of fluvial systems that can capture grain-scale morphologies seamlessly over large reaches (e.g., Bertoldi et al., 2011b; Brasington et al., 2012; Westoby et al., 2012; Williams et al., 2014; Vericat et al., 2017).

These very high-resolution topographic models are ideally suited to quantify morphodynamics, and reconstruct transport rates indirectly using the morphological approach (Ashmore and Church, 1998; Redolfi, 2014) and DEM differencing techniques (Wheaton et al., 2010; Wheaton et al., 2013; Vericat et al., 2017). However, while this approach has promise, data acquisition remains expensive and limited due to high costs of labour and sensor technology (Williams et al., 2011; Vericat et al., 2017). Moreover, most of the advances in topographic reconstruction have focused on sub-aerial surfaces and acquisition of high-quality bathymetric data, particularly during high flows and over vegetated areas remains challenging.

1.2.3 Numerical Modelling of Channel Morphodynamics: a new paradigm

Although the flume and field-based methodologies provide useful mechanisms to scrutinize fluvial processes and channel responses, few laboratory or field studies have the necessary depth of perspective to understand the long-term geomorphic trajectory of braided rivers (Ferguson, 1993). Such insights are increasingly important, given the growing stresses on braided rivers and the need to fulfil the human demands for flood protection, navigation, sustainable mining, hydropower and water supply while simultaneously conversing and maximizing the ecosystem services these rivers provide.

Over the last two decades, there has been increasing interest in the possibility of using numerical models to simulate the dynamics of braided rivers and provide new vehicles to understand their driving controls (e.g., Murray and Paola, 1994, 1997; Sapozhnikov et al., 1998; Enggrob and Tjerry, 1999; Doeschl-Wilson and Ashmore, 2005; Jang and Shimizu, 2005; Doeschl et al., 2009; Crosato and Saleh, 2011; Li and Millar, 2011; Nicholas, 2013; Schuurman et al., 2013; Williams et al., 2013; Ziliani et al., 2013; Sun et al., 2015; Javernick et al., 2016; Williams et al., 2016a; Singh et al., 2017). Early developments in this field focused largely on the development of reduced complexity models, often in the form of spatially explicit, cellular automata models; most notably the seminal framework of Murray and Paola (1994). While conceptually elegant, these models are gross simplifications and provide, at best, partial representations of the driving forces (Brasington and Richards, 2007). Nonetheless, these models appear able to capture some of the essential non-linear relationships between flow routing and sediment transport that lead to braiding (Murray and Paola, 1994; Sapozhnikov et al., 1998; Doeschl-Wilson and Ashmore, 2005; Doeschl et al., 2009). As computational resources have improved, the complexity of solvers used in numerical morphodynamic models has advanced and in the last five years, a number of numerical models have emerged that loosely-couple shallow water wave solvers and

mixed fraction sediment transport models (e.g., Delft3D, TELEMAC, BASEMENT and HSTAR, see Williams et al., 2016 for a review). These two contrasting modelling philosophies are reviewed below.

a) Reduced Complexity Modelling

Reduced Complexity Models (RCM) seek to simplify the key physical processes as a highly conceptualized set of rules. Philosophically, the approach rests on the principle that emergent system responses at one scale rest on the interactions between key variables at one scale below that (Werner, 1999). As such, the emergence of reach-scale braided networks is assumed to stem from interactions that reflect neighbourhood rules for the routing of water and sediment based on simple kinematic principles (Brasington and Richards, 2007).

The archetypal RCM is the Murray and Paola (1994, 1997) model, henceforth the MP model. This approach was motivated by the aim of identifying the minimum complexity required to produce branching, braiding patterns rather than to explore process-scale phenomena (Murray and Paola, 1997; Doeschl-Wilson and Ashmore, 2005). It discretizes spatial domain into a lattice of square cells, across which flow and sediment transport are routed kinematically based on the bed elevation difference between the participating cells. Sediment transport is calculated using a simple excess shear stress formula, based on a simple power law and the local sediment mass balance is calculated using the Exner equation (Doeschl-Wilson and Ashmore, 2005). This model has been shown to produce characteristic planform features of braided systems, such as braid bars, confluence scours, diffluence deposition, reworking, splitting, channel switching and migration (Murray and Paola, 1994, 1997; Sapozhnikov et al., 1998; Doeschl-Wilson and Ashmore, 2005). Doeschl et al. (2009) have, however, demonstrated the failure of the model to reproduce a universal topographic signature, such as the local slope distribution that reflects either flume or natural rivers. This discrepancy has been explained to arise from three mechanisms.

First, the model distributes the discharge and sediment according to the bed elevation difference instead of water surface elevation (Coulthard et al., 2000) or potentiometric surface (Thomas and Nicholas, 2002). Furthermore, routing is limited to maximum angles of 45 degrees and can only occur downstream, hindering the development of the diagonal channels. Secondly, the hydrodynamic solutions are based on a steady state kinematic assumption, and do not represent the inertial stresses that are critical for driving flow and sediment vertically out of pools (Brasington and Richards, 2007). Thirdly, there is no mechanism for the lateral redistribution of momentum. This results in unrealistic transverse water surface gradients and a tendency for exaggerated sediment transport at confluences that leads to deep scour pools (see Doeschl et al., 2009).

Even though these limitations are well understood, the convincing planform structure produced under such simplifying assumptions has promoted the further development of RCMs. For example, both CAESAR (Coultard et al. (2000, 2005; Van De Wiel et al. (2007)) and Thomas and Nicholas (2002) use modifications of the basic MP formulation to drive models of braiding. However, unlike MP, these formulations incorporate hydrostatic effects and allow wider angles of flow dispersion. More recently, such cellular frameworks have been used to simulate braided river response under varying sediment supply and vegetation colonisation (e.g., Thomas et al., 2007; Ziliani et al., 2013).

b) Physics-Based Numerical Modelling

Physics-based models (PBMs) seek to solve the governing 2D shallow water equations to predict the spatial distribution of flow and bed shear stress (Kleinhans, 2010; Wright and Crosato, 2011; Nelson et al., 2016). The latest generation of morphodynamic models typically involve loosely-coupled standard 2- and 3D hydrodynamic and sediment transport codes, and are solved using either finite different, element or volume methods (e.g., Mike 21, Delft3D, HSTAR, TELEMAC,

BASEMENT). These simplifying conditions (i.e., neglecting vertical pressure gradients) enable continuous simulation of river evolution over a wide range of timescales (Struiksma, 1985; Warren and Bach, 1992; Nelson et al., 2003; Lesser et al., 2004; Vetsch et al., 2017a; Nicholas, 2013; Siviglia et al., 2013; Nelson et al., 2016). These emerging tools offer the opportunity to create virtual laboratories to study the response of rivers under closely controlled conditions and with sufficient rapidity to enable robust analysis of predictive uncertainty (e.g., Williams et al., 2013; Javernick et al., 2016; Williams et al., 2016a). Moreover, these numerical models enable comprehensive quantification of the system across all relevant time and space scales, so that the constitutive mechanisms that control braiding in simulations are fully transparent.

Over the last decade, many physics-based numerical models have been developed to understand braided river form and process. Enggrob and Tjerry (1999) modelled the sand-bed braided Jamuna River, Bangladesh, using the numerical model Mike 21. Jang and Shimizu (2005) used numerical model to simulate the key features of a scaled physical model, capturing the mechanisms of bar growth, channel widening, scour holes at the lee side of bars, increasing of bar size with time, and dynamically varying sediment transport at the outlet. More recently, Crosato and Saleh (2011) used the popular Delft3D numerical model to demonstrate the role of bank vegetation to changing planform style. Nicholas (2013) developed the HSTAR numerical modelling framework to model the continuum of river channel forms, and to assess the vegetation control on the planform style. Schuurman et al. (2013) assessed the sensitivity of the Delft3D numerical model in producing bar and channel pattern. Sun et al. (2015) developed numerical modelling framework to reproduce the flume experiments of Egozi and Ashmore (2009) and assessed grain-sorting effects on braided rivers. Singh et al. (2017) assessed effects of sediment grading on bar and channel pattern using Delft3D.

While, this clearly represents a growing catalogue of research effort, approaches to model evaluation are inconsistent, with few studies focusing a range of metrics of model performance which are often based on ill-conditioned 2D, planform, characteristics without rigorous analysis of the quantitative internal process mechanisms that drive the emergent model responses. Given the heavy parametric load of such models, this creates the likelihood of significant ill-conditioning and the potential to generate apparently 'behavioural' planform predictions that are inconsistent with the predicted fluxes or the 3D morphology. There is therefore, a pressing need to develop a robust, consistent approach to the evaluation of these complex modelling systems that differentiates their performance across a spectrum of system characteristics, incorporating the predicted flux magnitude and distributions, the planform and fully 3D morphologies, and the evolving pattern of adjustment driven by sediment transfer.

1.3 Specific Research Context

1.3.1 Basement Numerical Model

This research focuses on an examination of a state-of-the-art physics-based morphodynamic model, BASEMENT (Basic Simulation Environment for Computation of Environmental flow and Natural Hazard Simulation, Version 2.2). Development by the Laboratory of Hydraulics, Hydrology and Glaciology at ETH Zürich, BASEMENT is a loosely coupled morphodynamic model. The model solves the shallow water wave equations and couples these with 2D bed material flux models to simulate the fundamental form-flow feedback process that drives fluvial morphodynamics using a flexible mesh. The equations are solved using an explicit finite volume scheme that enables the modelling of unsteady transcritical (where flows may contain both sub- and supercritical states) flows (see Vetsch et al., 2017a for detail). There are several advantages of this numerical model over its competitor formulations. First, the model is fully parallelized, enabling multi-threaded simulations that facilitate high time-space

resolution modelling that provides stable calculation of unsteady flows and high frequency hydrographs. Second, Bertoldi et al. (2014) have developed and coupled a dynamic vegetation sub-model with the BASEMENT framework. While simplistic, this model provides a basis to examine the feedback between flow, sediment and vegetation in braided rivers. Third, the BASEMENT uses a flexible mesh which provides an effective discretisation system to represent eroding banks or bar edges that doesn't suffer the serious numerical diffusion encountered with rectilinear grids. Lastly, BASEMENT provides multiple frameworks to represent bank erosion processes, including a simple geotechnical model that incorporates different angles of repose for dry, wet and deposited material (Vetsch et al., 2017a).

1.3.2 A Data Rich Natural Prototype System

The evaluation of BASEMENT will draw on a rich empirical record of data collection for the braided River Feshie, one of the most important Sites of Specific Scientific Interest (SSSI) in Scotland, and the most active gravel-bed river in Britain. Not surprisingly, the system has encouraged a long legacy of research focusing on braiding morphodynamics (e.g., Ferguson et al., 1992; Brasington et al., 2000; Rumsby et al., 2008; Wheaton et al., 2013). The site has also been used to test the development of novel methodological approaches. These include advanced geomatics methods to capture 3D morphological models of braided reaches and to pioneer methods to quantify topographic change detection (e.g., Brasington et al., 2003; Wheaton et al., 2010; Brasington et al., 2012; Wheaton et al., 2013), sedimentological analysis (e.g., Hodge et al., 2007; Hodge et al., 2009a, 2009b), and hydrological analysis (e.g., Ferguson, 1984; Werritty and Brazier, 1991; Soulsby et al., 2006). The river is also gauged in multiple locations and downscaling relationships available to quantify the hydrological boundary conditions around the key braided reach at Glenfeshie (from 1993 to 2010). This rich data record will be used to provide a robust parameterisation of the natural prototype for BASEMENT simulations.

1.4 Research Questions and Outline of the Thesis

The wider goal of this research is to examine the performance of a numerical morphodynamic model to simulate the development and maintenance of braiding under a range of boundary conditions and model parameterisations. An important contribution here is an attempt to use simulation modelling to interpret how braiding processes evolve and potentially differ under steady and unsteady flow conditions, in the absence and presence of vegetation. The research therefore focuses on the development of morphodynamic simulations for a prototype river in three scenario states: a) under a steady flow regime without vegetation growth; b) under an unsteady (variable) flow regime without vegetation; and finally, c) an unsteady flow on which vegetation colonization occurs according to a simple dynamical, disturbance-based framework. A governing principle underpinning the research is the critical evaluation of the model parameterisation required to capture the multifaceted character of braiding processes that extends across planform geometry, 3D topographic structure, and the internal distribution of forces and the transfer of sediments that drive channel evolution. Specifically, this research seeks to address four key research questions:

a) What characteristics of the structure and dynamics of braided rivers can be quantified as a hierarchical set of metrics and used to evaluate the performance of numerical models of braiding?
b) To what extent can the physics-based numerical model BASEMENT reproduce the characteristic behaviour of a natural prototype braided river under steady flow conditions?
c) How do the equilibrium model forms and forces derived at a steady flow condition differ from energetically-normalised different steady and unsteady simulations that incorporate variations in the frequency and magnitude of competent floods?

d) How does the interaction between vegetation growth rate and discharge flow regime govern the evolutionary morphology of braided rivers?

1.5 Structure of Thesis

The thesis is structured into eight chapters as follows:

Chapter 1: Thesis Introduction. This short chapter provides an overview of the research context, and wider goal of the research and the specific questions the thesis seeks to address.

Chapter 2: The Numerical Model, BASEMENT, and the Natural Prototype. This chapter describes the modelling framework used in the research and study site on the River Feshie that is used to parameterize the simulations and provide key empirical data for model evaluation.

Chapter 3: **Developing a Framework for the Validation of Numerical Morphodynamic Models.** This chapter seeks to address research question (a) directly. Drawing on the rich empirical data record for the prototype River Feshie, a four-fold hierarchical framework for model evaluation is proposed, incorporating planform character, 3D morphology, the internal distribution of forces and transport rates, and the morphodynamic behaviour captured by DEM differencing.

Chapter 4: Modelling the Development and Maintenance of Braiding under Steady Flow. This chapter addresses research question (b) and applies the model evaluation framework developed in Chapter 3 to examine the performance of BASEMENT to simulate equilibrium braided conditions from an initial plane bed condition. Particular focus is placed on evaluating the parameterisation of lateral sediment transport and bank erosion processes.

Chapter 5: Modelling the Development and Maintenance of Braiding under Unsteady Flow Regimes. This chapter examines unvegetated channel response to energetically normalised flow regimes that represent variations in storm hydrographs. Directly addressing research question (c), this chapter examines how different flow regimes, associated with differences in the pattern of inundation and transient sediment flux, lead to differences in the emergent channel form and dynamics.

Chapter 6: Modelling the Interaction of Flow, Sediment Transport and Vegetation. This final research chapter aims to synthesize the understanding in Chapters 3, 4 and 5, and evaluate how the geomorphic trajectory of braided river evolution responds when vegetation is introduced into the numerical system. Experiments with different vegetation growth rates are used to represent the effects of different vegetation communities or inter arrival storm frequency and demonstrate a strong dependence of the emergent channel form on this critical interaction.

Chapter 7: Discussion. This chapter synthesizes the research and re-examines the original four research questions posed.

Chapter 8: Conclusion. This chapter will present conclusion of the research.

Chapter 2: The Numerical Model, BASEMENT, and the Natural Prototype

Chapter Summary

This chapter firstly provides details about the BASEMENT numerical model that are relevant for studies in this thesis. Secondly, it provides a relevant detail about the study area particularly, hydrology, bed sediment and the reach averaged properties of the braided Feshie which is the natural prototype reference for this thesis.

2.1 Introduction

Predicting how a natural (or indeed man-made) channel responds to imposed water and sediment fluxes remains one of the most challenging areas of geomorphology and civil engineering. At a basic level, this reflects the sensitive mutual dependence of flow and form, in which the channel geometry controls the spatial distribution of flow and associated shear stresses, which in turn then erode and transport sediments altering the morphology (Brierley et al., 2013). This feedback can result in rapidly divergent predictions due to uncertainties in the boundary conditions, model parameters and the numerical solution (Oreskes and Belitz, 2001).

The desire to predict this complex problem is typically motivated by three factors (after Nelson et al., 2016). The first goal is to understand the channel form that arises spontaneously in a given catchment context, controlled by the imposed material fluxes, valley gradient and boundaries. This type of modelling is often more than a theoretical quest and is increasingly pursued in order to inform appropriate restoration strategies that reflect changes in the imposed conditions. The second concern is to predict how a given channel will adjust to alterations in the flow and sediment supply. This type of modelling could be used to predict changes in channel capacity associated with altered flood regimes, or more direct interventions such as the effects of river impoundment or re-grading. Finally, modelling is undertaken in order to design an equilibrium channel form -a regime channel- capable of carrying a given water and sediment load without long-term aggradation or degradation (Mackin, 1948).

In response to this range of questions, a spectrum of approaches to modelling morphodynamics has developed over the last two decades. As discussed in Chapter 1, these can broadly be classified into two distinct forms: reduced complexity modelling (RCM) and physically-based modelling (PBM). These two approaches share a common presumption, in that the time-scales associated with the

hydrodynamics are considerably shorter than the response times governing morphological evolution. This permits decoupling of the flow and sediment transport, so estimation of the flow field can be processed before the computation of the estimated sediment flux, which in turn is used to update the bed morphology. If the pattern of sediment flux leads to an adjustment in form, the flow field will adjust, and the bed will continue to evolve, in turn iteratively adjusting the distribution of flow.

Reduced complexity models seek to represent these feedbacks through a set of highly simplified, conceptual rules. While this offers a parsimonious 'Occam's razor' approach to the problem, it also reflects the computational difficulty of solving physically-based momentum and sediment flux equations numerically (Brasington and Richards, 2007). However, over the last five years, rapid increases in computational power have relaxed this constraint and enabled the development of a wide range of physically-based modelling frameworks (see Williams et al., 2016b for a review).

So-called physically-based models seek to solve the conservation equations governing fluid and sediment motion. However, the current generation of models use simplified versions of the full equations, neglecting certain terms or by integrating vertically and/or horizontally to develop averaged forms of the equations. In the limit, there is clearly a continuum between these simplified physics-based models and the RCM rules, which take such abstraction to a further level. Most PBMs use the 2D depth-averaged or shallow water approximation with an appropriate turbulence closure scheme (e.g., Lesser et al., 2004; Vetsch et al., 2017a; Wright and Crosato, 2011; Nicholas, 2013; Nelson et al., 2016). This approach has been shown to generate behavioural stress distribution, even in complex channels, despite the apparent simplifications of the fluid dynamics (e.g., Williams et al., 2013; Javernick et al., 2016).

In this research, the 2D version of numerical software BASEMENT which is called as BASEplan (Vetsch et al., 2017a) is deployed to simulate braiding processes. This is freeware software distributed as a set of binaries. However, in this case, the code was made available from ETH enabling access to a set of unpublished tools for the simulation of vegetation growth and senescence (Bertoldi et al., 2014). While the modelling framework lacks some of the parameterisation found in allied frameworks (e.g., representations of secondary, helical flow), the novel vegetation framework allows for dynamic growth and die-back which is essential to address research question (d) described in Chapter 1. This chapter provides an overview of the basic canonical form of the model and describes the numerical schemes available to solve the set of equations.

2.2 The BASEMENT Numerical Model

BASEMENT (Basic Simulation Environment for Computation of Environmental flow and Natural Hazard Simulation) is a loosely-coupled morphodynamic model developed by the Laboratory of Hydraulics, Hydrology and Glaciology at ETH Zürich (Vetsch et al., 2017a). The model solves the shallow water wave equations and couples these with 2D bed material flux models to simulate the fundamental form-flow feedback processes that drive fluvial morphodynamics. The equations are solved using an explicit finite volume scheme and enable modelling of unsteady, transcritical flows. The key components of the model that are relevant for this study are described below.

2.2.1 Hydrodynamics

a) Shallow Water Equations

BASEMENT solves the depth integrated Shallow Water Equations (SWE), comprising the mass and momentum continuity terms, assuming hydrostatic pressure to provide vertically averaged equations. The fundamental mass balance equation is;

$$\frac{\partial h}{\partial t}+\frac{\partial(\bar{u}h)}{\partial x}+\frac{\partial(\bar{v}h)}{\partial y}=0 \qquad \text{Eq. 2.1}$$

The momentum balance equation in the stream wise (x) direction is;

$$\frac{\partial \bar{u}}{\partial t}+\bar{u}\frac{\partial \bar{u}}{\partial x}+\bar{v}\frac{\partial \bar{u}}{\partial y}+g\frac{\partial h}{\partial x}=-g\frac{\partial zB}{\partial x}-\frac{1}{\rho h}\tau Bx+\frac{1}{\rho h}\partial\left[h\frac{(\bar{\tau}xx+Dxx)}{\partial x}\right]+\frac{1}{\rho h}\partial\left[h\frac{(\bar{\tau}xy+Dyx)}{\partial y}\right] \qquad \text{Eq. 2.2}$$

Similarly, the momentum balance equation in transverse (y) direction is given as;

$$\frac{\partial \bar{v}}{\partial t}+\bar{u}\frac{\partial \bar{v}}{\partial x}+\bar{v}\frac{\partial \bar{v}}{\partial y}+g\frac{\partial h}{\partial y}=-g\frac{\partial zB}{\partial y}-\frac{1}{\rho h}\tau By+\frac{1}{\rho h}\partial\left[h\frac{(\bar{\tau}yx+Dyx)}{\partial x}\right]+\frac{1}{\rho h}\partial\left[h\frac{(\bar{\tau}yy+Dyy)}{\partial y}\right] \qquad \text{Eq. 2.3}$$

Where: h is water depth in m; g is acceleration due to gravity in m/s^2; $\bar{u}$ and $\bar{v}$ are depth avearged velocity in x- and y direction in m/s; zB is bed elevation in m; ρ is water density in kg/m^3; τBx and τBy are bed shear stress in x- and y direction in N/m^2; Dxx, Dxy, Dyy and Dyx are momentum dispersion term in N/m^2; $\overline{\tau xx}$, $\overline{\tau xy}$, $\overline{\tau yy}$, and $\overline{\tau yx}$ are depth averaged viscous and turbulent shear stresses in N/m^2.

The momemtum terms (D_{xx} , D_{xy}, D_{yy} and D_{yx}) in the third and fourth term on the right hand side are required for the dispersion of momentum transfer due to vertical non-uniformity of flow velocity (see Vetsch et al., 2017a). However, in the current version of BASEMENT, this term is not implemented (see Vetsch et al., 2017a).

b) Numerical Solution

The constitutive equations are solved using an explicit, finite volume numerical scheme. There are a range of different numerical solvers available in the model, including exact Riemann solver (Godunov, 1983) and approximate Riemann solvers (HLL and HLLC). The exact Riemann solver is robust to solve strong wave interactions and flow with sharp gradients and shear waves. However, the use of this solver increases simulation times, particularly when dispersion and turbulence equations are included (Toro, 2001). The HLL (Harten, Lax and van Leer) solver is an

approximate Riemann solver formulated by Harten (1983) and based on a two-wave assumption which neglects intermediate waves (see Vetsch et al., 2017a for details). The HLLC (Harten-Lax-van Leer-Contact) is an approximate Riemann solver which accounts the effects of intermediate waves, such as shear waves and contact discontinuities. Toro (2001) suggests that approximate Riemann solvers (HLL and HLLC) may save approximately 20% of simulation time when compared to exact Riemann solvers. The choice of solver therefore remains a key choice in design of the modelling framework and must be tuned to account for the complexity of the hydrodynamic context, as well as the duration of the simulation and the available computational resources.

c) Turbulence Model

Turbulence is a tangle of vortices that appears unsteadily in all directions in a flow with high Reynolds numbers (Rodi, 1993). In order to represent the processes that a numerical model cannot resolve, diffusion terms are incorporated in the numerical models, and the turbulence model also adds a kind of diffusion. In the BASEMENT numerical model, the turbulence and viscous shear stress is modelled by using Boussinesq eddy viscosity concept (Vetsch et al., 2017a). The viscosity term in the Boussinesq's formulation is the sum of eddy viscosity and kinematic viscosity. The kinematic viscosity depends upon fluid property which is most often taken as constant (i.e. 1E-6) (see Vetsch et al., 2017a). The eddy viscosity is the key parameter representing the influence of turbulence in the numerical solutions, which transfer momentum created by turbulence and adds to the internal fluid friction on a larger scale. The eddy viscosity could be calculated dynamically or used as a constant value (Lesser et al., 2004; Vetsch et al., 2017a). The dynamic calculation requires higher simulation time, so may not be feasible for large scale and long-term modelling. As a consequence, use of constant eddy viscosity has been most often used in numerical modelling realm (e.g., Nicholas, 2013; Schuurman et al., 2013; Williams et

al., 2013; Singh et al., 2017). While the eddy viscosity term is one of the most important calibration parameter in determining water depth and velocity distribution, there is little evidence available in the field of braided river numerical modelling (Williams et al., 2013). The sensitivity of the horizontal eddy viscosity based on Delft3D numerical modelling was carried by Williams et al. (2013). Their experiment based on the braided Rees River measured hydrodynamics (water depth and velocity) revealed increase in homogeneity of water depth and velocity as the horizontal eddy viscosity coefficient was increased and has found optimum range of value in between 0.01 to 0.1 m^2/s at the grid size of around 2 m. In the BASEMENT numerical model, there is recommendation of eddy viscosity coefficient in between 0.1 and 1, but no published references are available for braided river simulation. The intensive experiment on Rees River, NZ by Williams et al. (2013) calibrated his hydrodynamic model at 0.1 m^2/s eddy viscosity.

d) Stability Condition

The hydrodynamic time step in the model is determined by satisfying the Courant-Friedrich-Levy condition where:

$$CFL = \left(\frac{\sqrt{u^2 + v^2} + c}{L} \right) \Delta t \leq 1 \qquad \text{Eq. 2.4}$$

Where: u and v are the velocity in x and y-direction in m/s; c is the wave celerity in m/s, $c = \sqrt{gh}$, h is water depth in m/s; L is the edge length of the computational cell in m. The model allows defining maximum and minimum time steps to reflect the CFL limit.

e) Wetting and Drying

To avoid numerical instabilities that could be created by very small water depths, a threshold water depth is typically parameterized (e.g., Lesser et al., 2004; Nicholas, 2013; Siviglia et al., 2013). When water depth drops below this threshold, the velocity

in the cell is set to zero to inhibit further hydrodynamic calculations. In BASEMENT, this value can be varied from 10^{-6} to 0.1 m, although in practice thresholds are typically set at between 0.05-0.1 m. Cells are assumed to dry when flow depth is below this critical threshold. Cells are assumed to be partially wet when the depth is below the threshold, but when adjacent nodes are submerged. Cells are assumed wet only when the water depth is above the threshold value. In most applications of morphodyamic simulations to date, a threshold of 0.05 m has been used for water depth in hydrodynamic calculations (e.g., Williams et al., 2013) and 0.1 m for the sediment transport estimation (Schuurman et al., 2013; Sun et al., 2015; Singh et al., 2017). It is important to bear in mind that increasing the threshold for water depth increases stability of the model but at the cost of losing hydrodynamic accuracy (Vetsch et al., 2017a). In BASEMENT, there is no option to use different threshold water depths for hydrodynamic and sediment transport calculations which means that a similar threshold water depth should be used.

f) Bed Roughness

Bed roughness can be varied for each element in the model domain and can be parameterized separately for the closed boundaries (side walls). The side wall friction may be set to a given percentage of bed friction or equivalent to the main channel friction or simply neglected, depending upon objective of the study (see Vetsch et al., 2017a). The bed roughness can be determined through different relationships such as composition of bed material, bed form, type of channel cross section, obstructions and vegetation (e.g., Cowan, 1956; Arcement and Schneider, 1989).

g) Bed Shear Stress

The bed shear stress is calculated using the established quadratic function comprising velocity and friction coefficients:

$$\tau_{Bx} = \rho \frac{|u|u}{cf^2} \text{and } \tau_{By} = \rho \frac{|u|v}{cf^2} \quad \text{Eq. 2.5}$$

$$|u| = \sqrt{u^2 + v^2}$$

Where: u and v are the velocity in x and y-direction in m/s; $cf = \frac{K_{str} R^{1/6}}{\sqrt{g}}$; K_{str} is Manning's Strickler coefficient in $m^{1/3}/s$; R is hydraulic radius in m; g is the acceleration due to gravity in m/s^2.

h) Closed and Open Boundaries

The side walls are assumed to represent closed boundaries, whereas the upstream and downstream boundary are taken as open boundaries. A range of formulations are available to parameterize the flow-depth at the open boundaries (see Vetsch et al., 2017a). At the upstream boundary, discharge is typically imposed assuming sub-critical flow conditions. This is assured by setting the average bed slope perpendicular to the inlet section. Both steady and unsteady flow conditions can be represented by changing the wet cross-sectional area corresponding to normal water depth over time. Cells above the water elevation are treated as impermeable boundaries. The discharge on wetted cells is distributed in proportion to local conveyance which depends upon hydraulic radius, wetted area and friction factor, or the local wetted area of cells, which assumes a uniform boundary velocity.

Different formulations are available for the downstream boundary condition, including free elevation, weir, normal depth, a depth-discharge relationship and fixed sluice gates. For modelling free flowing rivers where there are no interventions such as weirs or gates, it is common to use free elevation boundary. BASEMENT uses a zero-gradient boundary condition in order to maintain zero hydraulic gradients at the boundary to avoid instabilities (see Vetsch et al., 2017a). A zero gradient boundary may encourage propagation of boundary errors up to five to ten grid cells upstream,

so it common practice to extend the modelled domain beyond the area of interest (see Vetsch et al., 2017a).

2.2.2 Morphodynamics

a) Spatial Domain Discretisation

The hydrodynamic discretisation is based on an unstructured grid in which the bed elevation is defined at the vertices that delimit the edges and then the perimeter of each element. While computationally more demanding than a regular Cartesian grid, this approach enables accurate representation of irregularly sampled bed topography and the preservation of sharp edges. However, the approach does prove problematic for morphodynamic simulation, due to the decoupling of the sediment and water fluxes. First, it is difficult to define a robust rule to redistribute the change in mass of an element to the associated nodes that require topographic updating. Second, any changes to vertices directly affect neighbouring elements. Consequently, this poses problems for conservative schemes and may result in unstable fluxing into neighbouring cells and excessive numerical diffusion.

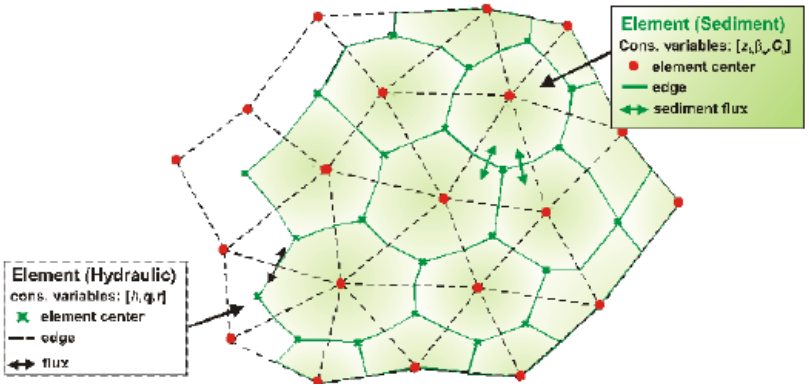

Figure 2.1 Dual mesh approach in domain discretisation in BASEMENT. Hydrodynamic calculations are based on the bed elevation defined at cell vortexes. Morphodynamic simulations are based on the new mesh (green) which is created by connecting centre of edge cell and cell centre (Source: Vetsch et al., 2017a).

In order to overcome with these problems with the sediment calculation, a separate mesh around each node is automatically created by connecting the midpoint of edge of cell and cell centre (hydraulic of each cell) (Figure 2.1) (see Vetsch et al., 2017a

for details). As all the sediment variables are defined in the sediment element centre, change in sediment volume is solely used to update the corresponding sediment element centre, avoiding any diffusive influx into neighbouring cells (see Figure 2.1).

b) Bed Layer Discretisation

The first step in morphodynamic simulation is to schematize bed configuration to allow flow-form feedback. In BASEMENT, each cell is divided into three main control volumes as shown in Figure 2.2. The upper layer comprises the momentum and suspended sediment; the middle active layer is used for bedload transport and sediment sorting; and the bottom sub-layer for sediment exchange.

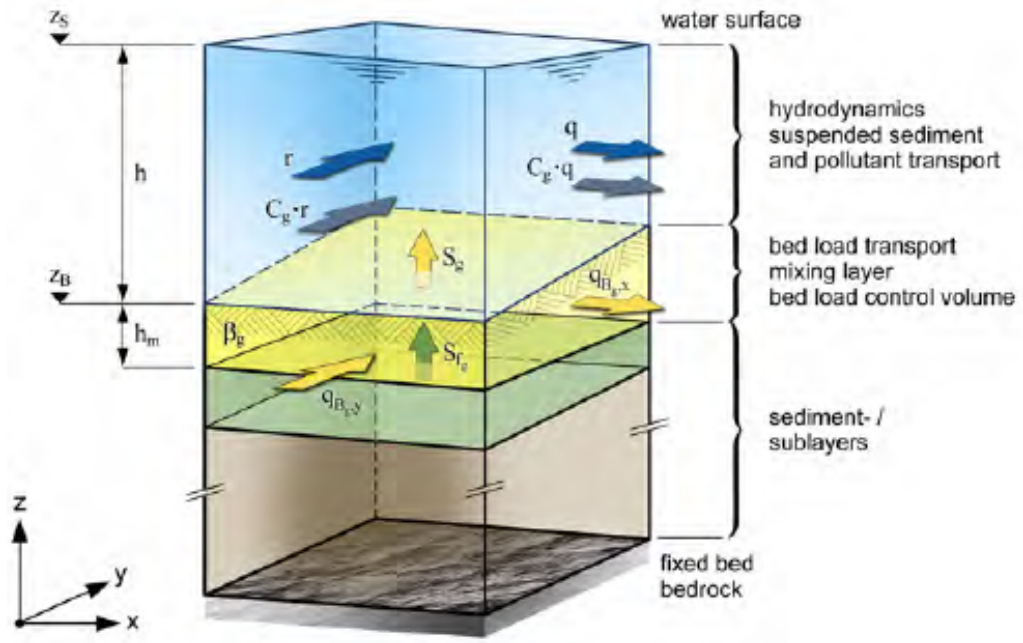

Figure 2.2 Vertical discretisation of cell. (Source: Vetsch et al., 2017a). The unknown variables in upper layer are water depth (h), specific discharge (q) and r in the direction of Cartesian coordinates x and y. In the active layer, $q_{Bg,x}$ and $q_{Bg,y}$ represent the specific bed load flux (index g refers to grain size class). The balance equation of water, sediment and exchange or source term determines the bed elevation.

For simulations with mixed-sized sediment mixtures, the bed can be schematised with an active layer and substrate layer (Figure 2.2). The active layer is the region where fluvial processes (erosion and deposition) take place, and is generally considered to have a thickness that is taken to be a fraction of a characteristic bedform dimension,

such as bar height or dune height; the latter being used in sand bed rivers (Ribberink, 1987). A substrate or sub-layer is defined below the active layer. This represents a store of sediment (mass) which is inactive (Sloff and Mosselman, 2012). Sometimes, an exchange layer is also added between the active layer and substrate layer in order to allow formation of sporadic deeper troughs (Sloff and Mosselman, 2012). Exchange between the active and sub-layer is required to enable the formation of deep scours (e.g., Sun et al., 2015; Singh et al., 2017).

This multi-layer formulation is particularly important for mixed-size simulations, but is not required for models based on uniform sediment fractions, as there is no need to account for vertical variation in grain size (Vetsch et al., 2017a; Sloff and Mosselman, 2012). For such single grain size simulations, the maximum height of bedforms such as bar height can be used to define the total bed thickness (Sloff and Mosselman, 2012). By default, BASEMENT automatically divides the defined bed thickness into number of slices in a proportion of 0.1 m (Vetsch et al., 2017a).

c) Stability Condition

The CFL criterion described above for ensuring stable numerical solution of the water fluxes is subject to a further condition for morphodynamic modelling. In this, it has to be assumed that the wave speed is much larger than the expansion velocity of the bed (Vetsch et al., 2017a). Calculation of the bed wave speed is complex and dependent on various factors including bed load, and lateral and gravity induced transport so, its local, exact determination is a difficult task. In its simplest form therefore, BASEMENT adopts the global hydrodynamic time step to solve sediment fluxes.

d) Open Boundaries

Defining appropriate upstream and downstream boundary conditions is a critical step in numerical modelling of river systems. The options for modelling the open hydraulic boundaries were described above. For the sediment fluxes, there is currently only one option available for the upstream open boundary, termed the IOUP. This boundary condition calculates the sediment influx based on the transport capacity of boundary cells. However, the amount of sediment transport supplied can be manipulated through a simple weighting coefficient (0-1) that can be used to modify the estimated flux; where a coefficient of zero implies no sediment, and unity implies influx at 100 % of the transport capacity.

At the downstream boundary, sediment efflux is modelled using the IODOWN scheme, which is based on a similar principle. In this, the sediment efflux is set equal to the influx of the boundary cells, so that all the sediments entering the downstream boundary is passed out of the model and the downstream slope is preserved. For practical purposes, there is again the possibility to allow certain percentage of sediment that enters into the boundary cell to be stored; and this has been found to enhance the stability of the model (Vetsch et al., 2017a). By default, BASEMENT sets this sediment storage factor to 0.9.

e) Bed Sediment Transport Model

A range of sediment transport formulations are available to quantify bed material flux (see Vetsch et al., 2017a for detail). As an example, the Meyer-Peter and Müller model (MPM) considers transport relations based on the median particle size (D_{50}) and is most often used in the simulation of gravel-bed rivers. The MPM sediment transport formula determines bed load transport as;

$$q = 8\sqrt{(\Delta g d_g^{\ 3}}\sqrt{(\theta - \zeta\theta_{cr})^3} \qquad \text{Eq. 2.6}$$

Where: q = total bedload transport in $m^3/s/m$; $\Delta = (\rho_s-\rho)/\rho$ is relative sediment density; g is acceleration due to gravity in m^2/s; dg is grain class size (D_{50} for single grains size here) in m; ζ is hiding-exposure coefficient which is only relevant in the case of simulation with multi-grain size sediment (Ashida, 1971); θ is dimensional shear stress (Shield number) which is calculated as;

$$\theta = \frac{\tau B}{(\rho s - \rho) g dg} \qquad \text{Eq. 2.7}$$

Where: τB is bed shear stress in N/m^2 which is calculated by Eq. 2.5; g is acceleration due to gravity in m^2/s; ρ_s is sediment density (2650 kg/m^3); ρ is water density (1000 kg/m^3).

BASEMENT uses the Van Rijn (1984) criteria to determine the critical Shields parameter based on the dimensionless particle diameter (Vetsch et al., 2017a). For graded sediment mixtures, different critical dimensionless shear stresses should be used for each fraction. The coefficient ζ is therefore included in the classical formulation to account the hiding-exposure coefficient for different sediment class. This study will use single grain size sediment which means ζ =1 is used (see Vetsch et al., 2017a). For simplified simulations based on single grain size sediment as used here, the commonly adopted value of θ_{cr} is 0.047, a typical value suggested by Meyer-Peter and Müller (1948).

f) Local Slope Effect Model

The critical dimensionless Shield stress used in the MPM formula is based on experimental results for gravel transport over a horizontal bed. In real rivers however, the bed frequently slopes in both the longitudinal and transverse directions (Figure 2.3). To account for the additional influence of gravity on the bed material flux BASEMENT employs a correction term to adjust the critical shear stress for inclined beds. The approach used is based on van Rijn (1993), and involves the definition of

gravity correction factors for both longitudinal (aligned to the principal flow) and transverse (orthogonal) slopes, so that the corrected critical shear stress becomes;

$$\theta_{cr}^{*} = k_{\beta} k_{\lambda} \theta_{cr} \quad \text{Eq. 2.8}$$

In which K_β and K_λ are the local slope factors in the longitudinal and transverse axes respectively. These factors are derived using the relationship between the local slope and the angle of repose of the sediment aggregate, so that the longitudinal bed slope factor is taken to be;

$$k_{\beta} = \frac{\sin(\gamma - \beta)}{\sin\gamma} \text{ for slope <0} \quad \text{Eq. 2.9}$$

$$k_{\beta} = \frac{\sin(\gamma + \beta)}{\sin\gamma} \text{ for slope >0} \quad \text{Eq. 2.10}$$

and the transverse slope correction factor a

$$k_{\gamma} = \cos\delta\sqrt{1 - \frac{\tan^2\delta}{\tan^2\gamma}} \quad \text{Eq. 2.11}$$

Where: γ is angle of repose; β is longitudinal slope; δ is transverse slope. A similar formulation has been also used by Sun et al. (2015) for modelling braided rivers.

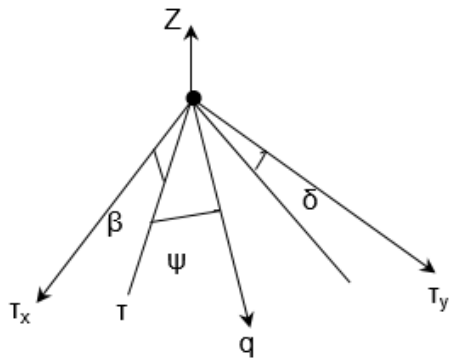

Figure 2.3 Three-dimensional sketch showing shear stress (τ) in longitudinal (x) and transversal (y) directions, longitudinal slope (β), transversal slope (δ) and the resultant sediment transport direction (q).

g) Lateral Transport Model

In common with most models of sediment transport, the MPM formulation was derived for fluxes aligned to a uniform flow direction (Meyer-Peter and Müller, 1948). To solve sediment fluxes over a 2D domain, a calculation for the effect of gravity in the direction of sediment flux must also be made (Ikeda, 1982; Talmon et al., 1995; Siviglia et al., 2013; Sun et al., 2015; Nelson et al., 2016). Essentially, this reflects the effect of the pull of gravity on an inclined bed. In BASEMENT, the magnitude of gravity-induced lateral transport is determined following the established method outlined by Ikeda (1982), where;

$$q_l = \beta\left(\frac{\theta_{cr}}{\theta}\right)^{\gamma} q_x * \tan\delta \qquad \text{Eq. 2.12}$$

Here, q_l is the lateral transport in m^3/s; θ_{cr} is the critical dimensionless shear stress (0.047) for initiation of motion before the local slope correction; γ is lateral transport exponent, which is generally taken as 0.5 (Ikeda, 1982); q_x is the sediment transport in longitudinal slope direction in m^3/s calculated by the Eq. 2.6, where θ is the dimensionless bed shear stress; δ is lateral slope; and β is lateral transport tuning factor. The BASEMENT manual (Vetsch et al., 2017a) recommends the β factor in the range of 1.4 - 2.7.

h) Bank Erosion Model

Bank erosion facilitates channel mobility, habitat development and turnover, and overall floodplain evolution, so that understanding the bank erosion process is vital in river morphodynamic study. Bank erosion occurs primarily as the result of combination of three main interacting processes such as weathering and weakening, fluvial erosion and mass failure (Rinaldi and Darby, 2007). In gravel-bed rivers, the fluvial erosion and mass failure processes primarily controls the overall bank erosion

(Rinaldi et al., 2008). Bank erosion involves the removal of material by the direct action of hydraulic (near bank boundary shear stress) and gravity forces which, in some cases, may also be facilitated by increased pore pressures within the substrate and weathering and weakening processes that reduce likelihood of failure (Thorne and Tovey, 1981; Prosser et al., 2000; Couper and Maddock, 2001). When the boundary shear stress exceeds the critical threshold required for entrainment of bank material, fluvial erosion occurs (Partheniades, 1965; Arulanandan et al., 1980; Ikeda et al., 1981; Crosato, 2008). The quantity of fluvial erosion therefore depends upon the competent flow pattern and the geotechnical properties (erodibility) of bank materials (Rinaldi et al., 2008). Mass failure occurs when the destabilizing (gravity) force exceeds the stabilizing force i.e. shear strength of the bank materials (Mosselman, 1998; Rinaldi and Darby, 2007). As compared to fluvial erosion, mass failure occurs discontinuously in large scale and in combination with other mechanism (Thorne, 1982).

Bank erosion may lead to the formation of toe scour and overhanging, cantilever failures that occur when threshold slope is exceeded (Thorne and Tovey, 1981; Nagata et al., 2000; Rinaldi and Darby, 2007). In order to model these physical processes, coupling of channel hydraulics, surface and ground water fluctuation and bank dynamic process is necessary (Rinaldi and Darby, 2007). There have been some attempts in coupling these key processes while modelling small-scale bank erosion processes (e.g., Rinaldi and Darby, 2007; Rinaldi et al., 2008). However, such coupled models have yet not been implemented in the large-scale morphpodynamic modelling due to difficulties in the prediction of near bank shear stress; drag partitioning and changes in slope stability with moisture content. In large scale models therefore, bank erosion processes are typically been parameterized using simple formulations, such as a single material angle of repose (e.g., Jang and Shimizu, 2005; Sun et al., 2015). This approach involves assigning a critical angle of repose as a

threshold for collapsing of mass, which continues until the gradient is stabilised (Sun et al., 2015). In BASEMENT, bank erosion is represented through the definition of a critical response angle for slope failure, which maintains banks at this value or lower. Sediment is supplied to the adjacent cell from banks to account the necessary loss of material to achieve this gradient. The critical repose angle can be defined separately for fully wetted (γ_{wet}), partially saturated or dry (γ_{dry}) and deposited material ($\gamma_{deposited}$). If the slope exceeds the critical slope (angle of repose defined), the slope is flattened to the user defined critical angle of repose. The combination of repose angles must fulfil the criterion;

$$\gamma_{dry} > \gamma_{wet} > \gamma_{deposited}$$

The computation of bank erosion in BASEMENT follows the five successive steps:

- Firstly, the steepness of a hydraulic cell is used as an indicator if slope failure has to be assumed. The externally defined critical failure angle for dry, wet and deposited material is assigned depending upon whether the cell is dry or wet or has previously deposited sediment, depending upon the water elevation.
- Secondly, the amount of sediment volume which must flow over the sediment edge is calculated as such the slope does not exceed the critical failure angle. Here, the sediment volume is determined by differencing the instantaneous slope and the failure angle slope.
- Thirdly, the amount of sediment volume is then divided by the time step used for the bank erosion computation.
- Fourthly, sediment fluxes are put in the Exner's equation in order to update the bed elevation ensuring mass balance.

- Bed level update of one cell or slope change may affect neighbouring cell so that bank erosion model is applied iteratively until all cells achieve slope not more than critical slope defined.

The bank erosion model can be applied in each time step or in a cyclical way to make simulation feasible. By default, BASEMENT considers a 5-cyclic step which means that the bank erosion calculation is carried out at an interval of 5-timesteps. Since this is a complex geotechnical model, it requires fine-tuning to consider the different sets of repose angles. Additionally, the model is sensitive to both the grid size and hydraulic conditions. For example, the bank erosion model will be active only when water depth reaches or exceeds the value given by grid size times the repose angle. This criterion is unlikely to be met in models of natural channels (with gravel response angles of 30 °- 45 °) where large grid sizes are required to capture the modelled extent, so this scheme can only applied effectively for very small models such as simulations of flumes (e.g., Jang and Shimizu, 2005; Sun et al., 2015). Therefore, it is common practice to 'calibrate' the response angles, reducing them significantly below the physical parameterisation (e.g., Williams et al., 2016). In the limit, it is important to recognize therefore that the treatment of bank erosion is actually little more than a basic conceptual model and offers little of the physical representation associated with the modelled systems.

In the widely used Delft3D morphodynamic model, the amount of erosion flux distribution is governed by a user-defined factor, which determines the fraction of the erosion to assign (evenly) to the adjacent cells. If factor equals zero all erosion occurs at the wet cell. If factor equals 1 all erosion that would occur in the wet cell is assigned to the adjacent dry cells (e.g., Williams et al, 2016; Singh et al., 2017). The 'wet' and 'dry' cells are defined as cells at which the water depth is, respectively, more and less than the threshold depth for computing sediment transport.

i) Bed Level Update

Bed level is updated according to the Exner's equation (Exner, 1925). For a case with single grain size without any point input, the simple Exner's equation is used as:

$$(1-\rho)\frac{\partial zb}{\partial t}+\sum\frac{\partial qx}{\partial x}+\frac{\partial qy}{\partial y}=0 \qquad \text{Eq. 2.13}$$

Where: ρ is porosity of sediment which is taken as constant, 0.4; $\partial zb/\partial t$ is bed level change in time step ∂t; qx is sediment flux in m^3/s in x (flow) –direction calculated by the equation 2.6; qy is sediment flux in m^3/s contributed by direct gravity pull in y (lateral)-direction calculated by the equation 2.12.

The sediment flux contributed from the bank erosion (section 2.2.2) is also solved by using Exner's equation, but this need to be done in a cyclical basis to make simulation feasible. By default, BASEMENT uses a 5-step cycle which means that after each 5-global time step, the bank erosion model is applied, and the bed is updated according to Exner's equation.

2.2.3 BASEMENT Model in Practice

BASEMENT has been applied to model a diverse array of fluvial problems. Faeh (2007), for example, used 2D (BASEplan) to simulate the effects of dyke breaches on the Elbe River, Central Europe. In this study, they used different repose angle for dry, wet and deposited material to represent the erosion processes. Rüedlinger (2010) applied both 1D (BASEchain) and 2D (BASEplan) versions of BASEMENT to understand the event-based morphological response of the braided Pfynwald reach of the Rhone River in Switzerland. Their 2D hydrodynamic simulations closely approximated the water depth distribution observed in the natural prototype. However, the 1D sediment transport modelling revealed an inconsistent pattern of erosion and deposition when compared to the natural prototype. Their 2D simulations of erosion and deposition patterns, also revealed unrealistically deep scours that were not

evident in the natural system. Building on these simulation experiments, they suggested that the parameterisations of lateral transport model and bank erosion model were critical to ensure appropriate dispersion of the sediment flux and prevent localized incision. Radice et al. (2012) applied BASEMENT to understand the 2D morphological response of a small single thread reach of the Rossiga River to intense sediment supply during an extreme flood. In this case, the numerical model was found to predict a similar pattern of erosion and deposition as observed in the field. BASEMENT has been also used to simulate dam break processes observed both in flume (Volz et al., 2012) and field (Worni et al., 2012; glacier lake outburst flood at Ventisquero Negro, Patagonian Andes (Argentina)). More recently, Bertoldi et al. (2014) undertook 2D morphodynamic simulations to investigate the feedback between flow, sediment and vegetation colonisation and die-back as controls on the morphological evolution of a straight hypothetical channel. Their simulation results reproduced some of the key processes of vegetation colonisation, such as expansion of vegetation during low flow and complete removal during very high flows. Brestolani et al. (2015), also used BASEMENT in its 1D form to simulate the impact of gravel mining in Orco River, Italy.

To date, however, there are no published studies that examine the performance of BASEMENT to simulate the long-term evolution of braided rivers. Nevertheless, as many of the key physical processes required to characterize braiding, such as lateral transport and the bank erosion model have already been incorporated, a critical evaluation of the model's performance is now timely.

2.3 The Natural Prototype

2.3.1 General

The River Feshie drains a 232 km^2 catchment area and is a major tributary of the River Spey in north-east Scotland (Figure 2.4). The Allt Chomraig, the Allt Mharcaidh,

the Allt Lorgaidh, the Upper Feshie, and the Eidart are the main tributaries which contribute to its total runoff. The catchment is underlain by granite and schist while surficial soils and deposits include extensive upland peat, podsol soils and extensive alluvial and outwash cover along the principal valley floor (Soulsby et al., 2006).

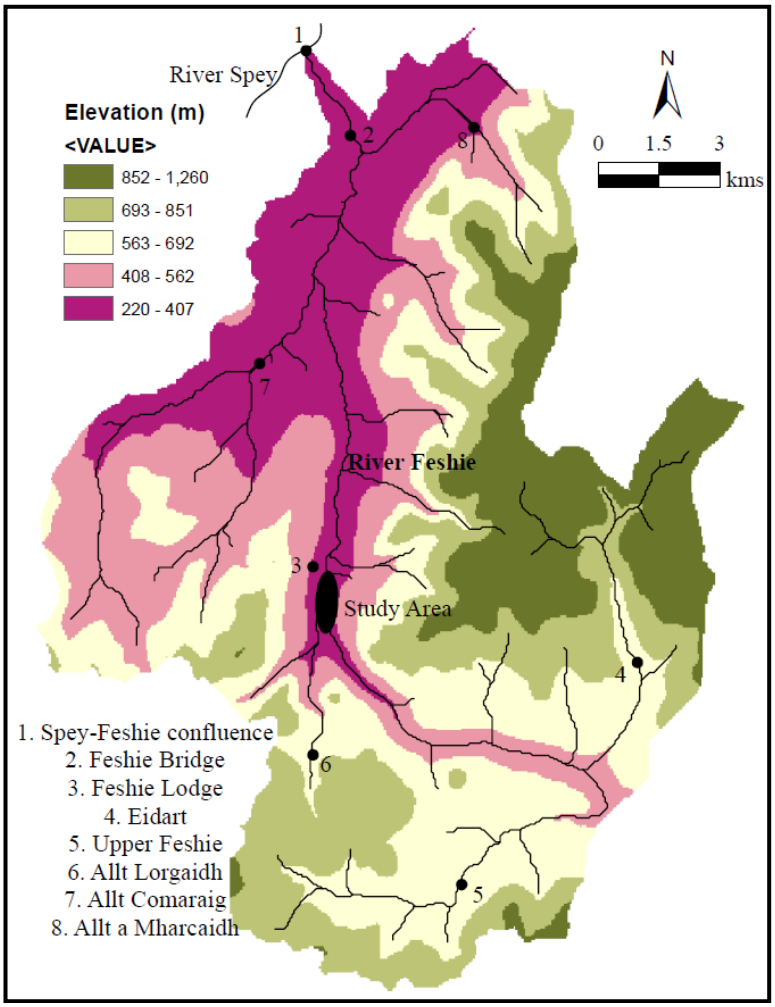

Figure 2.4 River Feshie catchment and location the study area.

The land-cover includes peat bog, heather grass, and woodland - incorporating both plantations and regenerating boreal forest (Soulsby et al., 2006). The annual precipitation in the catchment varies locally in between 1307 mm and 1654 mm (Feshie Bridge = 1317 mm, Allt Chomraig = 1095 mm, Allt Mharcaidh= 1419 mm, Feshie Lodge = 1472 mm, upstream of the braided reach = 1505 mm, Upper Feshie = 1423 mm, Eidart 1654 mm; cf. Soulsby et al. (2006)). Convective precipitation and winter snowmelt are the main sources of flood discharges (Werritty and Brazier,

1991). The highest flows occur typically either during January-March from rapid snowmelt or rain-fall events, or during October-December as a result of autumnal storms (see Figure 2.5 for the hydrograph pattern). From March to June, the river shows diurnal variation in discharge due to the dominance of snowmelts in runoff contribution (Ferguson, 1984).

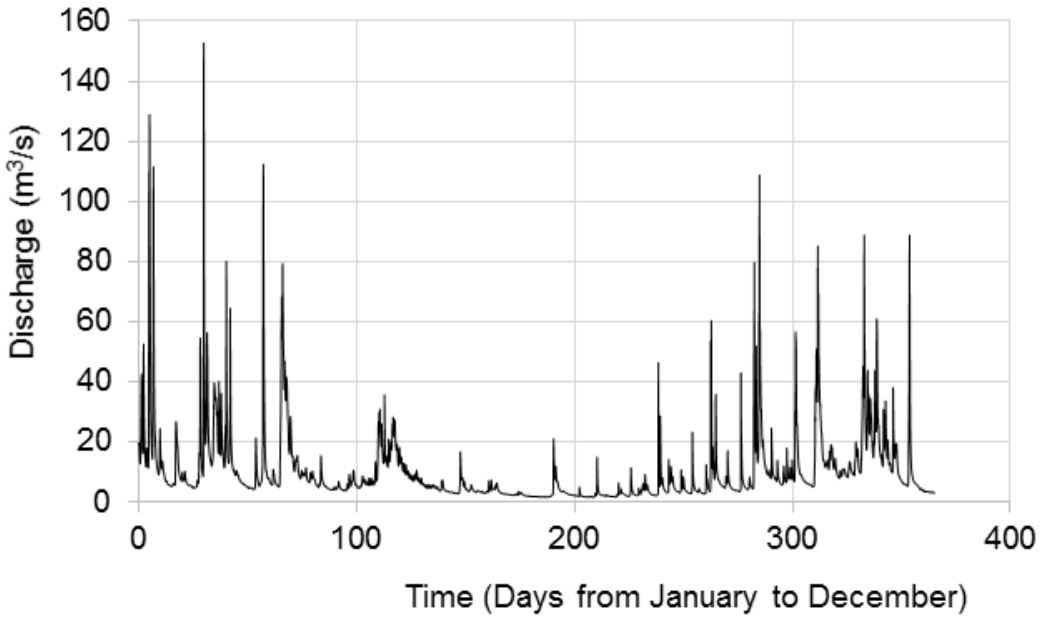

Figure 2.5 A typical daily hydrograph of the year 2000 at Feshie Bridge measured by Scottish Environment Protection Agency (SEPA). The Feshie Bridge is situated around 12 km downstream of the study reach (see Figure 2.4 for location of the Feshie Bridge, the Feshie Lodge and the study prototype reach).

The braided reach of the River Feshie used as the prototype to develop numerical simulations in this research is approximately 12 km upstream of Feshie Bridge in the immediate vicinity of Glenfeshie Lodge (see Figure 2.4 for these reference locations). The drainage area to this reach 115 km^2 including the three main tributaries: the Allt Lorgaidh, the Upper Feshie, and the Eidart (Figure 2.4). In this reach, the river is moderately braided for over 3 km, where the river is unconfined (Figure 2.6a). The valley slope through this section is a moderate 0.92%. This braided sedimentation zone comprises Holocene outwash gravels and contemporary fluvial deposits (Brasington et al., 2000). The fairway has a maximum historic width of c. 200-400 m,

although the active belt currently being reworked typically varies between 130 - 200 m (Figure 2.6a and b).

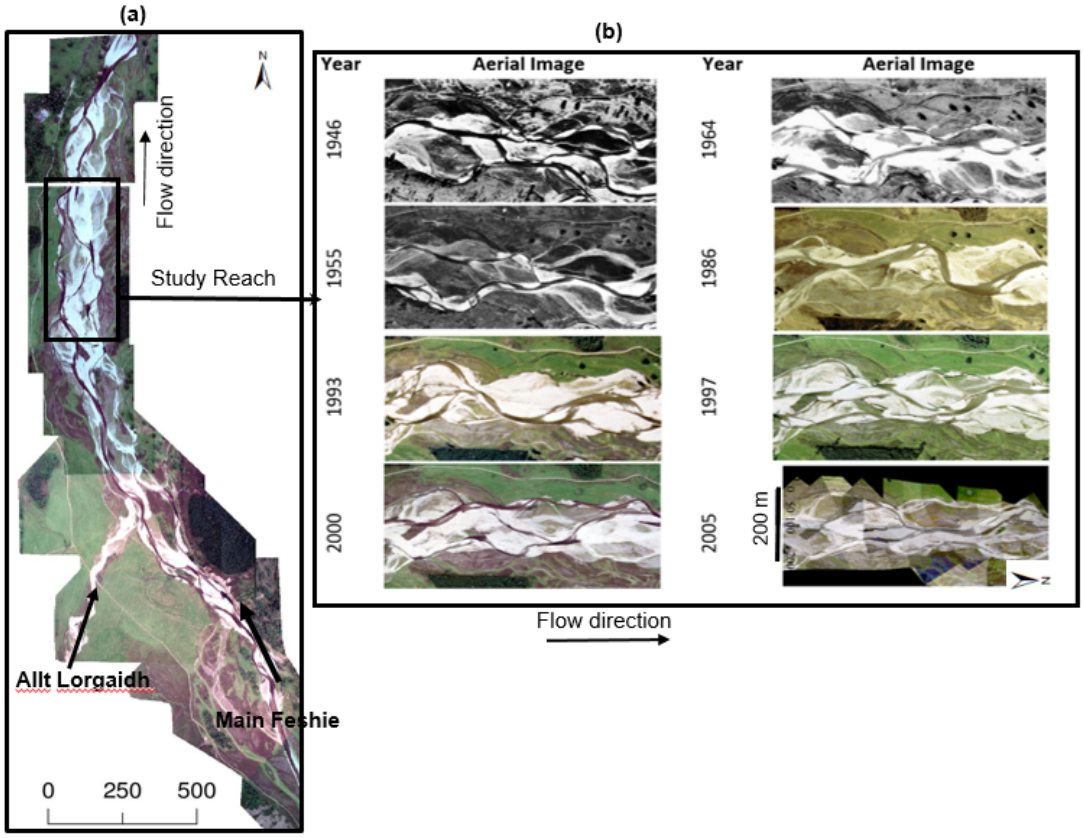

Figure 2.6 (a) The braided 3 km reach. Ferguson and Werritty (1983), Ferguson and Ashworth (1992), Brasington et al. (2000) and Brasington et al. (2003) considered the reach just upstream of the Allt Lorgaidh - main Feshie confluence. (b) The 700 m main active braided reach in different years which is the reference natural prototype for this study. Studies of Brasington et al. (2012), Wheaton et al. (2010) and Wheaton et al. (2013) were also based on the same 700 m reach.

The Figure 2.6b shows a georeferenced set of historic aerial images spanning 60 years, for a downstream 700 m reach which was extensively surveyed between 2000-2013 (Brasington et al., 2012). This series of images are not sampled regularly, but clearly illustrate the interplay between sediment and vegetation with colonisation of exposed gravel surfaces occurring through a sequence of successive stages, requiring ~10-15 years to develop to extensive shrub and tree cover. The sampled distribution of images shown in Figure 2.6b appears to indicate strong variations in the dominance of vegetation cover over the 60-year period. For example, the majority

of gravel bars were covered in vegetation during 1986, 1955 and 2005, while exposed gravel dominated bars appear to dominate in 1993, 1997 and 2000.

2.3.2 State of Morphodynamic Knowledge about the Braided Reach

The braided site is one of the most important Sites of Specific Scientific Interest (SSSI) in Scotland and one of the most active gravel-bed rivers in Britain. Not surprisingly, the system has encouraged a long legacy of researchers to study fluvial processes. This dates back to early work by Ferguson and Werritty (1983) who developed an early conceptual model of bar formation and maintenance, based on surveys in the immediate upstream vicinity of Allt Lorgaidh and main Feshie confluence (Figure 2.6a). In this reach they documented the progradation of bars into sloughs and sheet flow of sediments during the rising stage of floods, followed by the deposition of thin gravel sheets on the bar tops during falling stages. In addition, they observed more than 10 m/a of erosion in the same corridor based on the data between 1977 and 1981. Latterly, at the same site, Ferguson and Ashworth (1992) carried out a cross section survey at 15 m intervals for a 100 m anabranch channel and observed sediment transport during two discharges - 14 m^3/s and 20 m^3/s in spring 1986. Differencing the cross-section taken on 18th April 1986 and on 4th June 1986, they found about 1 m of bank erosion and 0.2 m of channel scour at some sections (cf. Ferguson and Ashworth (1992); Figure 2C). Werritty and Hoey (2004) analysed historical aerial photographs for the whole 3 km braided reach. While they suggested there was no clear trend in the planform trajectory of the river, they attributed significant post-1945 changes of river pattern to hydrological forcing and local bank erosion (10 m per year), reduced sediment supply and rapid avulsion or cut off formation.

Brasington et al. (2000) later sought to understand links between river form, process by examining the sediment budget and pattern of 3D channel adjustment using DEM differencing techniques based on high resolution GPS survey data. They focused on

a 200 m reach just upstream of the main Feshie-Allt Lorgaith confluence and reported differences derived from annual summer low flow surveys in 1998 and 1999. Their study found little change (some minor degradation) to the overall macro-scale morphology but did provide evidence on the scale and depth and typical units of erosion and deposition. Furthermore, their DEM differencing showed the presence of process scale phenomena such as confluence scour, deposition at the start of bifurcation (bar head), trimming of major mid channel bar, and erosion of fines from the slough as observed by Ferguson and Werritty (1983). More recently, Wheaton et al. (2010) employed annual morphometric analysis of the comparatively more active braided 700 m reach just upstream of the Glenfeshie Lodge, which is also taken as the prototype reach for this research (Figure 2.6b). They found annual erosion varying from 570 m^3/year to 1970 m^3/year. Additionally, their study has shown that channel adjustment is driven principally by bank erosion, outer bend or confluence scour and erosion from the major channel thalweg. They highlighted the importance of continuing lateral migration as a key source of locally derived sediment that was sufficient to maintain braiding by encouraging sedimentation and flow separation.

This study will focus on the same 700 m reach analysed by Wheaton et al. (2010) and later by Brasington et al. (2012). For this reach, there are high resolution (1 m resolution or higher) DEMs derived from a combination of GNSS and TLS surveys straddling the period 2000-2013.

2.3.3 Hydrology

There is not any direct measurements of river discharge or sediment transport in the 700 m braided reach. However, an automated hydrometric station is maintained at Feshie Bridge approximately 12 km downstream of the braided reach. For this site, a long-term data series (1992 - 2010) of flow data at 15-minute intervals measured by the Scottish Environment Protection Agency (SEPA) was made available for this study. In order to derive flow series for the braided reach, a discharge conversion

factor was determined based linearly on the catchment area and precipitation ratio between Feshie Bridge and the braided reach (Feshie Lodge), using data from Soulsby et al. (2006).

The annual precipitation in the catchment varies locally in between 1307 mm and 1654 mm (Feshie Bridge = 1317 mm, Allt Chomraig = 1095 mm, Allt Mharcaidh= 1419 mm, Feshie Lodge = 1472 mm, upstream of braids = 1505 mm, Upper Feshie = 1423 mm, Eidart 1654 mm; cf. Soulsby et al. (2006)). The catchment areas at Feshie Bridge and Feshie Lodge are 230 km^2 and 1135 km^2 respectively. As a representative annual precipitation for the catchment at the Feshie Bridge and Feshie Lodge, the local annual precipitation upstream of these sections were simply averaged. This results in annual precipitation at Feshie Bridge and Glenfeshie Lodge as 1412 mm and 1514 mm respectively. Using this precipitation ratio (1.07) and the ratio of drainage areas (114.6/230.7), a correction factor of 0.53 was obtained as a simple linear product. This was used to downscale the Feshie bridge flow series to estimate a 15-minute data record for the braided study reach. All the subsequent hydrometric analyses are based on this synthetic, local data record.

a) Flood Frequency Distribution Analysis

Flood frequency analysis is commonly used to provide insights into the nature of flood events in a given section and to provide some instructive guidance on design criteria. Here, the maximum instantaneous flood recorded in the 18-year record (based on peak instantaneous 15 min flows) were used to compile a standard distribution of annual flood maxima (Figure 2.7a).

Log-Pearson III and Gumbel distributions were fitted to this empirical record using linearized regression (Figure 2.7b). The Log Pearson III flood distribution suggests 1 year, 2-year, 10-year, 25 year and 100-year flood magnitudes are of the order of 40 m^3/s, 70 m^3/s, 100 m^3/s, 115 m^3/s, and 150 m^3/s. The Gumbel distribution predicts

slightly higher flood magnitudes for the lower frequency events, with discharges typically of the order of 5-10 m^3/s higher for return periods > 10 years.

(a) Flood data

Year	Flood (m^3/s)
1993	92
1994	66
1995	82
1996	59
1997	104
1998	58
1999	118
2000	81
2001	71
2002	101
2003	65
2004	57
2005	54
2006	67
2007	45
2008	53
2009	72
2010	56
Standard deviation	20

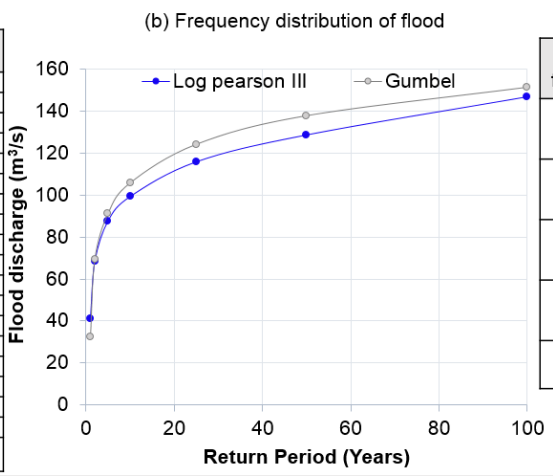

(b) Key flood statistics

Characteristic flood's statistics	Flood (m^3/s)
1 years flood	40
2 year flood	70
10 year flood	100
25 year flood	115
100 year flood	150

Figure 2.7 Flood information representative of the braided Feshie. (a) The maximum instantaneous flood in between 1993 – 2010; (b) Flood frequency based on the Log Pearson III and Gumbel frequency distribution; (c) Key flood statistics representative of the braided Feshie.

b) Flow Duration Curve

A flow duration curve represents the percentage of time a given flow is likely to be equalled or exceeded over a given time, usually a year. Here, flow duration curves were calculated for all 18 years separately and then an average curve estimated by averaging the individual series.

Figure 2.8a show the minimum, average and maximum flow duration curve based on the 15-minute data record, while the data are summarized in tabular form below. This reveals that the one-year flood magnitude is (40 m^3/s) exceeded for just less between 3 hours to 50 minutes (based on the differing methods of calculation), while the two-year flood (70 m^3/s) is exceeded for between 0.2 hours to 20 hours. For example, one-year flood (40 m^3/s) is available for 3 hours to 50 hours in a year and two-year flood (70 m^3/s) is available for 0.2 hours to 20 hours in a year (see Figure 2.8b).

(a) Minimum, Average and Maximum flow duration curve

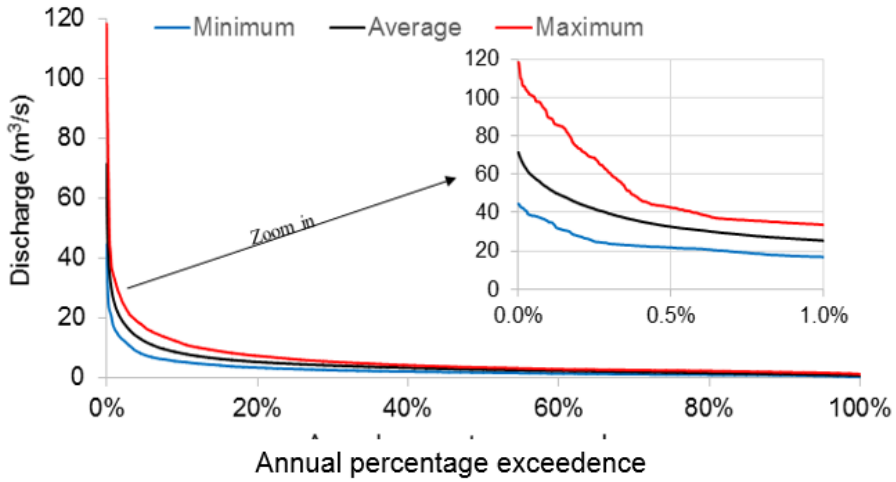

(b) Duration of key flood based on minimum, average and maximum flow duration curve

Key flood data	Discharge (m^3/s)	Annual exceedance (based on minimum FDC)	Annual exceedance (based on average FDC)	Annual exceedance (based on maximum FDC)
Half of 1 year flood	20	59 hours	163 hours	310 hours
1 year flood	40	3 hours	25 hours	50 hours
2 year flood	70	-	0.2 hours	20 hours
10 year flood	100	-	-	0.8 hours
25 year flood	115	-	-	0.4 hours
150 year flood	150	-	-	-

Figure 2.8 (a) Flow duration curves (minimum, average and maximum recorded in 18 years between 1993 - 2010); (b) Duration of key flood data based on the minimum, average and maximum flow duration curve.

2.3.4 Bed Sediment

The bed sediment comprises gravel-cobble sized, schistose material. There is no any direct measurement of bulk samples from the study reach. However, surface sediment sampling of Hodge et al. (2009b) suggests that D_{50} varies between 30 mm to 60 mm in the 700 m braided reach. Given observations of significant surface armouring (Brasington, pers. comm., 2015), it is likely that bulk samples would indicate a significantly smaller median particle size (Mosley, 1982). Given this uncertainty, the

lower value D_{50} = 30 mm suggested by Hodge et al. (2009b) was used to define an uniform grain size set as a spatial and temporal constant for all subsequent modelling.

2.3.5 Longitudinal Slope

The longitudinal slope of the 700 m braided reach was determined based on the 2005 topographic data. Firstly, longitudinal profile of the 700 m braided reach was developed based on the cross-sectional averaged value of elevation. Secondly, a best fit polyline was developed based on the longitudinal profile to determine the longitudinal slope. The longitudinal slope of the braided 700 m reach was revealed as 0.92 % (Figure 2.9).

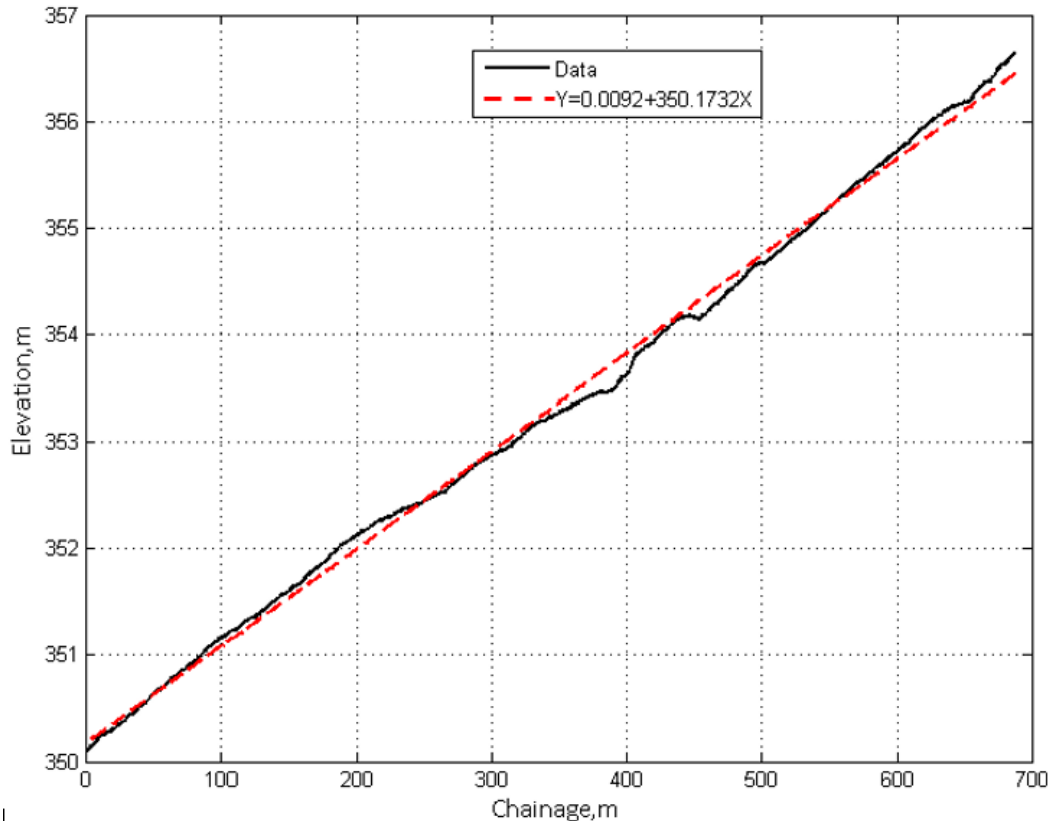

Figure 2.9 Longitudinal profile of the 700 m braided reach based on the 2005 DEM.

2.3.6 Main Corridor Width

The main channel corridor or fairway width was also derived from the 2005 DEM. The reach averaged main active corridor width was revealed as 173 m (Figure 2.10) which was rounded to 175 m.

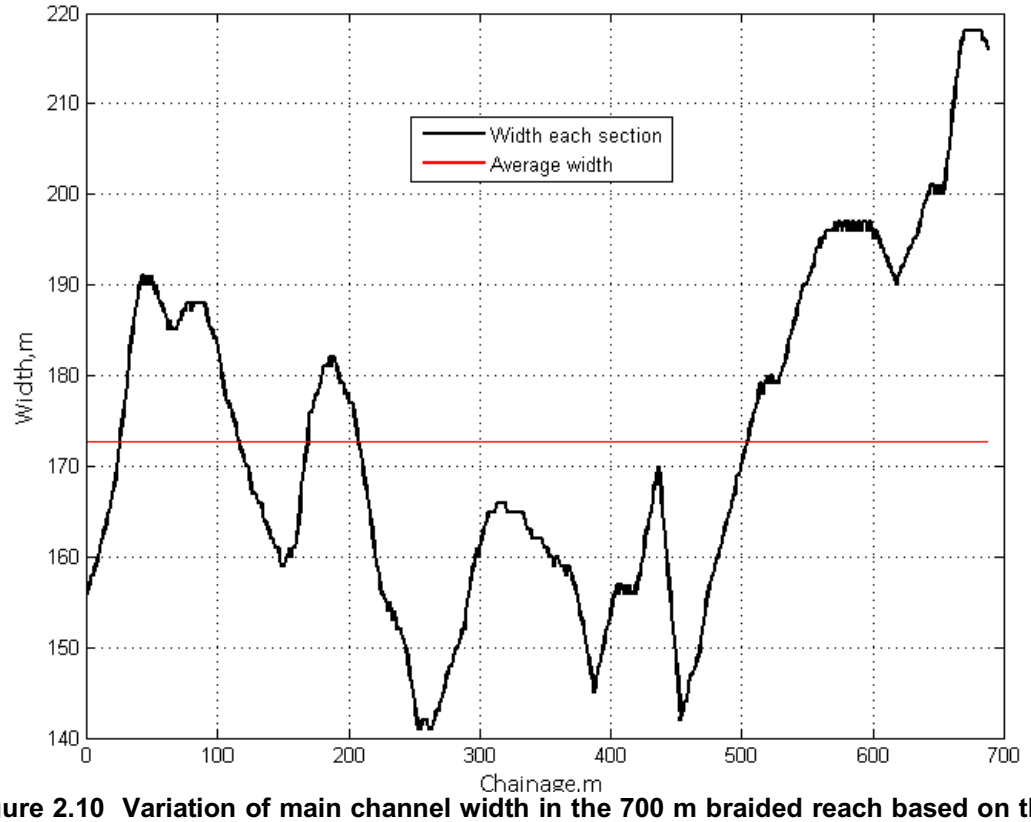

Figure 2.10 Variation of main channel width in the 700 m braided reach based on the 2005 DEM.

2.3.7 Summary of Prototype Characteristics

As revealed from the analysis in previous sections, some key characteristic of the braided Feshie can be summarized (see Table 2.1, highlighted row).

Table 2.1 Key hydrologic, sediment and topographic data of the braided Feshie as compared with some other famous gravel-bed braided rivers.

Key Data	Two year flood (m^3/s)	Sediment (D_{50}) (mm)	Longitudinal Slope (%)	Averaged Active Corridor (m)
Feshie, Scotland (for this study)	70	30.0	0.92	175
Waimakariri, NZ (Singh et al., 2017)	1520	25.4	0.5	900
Rees River, NZ (Williams et al., 2013)		19.9 (+/- 10.4)	0.5	700
Ahuriri River, NZ (Javernick et al. (2015)		29.0	-	650
Tagliamento River, Italy (Bertoldi et al., 2010)	1800	40.0	0.4	900
Ohau River, NZ Mosley (1983)	280 (historically at natural state)	20.0	0.65	600

Table 2.1 also includes key characteristic of some other famous gravel-bed braided rivers as collected from literatures. The braided Feshie appears as a typical small size braided river. As the braided Feshie has continuous series of topographic and hydrological data, this river serves as a suitable natural prototype to test performance of any numerical model.

2.4 Concluding Summary

The BASEMENT numerical model solves the shallow water wave equations and couples these with 2D bed material flux models to simulate the fundamental form-flow feedback processes that drive fluvial morphodynamics. Historical application of this model in a diverse array of fluvial problems such as, in modelling river hydraulics, morphodynamics and dam/dyke breach (see section 2.2.3) is promising for further application. As compared to other morphodynamic models (Lesser et al., 2004; Nicholas, 2013; Siviglia et al., 2013; Sun et al., 2015), there is lack of secondary flow representing sub-models (till the date when this thesis was started), which is critically needed to model the strong 3D processes in bends and confluences in depth-averaged model (Mosselman and Le, 2016). In terms of the wetting and drying threshold, which is often used to avoid numerical instability, it is very common to define a separate threshold water depth for hydraulic calculations (0.05 m common) and sediment transport (0.1 m common) (Lesser et al., 2004; Nicholas, 2013; Siviglia et al., 2013; Sun et al., 2015). BASEMENT does not provide this flexibility, so the same threshold water depth threshold must be used for both hydraulics and sediment transport calculation (see section 2.2.1.e for detail). This means that if both hydraulics and sediment transports are calculated with the commonly used threshold for hydraulics, i.e., 0.05 m, it will increase simulation time and may increase the chance of numerical instability. Conversely, if both hydraulics and sediment transports are calculated with the commonly used threshold for sediment transport, i.e., 0.1 m, it may

diffuse the topography and decrease the accuracy of simulation result. Numerical modellers need to find an appropriate option that works for the case in hand.

Nevertheless, BASEMENT incorporates the key sediment transport-related formulations such as local slope effects, direct gravity effects on sloppy beds (lateral transport), and, most importantly, the geotechnical approach of modelling bank erosion processes which are very critical when modelling the form-flow feedback particularly in modelling braided bar morphology (see Schuurman et al., 2013; Sun et al., 2015; Nelson et al., 2016; Williams et al., 2016a; Singh et al., 2017). Additionally, BASEMENT uses a flexible mesh which provides an effective discretisation system to represent eroding banks or bar edges that doesn't suffer the serious numerical diffusion encountered with rectilinear grids in other numerical models. In BASEMENT, both hydraulic and sediment transport calculations need to be carried out at the same (1:1) scale, unlike the other morphodynamic model where provision for the morphological acceleration factor (MORFAC) has been incorporated (e.g., Nicholas, 2013; Schuurman et al., 2013; Singh et al., 2017). This demands higher simulation time, but this problem is minimized as BASEMENT is fully parallelized enabling multi-threaded simulations simulation. Modelling hydraulic and sediment transport with 1:1 scale provides opportunity to model any unsteady form of hydrographs as there is no need to deal with management of morphological acceleration factor (e.g., Schuurman et al., 2013; Williams et al., 2016a; Singh et al., 2017). Indeed, modelling using MORFAC is a daunting challenge in the long-term morphodynamic modelling under unsteady flow condition (see Yossef et al., 2008) (Chapter 4 provides more detail on MORFAC). The numerical scheme without MORFAC will be exploited to simulate different forms of steady and unsteady hydrographs in Chapter 4. For this study, beside the freeware software, an extra code to simulate the interaction of flow, sediment and vegetation was made available from the developer (Bertoldi et al., 2014) which was needed to address the research question d. The vegetation model allows

non-linear colonisation and die-back of vegetation depending upon instantaneous flood condition (detail will be provided in the corresponding Chapter 6) as compared to other numerical model (e.g., Crosato and Saleh, 2011; Li and Millar, 2011; Nicholas, 2013), which consider either complete removal or maximum colonisation.

To date, there is no published literature which has used BASEMENT to simulate the long-term morphology of braided rivers. However, as the BASEMENT model incorporates all the key formulations (except secondary flow) in a similar manner as done by many other numerical models, its critical testing and evaluation appears as an urgent and timely step. Once the model is able to model long-term morphology, it will enable to simulate any type of unsteady hydrograph and interaction between flow, sediment and vegetation as mentioned above. Indeed, this led to the formulation of intensive sensitivity analysis of the model in Chapter 4.

The hydrologic, topographic and sediment data revealed from this analysis will guide schematisation of the spatial domain of model, hydrographs and bed sediment in subsequent chapters. In Chapter 3, stage-dependent hydraulics and morphodynamics of the braided Feshie will be quantified based on fixed-bed hydrodynamic simulation using 2005 DEM at different discharges between 5 m^3/s to 85 m^3/s. Here, the morphodynamic calculation will be carried out using single grain size sediment (D_{50}). In Chapter 4, the two-year flood in the steady form of hydrograph, uniform sediment D_{50}, longitudinal slope and main corridor width as shown in the Table 2.1 will be used to a generate synthetic braided river by the numerical model BASEMENT itself. In Chapter 5, the model set up in Chapter 4 will be used but the form of hydrographs will be changed in order to explore effects of different form of steady and unsteady hydrographs on morphodynamic evolution of numerically generated synthetic braided river under steady flow in Chapter 4. Here, different forms of steady and unsteady hydrographs will be designed by perturbing discharge at the rate of 20 m^3/s (one standard deviation of maximum instantaneous flood as shown in

the Figure 2.7a) starting from the two-year flood, 70 m^3/s. In this case, for unsteady triangular form hydrographs, low flow will be set equivalent to half of the one-year flood (40 m^3/s) which is 20 m^3/s (see Chapter 5 for details). In Chapter 6, all simulations will use 70 m^3/s of steady high flow for around eight hours to allow morphodynamic evolution and 20 m^3/s of low flow for one hour to allow vegetation succession (see Chapter 5 for details). Thus, the data presented here will support model schematisation in all subsequent chapters.

Chapter 3: Developing a Framework for the Validation of Numerical Morphodynamic Models

Chapter Summary

This chapter addresses Research Question 1: ***What characteristics of the structure and dynamics of braided rivers can be quantified as a hierarchical set of metrics and used to evaluate the performance of numerical models of braiding?***

This chapter review existing metrics that have been used to quantify the morphology of braided rivers and evaluate numerical models. Following this, a new hierarchical framework for river characterization that quantifies river morphology, hydrodynamics and kinematics is proposed. Lastly, the proposed framework is used to characterize the prototype braided Feshie to facilitate the numerical model validation in Chapter 4.

The quantitative framework proposed in this study, exhibiting different planform, topographic, hydraulic and morphodynamic reflecting metrics, is supposed to be useful to quantify braided rivers and to support model validation of numerical models. Its usefulness will be further demonstrated in Chapter 4.

3.1 Introduction

Braided rivers are rapidly evolving, complex systems governed by the interactions between network topology, topography, hydraulics and sediment transport. In the last few decades, understanding these different aspects of braided rivers has been advanced through a combination of empirical, field and flume experiments (e.g., Leopold and Wolman, 1957; Schumm and Khan, 1972; Hong and Davies, 1979; Sanyal, 1980; Ashmore, 1982; Mosley, 1983; Hickin, 1984; Ashmore, 1987, 1988, 1991; Ferguson and Ashworth, 1992; Germanoski and Schumm, 1993; Brasington et al., 2000; Tal et al., 2004; Bertoldi et al., 2009b; Egozi and Ashmore, 2009; Madej et al., 2009; Surian et al., 2009a; Bertoldi et al., 2010; Tal and Paola, 2010; Ashmore et al., 2011; Bertoldi et al., 2011b; Williams et al., 2011; Welber et al., 2012; Henshaw et al., 2013; Redolfi, 2014; Garcia Lugo et al., 2015; Kasprak et al., 2015; Sun et al., 2015; Redolfi et al., 2016a). There is now, however, an increasing awareness that numerical modelling may offer a powerful tool to support this enquiry, with the potential to provide a transparent insight into the processes controlling the evolutionary trajectory of braided rivers (Bristow and Best, 1993; Ferguson, 1993; Paola, 2001; Sambrook Smith et al., 2006; Brasington and Richards, 2007; Surian, 2015; Siviglia and Crosato, 2016; Williams et al., 2016b; Escauriaza et al., 2017). In the last 20 years, many numerical models, ranging from reduced complexity, rule-based algorithms (e.g., Murray and Paola, 1994, 1997; Sapozhnikov et al., 1998; Thomas and Nicholas, 2002; Doeschl-Wilson and Ashmore, 2005; Thomas et al., 2007; Doeschl et al., 2009; Ziliani et al., 2013) to physically-based models based on the canonical equations of flow and sediment transport (e.g., Enggrob and Tjerry, 1999; Jang and Shimizu, 2005; Nicholas, 2013; Schuurman et al., 2013; Sun et al., 2015; Singh et al., 2017) have been applied to study braiding processes. While these models appear to be able to reproduce, at least superficially, key characteristics of braiding, a framework for the critical evaluation of model performance remains to be

developed (Kleinhans, 2010; Murray, 2013; Surian, 2015; Williams et al., 2016b). This is an important next step as numerical simulation models contain, at best, only partial representations of the comprehensive set of physical processes and morphological structures present in natural rivers (Kleinhans, 2010; Wright and Crosato, 2011; Murray, 2013). Even then, the representation of the processes incorporated are based on approximate, discrete solutions to the governing partial differential equations and boundary conditions.

In order for simulation models to become established research vehicles, the development of methods to support their critical evaluation is an urgent imperative. In principle, this should incorporate internal verification and subsequent validation using observations and insights from field or laboratory prototype models (Anderson and Bates, 2001; Lane and Richards, 2001; Mosselman, 2005; Brasington and Richards, 2007; Kleinhans, 2010; Mosselman, 2012; Murray, 2013). To date, however, relatively few published studies have examined the comprehensive performance and process/parameters sensitivity of these models. In large part, this reflects the dearth of high-quality datasets available to characterize the morphology, hydrodynamics and morphodynamics of braided rivers at time and space scales relevant to simulation modelling. This is no trivial task, however, as braided rivers are typically characterized by subtle but complex topography, which is highly mobile and difficult to survey due to their extensive width and the high width-depth ratio (Williams et al., 2011). This has led to a reliance on planform descriptors of channel form, principally channel count indices (Egozi and Ashmore, 2008), which are highly sensitive to variations in stage and offer limited insight into 3-dimensional structure and evolution of river morphology (Brasington et al., 2012).

Recent developments in remote sensing and geomatics, in particular the advent of airborne and terrestrial LIDAR, softcopy and structure-from-motion photogrammetry now offer exciting new pathways to enable dense reconstructions of fluvial topography

in fully 3-dimensions (e.g., Bertoldi et al., 2011b; Brasington et al., 2012; Westoby et al., 2012; Javernick et al., 2014; Williams et al., 2014). The ability to acquire high resolution topography repeatedly through time also provides the unprecedented opportunity to quantify not only the full morphological structure of braided systems, but also to reconstruct transport rates and sediment budgets indirectly through DEM differencing (Ashmore and Church, 1998; Brasington et al., 2000; Redolfi, 2014; Vericat et al., 2017). Other advances in remote sensing such as optical depth mapping (e.g., Williams et al., 2014) and acoustic Doppler current profiling (aDcp) may also provide key information on water depth, velocity, shear stress and sediment transport (Williams et al., 2015; Rennie et al., 2017).

Such advances in data acquisition provide scope to define robust metrics of form and behaviour that could be used to describe the character of natural systems and afford a means to assess model predictions. However, the apparently simple task of comparing observations and predictions is fraught with difficulty within the context of braiding processes due to the sensitive dependence of the evolutionary trajectory of braiding on the initial topography, hydraulic and sedimentological system conditions. In this context, small uncertainties in channel morphology and flow distribution can give rise to variations in the spatial allocation of flow and boundary stress that become magnified rapidly by morphodynamic feedback. Consequently, simulations based on even well-conditioned models are likely to diverge from their natural prototypes over short time and space scales (Oreskes and Belitz, 2001) rendering direct, deterministic comparison futile (Anderson and Bates, 2001; Lane and Richards, 2001; Oreskes and Belitz, 2001).

Ultimately, therefore, the evaluation of model performance and sensitivity must instead rely on statistical measures of channel form and process, many of which are likely to be ill-defined. This raises the potential for generating apparently good measures of model performance from quite different deterministic outcomes, and

apparently similar predictions to be generated by radically different processes (Beven, 1993; Kleinhans, 2010; Mosselman, 2012; Murray, 2013). It is, therefore, necessary to identify a robust and systematic approach to model testing that interrogates a range of different characteristics of braiding and uses the 'sum of the whole' as a means to 'corroborate' rather than verify models.

3.2 Aim and Objectives

This chapter aims to **identify a systematic framework** for quantifying braided river with implication for evaluation of numerical models, and to **test the framework** to characterizing the natural prototype Feshie. This chapter is structured in four sections: (a) a review of existing metrics that have been used to quantify the morphology of braided rivers and evaluate numerical models; (b) a new hierarchical framework for river characterization that quantifies river morphology, hydrodynamics and kinematics; (c) an application of this framework to characterize the simulation prototype system, the braided River Feshie; d) a critical review of the approach; e) conclusions.

3.3 Review of Quantitative Data Models of Braided Rivers

A systematic review of approaches to characterizing empirically the form and processes of braided rivers is presented based on a four-fold typology of characteristics that include: a) planform structure (2D); b) bed topographic structure (3D); c) hydrodynamics; and d) morphodynamic behaviour (4D).

3.3.1 Planform Descriptors of Braiding

Given the difficulty of surveying braided rivers due to their subtle form and high width : depth ratio, approaches to quantifying river form have historically focused largely on planform descriptors that can be derived from oblique, aerial and/or satellite imagery (Egozi and Ashmore, 2008). A range of measures have been developed that provide

basic descriptors of the channel network structure and geometry of exposed bar surfaces.

a) Channel Count Indices

The most common approach to characterizing braiding is through a simple count of the number of wetted channels per cross-section. This is frequently referred to as the Total Braiding Index or TBI after Ashmore (2001) (see also Bertoldi et al., 2009b; Egozi and Ashmore, 2009; Ashmore, 2013). This measure is determined readily from vertical imagery and reflects the three-dimensional effect of topography and momentum on flow routing. Implicitly therefore, the measure provides an insight into the local complexity of channel form and the degree of bed dissection. The measure is determined easily for laboratory models and can be extracted from simulations of both fixed-bed and morphodynamic simulation models. However, despite the simplicity of the channel count approach, this metric is highly sensitive to discharge at the time of observation (Mosley, 1983; Egozi and Ashmore, 2008). Given the logistical limits on the sampling aerial imagery, it is likely that a river can display a wide range of index values without morphological change. Indeed, Bertoldi et al. (2009b) suggested that for many braided rivers the TBI may exhibit a bell-shaped relationship with discharge; initially increasing with flow and peaking at intermediate flows, before declining as the whole active channel belt is inundated under flood conditions.

One approach to relax the dependency of the TBI on discharge, is to use an alternative means to segment the braided fairway into wetted channels and bars based on a topographic threshold, such as the local mean bed level. For example, Schuurman et al. (2013) derive a measure based on the number of channels that lie below the mean bed elevation at a given cross-section. This approach enables a more robust tool for comparison of planforms between natural prototypes and their

simulation equivalents, but clearly requires distributed topographic data rather than more easily obtained planimetric photography.

b) Link Length

Confluences and bifurcations are critical nodes in the network topology of braided rivers (Ashmore, 1982, 1987). The non-linear relationship between shear stress and sediment transport implies that the convergence and divergence of flow at these respective points in the network magnifies the local morphodynamic response and exerts a fundamental control on the distribution of sediment transport and consequently on bar growth and channel scour (Bolla Pittaluga et al., 2003; Federici and Paola, 2003; Bertoldi and Tubino, 2007; Zolezzi et al., 2009; Kleinhans et al., 2013).

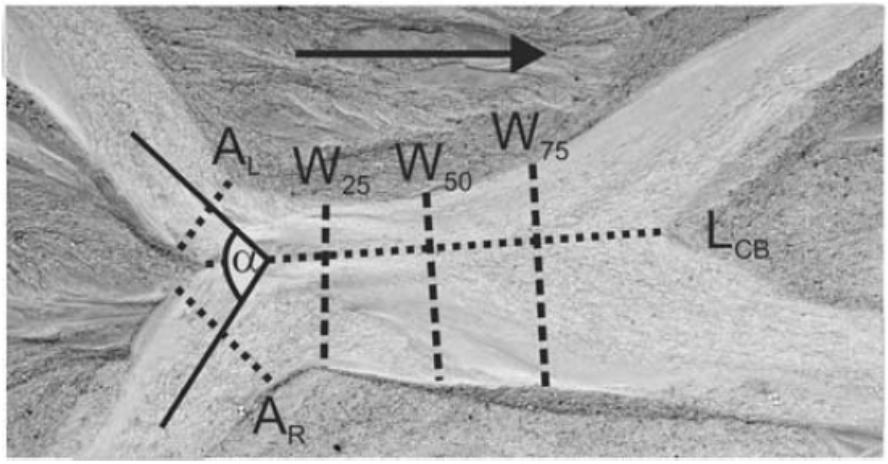

Figure 3.1 An example of planform showing link length (LCB) and widths at different cross-section. (Source: Hundey and Ashmore, 2009). They determined the average width of the linking channel and sought linear relationship between link length and the width.

The distance between adjacent confluences and bifurcations has been termed as the link length by Ashmore (2001). Ashmore (2001) asserts that, as the initial stage of braiding development commences through an organized sequence of bars and pools (e.g., Ashmore, 1991; Murray and Paola, 1994; Bertoldi et al., 2009b; Nicholas, 2013; Schuurman et al., 2013), there must exist some characteristic relationship between link length and channel width which persists in mature channel networks. In

subsequent research, Hundey and Ashmore (2009) revealed the link length scales as between 4-5 times the average width of the channel (see Figure 3.1 after Hundey and Ashmore (2009)); a pattern that closely resembles the relationship between bar and pool distance in low sinuosity single thread rivers.

The distribution of link lengths has been found to be negatively skewed both in the case of natural braided rivers (see Ashmore, 2001) and also in physical models of (see Hundey and Ashmore, 2009). This observation was used by Doeschl et al. (2009) to test the performance of the Murray and Paola (1994; 1997) rule-based simulation model. In this analysis, they observed similar distributions of dimensionless link length across a wide range of natural prototype braided rivers and laboratory models that were consistent with the numerical simulations (see Figure 3.2).

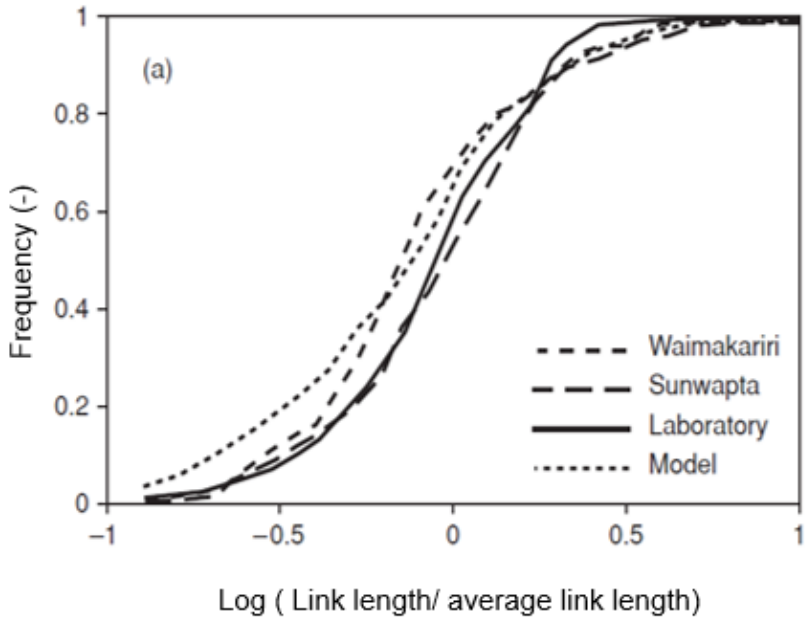

Figure 3.2 Cumulative frequency distribution of dimensionless link length exhibiting similar shape across a wide range of natural, flume and model generated rivers (Source: Doeschl et al., 2009).

c) Bar Shape

Different approaches have been proposed to analyse the shape of bars in braided rivers. For example, Sapozhnikov et al. (1998) used the relationship between the major and minor axis of bars as a measure of similarity between a prototype river and

the Murray and Paola (1994; 1997) model. More recently, Kelly (2006) identified a range of scaling relationships including: bar area and perimeter; length of major axis with minor axis; braid belt width to length of major axis; and length of minor axis with channel depth, as described below:

$y = 5.68x^{0.5}$ - bar area (y) and bar perimeter (x) Eq. 3.1

$y = 4.62x^{0.96}$ - bar major axes (y) and bar minor axes (x) Eq. 3.2

$y = 1.04x^{0.82}$ - bar major axes (y) and braided corridor width (x) Eq. 3.3

$y = 7.38x^{1.46}$ - bar minor axes (y) and channel depth (x) Eq. 3. 4

These scaling relationships (see Figure 3.3 after Kelly (2006)) provide a useful framework to assess the character of bar forms generated by numerical models. Both Nicholas et al. (2009) and Schuurman et al. (2013) used geometrical relationships for bars to assess and compare model simulations. In related work, Takebayashi and Okabe (2009) analysed the bar shapes generated by their numerical model under both steady and unsteady driving discharges based on visual observation and found significant differences in the elongation of bars along the principal flow direction between the two discharge conditions. The elongation of bars was further found to vary when the model was adapted to incorporate the effects of vegetation colonisation of bar surfaces. Quantification of bar shape thus appears as an important metric to detect differences between simulations and natural prototype under consideration.

As bar shape varies through space and time, the derivation of such scaling relationships first requires a working definition to identify bar forms. In common with the TBI metrics discussed above, this is not straightforward as the segmentation of bars from channels is an arbitrary planform characterization based on a given flow at

the time of observation and fails to recognize the continuous nature of these topographic perturbations. So, in addition to manual measurement of bars at given discharge, previous research has also used digital elevation models of braided morphologies to estimate more robust statistical metrics. For example, Schuurman et al. (2013) used two approaches to characterize bar geometries of synthetic (model generated) terrain models. First, bar length was derived using spectral analysis of channel profiles based on a wavelet decomposition in which the dominant frequency was used to estimate the average bar length. The second approach followed the method used to derive a topographic-based TBI as discussed above, in which the terrain model was segmented into bars and channels using the local mean bed level (MBL) as a threshold. Bars were then classified as areas above MBL and vice versa for channels (see also Singh et al., 2017).

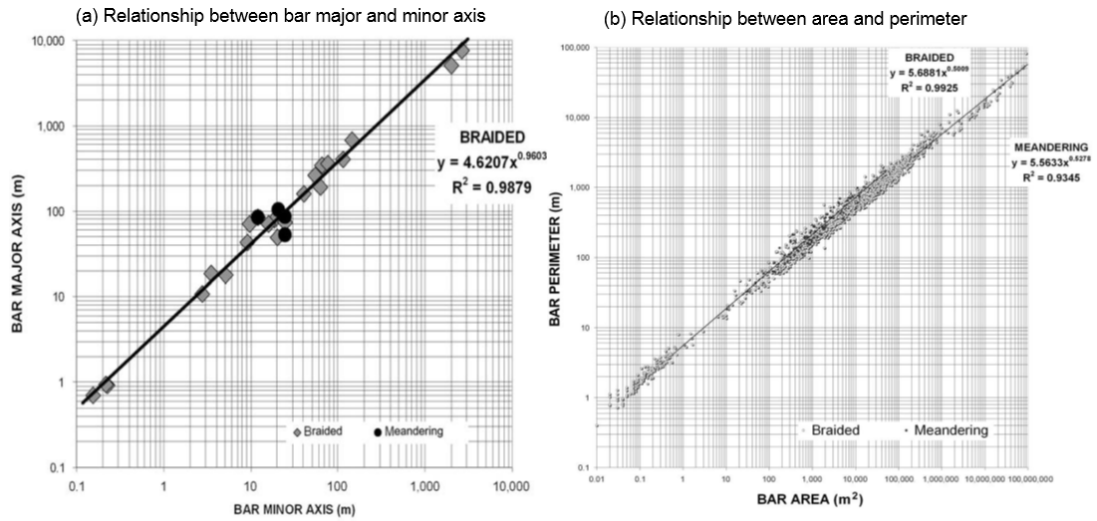

Figure 3.3 Bar length, bar width and aspect ratio (a) and the relationship of bar area with perimeter (b) as revealed by Kelly (2006). (Source: Kelly, 2006).

d) State - Space Plots

All the approaches to planform characterization discussed above describe reach average characteristics. An alternative approach that explores the spatial structure of braiding is the use of state-space plots that characterize the spatial autocorrelatory structure of planform geometry as described by Sapozhnikov et al. (1998). This approach is based on a spatial analysis of bar form using delay coordinate embedding

of sequential channel widths as shown schematically in Figure 3.4 below. By extracting and then plotting widths in series, this approach characterizes the spatial trajectory of channel geometry and provides an insight into the morphodynamic feedbacks that control longitudinal channel form. This technique has been applied to quantify the planform structure of braided rivers and to test the model performance (e.g., Murray and Paola, 1994, 1997; Sapozhnikov et al., 1998). If this approach is applied to large reaches, the density of the plot about the one-to-one diagonal indicates the presence of a systematic sequence of narrowing and widening, indicative of serial confluence and bifurcation geometries. By contrast, deviation of coordinates from the diagonal line that suggests sudden narrowing and widening of channel width, which can imply abehavioural geometries, uncommon within natural river systems (see Figure 3.4 after Sapozhnikov et al. (1998)). To date, however, this approach has only been applied to whole channel belts, using wetted width to characterize average form, and as such provides less information on the characteristic scale and structure of individual anabranches.

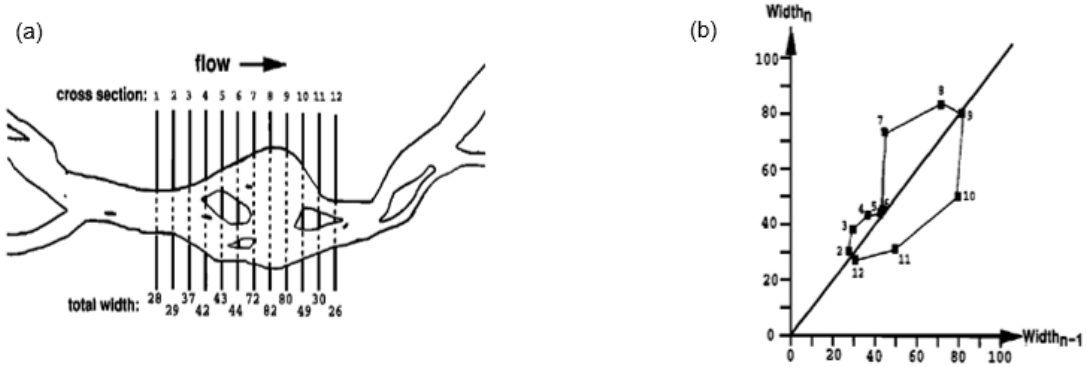

Figure 3.4 An example of planform having systematic narrowing and widening of width showing width of cross-section (a) and state-space plot of corresponding data (b). (Source: Sapozhnikov et al., 1998).

3.3.2 The Topographic Character of Braided Rivers

The planform metrics discussed above all suffer from sensitivity associated with their definition at a given flow. While the variability of metrics, such as TBI with discharge, may provide an insight into the morphological response associated with the feedback

between flow and sediment transport, field observations rarely provide such rich information and are typically limited to one-off snapshots of system behaviour that are difficult to generalize. Recent advances in remote sensing and geomatics leading to the advent of data rich digital elevation models have, however created the opportunity to examine the fully 3D character of channel form directly, free from the arbitrary classification of wetted channels and bars (Bertoldi et al., 2010; Wheaton et al., 2010; Bertoldi et al., 2011b; Brasington et al., 2012; Wheaton et al., 2013; Williams et al., 2014) . These spatial models typically take the form of 2.5D raster elevation grids and are used as the boundary conditions for distributed morphodynamic models (e.g., Williams et al., 2013; Javernick et al., 2014) and consequently have a data structure that is directly comparable to synthetic model generated topography. Given the continuous nature of these data models, a wide range of morphological descriptors have previously been determined from these data and are reviewed below.

a) Statistical Distribution of Elevations

One of the most widely used descriptors of landforms is the hypsometric curve (Langbein, 1947; Willgoose and Hancock, 1998). This describes the cumulative elevation distribution measured with respect to a datum, normally taken to be regional sea level (Willgoose and Hancock, 1998). In the case of fluvial hypsometry, it is common practice to quantify the relative elevation distribution measured with respect to a local valley average or mean bed level (e.g., Wheaton et al., 2010; Bertoldi et al., 2011b). Previous examination of natural channels and physical models have demonstrated that braided rivers commonly exhibit a negatively skewed elevation distribution in which the median elevation is higher than mean (e.g., Doeschl et al., 2009; Garcia Lugo et al., 2015). This reflects the presence of localized, deep scour pools with elevations well-below mean bed level and the large areal contribution of relatively high bar top surfaces. Doeschl et al. (2009) used this topographic ‘signature’ to examine the differences between the Sunwapta River against flume and synthetic

channel topographies (simulated using (Murray and Paola, 1994, 1997). As illustrated in Figure 3.5, they observed similar shaped distributions in all three cases, despite significant differences in the qualitative character of the morphologies. This led them to conclude, that the hyposometric curve alone is not an effective measure for model testing as the statistical structure of elevations can obscure significant deterministic differences between surfaces.

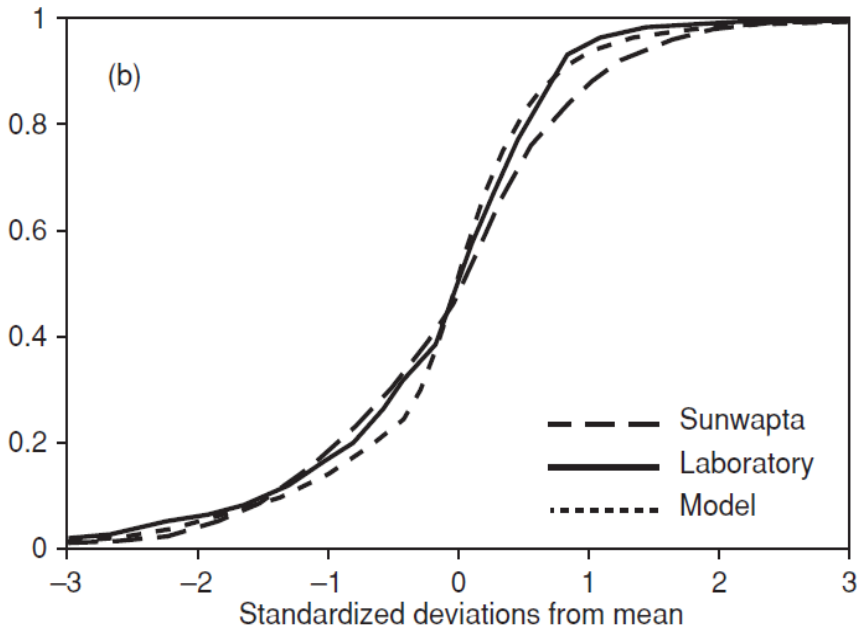

Figure 3.5 Cumulative frequency distribution of standardized elevation (Source: Doeschl et al., 2009). They determine the standardized elevation about mean elevation of cross-section from original elevations, which is then divided by standard deviation of elevations of the cross-section.

Nevertheless, in some cases the frequency distribution of elevation has proved to be a useful tool to capture topographic signatures that differentiate surfaces. For example, Bertoldi et al. (2011b) found significant differences in the skewness and kurtosis of elevation distributions derived for vegetated and unvegetated reaches of the braided Tagliamento River in the Italian Piedmont using terrain models derived from airborne lidar. Using distributions detrended by the mean bed level, they showed that less vegetated reaches had distributions centred symmetrically about the mean, with high variance and low kurtosis, indicating relatively low rugosity and low relief topography (see Figure 3.6C after Bertoldi et al. (2011b)). By contrast, reaches

characterized by vegetated bars had strongly skewed distributions, due to the areal dominance of very high bar surfaces and a heavy tail reflecting deeply dissected channels that separate the bars (see Figure 3.6D after Bertoldi et al. (2011b)). They suggested this statistical 'topographic signature' reflected the role of vegetation in reinforcing bank stability, leading to reduced lateral mobility and greater rates of local channel incision.

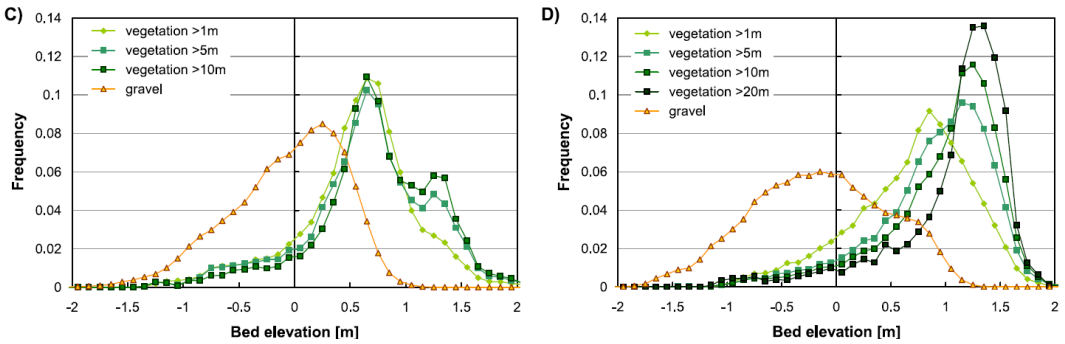

Figure 3.6 Frequency distribution of bed elevation of relatedly less vegetated reach (C sub-reach - 8) and highly vegetated reach (D sub-reach - 13), Tagliamento River (Source: Bertoldi et al., 2011b). The distribution depicts the frequency of different classes of vegetation with respect to the bed elevation. In both the reaches, the vegetation appears from just below the average elevation, which becomes significant above elevation of 0.5 m, and noticeably above 1 m elevation, bare gravel disappears implying vegetation cover of 100 %.

b) Distribution of Slope

Empirical digital elevation models and synthetic modelled terrains can also provide an insight into the characteristic distribution of local gradients that are critical controls (and responses) on flow and sediment transport. Doeschl et al. (2009) compared the distribution of local slope derived from DEMs of natural channels with the Murray and Paola (1994; 1997) model generated topography. In this study, they determined separate distributions of slope for cells with elevations above (bars) and below (channels) the median elevation. For natural and flume generated terrains, they observed a significantly wider distribution of local slopes for areas below the median elevation than those above this threshold. Such distinction in between high and low stage topography was not however evident in the synthetically generated data (see

Figure 3.7 after Doeschl et al. (2009)). They attribute this to the rule-based representation of flow and sediment transport in the Murray and Paola model, and specifically the kinematic routing scheme which, by lacking the lateral dispersion of momentum, creates a tendency to generate spikes or pits in the topography due to exaggerated feedback between the unrealistic convergence and divergence of flow and sediment transport.

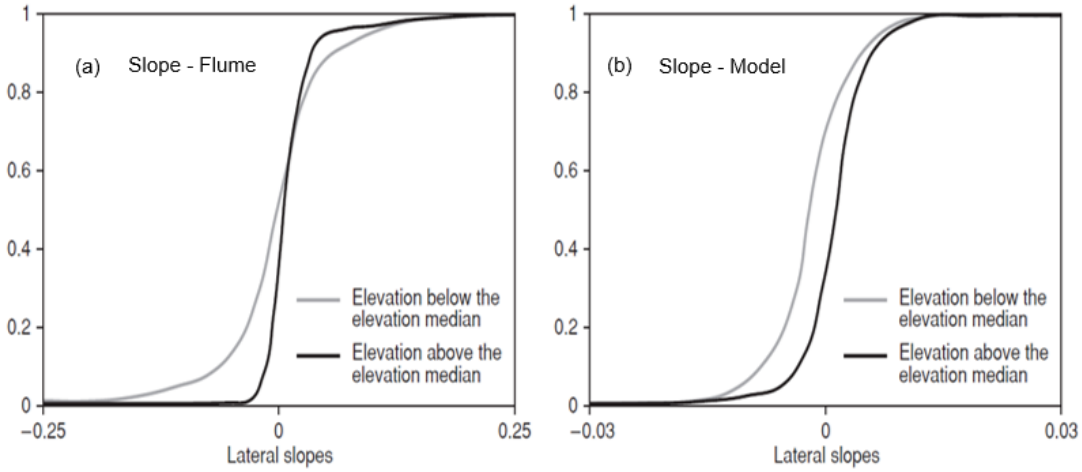

Figure 3.7 Cumulative frequency distribution of standardized elevation (Source: Doeschl et al., 2009).

c) Channel Shape

Over short timescales, in which the bed can be considered immobile, channel shape (along with hydraulic factors, principally friction) controls how cross-sectional area and thus velocity and depth vary with discharge and thus define the at-a-station hydraulic geometry (Jowett, 1998). Over the longer term, it is however appropriate to view channel shape as both a control and response variable, reflecting the interaction of flow and sediment transport which in turn drives morphological adjustment and the development of an emergent channel form (James, 1991; Redolfi et al., 2016b). The analysis of channel shape has therefore been a primary area of interest to understand the nature of these feedbacks in wide range of different drainage context, from estuaries (e.g., Toffolon and Crosato, 2007) to braided rivers (e.g., Redolfi et al., 2016b).

Measurements of channel shape have been derived conventionally from cross-section measurements. Using these data, Jowett (1998) defined the channel shape as the power relationship of width (W) with respect to the deepest point or minimum elevation of the section (Y_{min}), where:

$$\boldsymbol{W = a_c(Y - Y_{min})^{b_c}} \quad \text{Eq. 3. 5}$$

Where, b_c is a 'shape exponent' and a_c is a coefficient of proportionality and Y is the elevation. A similar approach was developed by Redolfi et al. (2016b) except in this case, the approach is applied to multiple sections extracted from a DEM and the results are averaged over a representative number of channel widths. The functional relationship between effective width and height is again modelled as a power function (see Figure 3.8 after Redolfi et al. (2016b); where the power is denoted as α). In both approaches, values of the shape exponent (b_c or α) of less than unity reflect channels with little variation in width with height, whereas values above one corresponds to rapid increases in width with height. Conveniently, if the relationship is plotted with width on the x-axis and depth above minimum on the y-axis (Figure 3.8), the plot resembles a half-plot of the reach-average cross-sectional channel shape. For exponents of less than unity, the plot resembles a U-shape, a straight line for values close to unity, and Y-shaped form for values above unity. Both Jowett (1998) and Redolfi et al. (2016b) found this measure to be an effective discriminant of channel type, with high values of α (or b_c) corresponding to unconfined braided channels. This reflects the shallow relief of braided fairways in which, once the lowest pools are filled, further increases in height (water level) are associated with rapid extensions of wetted width. This pattern mirrors the at-a-station hydraulic geometry measurements of Ashmore and Sauks (2006) which showed that, for the braided Sunwapta River, increases in discharge were accommodated principally by increases in width (see also Mosley, 1983). Their measurements even indicated that width exponents of fitted hydraulic geometry power laws could exceed unity, suggesting that increased

discharge was accommodated by extensions of width that led to decreases in either velocity or depth.

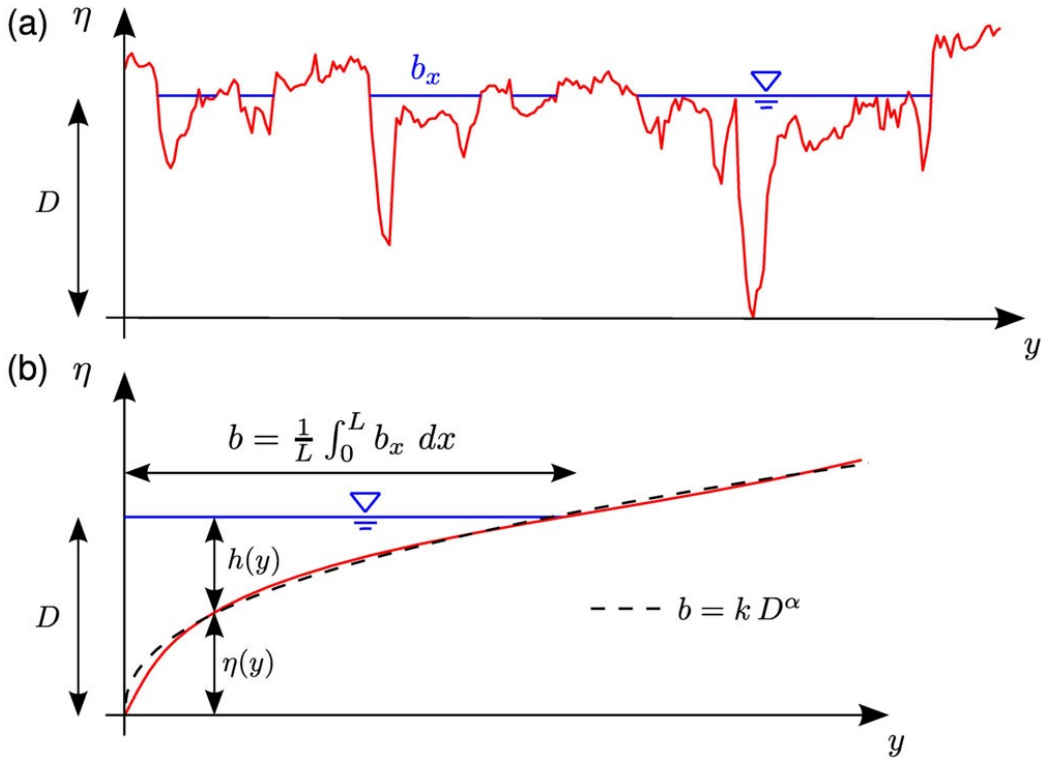

Figure 3.8 Schematic diagram for the determination of power relationship between depth and width based on bed elevation (Source: Redolfi et al., 2016b).

d) Bar Height

A well-established anomaly associated with many morphodynamic models is the tendency for channels to become progressively over-deepened (e.g., Schuurman et al., 2013; Singh et al., 2017). This is largely thought to relate to limitations in the representation of bank erosion processes which inhibit lateral bank migration and intensification of channel bed scour (see Schuurman et al., 2013). Such effects may give rise to a progressive detachment of bars and channel, resulting in the loss of braiding intensity (cf. Singh et al., 2017) and an evolutionary trajectory from braiding to single thread (e.g., Doeschl-Wilson and Ashmore, 2005; Ziliani et al., 2013). A useful metric to assess this trajectory is changes in bar height through time, where height is measured simply as the average channel relief (maximum minus minimum in a cross-section). Alternatively, in order to skip from spurious height (sloughs) that

may encounter, it is also common to consider bar height as the difference between 95% and 5 % of elevation (e.g., Schuurman et al., 2013; Singh et al., 2017). Both Schuurman et al. (2013) in sand-bed rivers and Singh et al. (2017) in gravel-bed rivers used this approach to analyse the evolution of reach-averaged bar height in morphodynamic simulations of braiding using Delft3D. In both studies, progressive channel deepening was observed, which they attribute to inadequacies in the bank erosion algorithm. These results indicate a critical weakness of their morphodynamic models, as chute cut off, bar dissection and local channel avulsion that are needed to counter the effects of channel incision and make the braided river mobile (Jerolmack and Mohrig, 2007; Wheaton et al., 2013) were absent.

3.3.3 The Hydraulic Characteristic of Braided Rivers

The planform and topographic metrics discussed above provide an insight into the emergent spatial form of channel morphology but offer only indirect insights into the forcing hydraulic processes that drive sediment transport and lead to the adjustment of form through time. Direct observations of the distributed hydraulics of braided channels are notoriously difficult to acquire in the field (Mosley, 1983; Williams et al., 2013). Consequently, there exists relatively little prototype data against which the behaviour of numerical models could be compared.

a) Distributions of Water Depth

Advances in remote sensing, in particular the development of optical-bias depth estimation from aerial imagery and novel acoustic methods (e.g., Marcus and Fonstad, 2010; Williams et al., 2013; Javernick et al., 2014; Williams et al., 2014) have created the opportunity to acquire broad-scale data models of water depth. These emerging datasets now provide a basis to map the spatial and statistical distribution of flow depths for a given discharge, data which can be directly compared to model simulations from either fixed-bed (e.g., Williams et al., 2013; Javernick et al., 2016) or morphodynamic models (Williams et al., 2016a).

b) At - a station Hydraulic Geometry (AHG)

Hydraulic geometry quantifies the relationship of channel width, depth and velocity with discharge as a set of power functions that describe how changes in discharge are accommodated (Leopold and Maddock, 1953):

$$W = aQ^b; D = cQ^f; V = kQ^m \qquad \text{Eq. 3. 6}$$

Where, Q is discharge in m^3/s, W, D and V are width in m, depth in m and velocity in m/s, respectively; a, c and k are the coefficients, and b, f and m are the exponents. The plot of discharge verses width, depth and velocity in log-log scale gives the value of coefficients and exponents (e.g., Leopold and Maddock, 1953). As discharge is simply the product of width, depth and velocity; the product of the resulting coefficients (a x b x k) and the sum of resulted exponents (b + f + m) should be unity (Leopold and Maddock, 1953). The width, depth and velocity exponents in the case of single thread rivers are commonly taken to be in the region of 0.26, 0.4 and 0.34 respectively, following the seminal work of Leopold and Maddock (1953). This suggests that accommodation of discharge is achieved principally by depth, then velocity and only then width, a pattern reflected also in the low (< 1) channel shape exponents discussed above in Section 3.2.3. Observations of AHG in braided rivers are rare (largely as gauging braided reaches is rarely undertaken and certainly not routinely monitored) but the few data that do exist indicate much higher width exponents, typically in the range of 0.4 - 0.7 and occasionally higher or near to one (see Table 3.1 below).

Some of the earliest measurements of AHG in a braided channel are from (Mosley, 1983) who examined the channel response to increasing discharge on the Ohau River, NZ. Here, well-constrained dam releases generated a spectrum of flows varying across a 20-fold range of discharge. Mosley's observations suggest that much of the accommodation of discharge was achieved through a high rate of width

increase, associated with the activation of new channels across previously dry areas of the braidplain that were filled by the addition of water from faster flows in the core anabranches. Ultimately, increases in the depth and velocity of existing channels is therefore balanced by the addition of flow to shallow, slow moving water and the broadband statistical distribution of flows (and shear stresses) remains similar despite an overall increase in the total wetted width. Similar observations have been found in other braided channels, both in the field and within physical models (e.g., Smith et al., 1996; Ashmore and Sauks, 2006; Bertoldi et al., 2009b; Welber et al., 2012; Ashmore, 2013). The Table 3.1 summarizes width, depth and velocity exponents revealed by different studies. These studies suggest collectively that the most common range of the width exponent is 0.4-0.7, although Ashmore and Sauks (2006) observations on the braided Sunwapta River in Alberta suggested that the width exponent (b) may actually exceed unity as discussed above.

Table 3.1 At-a-station hydraulic geometry relationships related exponents compiled from literatures with particular focus on braided rivers.

Literature	Width exponent (b)	Depth exponent (f)	Velocity exponent (m)	Remarks
Leopold and Maddock (1953)	0.26	0.4	0.34	Single thread rivers
Mosley et al. (1983)	0.5	0.253	0.39	Ohau River, NZ (Braided)
Ashmore (2013)	0.453	0.338	Not shown	Field (Braided)
Ashmore (2013)	0.473	0.345	Not shown	Flume (Braided)
Smith et al. (1996)	0.51 - 0.65	0.16 - 0.29	0.19 - 0.2	Tanana, Taku, and Iskut, Canada (Braided)
Ashmore and Sauks (2006)	1.06	Not shown	Not shown	Sunwapta River, Canada (Braided)
Bertoldi et al.(2009b)	0.7	Not shown	Not shown	Trento Flume, Italy (Braided)
Welber et al. (2012)	0.52 - 0.53	Not shown	Not shown	Tagliamento River, Italy (Braided)

While AHG is difficult to measure in the field, the relevant data could be readily extracted from numerical models. Computing these relationships for comparison against a prototype system remains challenging due to the dearth of natural data. However, an alternative approach could be to derive AHG relationships for a prototype using observed morphology as the boundary conditions of a fixed-bed hydrodynamic simulation. This would result in a hybrid approach, essentially a comparison of two

synthetic data records, but where the observed and modelled topography play a fundamental role in driving the derived relationship.

3.3.4 Sediment Transport and Morphodynamic Adjustment in Braided Rivers

a) Sediment Transport

Understanding the nature of sediment transport is important because it is strongly associated with the bed morphology, both as a control and a response. The process of sediment transport in gravel-bed braided rivers is, however, complicated by uncertainties in key variables (turbulent shear stresses, particle size and packing, bed armouring and breakup) that are arguably unknowable at relevant spatial scales. These uncertainties are further, magnified, when extrapolated to the heterogeneous reach-scale geometry of braided rivers (Bogen, 1980; Reid et al., 1985; Mao et al., 2014). However, laboratory-based models of braiding, evolving under steady discharge conditions have shown that bed material transport often fluctuates around a constant value at equilibrium conditions (e.g. Ashmore, 1987, 1988; Young and Davies, 1990; Warburton, 1996; Bertoldi et al., 2009b). These fluctuations have been attributed to autogenic dynamics of braiding, that include the formation and break-up of bedforms and the processes of channel (bar) migration, such as chute cutoff, avulsion and bank or bar edge erosion (see Bogen, 1980; Ashmore, 1987, 1988; Wheaton et al., 2013; Mao et al., 2014).

Such qualitative insights have been used to help interpret the outputs of previous experiments with numerical simulation models of braiding. For example, both Jang and Shimizu (2005) and Thomas et al. (2007) used time series of outlet sediment flux (see Figure 3.9 after Jang and Shimizu (2005)) to evaluate the transport dynamics of morphodynamic models. More recently, Schuurman et al. (2013) examined the reach-averaged sediment transport capacity of a modelled sand-bed channel as it fluctuated throughout an evolutionary cycle; from an initial plane bed to a fully developed braided channel. They observed, perhaps surprisingly, that transport capacity decreased after

the initial stage of linear bar development and ultimately tailed off to unrealistically negligible rates as fully mature and complex bars emerged. At this stage, further evolution was limited by the absence of key braiding processes such as chute cutoff, avulsion and lateral migration. As discussed above in Section 3.3.2, they again attributed this behaviour to the gradient-based bank erosion algorithm used in Delft3D.

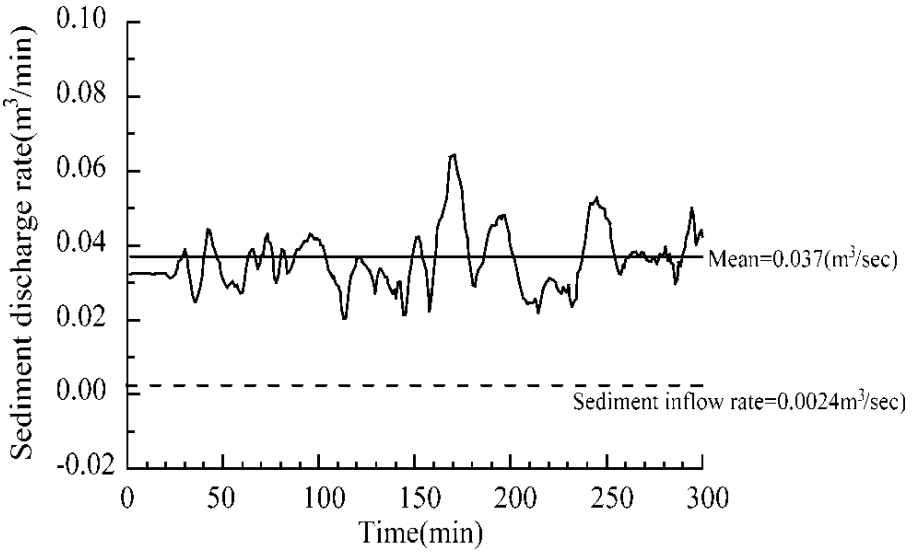

Figure 3.9 Sediment inflow and outflow from the open boundaries in the numerically generated braided river by Jang and Shimizu (2005).

While laboratory simulations provide a useful insight into transport fluxes and pathways, such physical models offer only a partial representation of the complexity associated with the characteristically unsteady flow and sediment input conditions found in natural prototypes. Advances in the measurement of transport fluxes in the field now create some useful opportunities to develop this theme (see section 3.6.4 a below) although it is likely that, given the difficulty of mounting and sustaining field campaigns, such data are likely to remain rare.

An alternative insight into the material fluxes in a given system can be gained from simplified one-dimensional transport formulations derived using cross-section data (Nicholas, 2000; Ferguson, 2003; Bertoldi et al., 2010), or from fixed-bed 2D hydrodynamic models (e.g.,Redolfi et al., 2016b) as discussed above. This numerical

approach can provide insights into the potential range of transport fluxes associated with varying discharge, for example, in the form of a sediment transport rating curve and its associated exponent (typically found to lie in the range 1.5 - 2.8 (cf. Ashmore, 1988; Garcia Lugo et al., 2015). Such synthetic data offer a basis to corroborate, if not formally test, the simulations based on fully morphodynamic models.

b) Active Width

Active channel width, defined as the cross-section width through which sediment transport actually occurs (Ashmore et al., 2011; Ashmore, 2013). As active channel width is based on the sediment transport or morphological change, this metrics has been considered as a morphodynamic metric in this study. This metrics provides an interesting alternative definition of the conventional hydraulic metric of wetted width. Laboratory studies have shown that gravel transport is typically restricted to a small fraction of the wetted width, often comprising between 15-40% of the total wetted channel area (see Bertoldi et al., 2009b; Egozi and Ashmore, 2009; Marti and Bezzola, 2009; Ashmore et al., 2011; Garcia Lugo et al., 2015). Recent field-based research using acoustic Doppler current profiler (aDcp) bottom-track bias estimates of sediment transport pathways in the braided Rees River in New Zealand (e.g., Williams et al., 2015) has revealed similar relationships in natural prototypes (see Figure 3.10 after Williams et al. (2015). Ashmore et al. (2011) also analysed the stage dependence of active width, demonstrating the existence of key thresholds in the driving discharge or stream power followed by relatively predictable monotonic increases in active width. Such insights from field and laboratory-based models remain rare within the literature, so that again, fixed-bed hydrodynamic simulations may be useful to examine and establish relationships under relatively well-constrained conditions.

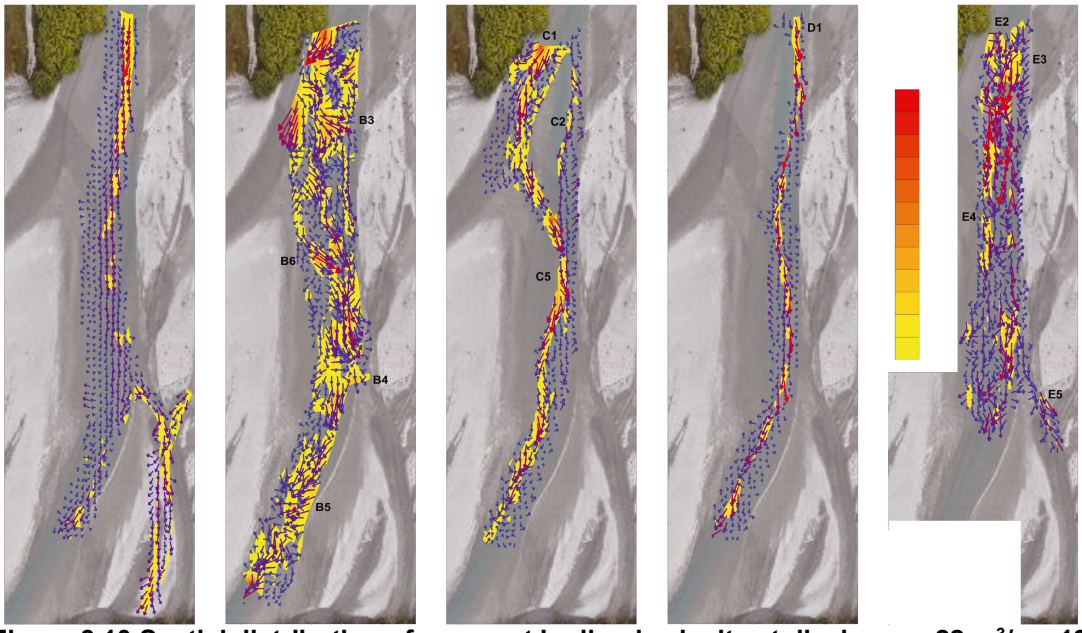

Figure 3.10 Spatial distribution of apparent bedload velocity at discharges 22 m^3/s - 19 m^3/s, 75 - 70 m^3/s, 40 m^3/s, 20 m^3/s -20 m^3/s - 21 m^3/s, and 39 m^3/s - 30 m^3/s from left to right respectively, measured by Williams et al. (2015) in the Rees River, NZ. Flow is from top to bottom and the background map shows the corresponding inundated area.

c) Active Braiding Index

A similar refinement of the channel count (braiding) index is the definition of an Active Braiding Index (ABI). This can be defined as the number of morphologically active, or sediment transporting channels per cross-section width (Ashmore, 2013). Observations in natural braided rivers have revealed that relatively few channels contribute most of this 'geomorphological' work. For example, Mosley (1983) found from observations of piedmont braided rivers in NZ, that as much as 70-80% of the total bed material flux was conveyed by just two anabranches. Similar results have been obtained in well-controlled laboratory experiments (Bertoldi et al., 2009b; Egozi and Ashmore, 2009), which have shown that at dynamic equilibrium, sediment transport was typically confined to just 1-2.5 anabranches. These studies suggest the ratio of Total Braiding Index (TBI) to Active Braiding Index (ABI) at formative condition stabilized at ~0.4. This provides basis for a quantitative criteria to evaluate a numerical simulations (e.g., Schuurman et al., 2013). However, it should be noted that active channels in braided rivers are time-transgressive (Egozi and Ashmore, 2009) so that

the pattern of active channel migration is strongly contingent on the evolutionary history of the system (Surian, 2015), giving rise to often unpredictable, non-linear adjustments. Additionally, there is some inconsistency in the definition of Active Braiding Indices. For example, in flume based studies (e.g., Bertoldi et al., 2009b; Egozi and Ashmore, 2009), the ABI has been determined by counting channels that transport significant amount of sediment or where changes occurs. By contrast, in numerical model based studies (e.g., Schuurman et al., 2013; Singh et al., 2017), the ABI has been defined as the number of channels which transport sediment above the mean transport of the entire braid plain width. Here again, fixed-bed hydrodynamic simulations could be used to determine the distribution of sediment transport across a range of driving discharges and subsequently generate a theoretical active braiding index.

d) Erosion and Deposition

Insights into the deterministic pattern and magnitude of erosion and deposition in braided rivers can be derived from field surveys which also offer a robust test of model performance. Historically, such data were derived from cross-section surveys, and/or interpolated from aerial photos (e.g., Sanyal, 1980; Mosley, 1983; Ferguson and Ashworth, 1992; Warburton et al., 1993; Bertoldi et al., 2010). Recent developments in remote sensing and geomatics have enabled fully 3D models of channel change to be derived using dense channel models derived from airborne and terrestrial lidar, softcopy and structure-from-motion photogrammetry (e.g., Lane et al., 1993; Bertoldi et al., 2011b; Brasington et al., 2012; Westoby et al., 2012; Williams et al., 2014). The very high-resolution topographic models are ideally suited to quantify morphodynamics (e.g., Wheaton et al., 2013), and even to reconstruct transport rates indirectly and derive detailed sediment budgets through DEM differencing techniques (e.g., Ashmore and Church, 1998; Redolfi, 2014).

Patterns of erosion and deposition obtained from the DEM differencing can be analysed in a variety of ways. For example, the overall structure of channel adjustment can be presented as planform maps or the total volumetric analysis of erosion and deposition quantified statistically and the change in mean-bed level derived (e.g., Wheaton et al., 2010; Williams et al., 2014; Vericat et al., 2017). Wheaton et al. (2013) have also demonstrated how segregation of channel changes can be used to identify the contribution of particular braiding mechanisms (e.g., chute cutoff, avulsion and bank erosion) to sediment storage and mobilization (see Figure 3.11 after Wheaton et al. (2013)). Using high-resolution repeat topography from braided River Feshie, they identified chute cut off as the critical mechanism involved in the maintenance of braiding, a pattern consistent with previous flume and planform field studies (e.g., Ashmore, 1991; Ferguson et al., 1992; Ferguson and Ashworth, 1992; Bertoldi et al., 2009b). This mechanism was also observed to have a clear morphological signature, measured in terms of frequency of channel changes (volumes of scour/fill) with erosion observed across wider elevation of the bar. By contrast, the deposition associated with chute cutoff processes was characterized by a narrow, peaked distribution of relatively low magnitude change, facilitating diagonal bar growth. Lobe dissection was defined by consistent degradation, whereas the central bar development and transverse bar conversion showed net aggradation. Bank erosion processes widened the channels around mid-channel bars, contributing to net degradation.

While this approach provides a detailed insight on the contributions of different channel change mechanisms in the maintenance of braiding, it requires expert judgment to define regions of interest that surround the changes and is therefore subject to a high degree of qualitative judgement. Nevertheless, analysing individual braiding mechanisms both in natural and numerically generated braided rivers could provide a step forward as a test of the performance of morphodynamic models.

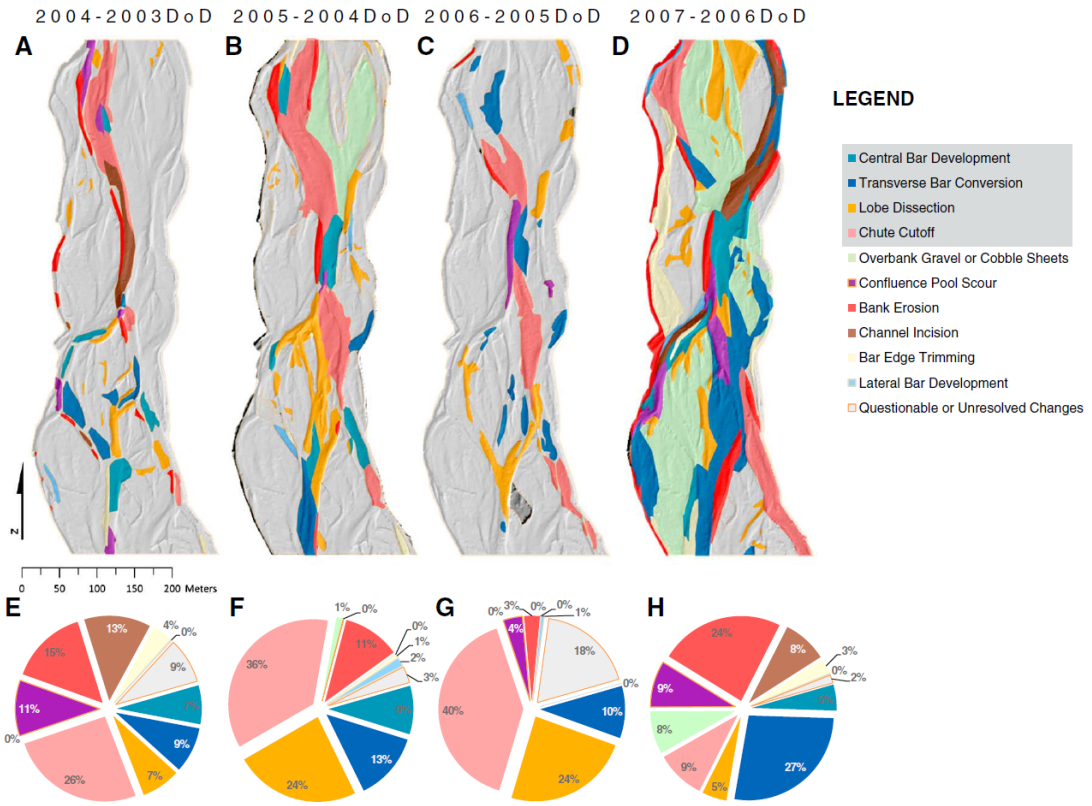

Figure 3.11 Spatial pattern (top) and the volume (top) of change in sediment storage through different braiding mechanisms. (Source: Wheaton et al., 2013).

e) Turnover of Erosion and Deposition

Finally, and linked to the pattern of channel change, a further useful metric that can be derived from multiple DEMs of difference is the channel turnover rate (e.g., Wheaton et al., 2013). This can be defined as the areal percentage of the bed that is 'renewed' by channel disturbance (i.e., incorporating the effects of both erosion and deposition) during a given time frame (e.g., Surian et al., 2015). Such data are extremely rare in field studies, but the emergence of repeat topographic surveys (as described above) potentially provides the opportunity to derive this insight which is critical not just in terms of morphogical evolution, but also to the ecological functioning of the channel (Wheaton et al., 2010).

f) New Metric to Quantify Erosion and Deposition Pattern

Using the approach of Wheaton et al. (2013) to scrutinize the contribution of each braiding mechanism to sediment storage dynamics demands expert judgement and

time. Alternatively, to gain a broader insight into the pattern of erosion and deposition, a new metric based on less subjective approach is used here (Figure 3.12).

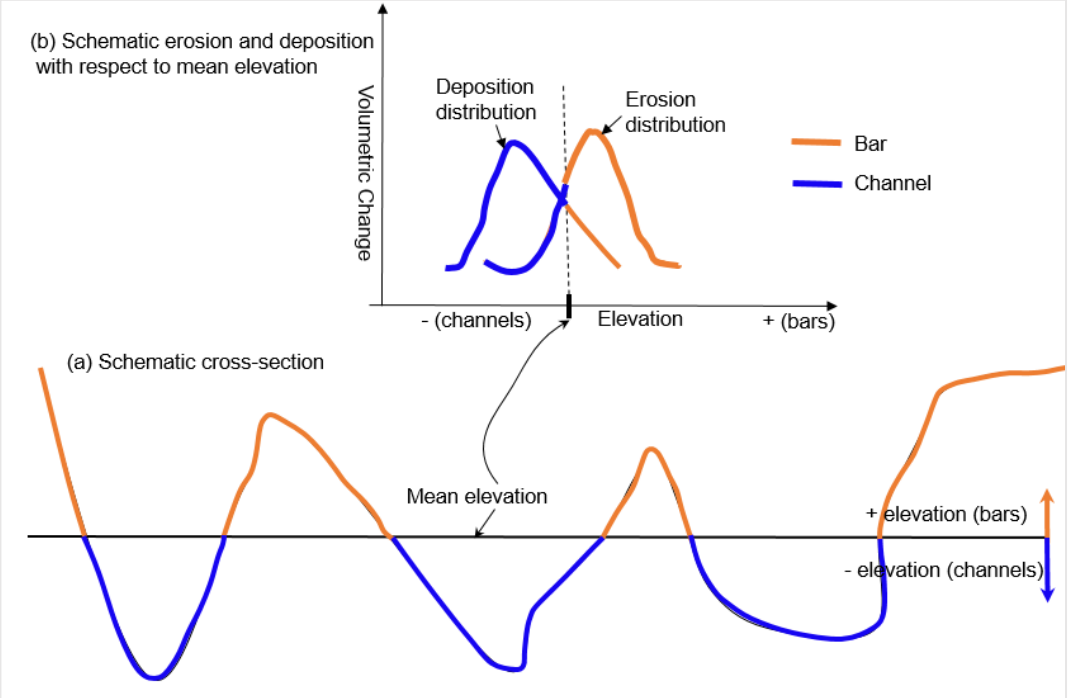

Figure 3.12 (a) Schematic cross-section. (b) Schematic of volumetric change (erosion and deposition) with respect to mean elevation of preceding state DEM under consideration. The areas on the positive and negative elevation side could be thought of bar and channel, respectively.

This involves determination of the volumes of erosion and deposition that occur at specific height (elevation) intervals. This provides an insight into the dominance of erosion and scour at low and high stages, and by inference, the likely location (channel bottoms, bar tops) of material being eroded or deposited. For this analysis, the prior DEM is used to define the range of elevation intervals (expressed relative to mean bed level). The volume of erosion above and below mean elevation of cross-section (as shown in Figure 3.12a) can be thought as representative of erosion on bars and channels respectively, and similarly for deposition (Figure 3.12b). At formative discharge conditions, when bars are partially submerged, morphological activities such as erosion of bars and deposition on nearby channel could be expected (Surian et al., 2009a; Bertoldi et al., 2010; Ashmore, 2013). Under such conditions, a skewed distribution of erosion with respect to mean elevation is likely and with a bias

to positive elevations (Figure 3.12b). The pattern of deposition is then likely to exhibit a bias to topographically low areas of the surface (Figure 3.12a). In a broader scale, dominance of bar erosion over channel erosion indirectly indicates the suite of morphological processes that are active, and can be used to indicate the presence of processes such as local channel avulsion, channel widening, cut off development and dissections that have been recognized as the main ingredients for maintenance of active braiding (Ashmore, 1991; Bertoldi et al., 2009b; Wheaton et al., 2013). Interrogating a synthetic braided river produced by a numerical model, using this approach, provides a high order, mechanistic test of behaviour.

3.4 Proposed Quantitative Framework

As discussed in the previous section, there are a range of metrics that could provide useful to evaluate the behavioural responses of numerical morphodynamic models. Here, a systematic quantitative framework, comprising four key attributes that characterise braided rivers, is proposed in order to provide a holistic assessment of model performance. This framework is schematised in Figure 3.13 below, and incorporates metrics describing channel planform, topography, hydrodynamics and morphodynamics.

In this framework, specific planform metrics including the analysis of bar shape (e.g., Kelly, 2006) and the link length (e.g., Ashmore, 2001) have not been included as the validation data from the prototype channel analysis incorporate only a small 700 m reach, with only two or three compound bars. Similarly, the State–Space plots of Sapozhnikov et al. (1998) have also been omitted in the framework. Additionally, the analysis of individual braided river mechanisms (e.g., Wheaton et al., 2013) has also not been included due to the difficulty of subjectively defining channel mechanisms. Alternatively, the additional measure describing the relationship between erosion and deposition volumes with respect to elevation (Section 3.3.4) has been added to the

framework, which indirectly provides insight into the mechanisms of channel adjustment.

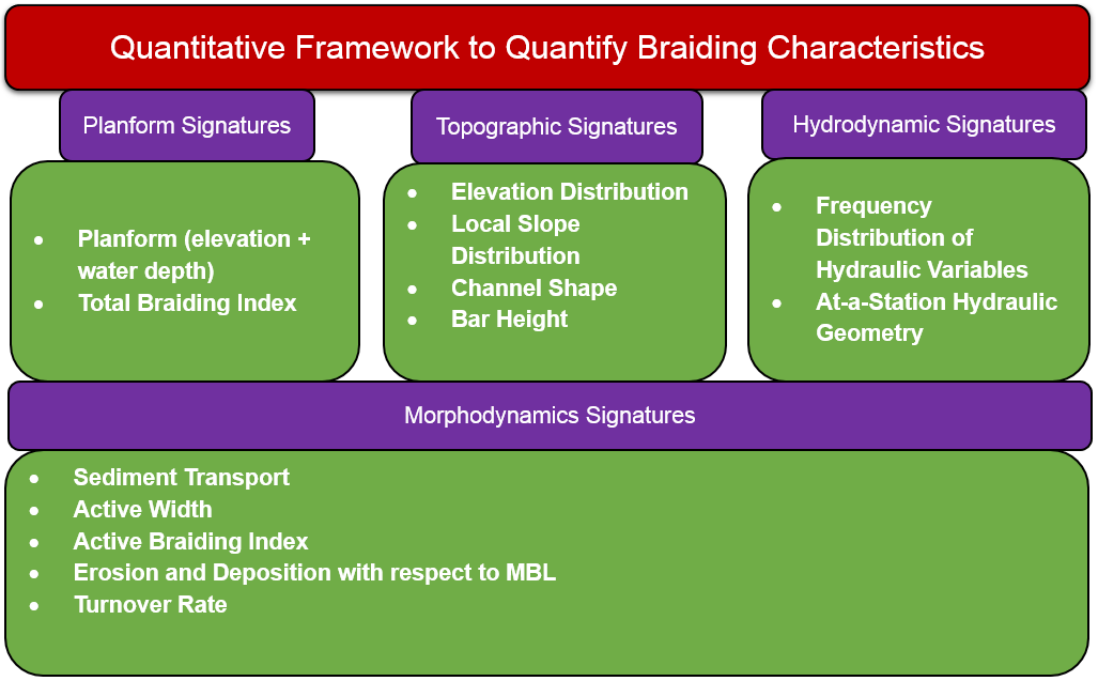

Figure 3.13 Proposed framework for quantification of braiding characteristics.

3.5 Methods for Quantifying the Natural Prototype Feshie

The framework proposed in the previous section is applied here in order to characterise the natural prototype used in this study, the braided River Feshie. This analysis reported below, provides the key data to support later model testing and validation in subsequent chapters.

DEMs of a 700 m braided reach of the Feshie acquired using a combination of Global Navigation Satellite System (GNSS) and Terrestrial Laser Scanning (TLS) surveys were made available for this study (Brasington, pers. comm.). This included comparable datasets acquired in 2003, 2004, 2005, 2006 and 2007 (Wheaton et al., 2013).

First, the five DEMs were used to abstract the planform structure (based on the detrended elevation) and topographic signatures. Second, the numerical model BASEMENT was used to calculate hydrodynamic variables based on fixed-bed

simulations across a range of relevant discharges. To simplify the computational workload, simulations were obtained using only the topographic models for 2003 and 2005 which were taken to be representative of the wider set. In order to maintain uniformity in model variables and parameters, simulations for each DEM were constructed using: a constant grid resolution (2 m^2), a spatially uniform Manning's-Strickler coefficient (30 $m^{1/2}/s$), and uniform eddy viscosity (0.1 N/m^2). The EXACT numerical solver was used to compute the hydrodynamic equations. This same set of numerical conditions was then applied in the following chapter, in which the channel morphology is allowed to adjustment dynamically.

Hydrodynamic simulations were computed for range of steady discharges varying from 5 m^3/s (annual average flow) up to 85 m^3/s (just above two-year flood) at 5 m^3/s intervals. The simulations were obtained in sequence, with flows increased linearly with time between each discharge step, and then held steady for three hours simulation time to ensure equilibrium conditions, monitored through the model mass balance. The hydrodynamic properties obtained from the model were used to estimate the rate of sediment transport at each discharge, using a routine developed separately in MATLAB. Sediment transport was determined using a fixed D_{50} and the classical MPM sediment transport formula (Meyer-Peter and Müller, 1948). Calculations were obtained based on the hydrodynamic calculations determined for cross-sections spaced at the grid resolution and then averaged and expressed as a rating curve for bedload transport. The spatial distribution of modelled flow for each discharge was then also used to determine the at–a-station hydraulic geometry relationship over the 5-85 m^3/s discharge range. Similar spatial hydraulic predictions were used to obtain data on the distribution of shear stress, water depth, active width and active braiding index. Modelling the hydrodynamic and morphodynamic patterns based on two topographic models provides an insight into the likely degree of variability. Data from the entire set of six models were used to compute the pattern of annual changes.

Finally, the five DEMs were used to determine the pattern of erosion, deposition and turnover rate using DEM differencing techniques.

3.6 Results

3.6.1 Planform Signatures

Synthetic planform statistics were obtained from each DEM using the approach described in 3.3.1. This involve first detrending each elevation model, with respect to the plane fitted by least squares to the longitudinal trend of mean-bed level. The longitudinal pattern of mean-bed level was derived for each DEM individually, and the results averaged to provide a consistent surface for detrending which was then applied to all models. The resulting set of models is shown in Figure 3.14.

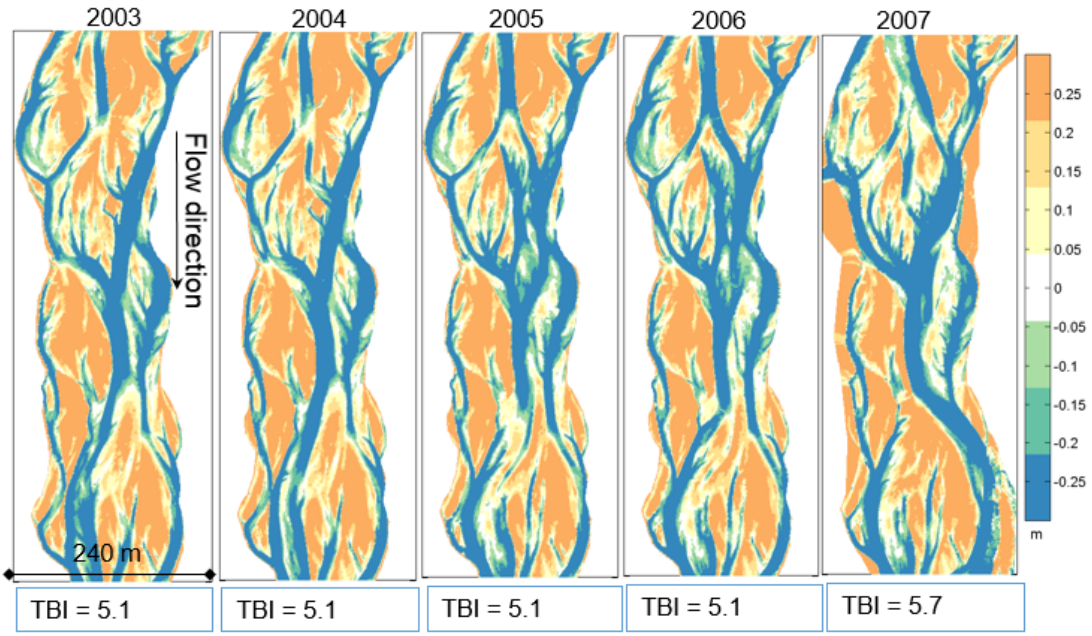

Figure 3.14 Detrended elevation with reference to mean elevation plane derived from the cross-sectional averaged longitudinal profile. The blue and grey colours represent the area below and above mean elevation which could be thought of channels and bars, respectively. The values presented at the bottom of each DEM are the Total Braiding Index in the corresponding year. River longitudinal slope or flow is from top to bottom.

The detrended surfaces were then used to determine total braiding index (TBI) based on the number of channels identified below mean bed level for each section extracted from the model, and the results then averaged longitudinally. The estimated TBI for

each DEM is shown beneath each DEM in Figure 3.14. The TBI was found to be consistent (5.1) in 2003-06 but rose to 5.7 in 2007.

3.6.2 Topographic Signatures

The detrended elevations for each cross-section were divided by the standard deviation of the corresponding cross-section to determine standardized frequency distribution (e.g., Doeschl et al., 2009). In all years, the distribution of elevation values for areas above mean bed level is consistently wider and flatter, whereas the distribution below mean-bed level is characteristically narrower (Figure 3.15a).

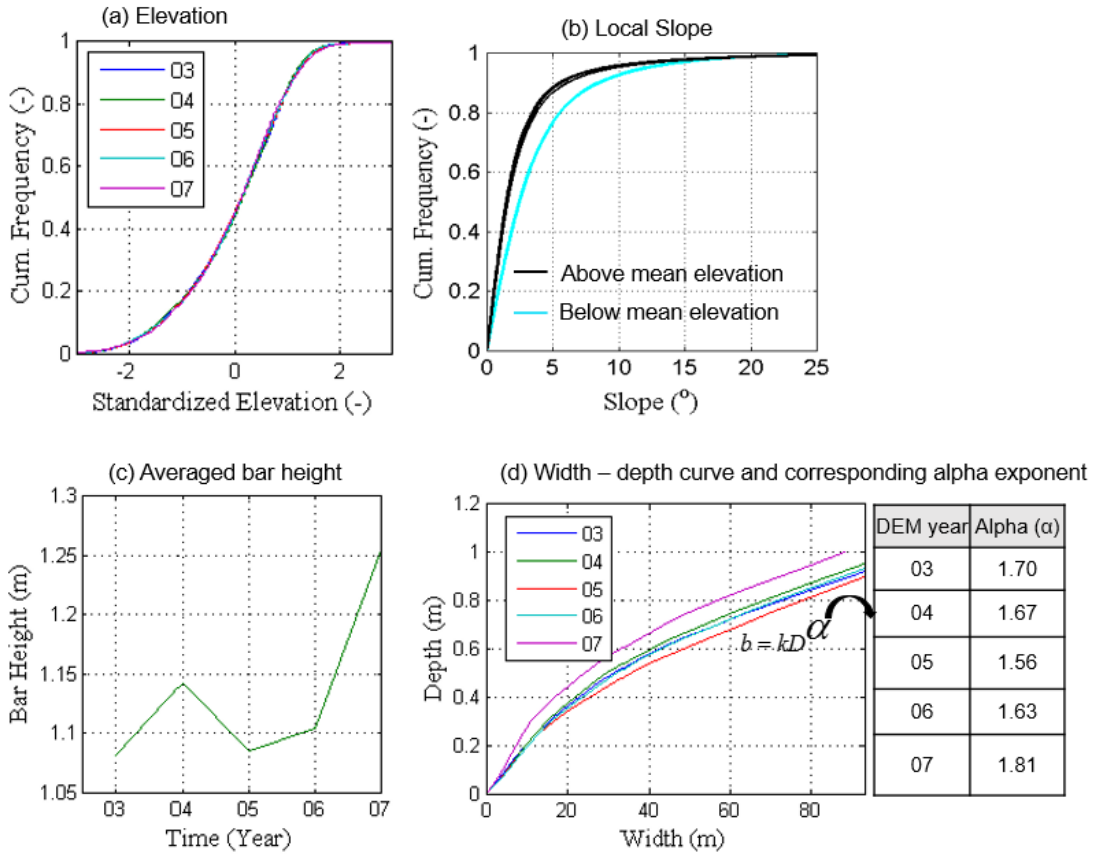

DEM year	Alpha (α)
03	1.70
04	1.67
05	1.56
06	1.63
07	1.81

Figure 3.15 (a) Frequency distribution of standardized elevations in six different years where negative and positive elevation represents below and above mean elevation area, respectively. (b) Frequency distribution of local slopes where the group of dark and faint lines show local slope above and below mean elevation in six different years, respectively. (c) Reach averaged bar height in six years. (d) Width (b) – depth (D) relationship and corresponding alpha exponent of the best power fit in six years (e.g., Redolfi et al., 2016b).

This reflects presence of dominant exposed bars as compared to channels. This type of trend in elevation distribution has been recognized as the universal signature of braided rivers that exist both in natural and flume experimented braided rivers (e.g., Doeschl et al., 2009; Garcia Lugo et al., 2015). The local slope distribution was determined by again separating the dataset into areas above and below mean bed level (e.g., Doeschl et al., 2009).

The local slope distribution of all years DEM resulted significantly wider distribution for the below mean than above mean elevation distribution (Figure 3.15b). Again, this pattern is consistent with previous findings (e.g., Doeschl et al., 2009) and reflects the wider range of gradients found the channels, associated with scour holes in particular.

The bar height for each cross-section was calculated as the difference between the 95% and 5% elevation confidence interval (e.g., Schuurman et al., 2013). The reach-averaged bar height was then determined by averaging all sections. The reach averaged bar height was revealed to vary between 1.08 m – 1.25 m (Figure 3.15c). However, it is worth noting that bar heights at individual cross-sections varied between 0.8 m and 2.5 m in all years.

The width-depth relationship curve (see section 3.3.2) was determined for each cross-section and then averaged to derive a characteristic curve for the entire reach (Figure 3.15d). The exponent (alpha value) for each DEM was determined (see the summary table on the Figure 3.15d). The alpha value was revealed to be fluctuating between 1.56 - 1.81. According to Redolfi et al. (2016b), alpha value less than 1 suggest a U shape channel which is typical for single thread rivers, and alpha value greater than 1 suggest a Y shape channel with higher complexity, which is typical for laterally unconfined braided rivers (see section 3.3.2 for details).

3.6.3 Hydrodynamic Signatures

At–a-station, hydraulic geometry relationships as described in Section 3.3.3 were determined using fixed-bed hydrodynamic simulations based on the topographic models from 2003 and 2005 as the lower boundary conditions. Figure 3.16 illustrates the resulting spatial distribution of water depths for three specific discharges 20, 40 and 70 m^3/s, clearly illustrating the rapid extension of wetted width with discharge (e.g., Mosley, 1983).

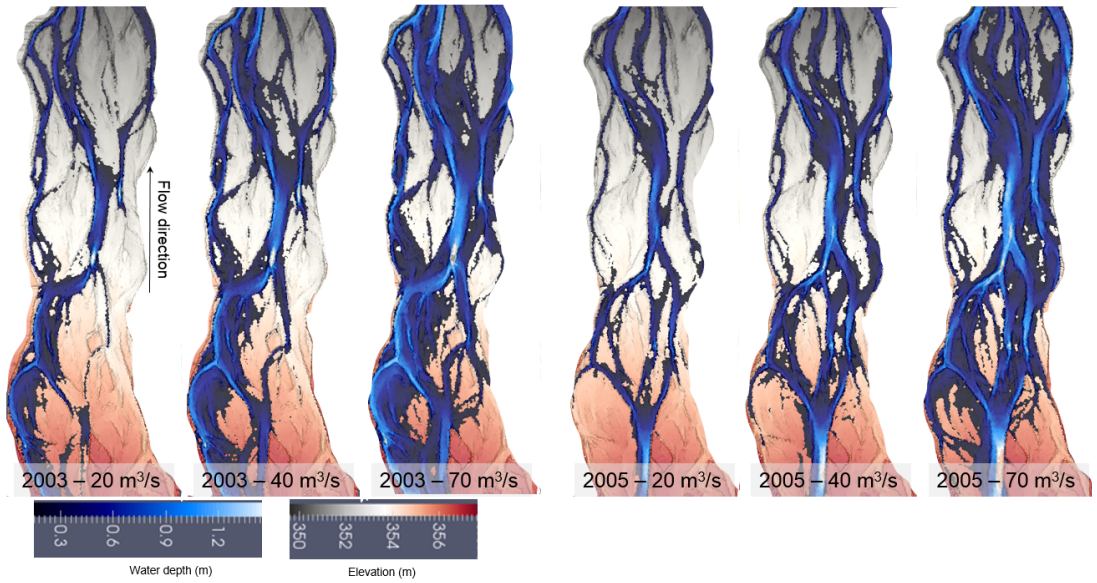

Figure 3.16 Spatial distribution of water depth at different discharge condition as determined by fixed-bed hydrodynamic simulation based on the topography 2003 and 2005. Flow is from top to bottom. The 20 m^3/s discharge is half of the annual flood; 40 m^3/s is annual flood and 70 m^3/s is two years flood of the braided Feshie (cf. Chapter 2).

The simulated hydrodynamic data were used to determine synthetic hydrodynamic metrics associated with the two topographic boundary conditions. Specifically, this included the reach averaged mean cross-sectional wetted width, depth and velocity determined for each discharge, and then aggregated in order to derive the hydraulic geometry relationship (e.g., Leopold and Maddock, 1953; Mosley, 1983). The power fitted width exponents were revealed to be 0.48 in 2003 and 0.47 in 2005, while the velocity exponent was 0.3 in 2003 and 0.31 in 2005 and the depth exponent 0.27 in both years (see Figure 3.17). The high width exponent reflects the Y-shape cross-section identified above, and in common with other braided rivers (Table 3.1),

suggests that increases in discharge are associated with rapid changes in width, as indeed was shown graphically in Figure 3.16 above.

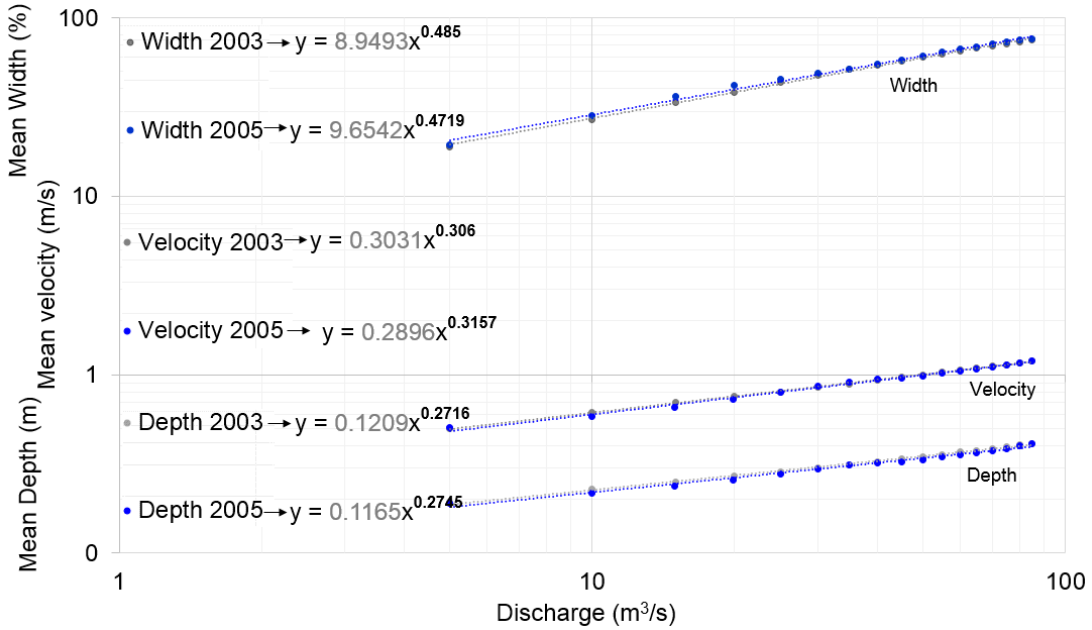

Figure 3.17 Power relationship of width (W), depth (D) and velocity (V) based on the hydrodynamic variables derived from fixed-bed hydrodynamic simulations.

3.6.4 Morphodynamic Signatures

a) Sediment transport, Active Braiding Index and Active Width

Estimates of bed shear stress obtained from the fixed-bed hydrodynamic simulations were used to calculate the spatial distribution of sediment transport rate using the standard Meyer-Peter and Müller (1948) formula. These calculations were based on a uniform sediment (D_{50} = 30 mm) and with a threshold dimensionless shield stress of 0.047 for initiation of motion (cf. Meyer-Peter and Müller, 1948). Based on the spatial distribution of sediment transport, three key morphodynamics indices such as the cross-sectional transport, the active braiding index and the active width, were subsequently determined.

Total transport capacity at each cross-section was calculated by summing the transport capacity of all cells across the section and then averaged across the reach to determine a representative areal relationship. The sediment transport rate for the two simulations (2003 and 2005) appear to be more or less similar across a wide

range of discharges, however the 2005 model appears to suggest higher rates of sediment transport at high flows (Figure 3.18a). The modelled pattern of shear stress was examined in order to interpret this difference and as shown in Figure 3.18d, the 2005 model is associated with a larger area of the bed with stresses between 2-3 times the threshold for entrainment (see the tail Figure 3.18d). Field-based observations of sediment transport in braided rivers (e.g., Williams et al., 2015; Rennie et al., 2017) have shown that the presence of high shear stress zones are important conduits for the efficient transfer sediment. The difference between the two years therefore effectively illustrates the differing flow-form-flow feedback to drives the adjustment of the bed.

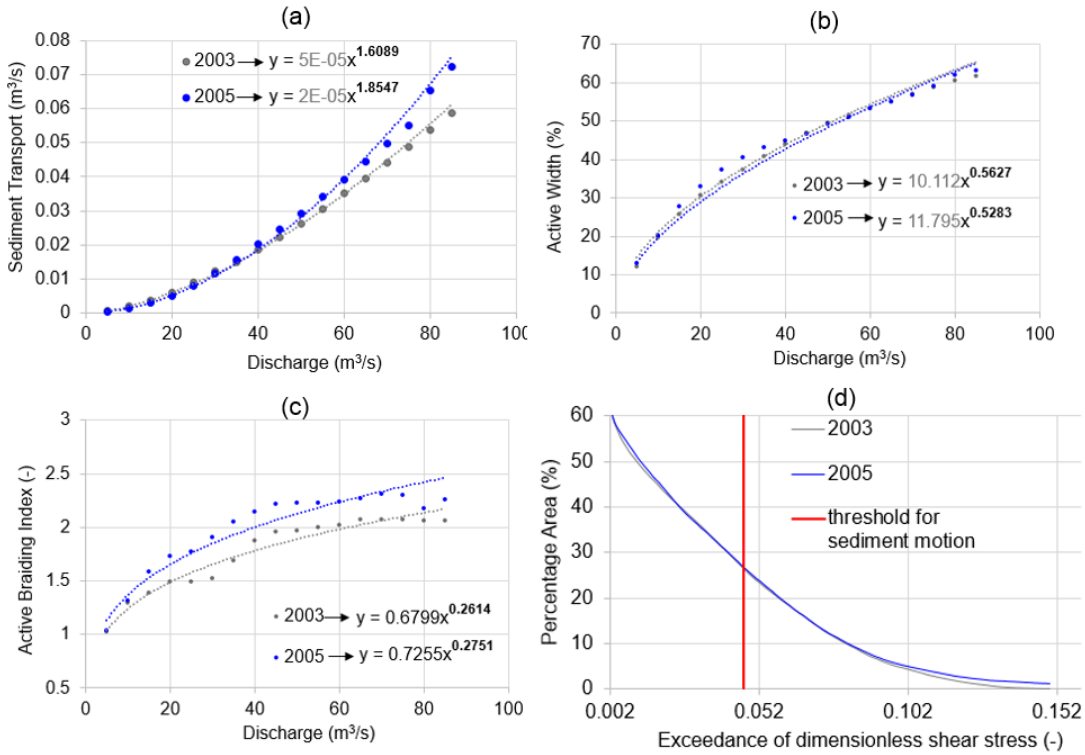

Figure 3.18 (a) Reach averaged cross-sectional sediment transport rate based on the uniform size of sediment (D_{50} = 30 mm). (b) Reach averaged active width. (c) Reach averaged active braiding index. (d) Percentage active area at different value of exceedance dimensionless shear stress.

Another most useful approach to understanding the sediment transport regime is to determine a discharge-bedload rating curve, characterised again by the exponent of a fitted power relationship. In this case, the bedload discharge exponent value was

found to vary between 1.6 and 1.85 in 2003 and 2005, respectively. This falls into broad range (1.5 - 2.8) previously suggested for physical models of braiding obtained from the laboratory (cf. Ashmore, 1988; Garcia Lugo et al., 2015).

The active width of each cross-section was determined by summing all the cells with a transport capacity greater than zero, which is then expressed as the percentage of the total cross-sectional width. Again, the reach average was obtained from the set of individual cross-section measurements. There was no significant difference in the active width between in 2003 and 2005 (Figure 3.18b) and the exponent of the width-based on the power relationship was found to be 0.56 and 0.52 in 2003 and 2005, respectively.

The Active Braiding Index (ABI) of each cross-section was determined by counting the number of channels transporting sediment higher than the mean transport of the section and then averaged across the reach. The reach averaged ABI was found to be higher in 2005 when compared to 2003 at all discharges (Figure 3.18c). The ABI varied from 1.0 at 5 m^3/s discharge to 2.3 at highest 85 m^3/s. The power fitted curve predicted discharge exponent as 0.26 in 2003 and 0.27 in 2005.

b) Erosion and Deposition Pattern

The spatial pattern of erosion and deposition were determined by differencing DEMs (i.e., new DEM - old DEM) vertically to obtain the observed geomorphic change. Data from all five years where computed (Figure 3.19). The distribution of changes (scour and fill) in 2004-2003 showed localized changes which reflect low formative discharge conditions, associated with the predominately dry (flood poor) period. By contrast, the pattern of channel adjustment in 2005–2004 and 2007-2006 demonstrate much higher intensity of change, indicating the presence of high stage conditions during floods at this time.

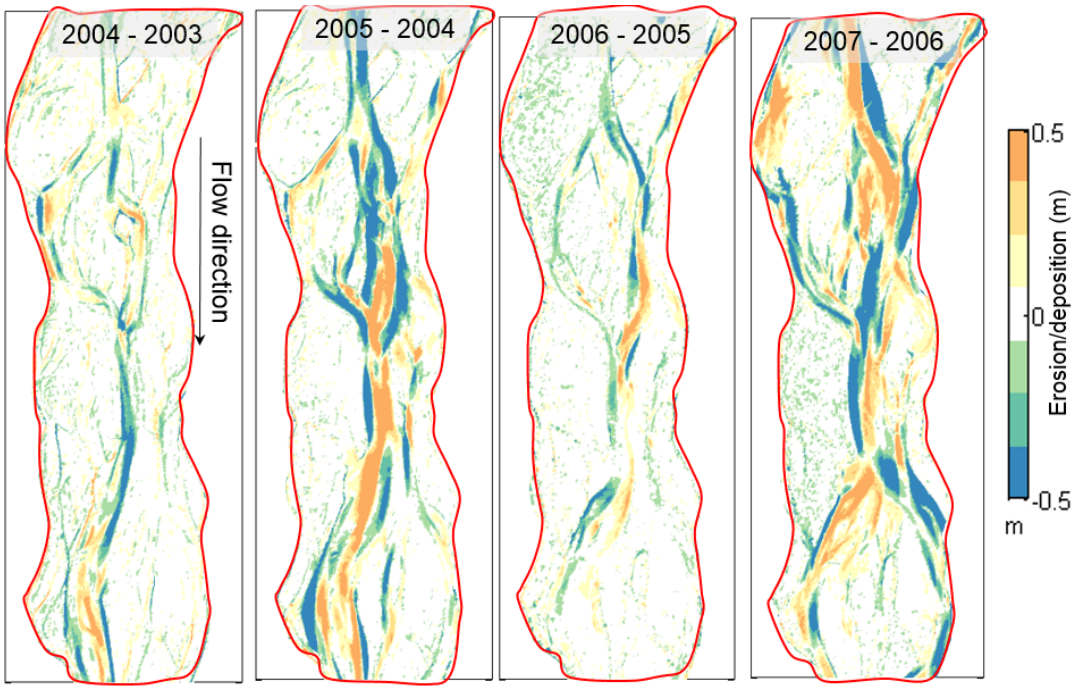

Figure 3.19 Spatial pattern of erosion and deposition at 0.05 m of threshold of detection. The outer bold red line shows the margin of active corridor considered in the analysis.

The total volume of erosion and deposition was determined based on the spatial pattern above in Figure 3.19 (see Figure 3.20a). Changes in all years revealed to be net erosional (Figure 3.20b).

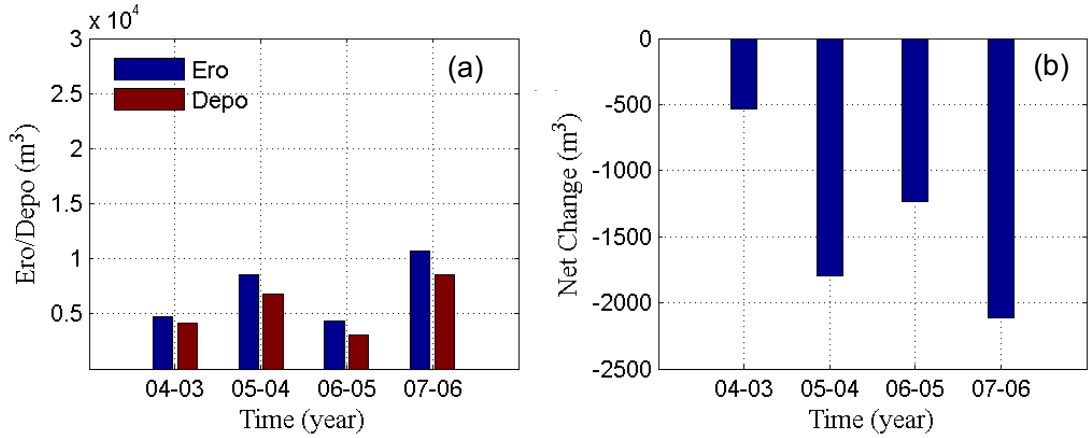

Figure 3.20 (a) Total volume of erosion and deposition. (b) Net change. This analysis of based on the threshold of detection 0.05 m.

While this recent record of activity indicates a weakly degradational trend for the Feshie, it is important to note that the empirical analysis of the DEMs of Difference represents an extremely short-term perspective and is not a reliable basis to infer any longer term 'trajectory'. Indeed, a continuing trend of degradation would be expected

to have led to the formation of extensively longitudinal terraces around the active fairway, which are notable by their absence. Given the lack of this morphological signal, and the inconclusive recent trend in the DEMs, it is reasonable to assume that over the short-term period relevant to the simulations explored in this thesis (extending over no more than 15 years at most), the system can be treated as being in a quasi-equilibrium state over timescale.

In order to get an insight into location of adjustment relative to the mean bed elevation, the novel approach proposed in section 3.3.4 was used. In this, the volumes of erosion and deposition occurring at a given surface elevation were computed (based on the prior DEM; see Figure 3.21).

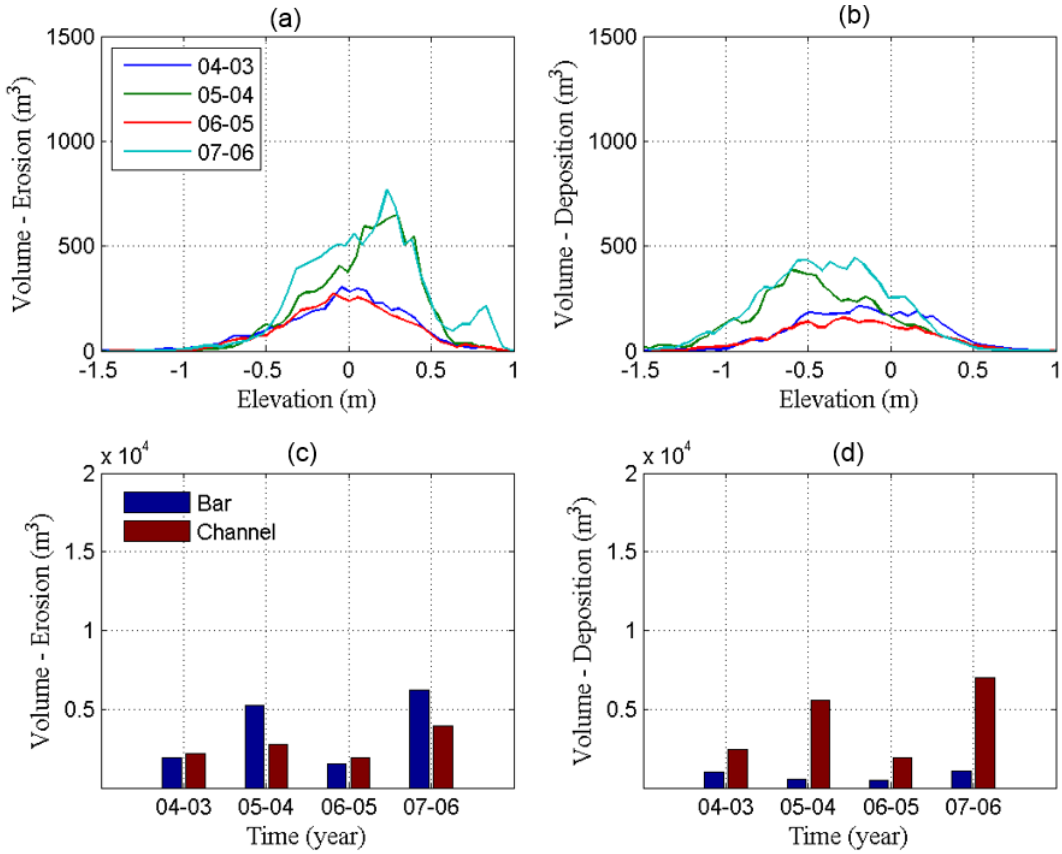

Figure 3.21 (a) Distribution of erosion volume with respect to the elevation of preceding years DEM at threshold of detection 0.05 m. (b) Distribution of deposition volume with respect to the elevation of preceding years DEM at threshold of detection 0.05 m. Figures (c) and (d) show the total volume of erosion and deposition on positive and negative elevation side which could be referred to bars and channel, respectively. Bar erosion dominates over channel erosion in 05-04 and 07-06, and vice versa in 04-03 and 06-05. Channel deposition dominates bar deposition in all the years.

The positive and negative elevations in these curves therefore represent the elevations above and below mean bed level respectively. In simple terms, the above and below mean elevation erosion and deposition volumes could be considered to be the morphological changes occurring on bars and in channels, respectively. For the morphologically quiet years (2003/04 and 2005/06) the distributions of erosion were revealed to be more or less symmetrical about mean bed level elevation, suggesting a mix of bar top erosional processes (bank erosion and surface scalping) and channel scour (Figure 3.21a; 04 - 03 and 06 – 05). The deposition curve peaked at negative elevations (Figure 3.21b; 04 - 03 and 06 – 05), implying the dominance of channel deposition over bar top deposition (see Figure 3.21d). However, for the morphologically more active periods (2004/05 and 2006/07) the distribution of erosion was skewed to positive elevations (Figure 3.21a; 05 - 04 and 07 – 06) suggesting the dominance of bar and bank erosion over channel scour (see Figure 3.21c). This morphodynamic behaviour could be expected when bars are partially submerged during moderate to high intensity flood events (Surian et al., 2009a; Bertoldi et al., 2010; Ashmore, 2013). The deposition curve is skewed to negative elevations (Figure 3.21a; 05 - 04 and 07 – 06), which again implies dominancy of channel fills over bar-top deposition (see Figure 3.21d).

c) Turnover Area

The total areal change (or turnover area) was calculated for two threshold levels of change detection (0.05 m and 0.1 m) in order to account for data uncertainties in the empirical DEMs. At the 0.05 m threshold level of detection, the total turnover was found to fluctuate between 40% to 60% (Figure 3.22a) and as expected declines for the more conservative 0.1 m threshold of change to between 20-40%. Both figures clearly indicate a highly labile fairway, in common with many gravel bed braided rivers, so that they evolve as a complex mosaic of surfaces of differing age.

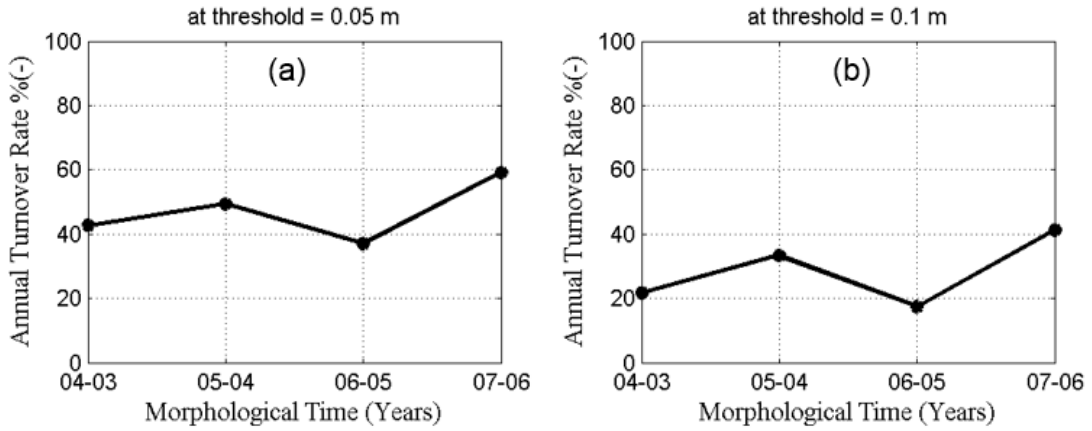

Figure 3.22 Total turnover rate expressed as percentage of total area of the braided reach; (a) at threshold of detection 0.05 m, and (b) at threshold of detection 0.1 m.

3.7 Discussion

3.7.1 Framework for Quantification of Braiding Characteristics

Building upon published literature, this chapter has presented a new quantitative framework to characterize the complex 2- and 3D morphology, processes and kinematics of braided rivers. Specifically, the proposed framework assembles planform, topography, hydraulics and morphodynamic metrics that capture a broad-based perspective on channel characteristics. While useful for intercomparison of river systems more generally, this framework has been devised to address the complex problem of evaluating the performance of numerical morphodynamic models. This is a challenging problem, as direct, deterministic comparisons are difficult to achieve, due to missing data on boundary conditions, for example knowledge of the prior state of the channel, or sediment influx. More profoundly, such simple approaches to model testing are likely to fail due to the sensitive dependence of channel adjustment on form-flow feedback which is likely to lead to a rapid divergence of model and prototype characteristics given even small uncertainties in the model parameterisation and input data, let alone incomplete and numerical representation of the key process mechanisms.

The strategy presented is designed to make optimal use of high resolution morphological data in the form of digital elevation models that are becoming increasingly available through developments of geomatics and remote sensing. These data provide continuous representations of river morphology and permit the redefinition of traditional descriptors of channel form, such as channel count indices, and shed new light through more robust statistical descriptors such as the frequency distributions of elevations and local gradients. In addition to direct characterisation of the morphology, the approach also uses these DEMs to provide fixed-bed boundary conditions to simulate the effect of channel form on the driving hydrodynamic properties of the channel. This enables an insight into how the forces driving channel evolution (e.g., shear stress) change with discharge, and indeed how discharge is partitioned in terms of width, depth and velocity, which is highly sensitive to channel form. Additionally, when multiple DEMs are available, these data can be used to directly quantify the pattern of channel adjustment, quantifying the typical structure of erosion and depositional areas, and through the use of novel metrics such as the relationship between erosion/deposition and prior channel bed elevation that provides a powerful insight into the mechanisms of change.

While the framework provides a multicriterion perspective on model evaluation, there is no formal measurement of model performance by which to judge or validate model simulations, such as the classic Nash-Sutcliffe efficiency used in rainfall-runoff or flood inundation modelling (see Nash and Sutcliffe (1970) and Beven (2011) for a discussion). Ultimately, the framework provides a range of criteria against which simulations can be benchmarked and expert judgement is required to interpret the wider set of results. Nonetheless, it is useful to consider what forms of behaviour would be considered characteristic of braiding and to use these as a basic template for what could be considered ‘behavioural’ simulations (see Beven, 2006).

While there is no clear recipe that uniquely distinguishes braiding, there are some commonly observed characteristics that should ideally be reflected in the model performance. They could be summarized as: a) braided rivers are characterised by multi-channel networks separated by bars that reconfigure through time; b) channels exhibit systematic spatial trends of narrowing and widening (Sapozhnikov et al., 1998); c) braided networks have average link-lengths (confluence and bifurcation distance) more or less equal to 4 to 5 times the width of bifurcating channel (Hundey and Ashmore, 2009); d) exhibit strong scaling relationship between bar axes, areas and perimeters (Kelly, 2006); e) are characterised by wider distributions of elevations above mean bed level than below mean bed level (Doeschl et al., 2009); f) have higher variance of local slope below mean bed level than above (Doeschl et al., 2009); g) are characterised by 'Y shape' relationships between width-depth and alpha coefficients above unity (Redolfi et al., 2016b); h) wetted width increases at higher rate than depth or velocity as discharge increases (Mosley, 1983); i) confluences scour and leads to deposition driving channel bifurcation (Ashmore, 1982, 1987, 1988); j) a ratio between active braiding and total braiding less than 1 (a typical value 0.4) (Bertoldi et al., 2009b; Egozi and Ashmore, 2009); k) dominance of bar erosion over channel erosion at formative (high stage) discharge conditions when bars are partially submerged.

This broad set of characteristics provides a working series of hypotheses that can used to critically examine model behaviour.

3.7.2 Characteristics of the Natural Prototype Feshie

The framework described above was applied to characterise the prototype river for this study, a 700 m braided reach of the River Feshie near Glenfeshie Lodge. Here, high resolution DEM data were created from annual low flow surveys between 2003-2007. This derived result provides a baseline against which future simulations using BASEMENT can be assessed, and some key insights emerge from this analysis.

The planform analysis revealed the (stage independent) total braiding index (TBI) to be around 5 (varying between 5.1 – 5.7), while the active braiding index (ABI) was between 1 and 2.3 (varying with discharge). Thus, the ratio of active and total braiding index is ~0.2 at low discharge (5 m^3/s) rising to 0.45 at high formative flows (85 m^3/s) (see Figure 3.23). Previous studies based on laboratory models have found steady state ratios of 0.4 at formative discharge conditions (e.g., Bertoldi et al., 2009b; Egozi and Ashmore, 2009), which are therefore consistent with the observations here. The one and two-year flood of the braided river Feshie is around 40 m^3/s and 70 m^3/s, respectively. Notably, as shown in Figure 3.23 below, the ABI/TBI ratio increases until discharge exceeds 40 m^3/s where it stabilizes, even though (as shown on Figure 3.17 and Figure 3.18) the wetted width and active width continue to increase with discharge up to 80 m^3/s. This suggests that up to this discharge, increases in local depths continue to drive increased sediment transport through increases in the area of above threshold shear stress. However, increases in discharge above this level, while increasing the overall active width and sediment transport maintain the same statistical distribution of shear stress, but extend the pattern over a wider spatial area(e.g., Mosley, 1983).

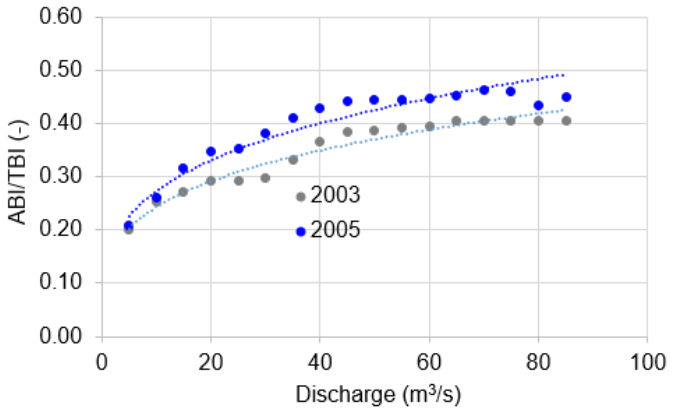

Figure 3.23 Ratio between Active Braiding Index (ABI) and Total Braiding Index (TBI) as determined through fixed-bed hydrodynamic simulation and sediment transport-based calculations. The ratio varies between 0.2 to 0.45.

The River Feshie also exhibits key topographic signatures associated with braided morphologies, as evidenced through the statistical distributions of elevation and

slope, and the geometric model of channel shape (the alpha-exponent). For example, the above mean bed level has a wider distribution of elevation above mean elevation as compared to below mean elevation areas which has been recognized as the universal topographic signature of braided rivers (e.g., Doeschl et al., 2009; Garcia Lugo et al., 2015). Similarly, it also exhibits greater variance of local gradients below mean bed level, reflecting the topographic complexity of anabranches that are characterized by confluence scours and shallow diffluences. The Feshie also has a Y-shape statistical average channel morphology, with alpha values well above unity. This is consistent with unconstrained channels formed in flume experiments and other natural laterally migratory systems (e.g.,Redolfi et al., 2016b).

The analysis also found the River Feshie to exhibit the widely recognized pattern of at-a-station hydraulic geometry (AHG) in which increases in discharge are accommodated principally by increases in width (see section 3.3.2). This pattern has been recognized as one of the signature characteristics of braiding (e.g., Mosley, 1983; Smith et al., 1996; Ashmore and Sauks, 2006; Bertoldi et al., 2009b; Welber et al., 2012; Ashmore, 2013) and provides a useful discriminator when comparing multichannel and single thread rivers (Leopold and Maddock, 1953).

Hydraulic modelling lead to the calculation of a bedload rating curve with an exponent of 1.6 in 2003 and 1.85 in 2005. These values falls in the range (1.5 - 2.8) that has been found in earlier laboratory models of braiding (cf. Ashmore, 1988; Garcia Lugo et al., 2015). Notably, the pattern of observed morphodynamics varied through time, with both 2005-2004 and 2007-2006 characterized by a dominance of bar erosion over channel erosion, whereas in 2004-2003 and 2006-2005 the volumes of channel erosion exceeded those from higher stage bars. This pattern reflects interannual variability in the forcing discharge regime, with higher flows in 2004/05 and 2006/07 leading to a greater depth of submergence and hence greater reworking of high stage morphologies.

3.8 Conclusions

This study posited a noble quantitative framework to quantify the complex 2- and 3D morphology, processes and kinematics of braided rivers to address the complex problem of evaluating the performance of numerical morphodynamic models. It is worth acknowledging here that the strategy presented here was designed to make optimal use of high resolution morphological data in the form of digital elevation models that are becoming increasingly available through developments of geomatics and remote sensing. Therefore, this framework should not be taken as an absolute. For example, it may be worth considering metrics informing statistics of individual channels, bars shape, rugosity and contribution of erosion and deposition by each braiding mechanisms.

This framework will be used to evaluate BASEMENT model in Chapter 4. Additionally, the same framework will be used to quantify braiding evolution under different boundary forcing in Chapter 5, 6. This framework can also be used in the other case studies where 3D topographic data are available. For example, the planform and topographic signatures could be directly derived from the available topography. If continuous series of topographic data sets are available, erosion and deposition dynamic pattern can be directly abstracted from the DEM differencing as demonstrated here. Additionally, stage-dependent hydraulic and morphodynamic calculation can be carried out based on fixed bed hydrodynamic simulations and sediment transport calculations as demonstrated here in the case of the braided Feshie. This study also identified set of universal properties of braided rivers informing planform, topographic, hydraulic, and morphodynamic which can be utilized to evaluate numerical models. Overall, the posited framework, and the technique presented here to characterize the braided Feshie embrace potential to support quantification of other braided rivers and to evaluate numerical models (both PBMs and RCMs).

Chapter 4: Modelling the Development and Maintenance of Braiding under Steady Flow

Chapter Summary

This chapter addresses Research Question 2: ***To what extent can the physically-based morphodynamic model BASEMENT reproduce the characteristic form and processes of a natural prototype braided river under steady flow conditions?***

This chapter examines the simulation of channel morphology emerging from plane bed conditions under steady flow. Simulations are parameterized to reflect the prototype braided reach of the River Feshie and are evaluated using the four-fold validation framework outlined in Chapter 3.

Following a brief review of the model, the design of the simulation is described, identifying how the boundary conditions and the model time-scale are calibrated for the natural prototype. A systematic sensitivity analysis of the model is then evaluated, focusing on two uncertain aspects of the parameterisation that have been identified in previous morphodynamic research as critically important; bank erosion and gravitationally-driven lateral sediment flux, while other parameters, including the eddy viscosity, grain size and bed roughness are fixed. Simulations reveal that behavioural models of braiding emerge from plane bed initial conditions after an equivalent 5 years of simulation time, with the character of the multithread network strongly dependent on the formulation and parameterisation of the bank erosion model.

4.1 Introduction

Morphodynamic models comprise, at best, only partial representations of the comprehensive set of physical processes driving the behaviour and evolution of natural rivers. Even then, their representation is based on approximate, discrete solutions to the governing partial differential equations and boundary conditions (Kleinhans, 2010; Wright and Crosato, 2011; Murray, 2013). Consequently, in order to establish the suitability of a numerical model as an effective research vehicle to support river management programs, critical evaluation and sensitivity analysis, interrogating model responses against external prototypes field or laboratory models is imperative (Mosselman 2005, 2012; Kleinhans, 2010; Murray, 2013). To date, however, there are relatively few literatures that account the performance and sensitivity of two-dimensional morphodynamic models, particularly when applied to simulate the long-term geomorphic evolution of braided rivers.

This partly reflects the lack of detailed data on the topography, hydrodynamics and morphodynamics that are backbone for model parameterisation and assessment. Recent developments in remote sensing and geomatics, in particular the advent of airborne and terrestrial lidar, softcopy and structure-from-motion photogrammetry now, however, offer exciting new pathways to enable dense reconstructions of fluvial topography in fully 3-dimensions (e.g., Bertoldi et al., 2011b; Brasington et al., 2012; Westoby et al., 2012; Javernick et al., 2014; Williams et al., 2014). The ability to acquire high resolution topography repeatedly through time, also provides unprecedented opportunities to quantify not only the full morphological structure of braided systems, but also the possibility to reconstruct transport rates and sediment budgets indirectly through DEM differencing (Ashmore and Church, 1998; Brasington et al., 2000; Redolfi, 2014; Vericat et al., 2017). Other advances in remote sensing, such as optical depth mapping (e.g., Williams et al., 2014) and acoustic Doppler

current profiling (Williams et al., 2015; Rennie et al., 2017) may also provide key information on water depth, velocity, shear stress and sediment transport.

Such advances in data acquisition provide new scope to define robust metrics of form and behaviour that could be used to describe the character of natural systems and afford a means to assess model predictions. However, the apparently simple task of comparing observations and predictions is fraught with difficulty within the context of braiding processes due to the sensitive dependence of the evolutionary trajectory of braiding on the initial topography, hydraulic and sedimentological system conditions. In this context, small uncertainties in channel morphology and flow distribution can give rise to variations in the spatial allocation of flow and boundary stress that become magnified rapidly by morphodynamic feedback. Consequently, simulations based on even well-conditioned models are likely to diverge from their natural prototypes over short time and space scales rendering direct, deterministic comparison futile (Anderson and Bates, 2001; Lane and Richards, 2001). Ultimately, therefore, the evaluation of model performance and sensitivity must instead rely on statistical measures of channel form and process, many of which are likely to be ill-defined. This raises the potential to generate apparently good measures of model performance from quite different deterministic outcomes, and apparently similar predictions may be generated by radically different processes (Beven, 1993). It is therefore urgently necessary to carry a comprehensive assessment of morphodynamic numerical models, and to inform to what extent they can mimic natural processes, before establishing them as an effective means to investigate form and behaviour of natural processes at different environmental forcing.

Historically, the seminal work of Murray and Paola (1994, 1997) demonstrated the capability of the simple cellular models to reproducing some of the principal features of natural braided rivers, in particular the emergence of branching networks in a state of dynamic equilibrium (see Chapter 1). Their numerical experiments, initialled from

plane bed conditions produced key features associated with braiding such as, scour holes in areas of flow convergence, sedimentation in areas of flow divergence, and autogenic pulsing of sediment transport.

These encouraging results stimulated a significant body of research focusing on the use of simple rule-based algorithms to simulate mobile bed channels, evaluating model performance in a variety of dimensions. For example, Sapozhnikov et al. (1998) demonstrated that the MP model was capable of reproducing the broad planform patterning found in braided rivers, exhibiting characteristic spatial trends in anabranch narrowing and widening. However, Doeschl-Wilson and Ashmore (2005), who compared the MP model with comprehensive data from laboratory models of braided rivers, found a strong divergence between the planform and 3D characteristics of the model with their hardware prototype. Subsequently, Doeschl et al. (2009), compared MP simulations against both the natural and flume prototypes, focusing on the reproducibility of key planform and topographic signatures, such as link length and the statistical distribution of bed elevations and local gradients. They found that the MP model was able to closely approximate the shape and range of distribution of link length and elevation but failed to reproduce both the pattern and distribution of local gradients, with anomalous singularities dominating the topography. Such discrepancies were attributed to the highly abstracted routing algorithm used in the MP model that neglects the effects of lateral redistribution of momentum (Coulthard et al., 2002; Thomas and Nicholas, 2002). Thomas and Nicholas (2002) refined this routing scheme to incorporate the effects of water slope (a diffusion wave approximation) and subsequently, Thomas et al. (2007) demonstrated the success of this new scheme in reproducing planform properties, such as bar area and perimeter. Furthermore, their model was also shown to capture some of the dynamical responses characteristic of braiding, including changes in bar height and size following changes to sediment supply as observed in the flume experiments of

Germanoski and Schumm (1993). They observed that increased sediment supply resulted in widespread aggradation increasing braiding intensity and active width. By contrast, decreased sediment supply resulted incision, lower braiding intensity and disconnected, narrow single thread channels.

In a similar view, the cellular model CAESAR (Coultard et al. (2000, 2005; Van De Wiel et al. (2007) has been applied to simulate braided river systems. Ziliani et al. (2013) examined the performance of CAESER model when applied to model the long-term morphodynamics of the braided Tagliamento River, Italy. At a broad scale, they observed consistency in the long-term sediment efflux predicted by CAESAR that with observations from their prototype, although they highlighted significant differences between the modelled and observed braiding intensity.

Given the simplicity of cellular-based numerical models, their apparent capacity to generate many of the key features of natural braided networks is encouraging. However, it is also clear that the streamlined flow and sediment routing schemes used in these reduced complexity models, leads to unrealistic overconcentration of fluxes, which in turn results in the tendency to exaggerate flow-form feedback responses and the creation of over-deepened scour holes and unrealistically high bar heads (see Doeschl et al., 2009). The cause of this 'pathological' behaviour lies in the generalization of the low routing schemes, which ignore the inertial forces in the momentum equation, assume steady state conditions, neglect gravitational forces on the routing of sediment and limit flow dispersion to downstream directions (Coulthard et al., 2002; Thomas and Nicholas, 2002; Doeschl-Wilson and Ashmore, 2005; Brasington and Richards, 2007; Doeschl et al., 2009). These are well-understood simplifications and the continuing interest in RCM models of braiding does not reflect ignorance of these effects, but rather: a) an appreciation of the computational complexity of solving the coupled morphodynamic problem and desire to minimize the algorithmic burden of solution schemes to model long-term channel evolution; and b)

the dearth of available data to validate RCM simulations, so that their simplicity remains an attractive compromise to pursue in the absence of readily available alternatives. Perhaps more controversially, it could be argued that the MP model, which was developed essentially as an exercise in understanding the basic controls on braiding, has been extended beyond its validity as it was never intended to be used to predict detailed, localized, time-bound predictions (Murray and Paola, 1994, 1997).

In the last decade, in particular, there has therefore been a growing interest in the development of more complex representations of the hydrodynamic and sedimentological processes that drive morphodynamics. These approaches typically involve the solution of the vertically-integrated, shallow water wave (SWW) equations with various degrees of complexity incorporated to resolve the representation of higher dimensional (secondary) flows (see Chapter 1). A small, but growing literature has emerged in which these 'physically-based' models have been applied to understand the evolution of braided rivers (e.g., Enggrob and Tjerry, 1999; Jang and Shimizu, 2005; Nicholas, 2013; Schuurman et al., 2013; Sun et al., 2015; Singh et al., 2017).

Enggrob and Tjerry (1999) were the first to attempt to simulate the development of a braided river using with the MIKE21 code from DHI. They described simulations initiated from a flatbed topography with fixed outer banks and provided some qualitative insights into the evolution of hypothetical sand bed braided river. Jang and Shimizu (2005) extended this work using their own 2D modelling framework that employed a moving boundary coordinate system to enable simulation of evolving flow-form conditions incorporating bank erosion. This study was one of the first to evaluate model performance against the behaviour of an experimental channel allowing floodplain erosion and demonstrated the capability to reproduce channel planform, key network characteristics such as the number of nodes and broad-scale fluctuations in sediment transport that were consistent with their flume prototype. Takebayashi

and Okabe (2009) also described the simulations started from a flatbed topography and examined the evolution of braiding under steady and unsteady flow conditions and were among the first to examine of interaction of flow and vegetation. However, their model assessments are based on qualitative, visual analysis with results representing the short to medium-term evolution, without quantitative assessment of the morphodynamic (specifically, the change through time) characteristics of the model. More recently, Nicholas (2013) outlined a new approach to solving morphodynamics based on his HSTAR model. In this, he described simulations in a narrow channel allowing floodplain erosion, examining the long-term evolution of a hypothetical large sand bed braided rivers, in the presence and absence of vegetation. Again, however, assessment of the model was limited to a largely qualitative examination of planform characteristics.

Using the popular Delft3D framework, Schuurman et al. (2013) have also examined simulations of the long-term evolution of sand bed braided rivers, once again initiated from plane bed conditions. In this study, they compared their synthetic braided river against the generalized properties of braided rivers, in particular, bar shape (cf. Kelly, 2006), braiding index (cf. Crosato and Mosselman, 2009; Kleinhans and Van Den Berg, 2011) and the ratio of active and total braiding index (cf. Bertoldi et al., 2009b; Egozi and Ashmore, 2009). Intriguingly, their experiments suggested that braided morphologies emerged across a wide range of parameterisations, but that the development of an equilibrium channel form, characterised by steady-state braiding driven by the break-up, merging and migration of bars could not be achieved. They attribute this to the absence of a complete representation of bank erosion processes that is necessary to predict lateral migration of channels and autogenic sediment supply. More recently again, Sun et al. (2015) evaluated simulations incorporating non-uniform sediment, and compared simulations to the flume scale braided river of Egozi and Ashmore (2009). Their results suggested that the sediment size distribution

plays an important role in conditioning the width-depth ratio of channels, and that coarsening of near-bank sediment is important in reducing lateral channel mobility. Singh et al. (2017) have also examined the effect of sediment grading on morphodynamics, but this time parameterized to represent the large gravel-bed Waimakariri River, NZ. They evaluated model performance in respect of qualitative planform geometry, bed topography by comparison with predicted and observed hypsometric curves and bar height and morphodynamic responses through changes in braiding index. Notably, they showed a continuous increase of bar height through the simulation which extended well beyond the reach averaged of their natural prototype, indicating persistent unregulated channel incision. Again, they concluded that this tendency to scour the bed of anabranches reflects parameterisation of gravitational sediment transfer processes, in particular the direction of bed transport and bank erosion as also reported by Schuurman et al. (2013).

In summary, significant progress has been made over the past two decades using both reduced complexity and physically-based models to explore the emergence and maintenance of braiding. These models have shown that braiding emerges as the default channel pattern associated with laterally unconstrained settings and high rates of sediment influx. Nonetheless, the extent to which numerical models can mimic effectively both the form and behaviour of natural prototype systems, remains unclear, not least due to the lack of high quality data for model evaluation.

However, before addressing this question directly, an important first step is to examine whether synthetic braided rivers generated by numerical models can **develop** and **maintain** a dynamic equilibrium state driven by a steady discharge from an initial plane bed (e.g.,Bertoldi et al., 2009b in flume experiment). Here, we take a dynamic equilibrium state to refer to condition in which the morphology and associated system effluxes (water and sediment) vary about a stationary average (Schumm, 1988; Bertoldi et al., 2009b). While it is difficult to test whether such conditions do (could

ever) exist in a natural river, given the variability in the driving boundary conditions and lag time in the morphological response, the maintenance of dynamic equilibrium conditions has been demonstrated in laboratory models and has been taken as evidence that unsteady discharge is not a pre-requisite for braiding (e.g., Bertoldi et al., 2009b). This chapter, therefore outlines the first step in the evaluation of BASEMENT as a vehicle to simulate braiding processes, focusing on this critical question. The research presented here applies the model validation approach outlined in Chapter 3. A specific focus of the chapter is an evaluation of key processes/parameters of the model, specifically the gravitational lateral sediment flux and the bank erosion module, which have (as discussed above) resulted in a failure of previous research (e.g., Schuurman et al., 2013) to achieve the maintenance of braiding under steady-state conditions.

4.2 Aim and Objectives

The overall aim of this research is to undertake a comprehensive performance evaluation and sensitivity analysis of physically-based numerical model BASEMENT, focusing specifically on modelling the long-term morphology of gravel-bed braided rivers. In order to achieve this aim, this chapter provides an important first step in the evaluation of the model, focusing on four key objectives:

a) to examine the development and maintenance of synthetic braided river networks evolving under a steady discharge condition and assess whether the model can produce simulations that attain a dynamic equilibrium conditions, measured in terms of 2D/3D geometry, hydrodynamic behaviour and morphological evolution;
b) undertake a sensitivity analysis of the key process representations and parameters that drive model behaviour;

c) compare the resulting simulations to a natural prototype, the River Feshie, using the validation scheme described in Chapter 3;
d) to identify the power of the model performance metrics to distinguish differences between the model generated system and the natural prototype.

The subsequent sections of this chapter are therefore structured as follows: the first section provides detail on the methodology of this research focusing on the model set-up and design of the sensitivity analysis; the second section outlines the key results; this is followed by an analysis and interpretation of the results; and these are then brought into context in a critical discussion before the principal conclusions are outlined.

4.3 Methods

4.3.1 The Numerical Model: BASEMENT

This study focuses on the freely available two-dimensional model, BASEMENT, developed by the Laboratory of Hydraulics, Hydrology and Glaciology at ETH Zürich (Vetsch et al., 2017a). A detailed description of the model, comprising the process representation, numerical solution and parameterisation have been summarized previously in Chapter 2. The following section therefore outlines the approach to model construction, describing the strategies used for: spatial discretisation of the model domain; parameterisation of the hydrodynamic and morphodynamic boundary conditions; and the time-scaling of simulations to afford comparison with the natural prototype.

4.3.2 Model Design and Schematisation

Given the availability of high quality topographic models for the braided reach of the Feshie, it would be possible to use these data to provide the lower boundary condition for the model and examine how the model behaved relative to the deterministic time series of DEMs available for the site (2003-2007). Such direct comparison is however

complicated by uncertainties in the surveyed topography, but perhaps more significantly due to unknown variations in sediment supply, discharge, grain sorting and the effects of vegetation that could dominate the response of the natural system. It is likely therefore that the predictions of even a well-conditioned model would diverge rapidly from the natural system it aimed to represent. The rate of divergence is furthermore likely to be particularly rapid in this context given the close coupling between form and flow in a braided system. Indeed, studies have shown that attempts to predict the considerably more simple problem of estimating flood extent using the topography of natural or flume braided rivers have demonstrated high levels of predictive performance (e.g., Doeschl-Wilson and Ashmore, 2005; Thomas et al., 2007; Williams et al., 2013; Javernick et al., 2014). However, when the topography is allowed to evolve from the initial 'real' topography, the accuracy of predicted patterns of erosion and deposition are well below those achieved for the hydrodynamics (see Williams et al., 2016a).

Here, instead of using an existing (and uncertain) topographic representation to initialize simulations, therefore, this study seeks to examine the development of river morphology as it evolves from an initial plane bed (e.g.,Enggrob and Tjerry, 1999; Doeschl et al., 2009; Schuurman et al., 2013; Singh et al., 2017). These simulations are scaled to reflect the statistical properties in terms of the discharge, width, slope and grain-size of the prototype system. This affords the possibility to compare the model responses to the statistical structure of the reference system using the metrics described in Chapter 3, while also examining how braiding emerges from this initial condition.

4.3.3 Spatial Discretisation

A 700 m braided reach of the River Feshie, Scotland (cf. Wheaton et al., 2010; Wheaton et al., 2013) was used as the prototype to provide data to parameterize and validate the simulations. This 700 m reach has a reach averaged width and

longitudinal slope of 175 m and 0.92% respectively (see Chapter 2 for details). In order to represent this system, a rectangular domain of 1550 m x 175 m was discretized using a fixed triangular mesh with a minimum threshold cell area of 2 m^2. The resolution was set to provide a compromise between the fine spatial detail needed to represent near bank processes (see the earlier discussion p. 66-69; and also Williams et al., 2013; Williams et al., 2016a) and the computational benefits of using a fixed computational grid as opposed to a dynamically adjusting discretisation (see also section 4.3.5 about bank erosion model and grid size). BASEMENT does not incorporate an automated grid generation tool, so the freely available software called Quantum GIS (QGIS) was used (see., Vetsch et al., 2017b). Delaunay triangulation was used to generate a triangular tessellation of the surface (see., Vetsch et al., 2017b page 39). Based on the 2 m^2 of minimum threshold cell area, the total spatial domain (1550 m x 175 m) was discretized with 208,337 number of triangular cells (approximately 130 cells for 175 m width of the domain). Williams et al., (2016a, 2016b) also uses 2 m grid size in order to capture complex braided topography, hydraulics and sediment transport processes. In this spatial schematisation, the 1550 m reach comprised a central 700 m used for comparison with the prototype plus additional 425 m sections upstream and downstream to mitigate the effects of the open boundaries on the area of the model used for assessment. All future descriptions of the system and later comparisons with the prototype refer only to data extracted from the central 700 m section of the domain.

The initial plane bed topography was set to the reach-averaged gradient, 0.92%, of the prototype. The two outer longitudinal edges of the domain were defined as closed boundaries while the upstream and downstream transversal edges of the domain were set as open boundaries with the parameterisation of water and sediment influxes described below.

4.3.4 Hydrodynamic Parameterisation and Boundary Conditions

a) Boundary Conditions

The upstream boundary was set to provide an influx of a steady discharge of 70 m^3/s, representing the two-year return period flood of the study reach (see Chapter 2). This discharge thus corresponds, approximately, to bankfull discharge and therefore represents the critical discharge that alluvial channels are widely considered to be adjusted (e.g., Harvey, 1969). At this discharge, more than 50% of the spatial domain is submerged (see Chapter 3; Section 3.6.3). This discharge therefore corresponds to a relatively high formative discharge at which bars are partially submerged according to the criteria of Surian et al. (2009a). The discharge on wetted cells at the boundary was distributed in proportion to local conveyance which is determined based on the wetted area and the local slope. At the downstream boundary, normal water elevation was calculated based on the local bed slope and instantaneous discharge.

b) Flow Resistance

The formation and maintenance of braiding in previous numerical simulation of braided rivers (e.g., Schuurman et al., 2013) has shown marginal sensitivity to the parameterization of flow resistance. In this study therefore, a constant roughness over space and time was used in all simulations. Grain size from the River Feshie, specifically surface bed samples of Hodge et al. (2009b), suggest that D_{50} in the study reach varies between 30 mm to 63 mm. Arcement and Schneider (1989) calibrated Manning's roughness coefficients for different populations of bed material size, and found values of between 0.028 - 0.03 $s/m^{1/3}$ for bed with median sediment between 2 mm - 64 mm; between 0.03 - 0.05 $s/m^{1/3}$ for bed with median sediment 64 mm - 256 mm, and between 0.05 - 0.07 $s/m^{1/3}$ for bed with median sediment greater than 256 mm. Using these criteria as a reference, the Manning's roughness was set to 0.033 $s/m^{1/3}$ and fixed spatially. This equates to an equivalent to 30 $m^{1/3}/s$ in terms of the Manning's Stickler's roughness formulation.

c) Eddy Viscosity

The eddy viscosity is the key parameter representing the influence of turbulence in the numerical solutions, and reflects the transfer of momentum associated with turbulent flows and adds to the internal fluid friction on a larger scale (Lesser et al., 2004; Vetsch et al., 2017a). Sensitivity analysis of the horizontal eddy viscosity parameterization in Delft3D was explored for simulations of similar braided river topography on the Rees River, NZ (Williams et al., 2013). This research revealed smoother variation of water depth and velocity as the horizontal eddy viscosity coefficient was increased and a loss of high shear zones. Based on comparisons with detailed distributed velocity and shear stress mapping using mobile aDcp surveys, they found an optimum range of parameter values of 0.01 to 0.1 m^2/s for a grid size of 2 m. They subsequently developed full morphodynamic simulation using a value of 0.1 m^2/s eddy viscosity. Published guidance for BASEMENT suggests a recommended parameter values to lie in the range 0.1 and 1 m^2/s, although there are no published references using this model for braided rivers. Nonetheless, given the role of eddy viscosity affecting the spatial distribution and magnitude of velocity and shear stress (see, Williams et al., 2013) it is likely that this parameterization will have a significant influence on predicted morphological evolution. Following Williams et al. (2013; 2016a) it seems reasonable to predict that higher parameter values would be associated with simplified diffusive topography with weakly defined in-stream morphology and reduced erosion and deposition volumes. Based on this experience, the eddy viscosity here was set to 0.1 m^2/s for all simulations which is a lower range of the value suggested in the BASEMENT manual.

d) Numerical Solution and Stability

There are a range of different numerical solvers available in the model (see Chapter 2; Section 2.2.1), including an exact Riemann solver (Godunov, 1983) and approximate Riemann solvers (HLL and HLLC). The exact Riemann solver, which is

robust to solve strong wave interactions and flow with sharp gradients and shear waves, is most commonly used in published simulations using BASEMENT (e.g., Faeh, 2007; Radice et al., 2012; Tettamanti, 2013; Bertoldi et al., 2014) and was therefore adopted for this study.

The hydrodynamic time step in the model was determined dynamically according to the Courant-Friedrich-Levy condition (see Chapter 2). In BASEMENT, there is no option to use different threshold water depths for hydrodynamic and sediment transport calculations which means similar threshold water depth should be imposed. Commonly, existing numerical models uses a threshold of 0.05 m to separate the wet and dry domains of models for hydrodynamic calculations and 0.1 m for sediment transport calculations (cf. Schuurman et al., 2013; Sun et al., 2015; Singh et al., 2017). As a compromise here, the average value of 0.075 m was used to segment the domain into wet and dry regions.

4.3.5 Morphodynamics Parameterisation and Boundary Conditions

a) Boundary Conditions

The sediment influx from upstream boundary was set to 100% of the sediment transport capacity of the boundary section, determined on the basis of the local slope which was kept fixed throughout (see Chapter 2). The material size was set to equal the uniform grain size used inside the domain (D_{50} = 30 mm). The sediment efflux through the downstream boundary was set as the 80% of the transport capacity of the boundary cells, in order to avoid unduly high rates of erosion at the boundary, and therefore prevent instabilities propagating upstream (see Chapter 2). The BASEMENT manual suggests that schematization of the downstream boundary does not affect morphology upstream beyond few cells at the boundary. Nevertheless, in the result analysis, central 700 m domain was only considered to assure that the main area of interest is unaffected by slight deposition at the downstream boundary cells.

b) Grain Size

Gravel-bed braided rivers have graded sediment with different physical characteristics. While for single sized sediments, the size dependency of transport is well established, the behaviour of graded mixtures is more complex. Finer particles, for example may be less mobile if they are surrounded by coarser particles and protruded less to flow (Mao and Surian, 2010), a phenomenon termed 'hiding' (Mosselman, 2005). By contrast, coarser particles may be more mobile if they protrude significantly into the flow (Mao and Surian, 2010) and have greater 'exposure' (Mosselman, 2005). In the limit, these effects have been observed to lead to an unselective transport regime, reflecting the combined effects of hiding and protrusion (Andrews, 1983). However, both field and laboratory studies continue to indicate a tendency towards size-selective transport (Ashworth and Ferguson, 1989; Wilcock and Southard, 1988; Wilcock and Crowe, 2003) and the emergent characteristics of the bed ultimately reflect these sorting processes and provide one explanation for the development of a surface armour (Dietrich et al., 1989; Parker, 1990). Indeed, the presence of upward (and downward) coarsening of sediment in graded mixtures is commonly observed in river gravel beds. This can be explained by size selective transport of the finer fraction being winnowed away low shear stresses, washing surface and resulting in a coarser surface texture or armour layer (Hunziker and Jaeggi, 2002). The armour layer may be static or mobile depending upon the flow condition and sub-surface sediment mixtures (Hunziker and Jaeggi, 2002). For example, if the bed shear stress is slightly higher than critical and there is no continuing supply of fines from upstream, a static armour layer may develop nonetheless. If, by contrast, sediment finer than original sediment is supplied from upstream and is passed downstream without bed level change, a semi-armour layer may be formed. If the bed shear stress is higher than the critical shear stress threshold required for entrainment of sub-surface sediment but less than the condition for full mobility of the sediment mixture, grain sorting process may still continue to form a

mobile armour layer. If the bed shear stress is sufficiently high so that entrainment of all particles in the mixture is possible, morphology evolves under full mobility condition (see, Hunziker and Jaeggi, 2002).

During intense bed load transport events, the development of dunes may, by contrast facilitate downward coarsening within graded beds (Blom, 2003) caused by avalanching of coarse grains from leeward face dunes. In some cases, the winnowing of fine sediment from the trough of dunes has also been found to lead to the formation of downward coarsening (Blom, 2003).

At the cross-sectional scale, flow structures at confluences and associated downstream flow bifurcations around mid-channel bars may facilitate deposition of coarse sediment on the bar head, swiping fines towards the lee side of central bars (Ferguson and Ashworth, 1992; Powell, 1998). In compound bars and vegetated streams however, complex sediment sorting patterns may emerge through cyclical trajectories of erosion and deposition, such that bed sedimentology can only be understood through an understanding of the morphodynamic trajectory (Rice and Church, 2010). At reach scales, longitudinal fining (decrease in size of sediment downstream) of sediment also remains a key control on the composition and structure of bed material, reflecting the combined effects of particle abrasion and selective transport (Powell, 1998).

Representation of these sediment sorting processes within a numerical modelling framework is clearly complex, and implies the need to: (i) represent multiple grain size fractions; (ii) incorporate a sediment transport formulation suitable to model multi-grain sediment; (iii) a mass conservation equation for each fraction; (iv) modelling of hiding and exposure corrections for the critical shear stress of each fraction; (v) definition of an active transport layer participating in sedimentation and erosion; and (vi) representation of the vertical sedimentary composition (Blom, 2003; Mosselman,

2005; Sloff and Ottevanger, 2008). There are very few numerical modelling studies have effectively sought to parameterize the processes at the reach scale, in particular in the case of complex braided morphologies. Among the few published studies, Sun et al. (2015) found that deposition of coarse sediment near channel banks may facilitate the formation of comparatively deeper channels. In the similar theme, Singh et al. (2017) found an increase of braiding intensity and deepening of channels (or increase of bar height) for simulations with Delft3D using graded sediment as compared to uniform sediments.

Given the wide scope of this study (encapsulating the effects of steady, unsteady flow regimes and the role of vegetation) a uniform sediment mix was adopted for the sake of simplicity and to provide the necessary reduction in the computational overhead required for decadal scale simulations (see also Bertoldi et al., 2014). Nevertheless, the choice of a single grain size represents a significant simplification that is confounded by the wide variation in representative indices of grain size (e.g. D_{50}) spatially across even relatively small areas.

Some preliminary calculations were therefore conducted to guide the selection of a uniform sediment size for the future simulations using a steady state model of flow through the Feshie. Figure 4.1 shows the variation of active area for uniform sediments based on a representative 70 m^3/s discharge which was adopted as a steady discharge to represent typical bankfull flows in this study. Here, the bed shear stress distribution derived from the fixed bed hydrodynamic simulation at 70 m^3/s discharge using prototype Feshie topography (see Figure 3.16 in chapter 3) was used to calculate the dimensionless shear stress distribution at different size uniform sediment. The active area at different sediment size was determined by fixing the critical dimensionless shield stress for entrainment at 0.047 following Meyer-Peter and Müller (1948). The Figure 4.1 shows a mild decrease in active area with an increase in sediment size until 30 mm which is then followed by a dramatic decrease,

depicting a transition behaviour around 30 mm- 35 mm sediment size (changing from widespread mobility to concentrated mobility). The uniform sediment size was therefore selected from the transition region at 30 mm which is also the D_{50} of the river Feshie (see section 2.2.3) and was fixed in all the simulations. Nevertheless, it is to be aware that an increase and decrease in the selected sediment size may determine different braiding properties. As such, the bar mode predictor of Crosato and Mosselman (2009), suggests inverse relationship between bar mode and uniform sediment size (D_{50}) implying low bar mode or braiding index for higher sediemnt size and vice versa.

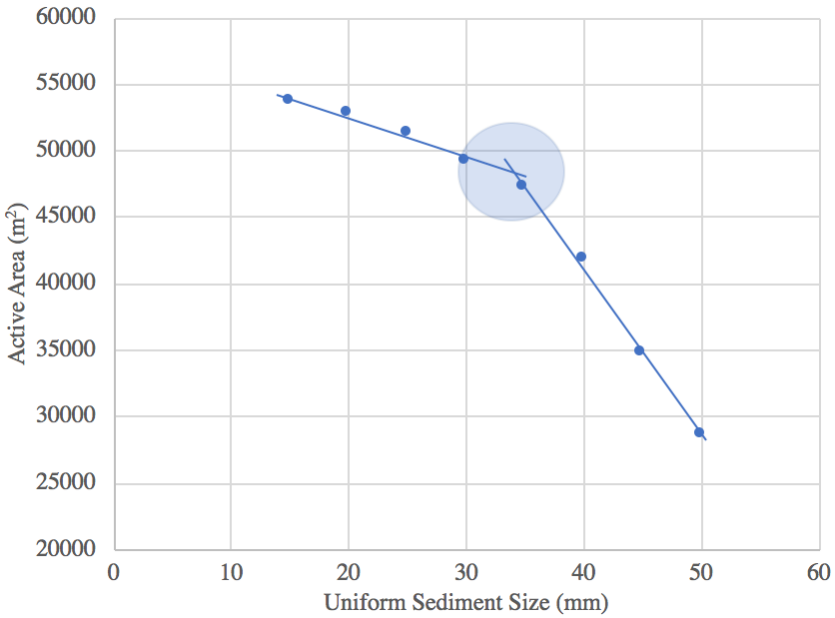

Figure 4.1 Variation of active area with respect to different uniform sediment size. These calculations were based on the dimensionless shear stress distribution derived from the bed shear stress obtained from the fixed bed hydrodynamic simulation at 70 m^3/s discharge using prototype Feshie topography. The active area represents total area having dimensionless shear above 0.047 (0.047 is the assumed critical shear stress for sediment entrainment).

c) Sediment Transport

There are several sediment transport formulas that have been used in determining bed load transport and modelling gravel bed rivers. The classic Meyer-Peter and Müller (MPM) sediment transport formula (see Chapter 2 for detail), which considers

transport relations based on the median particle size (D_{50}), was used to determine the sediment transport (e.g., Bertoldi et al., 2014). The bed thickness was set to 2.5 m and a uniform grain size (D_{50} = 30 mm) was used. The thickness of 2.5 m represents, approximately, the maximum bar height (including highest outer bank) of the prototype to ensure unhindered scour.

The critical dimensionless shear stress for sediment motion used in the MPM formulation was fixed to 0.047 for all simulations, as is a standard practice for gravel transport (e.g., Bertoldi et al., 2014). This critical dimensionless Shield stress is based on experimental results for gravel transport over a horizontal bed. In real rivers however, the bed frequently slopes in both the longitudinal and transverse directions (see Chapter 2). To account for the additional influence of gravity on the bed material flux, BASEMENT, by default, employs a correction term to adjust the critical shear stress for inclined beds based on Van Rijn (1993). In addition to the slope correction factors, sloping bed has a direct 'pulling' effect which affects the direction of the sediment transport vector (Ikeda, 1982; Talmon et al., 1995; Siviglia et al., 2013; Sun et al., 2015; Nelson et al., 2016). Developer guidance (Vetsch et al., 2017a) recommends setting the relevant β factor to reflect this lateral transport adjustment in the range of 1.4 - 2.7 (see Chapter 2; Section 2.2.2 d). Early studies (e.g., Schuurman et al., 2013; Sun et al., 2015) have suggested that the representation of this lateral transport process is critical to the formation and maintenance of bars and channels. For this reason, the experimental design described below sought to evaluate this lateral transport factor through a factor perturbation sensitivity analysis (see Table 4.1 below).

d) Bank Erosion

In BASEMENT, bank erosion is represented through the definition of a critical response angle for three repose angles namely, fully wetted (γ_{wet}), partially saturated

or dry (γ_{dry}) and deposited material ($\gamma_{deposited}$) (see section 2.2.2 for detail). This bank erosion model has been found to be effective for modelling the dam or embankment breach (e.g., Volz et al., 2012; Worni et al., 2012). Nevertheless, there are no published studies that have yet analysed the sensitivity of this process representation to the resulting formation and maintenance of bars and channel in braided rivers. Schuurman et al. (2013) who used Delft3D to model sand-bed braided morphology, using a simple bank erosion model that erodes dry cell when incision occurs in a neighbouring wet cell, revealed the critical importance of parameterizing bank erosion processes to determine continuous braiding evolution. Their numerical model indeed could not maintain dynamic equilibrium over the long-term, due to limited lateral channel mobility which they suggest reflects oversimplification of the bank erosion formulation. As a consequence, the simulations demonstrated a tendency for anabranches to incise, resulting in increased bar heights and lower rates of lateral reworking. Singh et al. (2017), who used the same numerical framework (Delft3D) but for gravel-bed braided simulations also encountered similar problems resulting from reduced lateral mobility and excessive channel incision. In this study therefore, the bank erosion model was also considered as part of the sensitivity analysis.

As suggested by Vetsch et al. (2017a), repose angles should be set so that they are highest for dry material, followed by partially (fully) wet cells and then for deposited (failed) material. The model grid-size, however, ultimately imposes a constraint on the effective repose angles that can be defined, relative to the maximum bank heights and the need for adjacent cells to reach a threshold water depth. For example (rough estimate), if the grid size is 2 m and the critical repose angle is 20°, the bank erosion model will only be active when the water depth roughly reaches to around 0.72 m (cf. Sun et al., 2015). Similarly, under grid size 5 m and 10 m and critical repose angle of 20°, the bank erosion model will be active when water depth reaches to 1.83 m and 3.6 m, respectively. In the case of gravel bed system like the Feshie, with low bar

height and bank edges in the range 1-2 m, this schematisation is therefore likely to be more sensitive than for a single thread system with typically higher bar or bank heights. Comprehensive investigations were therefore carried out by using a range of repose angle criteria for dry, wet and deposited material (see Table 4.1) in the sensitivity analysis described below.

4.3.6 Real Time Scaling of Simulation Hydrograph

a) Solving Flow and Sediment Transport

Solving and then updating the loosely-coupled hydrodynamic and mass transfer models poses a major computational overhead given the necessary short space and time scales required to ensure model stability. As such, in many previous studies, a 'Morphological Acceleration Factor (MORFAC) has been used, in which the fluid and bed material transport models are updated on different timescales (see Nicholas, 2013; Schuurman et al., 2013; Williams et al., 2016a; Singh et al., 2017). This is often justified by the short time steps needed to solve the high frequency fluid flows, whereas the bed material transport adjusts more slowly and the feedback to the driving hydrodynamics can be solved over much longer timescales. While this approach is computationally efficient, particularly in the case of steady flow simulations (Figure 4.2a), management of the morphological acceleration factor during unsteady flow (Figure 4.2b, c, and d) simulations is problematic due to need to adapt the scaling ratio as discharge increases (Yossef et al., 2008).

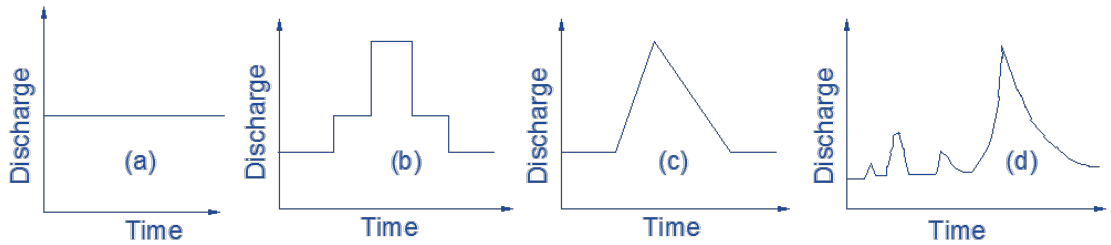

Figure 4.2 Way of approximation of natural hydrographs. Among is: a) the formative or constant throughout the time; b) is step increase and decrease of discharge; c) triangular type; d) real type of hydrograph.

For example, as discharge increases in any of the driving scenarios shown above (Figure 4.2b, c and d), the rate of morphological change is likely to increase too, but in a rather less predictable and locally non-linear manner. This implies a need to modify continuously any computational acceleration used to couple the hydro- and morphodynamics or alternatively risk generating problematic numerical instabilities. Additionally, the initialization or 'spin-up' time (i.e. time to stabilize the hydrodynamics before enabling morphodynamic updating) will vary for different driving discharges in order to avoid inducing hydrodynamic shocks with unrealistic consequences for morphodynamic predictions. Thus, management of these computational effects is particularly challenging for any simulation involving unsteady flow (see Yossef et al., 2008 for a review). While this represents the worst-case scenario, it is important to recognize that even under a steady flow boundary condition, rates of water flow and sediment transport will vary significantly across the modelled domain, so that any MORFAC used must nonetheless be set conservatively to reflect the most active areas of the domain.

The development in parallel processing technologies as used in BASEMENT provides some way to relax the need to solve the water and sedment fluxes separately. Instead, the computational power provided by parallelization of the code, offers the opportunity to solve both the hydrodynamics and morphodynamics efficiently at same scale, thus allowing simplifying solutions associated with unsteady boundary fluxes (Vetsch et al., 2017a). In this study, sediment transport calculation was therefore carried out at the same scale as hydrodynamic times without the use of MORFAC scaling.

b) Scaling Model Simulation and Real Time Scales

Even though hydrodynamic and morphodynamic calcuations are executed at same timescale, it remains impractical to extend simulations over periods when the the discharge is below the threshold for entrainment, which likely makes up the vast majority of time in natural river systems. It is, therefore, a common practice to 'remove'

morphologically inactive discharges from the forcing hydrodynamic timeseries of boundary flows in order to reduce the simulation time (e.g., Bertoldi et al., 2014). This implies the need to 'unwrap' or 'rescale' the resulting modelled timeseries to account for the pattern of adjustment that occurs over a comparable 'real' time in the natural system. For steady flows, a comparatively simple time equivalence can be estimated. For example, if a threshold flow of 30 m^3/s is defined as morphologically active, the total duration of flows above this threshold can be summed over a given time interval, e.g., one year. As a simple illustration, imagine therefore that flows on the Feshie exceeded 30 m^3/s for 9 hours in an average year, simulations based on a steady discharge of 30 m^3/s could then be scaled to represent a number of years, in which 9 hours = 1 year; 18 hours = 2 years etc.

Of course, this approach assumes that there is no additional increase in the magnitude of geomorphological work done with increasing discharge, which is a gross simplification. An alternative approach therefore, is to consider a normalization of time not based simply of the summation of time above a threshold, but using a more representative measure of system activity, such as total energy expenditure, which is defined as:

$$\omega = \int \mathbf{LQS}\, \mathbf{dt} \qquad \text{Eq. 4. 1}$$

Where, ω is the total energy expenditure (J/s), L is the reach length, Q is the discharge, and S is the gradient (where in this case, L and S can be taken as constant and discounted). To account for the non-linear relationship between geomorphic work and discharge, this approach can further be scaled using the discharge exponent of braided rivers with respect to sediment transport (cf. Ashmore, 1988; Garcia Lugo et al., 2015) (usually in the range 1.5-2.8) to reflect the non-linear dependence of bed material flux on discharge.

For this study, in order to determine the energy expenditure in the two-year return period flood, the annual maximum flood for each year was extracted from an 18-year record for the Feshie, between 1993-2010 (Figure 4.3). For each hydrograph, discharges below 20 m^3/s were assumed morphologically inactive, in the sense that their morphological effects will be very local and into the channel thalweg only.

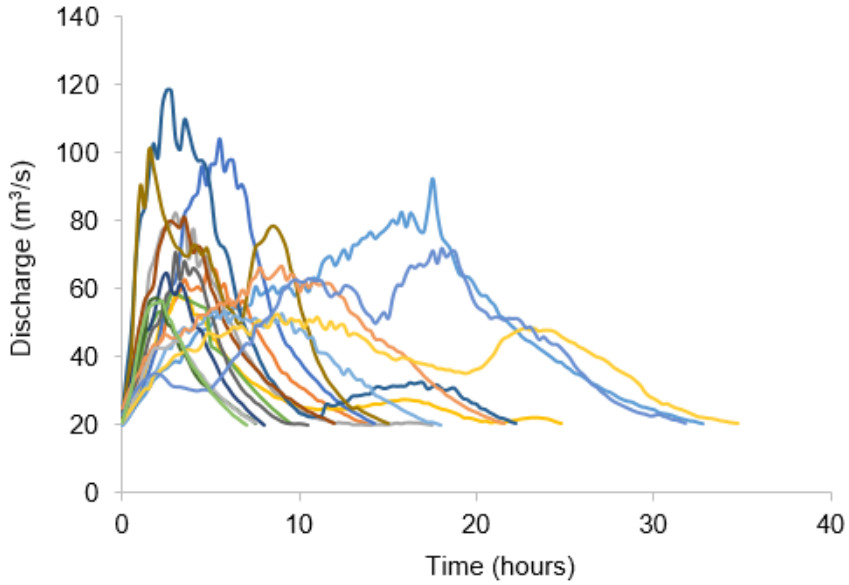

Figure 4.3 The 18 years (1993 - 2010) maximum recorded flood hydrographs representative of the braided river Feshie (after downscaling the Feshie Bridge data; see Chapter 2). All the discharges below 20 m^3/s were assumed to be morphologically inactive so were discarded in the analysis (see Ferguson and Ashworth (1992), where they have reported the presence of local channel erosion and deposition below 20 m^3/s discharge which is half of the one year flood).

The discharge exponent of braided rivers with respect to sediment transport typically varies between 1.5 - 2.8 (c. f., Ashmore, 1988; Garcia Lugo et al., 2015). Taking this range as a reference, the total normalised energy expenditure associated with each of the 18 hydrographs was obtained for exponent values n = 1.5-2.8. The Mean Annual Maximum Energy (MAME, here can be thought as ω) was then calculated by taking the average of the 18 years data. The n vs MAME curve (Figure 4.4) was then plotted to approximate the simulation time representing one-year morphology of the natural prototype. As an example, the red line in the Figure 4.4 represents one-year of morphologically active simulation time for different values of n, taking 70 m^3/s of

constant discharge as the formative discharge. The discharge-sediment transport rating relationship for the braided reach of Feshie calculated from a fixed-bed hydrodynamic model, was found to have an exponent in the range 1.6 and 1.85 (~ 1.9), so 1.9 can be considered as a typical reference value (see Chapter – 3 for details). For the exponent value 1.9, the mean annual maximum normalised energy in the curve (Figure 4.4) corresponds to 90,382,800 $(m^3)^{1.9}$. To dissipate this amount of energy using 70 m^3/s of constant discharge requires 7.836 hours of numerical simulation time, and this provides a scaling to equate changes in the model to those associated with the typical annual flood representing one-year in the natural prototype.

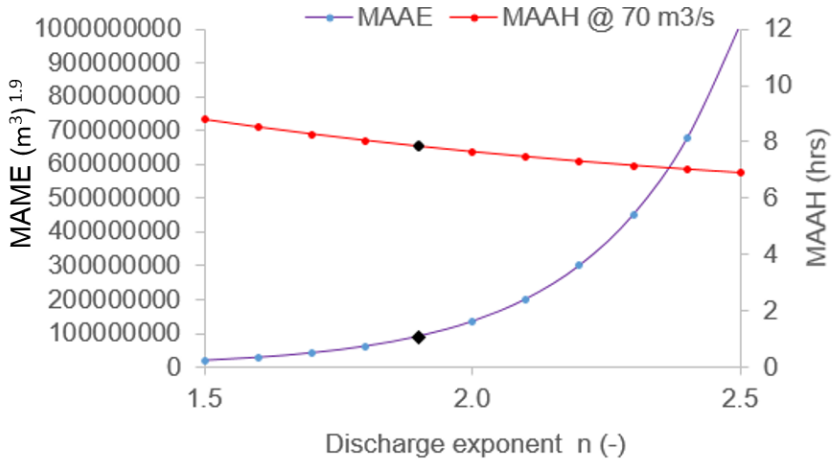

Figure 4.4 Scaling of numerical simulation time to reality. The Mean Annual Maximum Normalised Energy (MAME) is the mean of annual maximum dissipating energy base on the Q^n function after removing all discharges below 20 m^3/s. The Mean Annual Active Hours (MAAH) is approximate simulation time that crudely represents one year's morphology of natural prototype Feshie while simulating at 70 m^3/s of constant discharge. The MAME at 1.9 exponent (n) value is around 90,382,800 $(m^3/s)^{1.9}$. To dissipate the mean annual maximum energy (MAME), which represents one year's morphologically active dissipating energy of the natural prototype, a simulation utilizing constant form of 70 m^3/s discharge should be run for 7.836 hours. The same principle will be used to normalize different form of simulation hydrograph (see Chapter 5 below).

Based on this schematisation, the output of simulation was saved at time intervals comprising 3526.221 seconds (approximately one-hour interval). Thus, output file obtained after 8 x 3526.221 = 28209.8 seconds (eight outputs) crudely represents

one-year morphology change of the natural prototype Feshie. All simulations executed for a total of 96 hours, therefore equating broadly to 12 years of morphologically active flows in the natural prototype.

In any given year, it is possible that more (or less) than the morphologically active hours schematised above exhibits, however the above approach was chosen for the sake of simplicity although direct annual comparisons between the synthetic and natural systems needs to be treated cautiously.

4.3.7 Sensitivity Analysis

Sensitivity analysis and calibration are two independent steps in the assessment and application of a numerical model. Sensitivity analysis seeks to evaluate the response of model behaviour to defined changes in parameter values, perturbed either individual or as a combined set (Saltelli et al., 2000; Lane and Richards, 2001). The goal of this analysis is not to evaluate the model performance with respect to an observed (or analytical) benchmark, but to interpret rather the degree of sensitivity of outputs to the scale parameter variation. Sensitive analysis should therefore provide insight into the role of different parameters in the model, which in turn can be used to infer whether the model exhibits behaviour that is consistent or otherwise with the prototype (i.e., unduly sensitive or otherwise). Additionally, the analysis may help guide the user as to whether specific parameters with no or little impact on model behaviour could be neglected (implying revision of the canonical set of equations) or indeed should be the focus of later calibration (Lane and Richards, 2001).

Calibration, by contrast, is a process of parameter adjustment that seeks deliberately to optimize model performance. This process typically involves comparisons with some reference condition (i.e., field/lab observations or an analytical solution), which can be quantified through a 'goodness of fit' measure, typically referred to as an 'objective function' (e.g., Williams et al., 2013; Ziliani et al., 2013).

Spatially explicit morphodynamic models comprise an almost infinite combination parameter combinations, that reflect understood physical relationships, e.g., the hydrodynamic (roughness, eddy viscosity) and sediment-related parameters (bed composition and grain size, transport coefficients, angle of repose), but also choices associated with the numerical solution, including the spatial discretization and numerical solver. A comprehensive, spatially-distributed, sensitivity analysis of all parameter combinations represents an intractable problem, and a simplified experimental design is required that seeks to balance computational overhead with maximum explanation. Previous experience with morphodynamic simulations have suggested that the emergent predicted channel patterns are particularly sensitive to two aspects of model parameterisation: a) the lateral slope transport factor (that controls the gravitational effect on transport); and b) parameterization of the bank erosion model (i.e., angle of repose, Schuurman et al., 2013; Singh et al., 2017). As such, an experimental design was established to quantify the predictive response of the model to these key model aspects, while the remaining parameters were fixed. This clearly represents a highly simplified interrogation of the model parameterisation but was chosen to reflect a compromise between evaluating the critical aspects of the model and the run-times involved the long simulations required to reach an equilibrium state (requiring 10-14 days each on a High-Performance Computing cluster). This approach to parameterisation reduces the sensitivity analysis to consider just four parameters: the lateral slope factor (varying between 1.5 - 3); and three repose angles, corresponding to dry, wet and deposited material.

In order to represent variability in this set of free parameters, a set of 10 simulations were conducted, representing a range of parameterisations as shown in Table 4.1. Given the constraints on simulation time, this research design reflects a tailored series of experiments, drawing on previous experimentation with morphodynamic models in

the published literature, rather than an exhaustive factor perturbation methodology (e.g., Williams et al., 2016a).

The first simulation (R_1) represents a control scenario without bank erosion nor gravitational effects on lateral bed transport. The next four runs (R_2, R_3, R_4 and R_5), represent simulations in which the failure angle for bank erosion was kept vertically constant (same for dry, wet and failed material) but varied through 5-30 degrees. For these four runs, the lateral transport factor was kept constant in order to isolate the model sensitivity to the repose angle alone. Run R_6 and R_7 again keep the lateral transport factor constant but use a more sophisticated (geotechnical) approach to modelling bank erosion, using different combinations of repose angles for dry, wet and deposited material. The last three simulations (R_8, R_9 and R_{10}) use a consistent combination of repose angles for dry, wet, and deposited material, but now examine the effect of the lateral transport factor.

Table 4.1 Summary of simulated runs and **the numerical parameters.**

Run	*Strickler's Roughness* ($m^{1/3}/s$)	*Hoz. Eddy Viscosity* (m^2/s)	D_{50} *(mm)*	*Discharge* (m^3/s)	*Repose Angle*[a] *(degree)*	*Lateral Transport Factor*
R_1	30	0.1	30	70	-	-
R_2	30	0.1	30	70	5, 5, 5	3.0
R_3	30	0.1	30	70	12, 12, 12	3.0
R_4	30	0.1	30	70	18, 18, 18	3.0
R_5	30	0.1	30	70	30, 30, 30	3.0
R_6	30	0.1	30	70	18, 12, 10	3.0
R_7	30	0.1	30	70	18, 12, 5	3.0
R_8	30	0.1	30	70	25, 18, 5	3.0
R_9	30	0.1	30	70	25, 18, 5	2.0
R_{10}	30	0.1	30	70	25, 18, 5	1.5

[a] the order of repose angle from first to third are the erosion threshold for dry, fully wetted and deposited material, respectively.

4.3.8 Characteristic of the Prototype for Model Evaluation

In order to interrogate the synthetically generated channels, the planform, topographic, hydraulic and morphodynamics characteristics of the prototype reach of the Feshie were derived, following the methods and results described in Chapter 3. For this purpose, the DEM constructed from the 2005 annual survey was used. This terrain model was used to extract the planform and bed topography metrics and used again to provide the fixed-bed topographic boundary condition for hydraulic modelling of the hydrodynamic response of the reach and to estimate the effective sediment transport rate, active braiding index and active width from shear stress estimates obtained from the fix bed hydrodynamic simulation (this data were directly adopted from Chapter 3). The observed pattern of erosion and deposition in the prototype was derived from DEM differencing, using all available topographic maps (2003, 2004, 2005, 2007; this data was adopted from Chapter 3).

4.4 Results

4.4.1 Predicted Planform Geometry

a) Spatial Pattern of Detrended Elevation and Water Depth

The model-generated topography for each simulation was detrended with respect to the initial flatbed topography and the predicted water depth overlaid to provide an insight into the predicted evolution of the channel planform.

Figure 4.5 shows the predicted planform extracted for the final two 'years' (i.e., simulation hours = 88, 96 as each year corresponds to ~8 hours of simulation time) for runs (R_2-R_{10}). The control simulation, R_1, gave rise to exaggerated local scour pools and narrow channels during the initial stages of the simulation (0-4 years) and could not be continued over the full 12-year period due to persistent numerical instabilities. As an indication of how the remaining simulations progressed from the initial plane bed, to the final characteristic morphologies shown in after 11 and 12

years in Figure 4.5, the detailed evolution on a 'yearly' timescale (i.e., for each 8 hour interval) is shown for simulation R_9 in Figure 4.6.

The effect of varying the critical angle of repose globally (i.e., vertically constant) is illustrated by comparing simulations R_2-R_5. Simulation R_2, with the lowest repose angle (5^o) appears to result in highly smooth, low complexity, low relief topography comprising of similar size bars that have limited mobility. As the repose angle is increased (i.e., R_3 to R_5) the topographic complexity increases, as does bar size, though the dynamism of the planform is reduced, and the pattern locked into a static network of bars and channels. R_5, with the repose angle of 30^o evolved into a single-thread meandering channel with static lateral bars. The effect of varying the repose angle vertically can be seen in simulations R_6–R_8, in which the repose angles are higher for dry (18-25^o) than wet (18-12^o) and deposited material (5-10^o). All these simulations appear to exhibit increased mobility of bars compared to the vertically uniform repose angle simulations described above, though appear broadly similar between each other, albeit from a qualitative visual inspection. Introducing variability of the lateral slope factor, varying from 3.0, 2.0 and 1.5 in R_8, R_9 and R_{10}, respectively appears to demonstrate greater sensitivity, with lower parameter values leading to an increasingly diverse set of compound bars that are comparatively mobile and continue to be reworked throughout the entire simulated time.

At a broad scale, the evolutionary trajectory of the runs R_7, R_8, R_9 and R_{10}, starting from flatbed to the fully developed stage follows a similar pattern, as follow (see the typical result from the run R_9 in the Figure 4.6). In the initial year (0-1 year), a high number of small channels and migratory bars are generated arising from local imbalances between discharge and sediment transport. Between 1-2 years, the small bars begin to coalesce and merge, with the wave of transition sweeping longitudinally downstream. In the following 2-5 years, bar development accelerates, associated with classic morphodynamic processes, such as bar edge cutting, local avulsions and the

formation of chute cut-offs and the migration of submerged unit bars. These processes continue to cause further coalescence of the migratory bars resulting a fully developed braided river as observed in flume experiments (e.g., Ashmore, 1991; Bertoldi et al., 2009b), comprising of complex compound bars, migratory unit bars, confluences and bifurcations. The simulations appear visually to approach a dynamic equilibrium state (e.g., Bertoldi et al., 2009b) between 5-12 years, with bar edge trimming and providing an autogenic supply of sediment as suggested by field-based observations (e.g., Wheaton et al., 2013; Williams et al., 2015).

Subsequently, this local supply generates migratory unit bars (Ashmore, 1987, 1988) that in turn force localized avulsion through the development of chute cut-offs or avulsions occurs erosionally due to bar dissection (Jerolmack and Mohrig, 2007). This spatio-temporal pattern of bar breakdown and reworking is clearly evidence in R_7, R_8, R_9 and R_{10}. Qualitatively, there is little to separate these simulations in visual terms, though detail differences to emerge when considering the wider set of topographic, hydrodynamic and morphodynamic metrics described below.

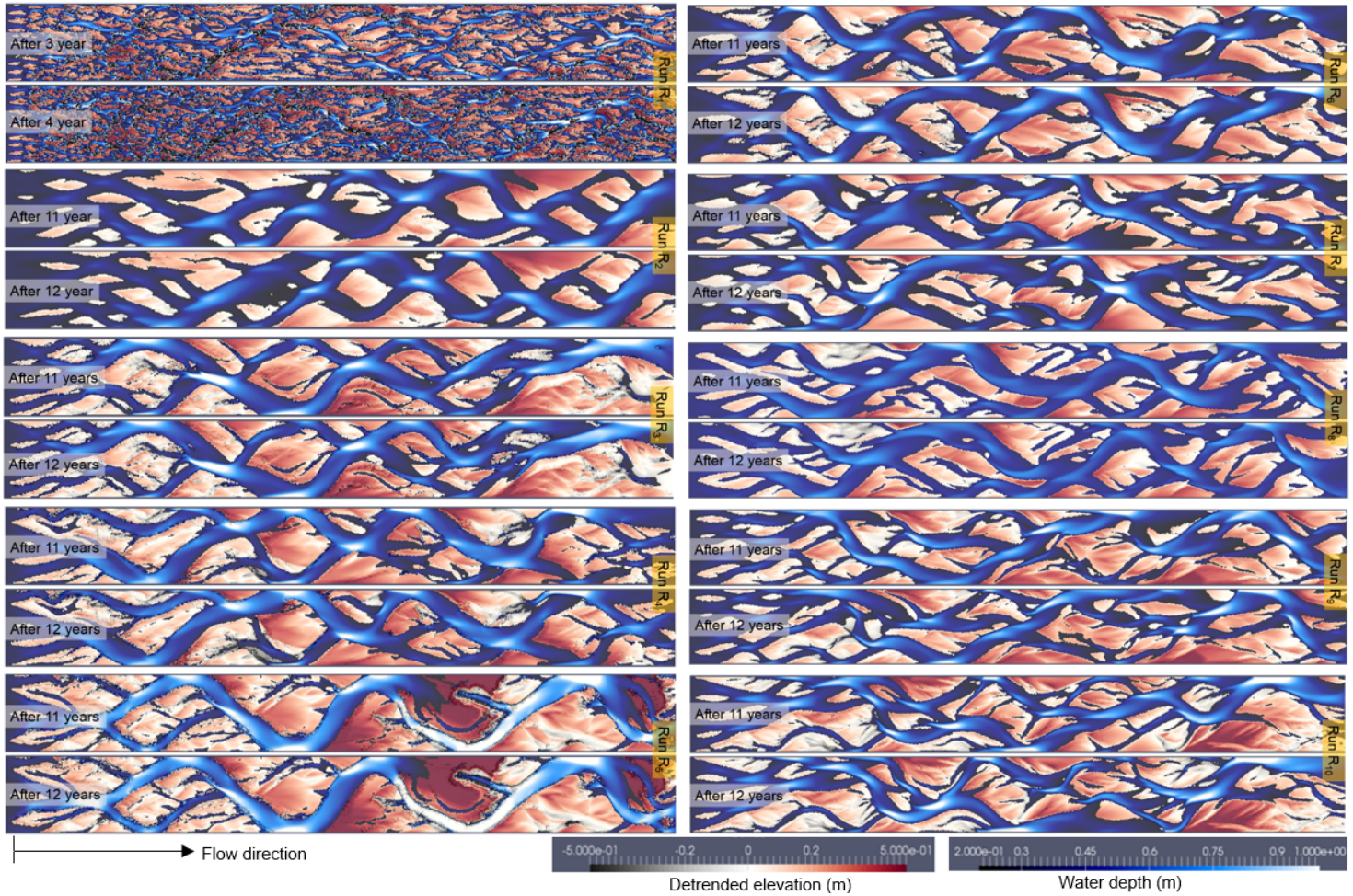

Figure 4.5 Planform evolution displaying detrended elevation and water depth during last two years. For the Run R_1 model crashed after four years. For visibility reasons, only water depth between 0.2 m – 1 m have been plotted. All domain (1550 m x 175 m) have been shown here but for quantitative analysis in the latter sections only the middle 700 m x 175 m has been considered.

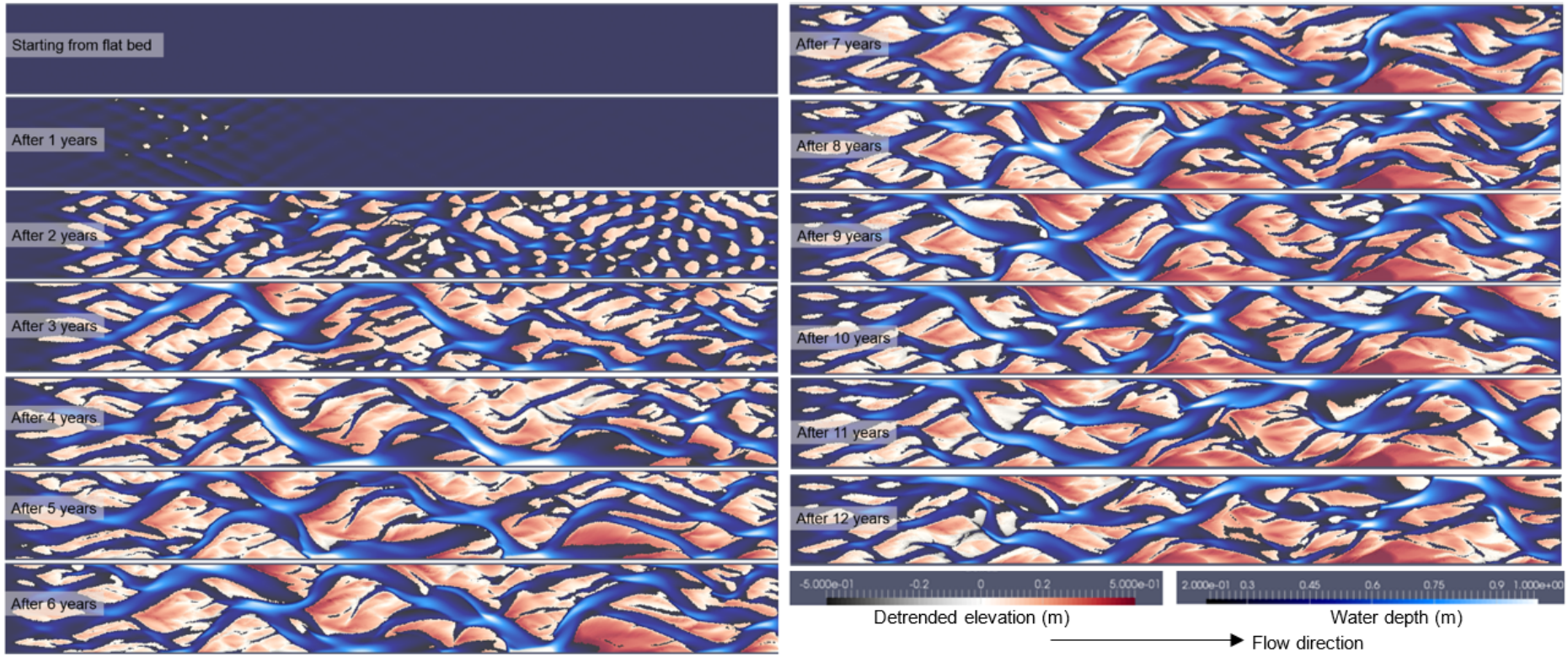

Figure 4.6 Example detail planform evolution displaying detrended elevation and water depth on annual (8-hour simulation time interval) basis produced by the run R_9. The water depths below 0.2 m have not been shown to highlight channel network. All domain (1550 m x 175 m) have been shown here, but for quantitative analysis in the latter sections only the middle 700 m x 175 m has been considered.

b) Total Braiding Index (TBI)

The Total Braiding Index (TBI) was calculated by counting number of channels below the mean elevation of cross-sections extracted longitudinally at the gridcell resolution (2 m x 2m during post processing in MATLAB), following the procedure of Schuurman et al. (2013). The resulting set of sectional analyses were then averaged to give a characteristic TBI for the entire reach (Figure 4.7).

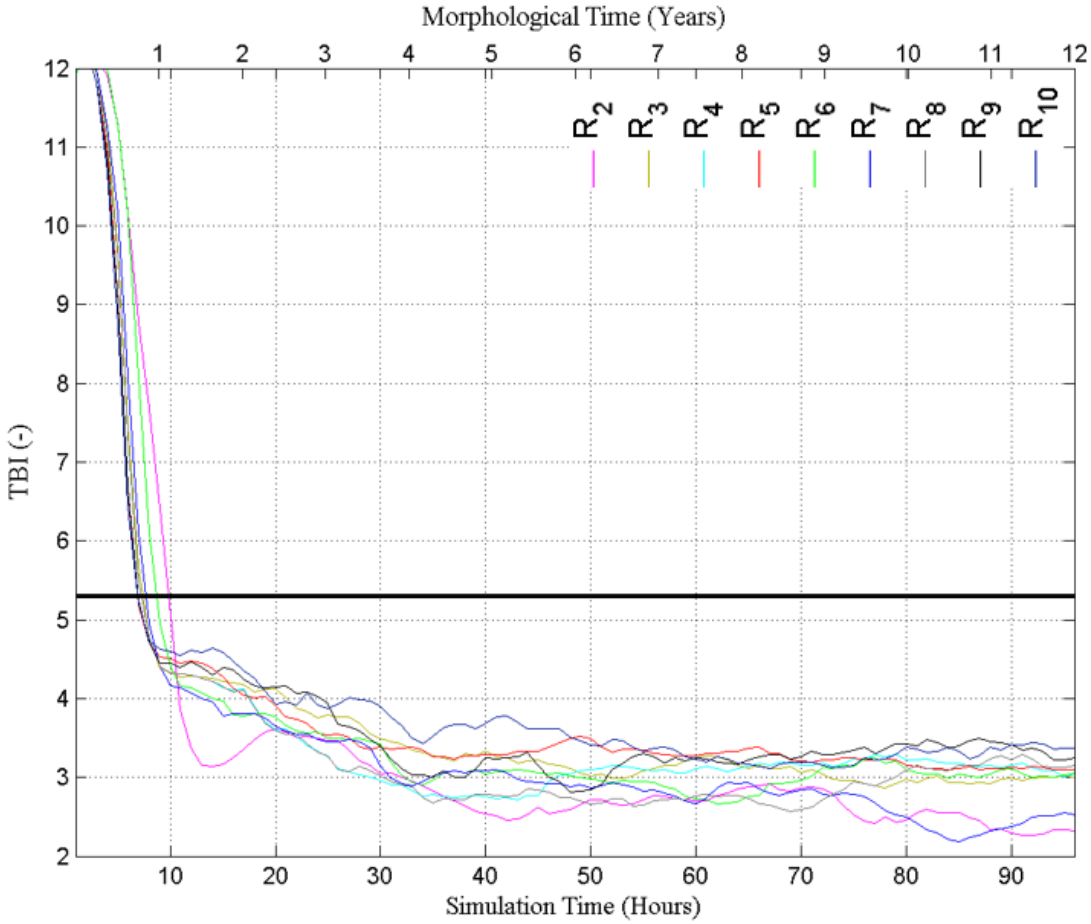

Figure 4.7 Total Braiding Index (TBI) starting from the beginning hours to the dynamic steady equilibrium state resulted by all nine runs (R_2 to R_{10}). The black bold line represents the TBI of the natural prototype Feshie in 2005.

The high frequency migratory bars that emerge in the first one-two years give rise to very high reach averaged TBI at the beginning of each simulation as shown in Figure 4.7. For all simulations, this initial state is characterized by TBIs of ~12 which then decreases rapidly in the first 1-5 years (1-40 hours). Following this transient state, the majority of runs appear to reach a dynamic steady state, with TBIs of between 3-3.5.

The exception to this pattern is R_2 and R_7 which appear to attain a dynamic steady equilibrium state only after 60 hours, and with a lower TBI of between 2 - 2.5. By comparison, the prototype system was found to exhibit a TBI of 5.3 (black bold horizontal line in the Figure 4.7). Therefore, even the more dynamic simulations, R_7, R_8, R_9 and $R_{10,}$ characterized by high rates of reworking are significantly less complex topographically, with TBIs between 30-40% lower than observed in the natural prototype.

4.4.2 Topographic Signature

The topography of the synthetic modelled channels was interrogated by deriving metrics the discussed in Chapter 3; specifically, the frequency distribution of the detrended elevation; the distribution of local slopes; bar height, and the width-depth relationship (α indicator).

a) Elevation Distribution

The Figure 4.8 reveals the standardized distribution of bed elevations predicted by all nine runs (R_2 - R_{10}), based here on the final topography generated after 12 years. The zero elevation corresponds to the mean bed level, so the form of the distribution either side of zero reflects the pattern of elevations above and below the mean, interpreted here as bars and channels respectively. This suggests a very similar statistical pattern of elevations is generated by all simulations, which broadly match the observed topography of the prototype (the bold curve). The distribution of elevation below the mean has a longer tail, reflecting the presence of local, deep scour holes, while the above mean elevation is truncated at 1.8 m, suggesting no anomalous peaks in the local bar surfaces. Previous studies using this metric to evaluate model performance also found a close match to the prototype topography, despite significant differences in the wider set of characteristics (e.g., Doeschl et al., 2009; Garcia Lugo et al., 2015). Ultimately, it appears that this is a relatively easy pattern to replicate and given the wide range of deterministic forms that have equivalent statistical distributions,

suggesting that this pattern is not a particularly powerful metric for discriminating model performance.

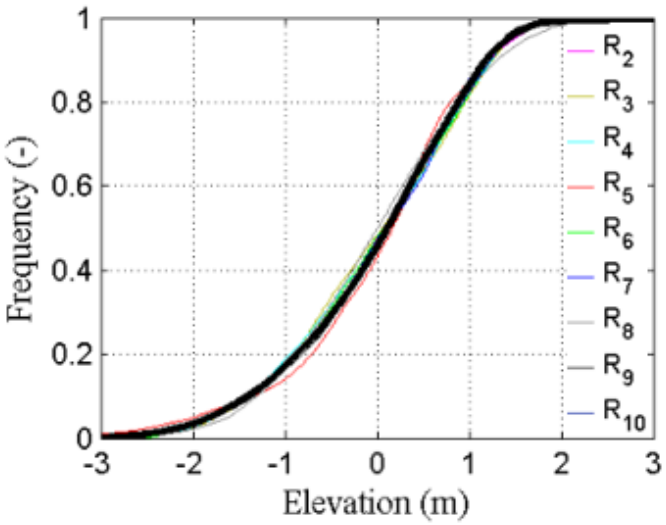

Figure 4.8 Standardized elevation distributions resulted by nine runs (R_2 to R_{10}) based on final topography. The black bold line represents the topography of the natural prototype Feshie in the year 2005.

b) Local Slope Distribution

Figure 4.9 shows the cumulative probability distribution for local slopes, plotted in two separate populations, one for areas above (bars) and one for below mean bed level (channels). All runs demonstrate greater variance of local slopes for the 'channels', reflecting the presence of steep bed waves corresponding to scour holes and avalanche faces which is also evidence in the natural prototype topography (see the last plot in Figure 4.9). Doeschl et al. (2009), using the MP model, was not able to predict this pattern which they attribute to the rule-based representation of flow and sediment transport in MP model, and specifically the kinematic routing scheme which, by lacking the lateral dispersion of momentum, creates a tendency to generate spikes or pits in the topography due to exaggerated feedback between the unrealistic convergence and divergence of flow and sediment transport. However, while the broad difference between bars and channels matches that found in the Feshie, in all cases, the range of slopes found in the modelled topography is lower than observed in the prototype. Not surprisingly, this is strongly linked to the critical angle of repose

used, with the lowest slopes found for R_2 which used a repose angle of just 5°. By comparison, R_5 with the highest repose angle (30°), results in topography with a broader range of slopes, varying up to 25°. The runs using the vertically varying angles of response (the so-called, geotechnical model), R_7, R_8, R_9 and R_{10}, also resulted in a lower range of local slopes, varying from 0° to just 10°. This poor level of performance is interesting, and potentially points to functional differences between the real and simulated topography, which is likely to relate to the effects of root reinforcement, and the presence of mixed grain sizes and organics, leading to much higher slope stability in the natural prototype.

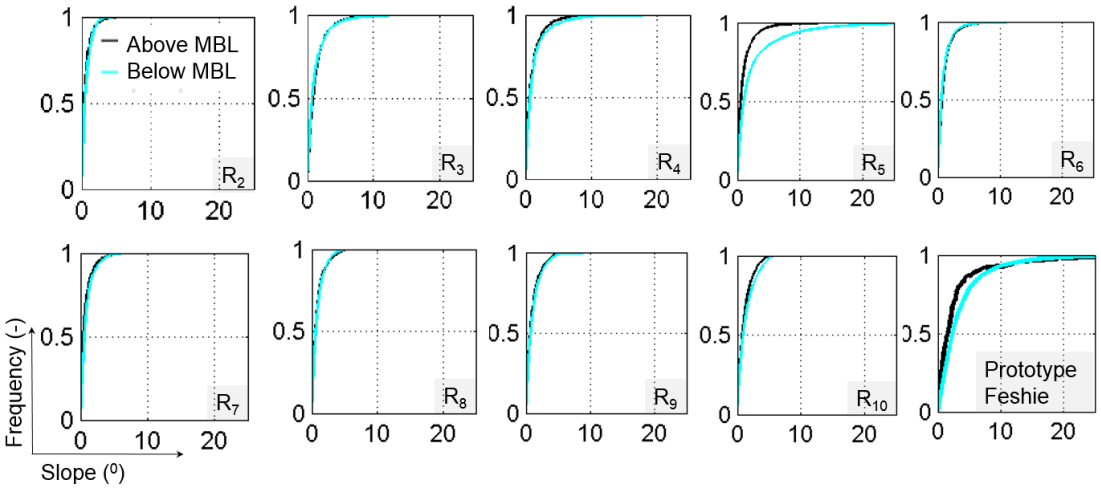

Figure 4.9 Local slope distributions based on final topography resulted by nine runs (R_2 to R_{10}). The legend above and below MBL means the local slope distribution of the area above and below mean bed elevation, respectively. The last plot inside the black box represents the local slope distribution of the prototype Feshie based on 2005 topography.

c) Bar Height

Bar height was calculated by extracted cross-sections longitudinally, and for each section, comparing the 95th and 5th percentile of elevation, following the procedure of Schuurman et al. (2013) and Singh et al. (2017). This was then expressed as a reach average bar height by taking the mean of the set of cross-sections. The result for each simulation is shown in Figure 4.10 which shows the variation in bar height through time. This shows that, for the majority of runs (R_2, R_7, R_8, R_9 and R_{10}), bar

height increases progressively (matching the increase in bar size) before reaching a dynamic equilibrium after c. 60 hours. By contrast, the runs R_3, R_4 and R_6 continue to trend significantly over the entire simulation with bar heights for R_5 (the highest angle of repose, 30°) continuing to increase rapidly, particularly after 60 hours. Using the same method of calculation, the natural prototype has bar height of around 1.2 m (so as a horizontal black bold line). By contrast, the runs attaining steady equilibrium state (R_2, R_7, R_8, R_9 and R_{10}) predict fluctuating bar height varying between 0.6 - 0.8 m, again linked positively to the angle of repose parameter (higher repose angle higher bar height and vice versa). These predicted heights are 35 to 50 % lower than the prototype, and again this likely reflects the effects of root reinforcement and mixed particles sizes, leading to the maintenance of high bar surfaces, exaggerated by local bar trimming.

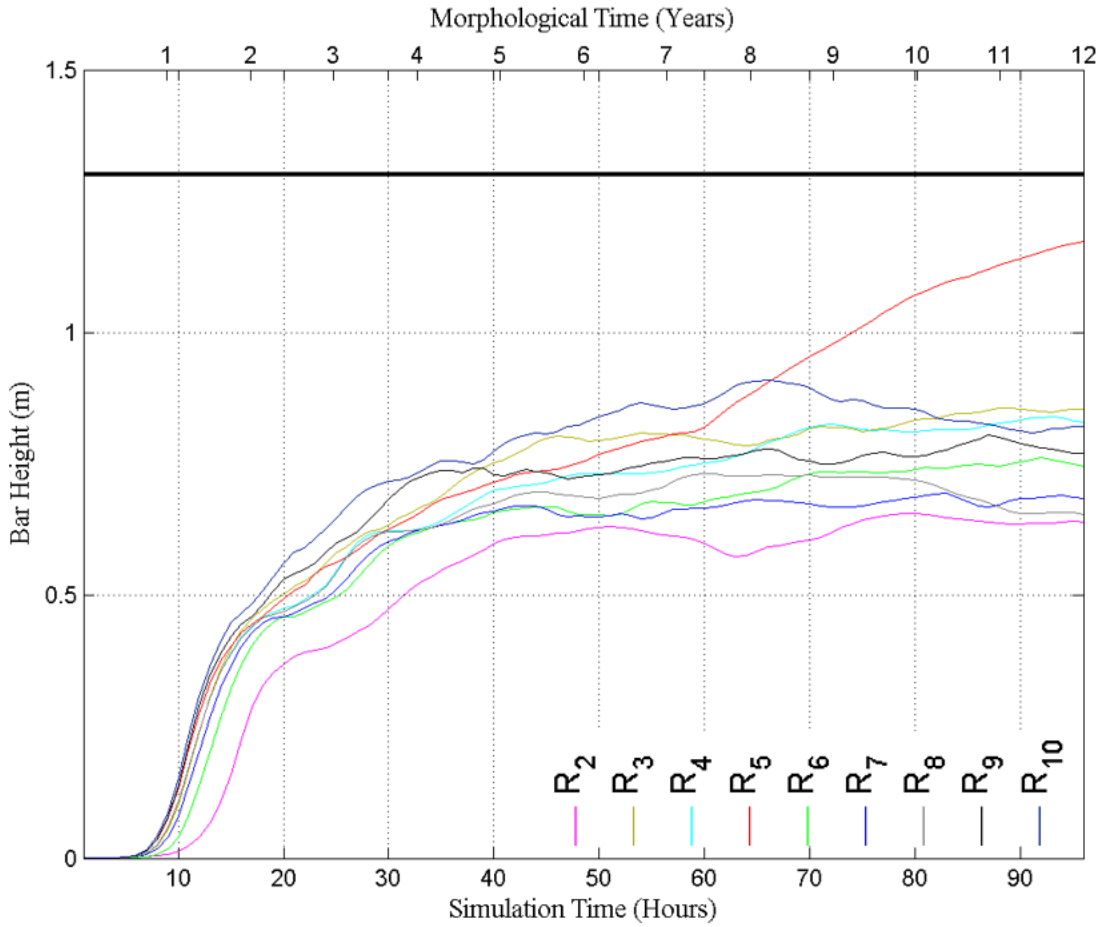

Figure 4.10 Reach averaged bar height evolution. The horizontal black bold line represents the reach averaged bar height of the natural prototype Feshie in 2005.

d) Channel Shape

Channel shape was determined as the power relationship of width with respect to the deepest or minimum elevation of cross-section following the procedure of Redolfi et al. (2016b). Cross-sections were again extracted longitudinally, and the wetted width determined at fixed intervals (1 cm) of depth above the minimum found at each section. This was repeated for each cross-section and then averaged to generate a width-height curve for each surface (see Chapter 3; Section 3.3.2 c). The Figure 4.11a shows an example of the width-depth curve for the final (after 96 hours) topography generated for all nine runs. The relationship observed for the Feshie in 2005 is shown in black bold on the same plot. Each curve was then modelled using the power function described in Chapter 3, in which the exponent, the α or alpha value, is used to provide an index of channel shape, after Redolfi et al. (2016b). Values of α were then fitted to reach averaged curves for all simulations, sampling the bed morphology at 1-hour intervals. The resulting change in the channel shape, indexed by α, is plotted through time in Figure 4.11b.

Until 20 hours of simulation time, the alpha value predicted by all runs were below one. For all simulations, α increases rapidly as the initial plane bed topography develops into a network of bars and channels. By 20 hours, runs R_5, R_9 and R_{10} exhibit average channel forms that are associated with α persistently above unity, corresponding to Y-shaped channel morphologies typically of unconstrained braided rivers (cf. Redolfi et al., 2016b). Here, it is worth noting that the alpha value of the run R_9 and R_{10} also demonstrate strong fluctuations indicating frequent breakdown and reworking of topography. By contrast, R_5 appears to have static channel form, which is likely to reflect the lack of channel mobility. The remaining simulations, R_2, R_3, R_4, R_6, R_7 and R_8 developed morphologies exhibits α both above and below unity, indicating typically incised, single thread channel forms (cf. Redolfi et al., 2016b). This suggests that the lateral slope factor (reduced to 2 and 1.5 in R_9 and R_{10} respectively,

cf 3.0 in all remaining simulations) is critical in promoting high rates of channel mobility, encouraging frequent channel swapping and lateral migration.

The prototype Feshie (Figure 4.11a, black bold line) exhibits an alpha value of 1.56 (Figure 4.11b; black bold horizontal line), significantly above that found in any of the simulation, suggesting that even the most mobile of simulations (R_9 and R_{10}) do not generate the comparable complexity of topography observed in the natural system.

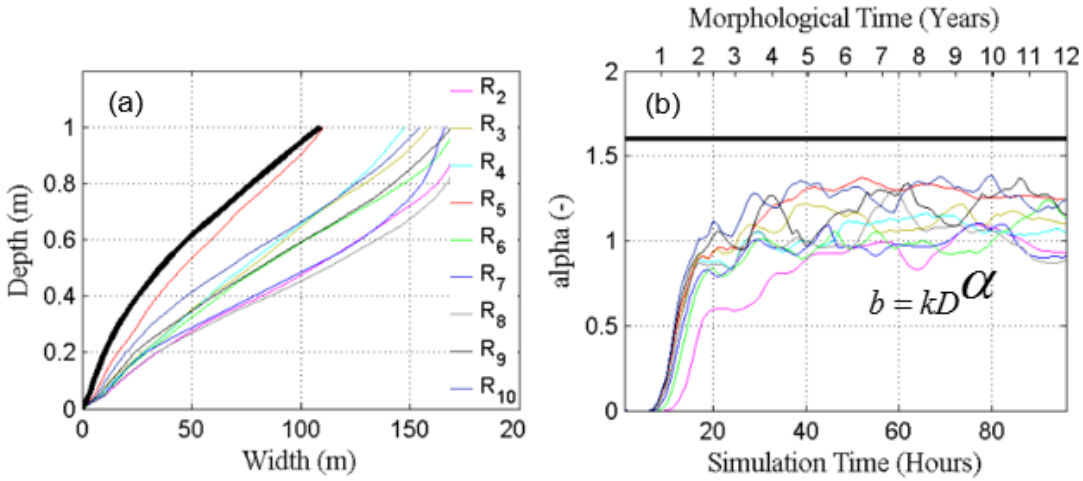

Figure 4.11 (a) Width (b)–Depth (D) relationships based on the final topography produced by nine runs (R_2 to R_{10}). The bold black line is the width-depth curve of the natural prototype Feshie in 2005. (b) Evolution of topography as characterized by the alpha value (exponent of the power fitted width-depth curve) on hourly basis produced by all nine runs. The horizontal black bold line represents the alpha value of the natural prototype river in 2005.

4.4.3 Hydrodynamics Signatures

a) Wetted Width, Mean Depth and Mean Velocity

Mean wetted width, depth and velocity were analysed on a cross-sectional basis to provide an insight into the characteristic hydrodynamic processes predicted by the set of simulations. These variables are again determined on a sectional basis but then averaged to provide a representative value for the reach. For the derivation of reach averaged variables, only the cells with water depths equal and above than 0.075 m (the threshold used to calculate sediment transport) are considered.

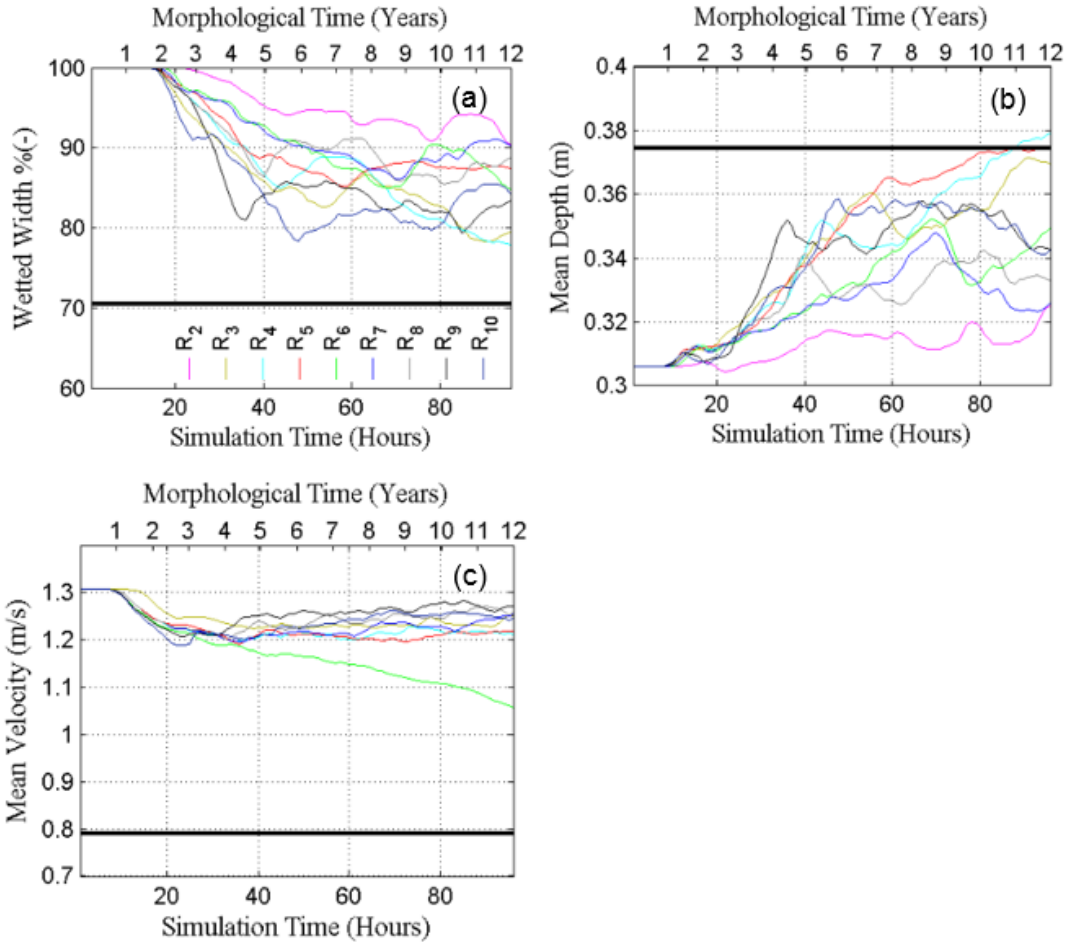

Figure 4.12 Evolution of cross-sectional mean width, mean depth and mean velocity produced by nine runs (R_2-R_{10}). The black bold line represents corresponding variable of the natural prototype Feshie in 2005 under similar stage condition based on fixed-bed hydrodynamic simulation. These mean values were calculated by considering only the cells having water depth greater than 0.075 m (threshold used for sediment transport).

As shown in Figure 4.12a, all runs with the exception of R_3 and R_4 achieve a dynamic equilibrium wetted width after approximately 50-60 hours (6-7 years). As similar pattern is observed for mean depth, except that non-stationary behaviour is found for R_5 as well as R_3, R_4 (Figure 4.12b). In terms of the mean velocity, only the run R_6 did not achieve the steady equilibrium state (Figure 4.12c). The remaining simulations, based on the geotechnical bank erosion model and lower lateral slope factor simulations, achieve equilibrium conditions, but significantly overestimate the mean wetted width and velocity found in the prototype at comparable discharge, and underestimate the mean depth (shown by the horizontal black lines in the figures

below). These patterns suggest a network of comparatively broad, but shallow and fast flows emerge from these simulations, compared to a more constrained, deeper and slower network of flows in the prototype. This is consistent with the lower gradients and more subdued topography revealed by the analyses described above, and again implies subtle more important differences in the character of braiding.

4.4.4 Morphodynamics Signatures

a) Spatial Pattern of Erosion and Deposition

Spatial distribution of erosion and deposition was determined by subtracting a more recent modelled topographic surface (DEMs) from an older surface (DEM) to create a DEM of Difference, or DoD, so that negative values correspond to scour and vice versa. As an illustration, Figure 4.13 shows changes found between the last three 'years' of the simulations, i.e., DoDs derived for 88-80 hours, and 96–88 hours. The analysis of change was however, conducted at an 'annual' frequency (i.e., every 8 hours) in order to reveal the composition of changes characterising the evolution of each simulation through time. This approach enables quantification of changing volumes of erosion and deposition over the simulation period. For simplicity, the timeseries of DoDs is shown here only for simulation R_9 in Figure 4.14.

As discussed above, simulation R_1 resulted in a highly unrealistic pattern of channel development, illustrated here by the high spatial frequency of units of erosion and deposition before the simulation became unstable. For the remaining simulations, it is clear that as the repose angle is increased from 5 to 30 degrees (i.e., R_2, R_3, R_4, and R_5) key braiding processes apparent in the DoDs, such as local avulsion, cut-offs and bar dissection, are gradually eliminated under all morphodynamic activity is collapsed into a single, meandering channel thalweg (cf. R_5). By contrast the simulations employing the geotechnical bank erosion formulation, R_7, R_8, R_9 and R_{10} all exhibit a dynamic pattern of bed reworking that extends to the end of the simulation period, continuing to promote lateral migration of channels and active braiding.

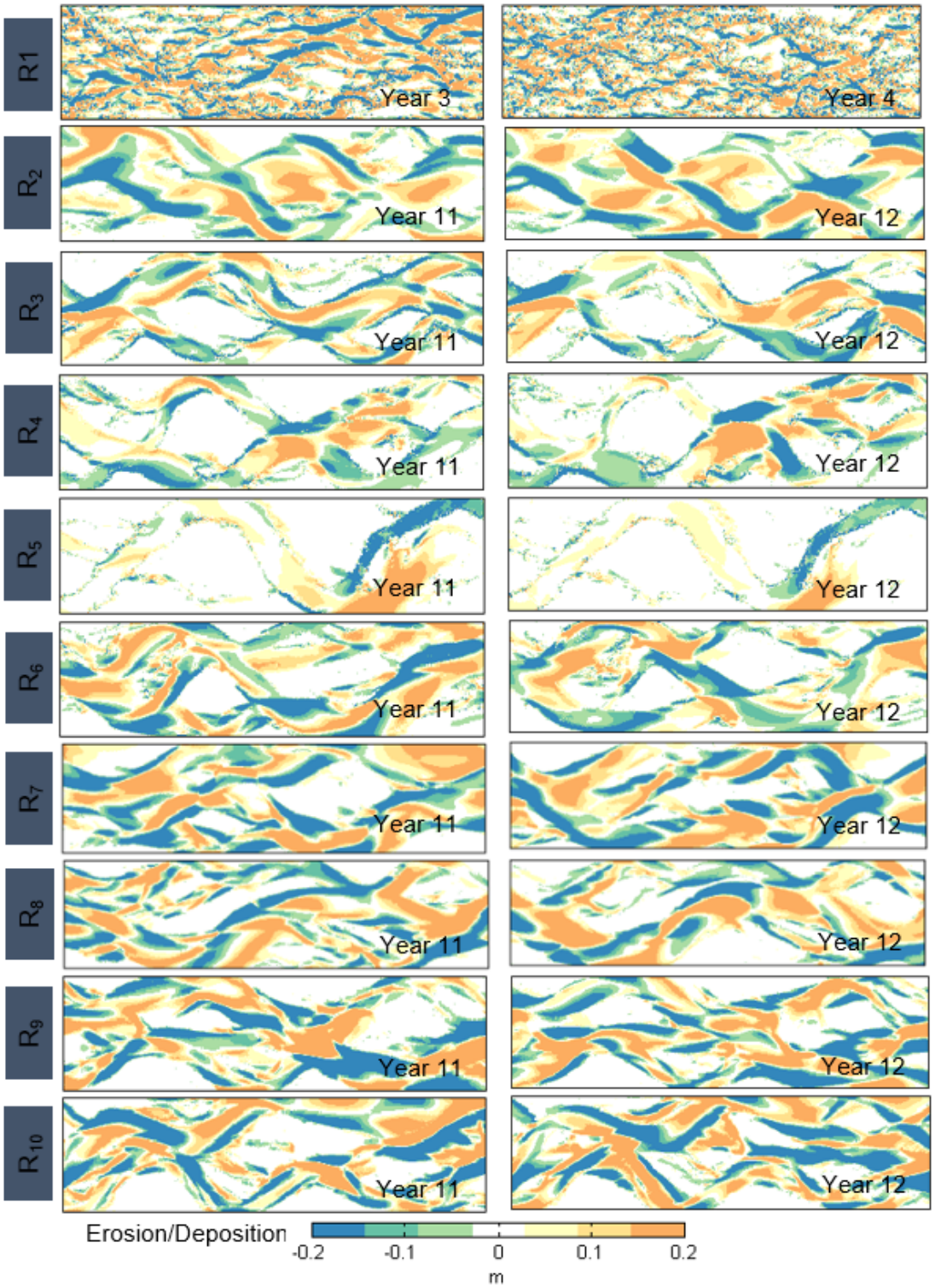

Figure 4.13 Spatial pattern of erosion and deposition based on the changes in the last two years produced by all runs. The run R_1 crashed after four years, so maps presented here represent only the change in years three and four.

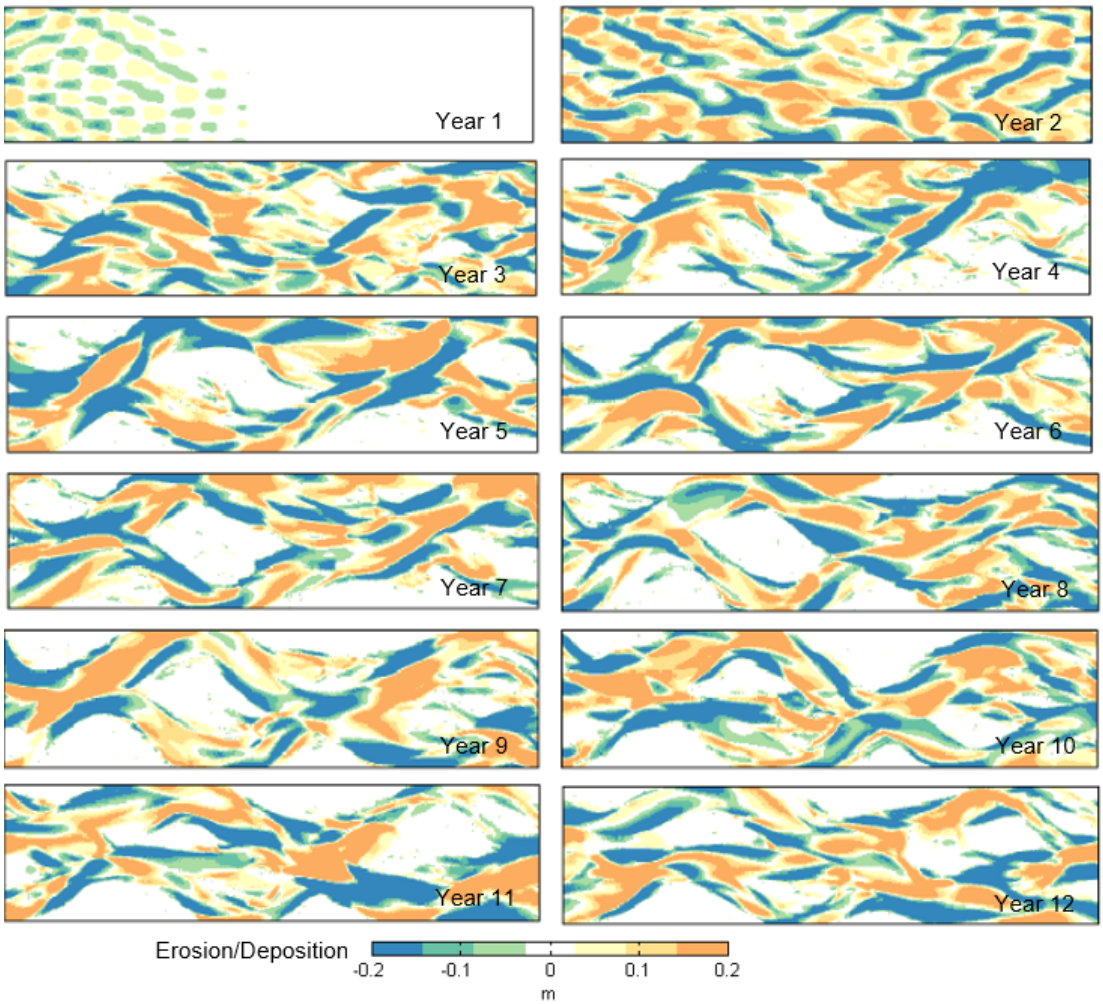

Figure 4.14 Spatial pattern of erosion and deposition based on changes on annual basis (8-hour simulation time interval) produced by the run R_9. One-year change means changes during 8-hour simulation time according to time scaling as mentioned in the section 4.3.6b.

A detail insight into the evolution of the bed is afforded by examination of the illustrative timeseries of DoDs shown for R_9 in Figure 4.14. In the first year of this simulation, while the multiple bars were submerged, erosion and deposition patches were well organized and uniform. Following this, between years 2-5 bars become exposed and processes such as bar edge trimming, local avulsion, chute cut-off develop and migration of submerged unit bars is also apparent. Concurrently, these small migratory bars begin to coalesce with existing bar forms, creating complex compound bars. By the end of year 5, a fully developed braided morphology is apparent, comprising of complex bars, migratory unit bars, active bifurcations and

confluences (e.g., Ashmore, 1991; Bertoldi et al., 2009b). This pattern of evolution appears to achieve a dynamic equilibrium state over the remaining years of the simulation, with active reworking of the channel bed continuing to maintain a complex, braided morphology (e.g., Bertoldi et al., 2009b).

b) Sediment Transport

The hourly sediment transport rate determined for each simulation, by extracting the predicted distribution of bed shear stress and estimating the transport rate using the Meyer-Peter- Müller formulation described in Chapter 3. This calculation was performed for extracted cross-sections and then summed for each section and then averaged across all sections to derive a reach-scale rate. The changing rate of bed material flux calculated in this manner is shown over time for each simulation in Figure 4.15. This reveals a rapid increase in bed material transport as the initial wave of erosion and deposition shown in Figure 4.14 (above) propagates downstream in the first 20 hours of the simulation. After approximately 40 hours, this transient condition stabilises, and transport rates fluctuate in the range of 0.03 - 0.045 m^3/s, varying significantly between the model parameterisations. Notably, run R_5, with the highest response angle appears to generate a very static timeseries of transport, reflecting the lock-down of the morphodynamics within the static meandering channel as discussed and shown in Figure 4.13 above. By contrast, the remaining simulations, in particular R_7-R_{10} exhibit strong autogenic fluctuations in transport, corresponding the breakup and formation of bed topography (e.g., Wheaton et al., 2013).

A representative bed material transport rate for the prototype Feshie at the same discharge (70 m^3/s) were derived using fix-bed hydrodynamic simulations with BASEMENT, using the same bed roughness and eddy viscosity parameter values. The result obtained suggests a predicted volumetric transport rate of 0.05 m^3/s which is shown as the horizontal line in Figure 4.15. While itself a modelled variable, this suggests the natural morphology of the prototype is adjusted to a significantly higher

rate of transport than that obtained in the morphodynamic simulations (some 10-30% lower). This observation is consistent with patterns of wetted width, depth and velocity discussed above, which imply a distribution of flows that is wider and shallower than the more concentrated, deeper and consequently higher stress flow regime of the prototype.

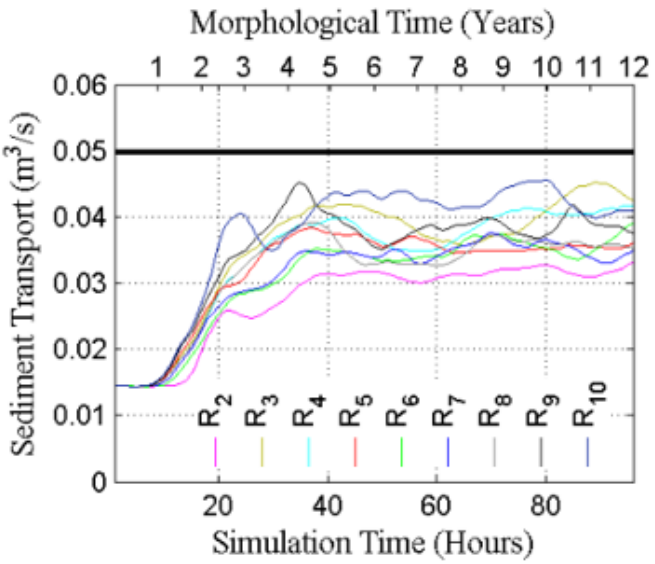

Figure 4.15 Evolution in terms of sediment transport rate produced by nine runs. The black bold line represents the sediment transport rate of the natural prototype Feshie at 70 m^3/s of discharge in 2005, as derived from fixed-bed hydrodynamic simulation and sediment transport calculation.

c) Active Width and Active Braiding

Active width of each cross-section was calculated as the percentage of the total corridor width, considering only channels actively transporting sediment as calculated above. This was then expressed as a reach averaged active width by taking the mean value across all cross sections (Figure 4.16a). As before, the timeseries of active width is characterised by an initial transient condition, which stabilises after 40 hours for all models. After 40 hours, runs R_2, R_6, R_7, R_8, R_9 and R_{10} exhibit a steady equilibrium state, with the active width fluctuating about an average of 60% of the total corridor width. By contrast, runs R_5 appears to show a persistent contraction of active width, again consistent with the observation described above. The estimated active

width in the prototype at 70 m^3/s is 55% which is broadly comparable with the predictions obtained here.

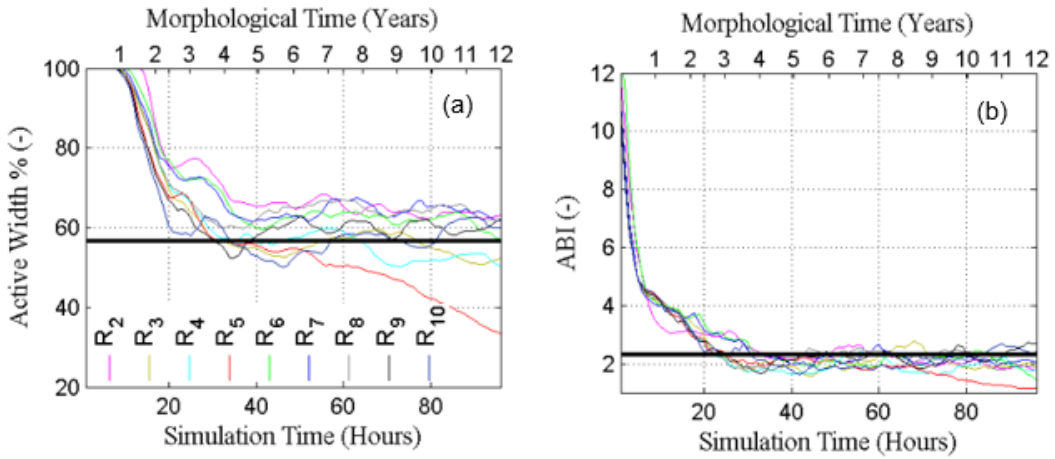

Figure 4.16 Evolution in terms of active width and Active Braiding Index (ABI) produce by all nine runs (R_2 - R_{10}). The black bold line represents the corresponding variable of natural prototype Feshie in 2005, as derived from fixed-bed hydrodynamic simulations at similar discharge.

The Active Braiding Index (ABI) of each cross section was calculated by counting number of channels transporting sediment higher than the mean sediment transport of the section, following the procedure of Schuurman et al. (2013) and then expressed as a reach average. The evolving pattern of ABI over time is shown in Figure 4.16b. This shows that after 40 hours, runs R_2, R_3, R_4, R_6, R_7 and R_8 attain a dynamic equilibrium, fluctuating about an ABI of between 1.7–2, while simulations R_9 and R_{10} with the lower lateral slope factor achieve, an equilibrium ABI of between 2 - 2.7. These match closely the ABI for the Feshie at 70 m^3/s (based on the fixed-bed hydrodynamic simulation and associated sediment transport calculations) which is 2.3 (shown as the black bold horizontal line). By contrast, run R_5 failed to reach an equilibrium state, collapsing towards an index of unity, consistent with the observations reported above.

d) Turnover Rate

The predicted rate of bed turnover (percentage of area undergoing erosion and deposition) was determined from the changes derived from the 'annual' or 8-hr DoDs.

To compare this with the prototype, only changes greater than a level of detection of 0.05 m were quantified (Figure 4.17a), reflecting uncertainty in the measured DEMs of the Feshie (Wheaton et al., 2010; Brasington et al., 2012). Following the transient period in the first two years, simulations R_2, R_8, R_9 and R_{10} achieve a rate of turnover fluctuating at between 50–60% of the bed after 5 years. By contrast, the runs with high global angles of repose (R_3, R_4 and R_5) appear to never achieve a steady equilibrium with bed activity declining progressively through time. This reflects the pattern of incision and lock-down of the network observed with these high angles of slope failure which inhibit the active lateral migration of the channels. DoDs for the Feshie derived over the period 2003-07 suggest an empirical turnover rate of 40-60% annually (Figure 4.17b), close to the modelled rate of R_7-R_{10}.

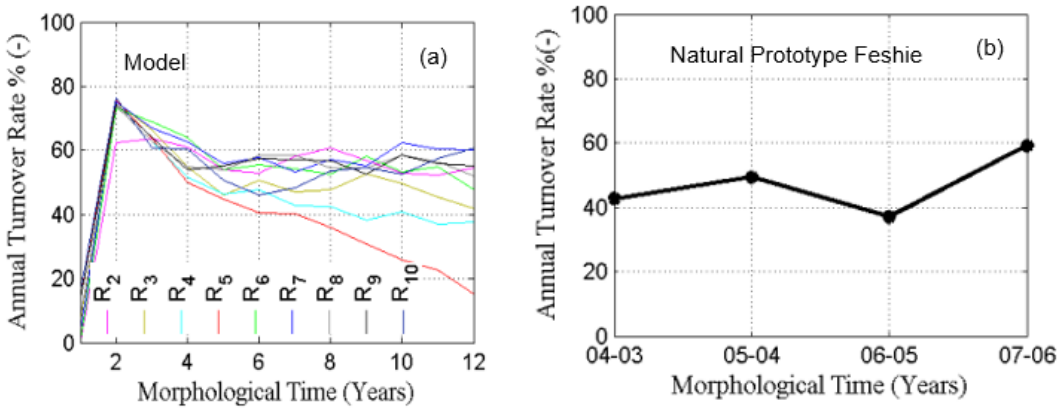

Figure 4.17 (a) Evolution in terms of annual turnover rate, at 0.05 m of threshold of detection, produced by all nine runs. (b) Annual turnover rate of the natural prototype Feshie, at similar threshold of detection (0.05 m) based on maps from 2003 to 2007.

e) Volumetric Sediment Storage Pattern and Dynamic

As discussed in Chapter 3, a useful tool to interpret the pattern of channel change is to quantify the surface elevation at which erosion and deposition occurs. By determining the relationship between the volumes of change and their prior bed elevation, it is possible to disentangle the dominance of processes such as channel scour (occurring at low prior elevations) and bar top dissection or avulsion (occurring at high prior elevations). This relationship has been calculated here for the volumes of erosion and deposition separately and mapped onto the initial bed elevation. The

resulting pattern of erosion and deposition by elevation only for the run R_9 has been shown for 0-96 hr DoD in Figure 4.18 (a = erosion; b = deposition). This clearly shows that at steady equilibrium state, erosional volumes occur dominantly on high initial surfaces, indicating the importance of processes such as bank erosion, chute cut-off, bar top scour and avulsion, versus topographically low processes such as channel bed scour. By contrast, depositional volumes occur at low elevations indicating the importance of migratory gravel sheets, coalescing to form compound bars.

This pattern can be simplified by summing the volumes of erosion and deposition that occur above and below mean bed level, taken here to imply changes on bars and within channels. This simplified pattern, evolving over time, is shown for R_9 only in Figure 4.18 (c = erosion; d = deposition).

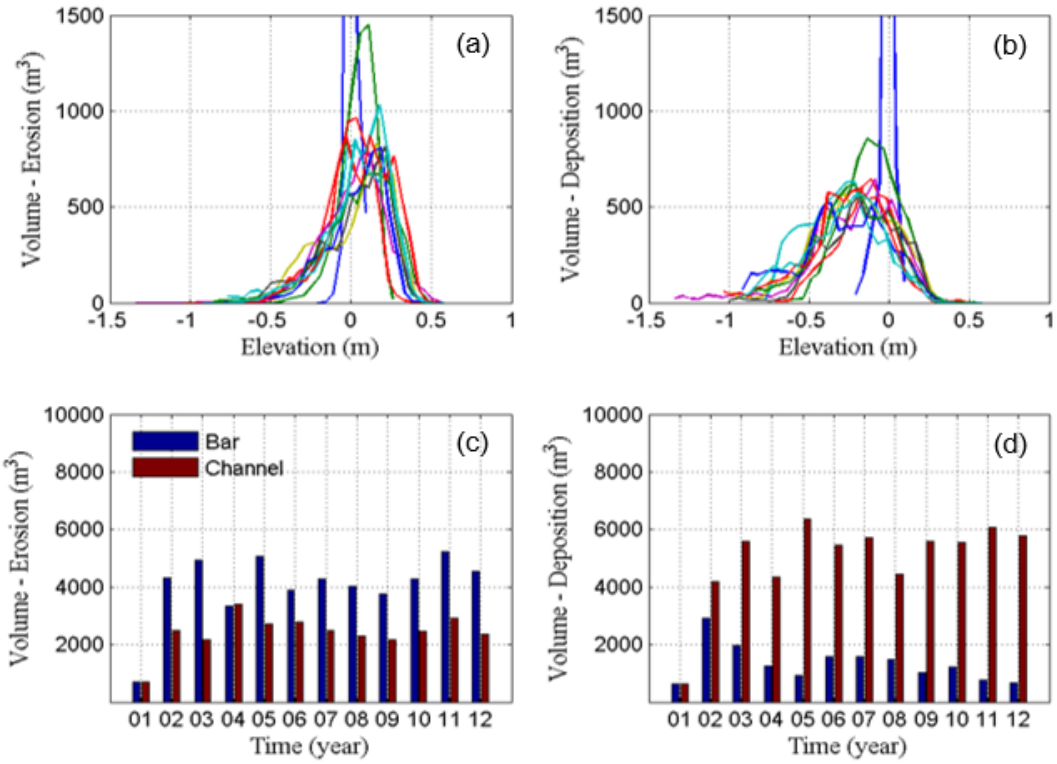

Figure 4.18 Erosion and deposition storage and dynamics for the run R_9 with respect to mean elevation of the prior year topography. The peak of erosion curve lays on the right side, indicating dominancy of bar erosion over channel erosion, which indirectly gestures at the existence of processes such as cut off development, bar edge cutting, and bar dissection. Conversely, the deposition mass lays on the left side of the curve indicating concentration of deposition activities into channel.

When this approach is used to examine the full set of simulations, it becomes clear that differences between runs are strongly evident in the distribution of erosion with elevation, while the pattern of deposition is very similar. Figure 4.19 summarizes this pattern of high stage (above mean bed level) and low stage (above mean bed level) erosion volumes on an annual basis changes for all nine stable runs.

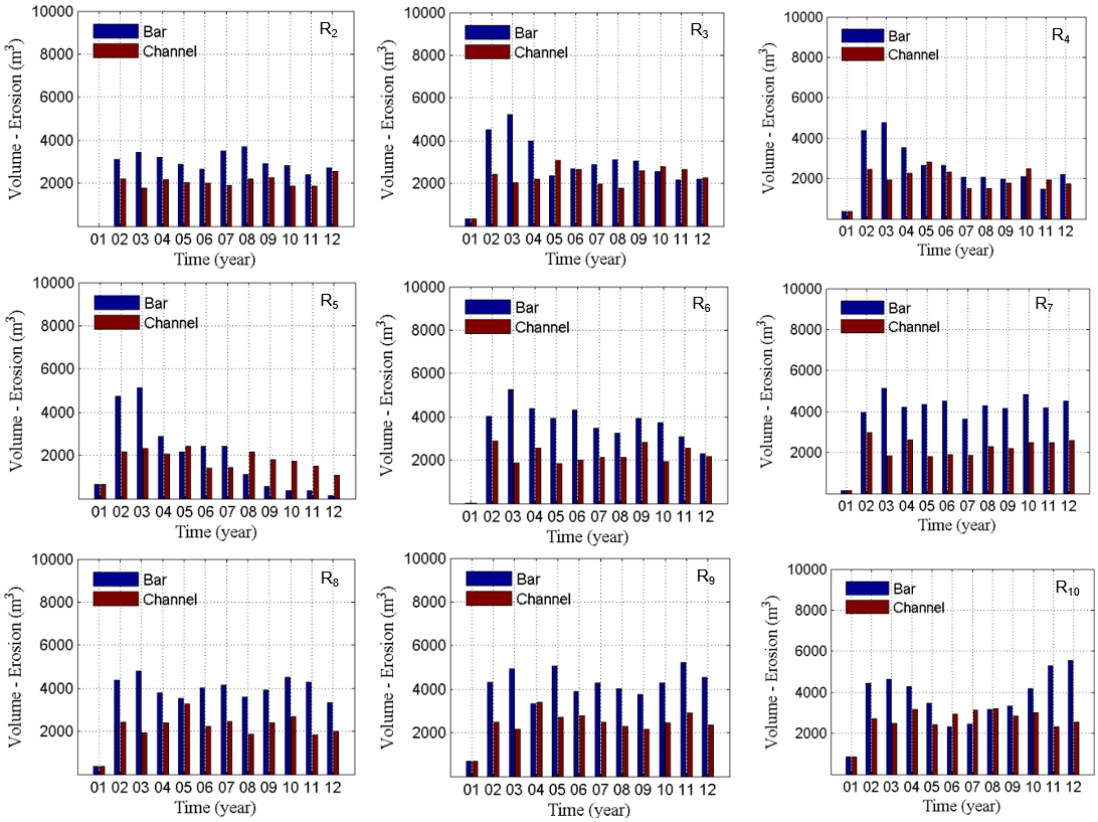

Figure 4.19 Volumetric erosion dynamic with respect to mean elevation of preceding year's topography for all runs.

Figure 4.19 reveals that during the initial four years, all runs dominated by high stage or bar erosion than low stage or channel erosion. However, in later stages of the simulations, it becomes clear that for run R_2, R_3, R_4 and R_5 channel erosion ultimately matches or becomes dominant source of erosion, as morphodynamic activity locked into channels and lateral migration ceases, consistent with the observations reported above. This distribution of erosion is however, strongly at odds with that observed in runs R_7, R_8, R_9 and R_{10} where bar erosion contributes as much as 75% of the total erosional budget. This is an important result, providing a clear, quantitative measure

that highlights differences in the form of morphodynamic processes dominating the different simulations. Simulations R_7-R_{10} with the geotechnical bank model and lower lateral slope factors maintain high active width, high ABI through the simulation of lateral bank erosion processes that are critical to maintain autogenic sediment supply, which in turn acts to fill channels and promote bifurcation. This, therefore, appears as a powerful metric to disentangle the dominant suite of processes.

The volumetric pattern of erosion and deposition was also analysed for the Feshie using the more limited set of DEMs available from 2003 to 2007 (these data adopted from Chapter 3). This reveals a strong pattern of interannual variability, in which for both 2004-03 and 2006–05, bar and channel erosion contributed equally to the total change budget (see Figure 4.20a and Figure 4.20c; years 04-03 and 06-05). In these periods, there were a limited number of high flow events and the total volumes of sediment mobilized were low. By contrast, in 2005-04 and 2007–06, bar erosion dominated over channel erosion significantly (Figure 4.20 a and c; years 05-04 and 07-06). This reflects an increase in flood intensity during this period, associated with high stage events and a higher intensity of erosional activity. The depositional pattern was characterized predominantly by channel processes (see Figure 4.20b and Figure 4.20d), a pattern matched by all simulations. However, the high intensity erosion pattern found for 2005-04 and 2007-06 is only evident for simulations R_7, R_8, R_9 and R_{10}.

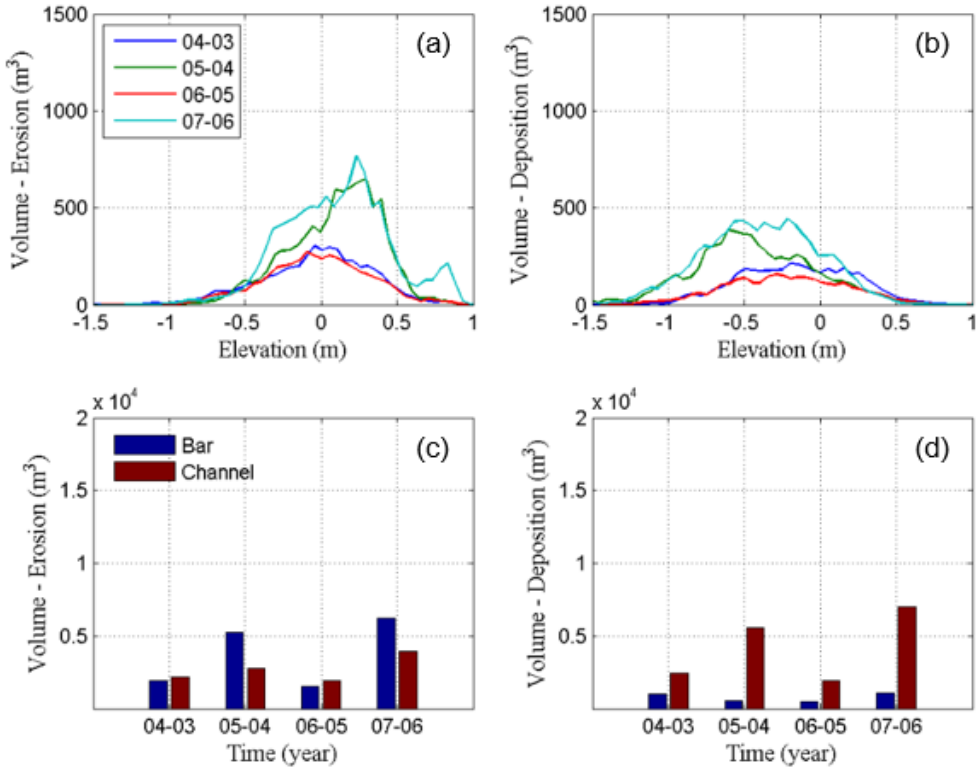

Figure 4.20 Erosion and deposition storage and dynamics in the natural prototype Feshie from 2003 to 2007, with respect to mean elevation of preceding DEM.

4.5 Analysis

4.5.1 Parameter Sensitivity

Based on the results presented in the earlier section, the simulated runs and their behaviour could be clustered into three groups.

Run R_1: Without Bank Erosion and Lateral Transport Model

Simulation R_1 does not employ either lateral transport or the bank erosion model. Consequently, it quickly gives rise to unrealistically narrow and deep channels (see Figure 4.5; Run R_1) due to the inability for channel to migrate laterally, and the model quickly encounters stability problems.

Run R_2, R_3, R_4 and R_5: With Uniform Repose Angle and Lateral Transport Model

The runs R_2, R_3, R_4 and R_5 incorporate bank erosion and lateral transport model. The lateral transport factor for all these runs were fixed at 3.0 and the bank erosion

parameters (repose angle) held constant for dry, wet and failed material, but increased from 5, 12, 18 and 30 degrees for R_2, R_3, R_4 and R_5, respectively.

Simulation R_2 with the lowest repose angle (5^o) generated highly diffuse topography characterized by low complexity, low rugosity morphology. This is evident in the visualization of the planform maps shown in Figure 4.5 and Figure 4.13 and reflected in the low value of the channel shape exponent α which quantifies the complexity of the average cross sectional geometry (Figure 4.11b). The ABI for R_2 was consistently below 2.0, which contrasts strongly with Feshie, having the ABI of 2.3 at the same discharge (70 m^3/s) (see Figure 4.16b). The morphodynamic behaviour again shows clear differences with the prototype, with approximately equally distributed erosion of bar and channel topography (see Figure 4.19). This pattern of behaviour reflects the very high rate of lateral channel mobility associated with the low critical angle of repose. This precludes the development of incised channels, resulting in the diffusive morphology with suppressed bar heights (see Figure 4.10).

Simulations R_3-R_5 involved systematic increases in the critical angle of repose from 12-30 degrees. For R_3 and R_4, this lead to more complex bed morphology, characterized by the shape exponent, α, fluctuating both above and below unity (Figure 4.11b). The wetted width, mean depth, active width and turnover rate did not achieve a steady equilibrium state during the simulated time (Figure 4.12). Additionally, although both runs resulted dominant high stage erosion during the initial simulation period, this pattern did not persist (see Figure 4.19).

Simulation R_5 failed to attain a dynamic equilibrium state when analysed in terms of bar height, mean water depth, active width and turnover rate. Notably, the ABI also decreased steadily towards a final value of unity, representing a single thread meandering channel after 12 years of evolution (Figure 4.16b). It is also noteworthy, that the predicted sediment flux is more or less constant after year 5, suggesting a

lock-down of the channel, without autogenic pulsing of transport associated with bar breakup and formation (Figure 4.15). These characteristics are explained by the high angle of repose, set here to 30°. Given the formulation of the bank erosion module, this implies that bank erosion starts only when the near bank water depth exceeds ~1 m. As a result, the flows are increasingly concentrated into a static single thread channel that is unable to migrate laterally, contributing local supply of sediment to the bed. Consequently, processes such as localised avulsion, cut-off development and bar dissection that play a key role in channel widening, and hence downstream bifurcation (Ashmore, 1982, 1987, 1988; Jerolmack and Mohrig, 2007; Bertoldi et al., 2009b; Wheaton et al., 2013) play a limited role in the morphodynamics.

Run R_6, R_7, R_8, R_9 and R_{10}: With Geotechnical Bank Erosion Model and Lateral Transport Model

These runs all employ the geotechnical approach to model bank erosion process, in which different critical angles of repose are set for dry, wet and deposited material, respectively. Simulations R_6-R_8 involve progressive increases in the angle of repose, while maintaining a similar scaling for dry, wet and deposited material, while the last two simulations, R_9 and R_{10}, use the highest angles of repose, but reduce the lateral slope factor to 2.0 and 1.5 respectively.

Simulation R_6 did not achieve steady equilibrium state in terms of mean velocity (Figure 4.12c) and the predicted ABI was significantly lower than that of the prototype Feshie (Figure 4.16b). As found for the previous simulations, R_2-R_5, run R_6 does not exhibit the characteristic pattern in which erosion of high stage, bar surfaces dominate channel scour as seen in the prototype. By contrast, R_7 achieved a dynamic equilibrium state in all these respects, however the predicted TBI and ABI remain significantly lower than found in the prototype Feshie. Additionally, the channel shape exponent, α, was found to be below unity at the end of the simulation, suggesting

uncharacteristically simplified channel forms with low a width-depth ratio. Interestingly however, the pattern of erosion with height revealed the dominance of bar erosion over channel erosion. This suggests that the low angle of repose (5°) set for deposited material was sufficient (a key) to enable lateral channel migration, leading to localised sediment supply that in turn drives bed mobility.

The runs R_8, R_9 and R_{10}, all set the angle of repose for dry, wet and deposited material to 25°, 18°, 5° respectively. However, in this case, the lateral transport factor for these runs were decreased progressively, from 3.0, 2.0 and 1.5 respectively. Run R_8 attained a dynamic equilibrium state with respect to all metrics and exhibited of high stage erosional activity, as found in the natural prototype Feshie. Nevertheless, the predicted ABI was found to be below 2 (Figure 4.16b). Additionally, the alpha value of the width-depth curve was also supressed (below unity) suggesting the lack of lateral mobility and the concentration of flows into less complex topographic forms (i.e., single thread channels). This behaviour reflects the high value of the lateral transport factor (3.0) which acts to pulls sediment downgradient to even out local discontinuities resulting in less complex, more diffused topography.

By contrast, the lateral slope factor for runs R_9 and R_{10} is reduced, decreasing the gravitational pull on the direction of bed material flux, and the tendency therefore to smooth the bed. The resulting ABI for these simulations is significantly higher at 2.0-2.7, consistent with the natural prototype (Figure 4.16b). Additionally, channel shape (alpha) exponents are also significantly above unity, indicating the maintenance of a comparatively complex channel morphology consistent with the prototype Feshie and unconstrained braided rivers (cf. Redolfi et al., 2016b).

4.5.2 Identification of Behavioural Parameter Sets

The analysis described above demonstrates significant sensitivity of BASEMENT to the bank erosion and lateral transport parameters. This is evidenced through

quantitative differences in the form and morphodynamics of the resulting simulations. Identification of an 'optimal' parameterisation from this set of experiments is complex. The validation criteria described above cannot be readily defined in hierarchical terms, and moreover, it should be noted that there is clearly scope for deeper interrogation of the model's parameter space.

Nonetheless, in an attempt to prescribe a behavioural parameterisation for use in the forthcoming chapters, a strategy was devised to summarize the analyses described above in order to identify the optimal simulation in terms of the range of model performance. This was achieved used a simple scoring system, in which the performance of the model compared to the prototype was defined as behavioural and abehavioural and marked as 1 and 0 accordingly. The overall model performance was then determined by summing the scores across all indicators, as shown in Table 4. 2. This approach identifies simulations R_9 and R_{10} as the optimal performers, with behavioural scores across all 13 metrics. These two runs employ the geotechnical approach to bank erosion, and set high critical angles of repose for dry, wet and failed material respectively (25, 18 and 5 degrees). However, unlike simulation R_8 which uses the same bank erosion parameters, both these simulations are associated with lower lateral slope factors, of 2.0 and 1.5 respectively.

While clearly qualitative, this process of elimination results in a coherent selection of the model parameters. The geotechnical approach to bank stability ensures the maintenance of lateral bank mobility, driven largely by the low repose angles for deposited and wet material, yet a high enough critical threshold for dry material to ensure channelization of flows as compared to the highly diffusive topography generated by simulations with globally low thresholds for slope stability. Similarly, the lower lateral slope factors used in these simulations reduces the tendency for gravitational infilling of channel topography. This prevents the development of flat,

planar topography with a concomitant reduction in channel complexity and reduced variability in shear stress and local sediment flux.

Table 4. 2 Scoring for all runs with respect to all metrics used in the results section. Run achieving equilibrium state and closely approximating natural prototype Feshie gets score one, otherwise, zero. The runs R_9 and R_{10} score one from all the respect, resulting in highest total score of 13, so were considered as the best runs.

Scoring	TBI	Elevation	Local Slope	Bar Height	Channel Shape	Wetted Width	Mean Depth	Mean Velocity	Sediment Transport	Active Width	ABI	Erosion Deposition	Turnover Rate	Total Score of each Run
R_1	0	0	0	0	0	0	0	0	0	0	0	0	0	0
R_2	0	1	1	1	0	1	1	1	1	1	0	0	1	9
R_3	1	1	1	1	1	0	0	1	1	0	0	0	0	7
R_4	1	1	1	1	1	0	0	1	1	0	0	0	0	7
R_5	1	1	1	0	1	1	0	1	1	0	0	0	0	7
R_6	1	1	1	1	1	1	1	0	1	1	0	0	1	10
R_7	0	1	1	1	0	1	1	1	1	1	0	1	1	10
R_8	1	1	1	1	0	1	1	1	1	1	0	1	1	11
R_9	1	1	1	1	1	1	1	1	1	1	1	1	1	13
R_{10}	1	1	1	1	1	1	1	1	1	1	1	1	1	13

Problems identified in runs:

R_1: Unrealistically deep erosion from the beginning and model instability.

R_2: Highly diffusive topography; TBI at steady equilibrium state significantly low; alpha parameter of channel shape, at steady equilibrium state, below one, which is typical for single thread rivers (cf. Redolfi et al., 2016); ABI at steady equilibrium state below 2 (natural prototype Feshie has ABI above 2); domination of bar erosion over channel erosion not guaranteed, which is instead typical in nature prototype Feshie at high flow periods.

R_3, R_4: Do not attain steady equilibrium state of wetted width, mean depth, active width, and turnover rate; ABI at steady equilibrium state below 2; Channel erosion dominates bar erosion.

R_5: Do not attain steady equilibrium state of bar height, mean water depth, active width, and turnover rate; ABI around 1; both erosion and deposition onto channel.

R_6: Mean velocity does not attain steady equilibrium state; ABI below 2; Channel erosion dominates bar erosion.

R_7: TBI at steady equilibrium state significantly low; alpha parameter of channel shape below 1; ABI below 2.

R_8: alpha parameter of channel shape below 1 at steady equilibrium state; ABI below 2.

Given the close similarity of model performance for simulations R_9 and R_{10}, there is little to choose between these two parameters sets, which ultimately rests on the value of the lateral slope parameter. Arbitrarily, therefore, the following analysis of model behaviour which focuses on understanding how channel morphology controls (and indeed responds), to changes in discharge beyond the steady 70 m^3/s scenario used

to model bed evolution, is based solely on the morphology generated by simulation R_9.

4.5.3 At-a-Station Stage Variability Based on the Best Run

As alluded above, this next analysis of model behaviour examines how the predicted topography generated by simulation R_9 is both the control and response to a range of discharges beyond the formative 70 m^3/s used to generate the morphology dynamically. Essentially, this provides an opportunity to examine how the predicted reach topography partitions discharge into width, depth and discharge (at-a-station hydraulic geometry), and how sediment transport rates, active width and active braiding index would be predicted to varying discharge.

These questions are analysed through the generation of fixed-bed hydrodynamic simulations using BASEMENT, in which the flow resistance parameter are kept constant, and the boundary topography is set to the 96 hour surface generated by R_9. These simulations were conducted to examine discharge and sediment flux relationships vary across a wide range of discharges, from 5 - 85 m^3/s at an interval of 5 m^3/s (see Chapter 3 for details). For each discharge influx conditions, the spatial distribution of flows was characterised in terms of the average channel width/depth/velocity (i.e., the at-a-station hydraulic geomorphology) while the predicted average rate of sediment transport was also calculated using the process described above in using section 4.4.4. For comparison, similar calculations were undertaken for the natural prototype (see chapter 3), using the DEM from 2005 to provide the topographic boundary condition.

a) Hydraulics

The cross-sectional mean wetted width, depth and velocity at all the simulated discharges (5-85 m^3/s) were determined for both the synthetic R_9 and natural prototype topography. This enabled the construction of reach-averaged hydraulic

geometry relationships (e.g., Mosley, 1983; Smith et al., 1996; Ashmore and Sauks, 2006; Bertoldi et al., 2009b; Welber et al., 2012; Ashmore, 2013) for the modelled topographies, that quantify how increases in discharge are accommodated in terms of changes in width, depth and velocity (see Figure 4.21).

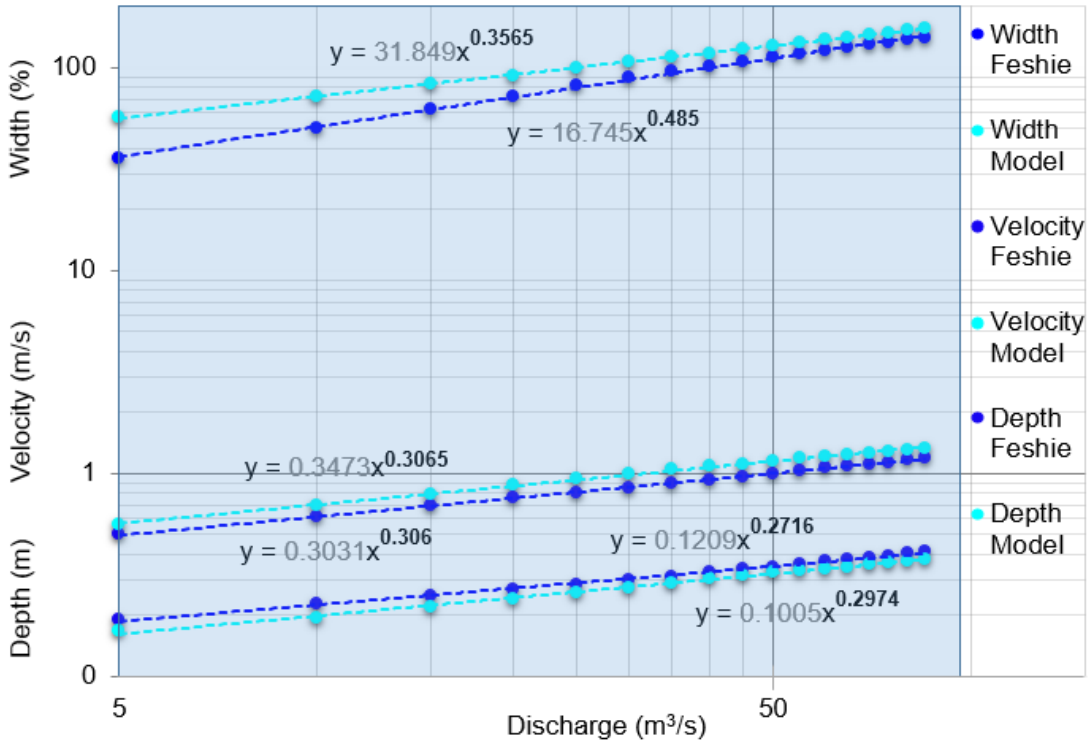

Figure 4.21 Hydraulic geometry relationship derived from fixed-bed hydrodynamic simulations. The legend Feshie and model stands for the case of synthetic braided river and Run R_9.

The resulting curves were fitted to standard power functions to quantify the hydraulic response to increasing discharge for both the modelled and prototype topographic models. The resulting hydraulic geometry relationships are shown below in Figure 4.21. The exponents of the fitted power laws for width, depth and velocity describe the role each geometric parameter plays in accommodating the increase in discharge (here assuming the bed is fixed). Typical observations for single thread rivers (i.e., Leopold and Maddock, 1953), suggests exponents in the order of 0.26, 0.4 and 0.34 for width, depth and velocity respectively, implying that increases in discharge are principally accommodated by increases in depth then velocity then width. By contrast, the very few hydraulic geometry relationships derived for braided rivers suggest the

dominance of the width exponent, which is found to range between 0.4-0.7 (e.g., Mosley, 1983; Smith et al., 1996; Bertoldi et al., 2009b; Welber et al., 2012; Ashmore, 2013) and may occasionally even exceed unity (e.g., Ashmore and Sauks, 2006). In this analysis, the width exponent for the Feshie is found to be of the order of 0.48, consistent with weakly braided rivers. By contrast, the width exponent of the synthetic braided river generated by simulation R_9 is somewhat lower at 0.36. Nevertheless, the synthetic braided river generated by simulation R_9 shows the classical behaviour of braided rivers i.e., faster increase in width as compared to depth and velocity (Mosley, 1983; Smith et al., 1996).

b) Sediment Transport and Morphodynamics

The rating relationship for discharge and bed material transport were extracted for the final topography generated by R_9 and the prototype, covering the range 5-85 m^3/s, using the approach to estimating sediment flux described above in Section 4.4.4. The resulting rating curves are plotted in Figure 4.22a, which also shows the change in the Active Width and Active Braiding Index (ABI) with respect to discharge.

The increase in bed material flux with discharge is follows a similar form for the modelled topography as the natural DEM but indicates a lower flux at comparable discharges. This reflects the observations reported in Section 4.4.4., and in particular the wider, shallower flows characterizing the more diffuse modelled topography, than the more channelled anabranches observed in the prototype. However, the exponents of the rating curves are more or less similar, at 2.03 and 1.85 respectively.

The stage-dependent active width of the synthetic model is also revealed to be significantly lower (Figure 4.22b), particularly at low flows than the natural prototype Feshie, although the ABI-discharge relationship is in broad agreement (Figure 4.22c).

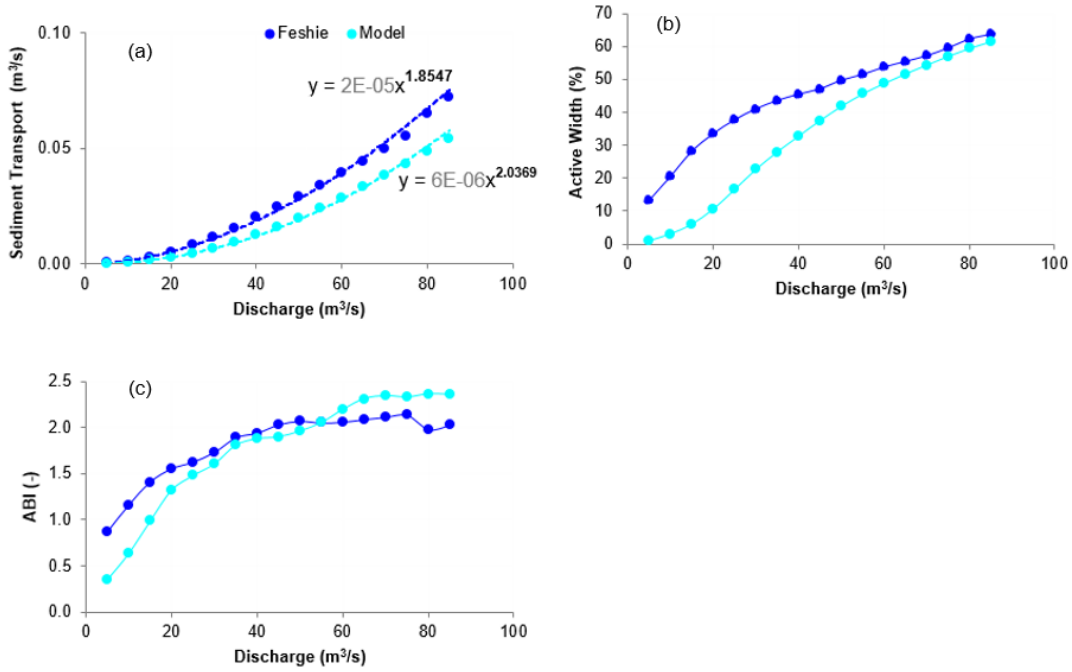

Figure 4.22 Stage-dependent morphodynamic properties (a = sediment transport, b = active width, and c = active braiding index) of the synthetic braided river generated by model and the natural prototype Feshie.

The discrepancies between the stage-dependent characteristics of the modelled and prototype topographies reflect the differences in the topographic complexity of these surfaces as indicated in Section 4.4.2. These differences should not, however, necessarily be taken simply as a predictive failure of the model (see Murray, 2013 for a review). The natural prototype incorporates a wide spectrum of characteristics that are deliberately not represented in the version of model used here. Mostly notably, this includes the effects of: (i) vegetation which increases bank stability and flow resistance, leading toward a tendency to channelize flows); (ii) mixed-grain sizes which affect the partitioning of bed shear stresses, the threshold for entrainment and flux rates, as well as the angle of repose; and (iii) unsteady discharges that may lead to a complex mosaic of sedimentary assemblages driven by different stage transport regimes. By comparison, the synthetic braided river was derived for only one formative discharge, a single grain size and in no way represented the feedback between flow, sediment and vegetation.

Nonetheless, it is important to note that there are less obvious but nonetheless significant simplifications in the model representation. For example, there is no attempt to account for secondary, helical flow structures that are important in driving near bank shear stresses, and vertical flows at confluences, bifurcations and bends (Engelund, 1974; Wu et al., 2005). Similarly, there is no accounting for the turbulent stresses, in particular through their impact of lift that has been demonstrated to play an important role in initiating gravel transport (see Roušar et al., 2016 for a review).

4.6 Discussion

4.6.1 Defining an Equilibrium State

In this study, the equilibrium state is taken to refer the condition in which a key characteristic response variable exhibits fluctuations about a stationary average (cf. Schumm, 1988; Bertoldi et al., 2009b). Such behaviour has been well-established in for laboratory models of braiding under constant flow and sediment supply (see Bertoldi et al., 2009b). Given the computational overheads involved in numerical morphodynamic modelling, it has been relatively rare for simulation studies to examine whether such a state can be achieved by simulation. Indeed, previous experience with long-term morphodynamic simulations has highlighted the difficulty of achieving dynamic steady-state conditions, due to the tendency for incision over lateral channel migration. This is manifested in an increase in bar height through time as illustrated in the recent work by Schuurman et al. (2013) and Singh et al. (2017). Ultimately this pattern leads to a disconnection between the wetted channel network and the bars, reducing the potential for key mechanisms of channel division such as chute cut-offs and avulsions (Ashmore, 1982, 1987, 1988; Jerolmack and Mohrig, 2007; Bertoldi et al., 2009b; Wheaton et al., 2013), leading ultimately to channel metamorphosis and a switch to a meandering planform.

Despite this track-record, the results of the experiments with BASEMENT appear to suggest that particular model parameterisations are able to maintain a braided channel form in a dynamical equilibrium state. Unlike previous studies (e.g., Murray and Paola, 1994, 1997; Sapozhnikov et al., 1998; Enggrob and Tjerry, 1999; Doeschl-Wilson and Ashmore, 2005; Jang and Shimizu, 2005; Doeschl et al., 2009; Nicholas, 2013; Schuurman et al., 2013; Sun et al., 2015; Singh et al., 2017), this interpretation is based on a thorough analysis of the 2D and 3D form, the hydrodynamic processes and the pattern and dynamics of channel adjustment.

The key factors necessary to achieve this equilibrium state appear to be the use of the geotechnical approach to modelling bank erosion and a low weighting of the gravitational effect on the direction of bed material transport. The former condition enables the parameterisation of variable angles of repose for banks, with low critical angles set for failed and wet material and a higher threshold for dry banks. This approach enables lateral bank erosion at relative shallow bankside depths, which leads to lateral channel migration, while the higher threshold for dry material maintains the gradient of the bank thus encouraging channelization of the flow as opposed to undue diffusion of the topography. The low lateral slope factor acts in a similar manner, reducing the tendency for gravitationally-driven infilling of topographic lows in the bed, which otherwise lead to flattening of the topography and unrealistically wide, shallow flows that become incompetent.

4.6.2 Simulation of Braiding Processes and Morphology

Simulations incorporating both lateral transport and geotechnical approach of modelling bank erosion processes, i.e., runs R_9 and R_{10} appear to reflect the behaviour of the prototype system relatively well. In the emergent equilibrium state (after 40-60 hours), the synthetic braided channel exhibits two principle bifurcating channels that continue to evolve dynamically as observed flume experiments (e.g., Ashmore, 1991; Bertoldi et al., 2009b). This evolution involves frequent exchange of

major flows and sediments between the two anabranches without resulting in a domination of one channel over another (e.g., Egozi and Ashmore, 2009; Tal and Paola, 2010). The suite of morphodynamic processes exhibited in these simulations also reflects the key processes identified by Wheaton et al. (2013) in their empirical analysis of the Feshie's pattern of adjustment between 2003-2007. This incorporates bar edge trimming that provides a key source of local sediment supply that in turn encourages within-channel deposition and local reductions in channel capacity that drive channel widening and division (Jerolmack and Mohrig, 2007).

At steady-state, the Total Braiding Index (TBI) and Active Braiding Index (ABI) fluctuate between 3.0-3.3 and 2.0-2.3, respectively. While the latter index closely corresponds to that derived for the Feshie (2.3) at the same discharge (70 m^3/s), the TBI is significantly lower as compared to the prototype Feshie (5.1) resulting the ratio ABI/TBI ≈ 0.7 against the prototype 0.4. It is difficult to isolate the cause of the lower TBI (higher ABI/TBI ratio), but it is notable that the numerical simulations were associated with increased wetted width, indicating the presence of a smaller number of dissected channels than observed in the prototype. Again, this is most likely related to the diffusive nature of the numerical simulations that lack the effects of vegetation and multiple grain sizes in stabilising bar surfaces and channelizing flows.

The predicted bar height at the steady-state is significantly low as compared to the natural prototype. The secondary flow model is very important in depth-averaged morphodynamic models to represent the strong 3D processes of bends and confluences (Lesser et al., 2004; Nicholas, 2013; Nelson et al., 2016). The famous Delft3D based numerical experiments of Schuurman et al. (2013) simulating sand bed rivers have suggested that secondary flow model helps to determine deeper channels. Sediment entrainment, transport and deposition in gravel-bed rivers are strongly associated with the multi-grain size sediment (Powell, 1998). The Delft3D based numerical experiments of Singh et al. (2017) simulating gravel-bed braided river have

observed lower bar height in the case of uniform sediment as compared to the runs with multi-grain size sediment. As the numerical experiments conducted here are without the secondary flow model and multigrain sediment, it seems therefore likely that secondary flow model and multi-grain size sediment share some part of discrepancies observed in bar height.

Moreover, natural topography is determined by historically varying discharge and related sediment transport mechanism. For example, low magnitude discharges may determine shallow channels as it is not able to produce deeper eroded channel due to its weaker force of water. By contrast, high magnitude discharge may determine deeper eroded channels due to its stronger force of water (see Ashmore and Sauks, 2006). Vegetation may have also some role in determining deeper channels as it restrain lateral mobility and forces water into fewer channel producing higher topographic relief (Tal and Paola, 2010). However, all the simulations conducted here are under constant formative discharge condition without accounting vegetation.

4.6.3 Sensitiveness of Bank Erosion and Lateral Transport Model

The constrained sensitivity analysis described in this Chapter has provided a clear indication of the importance of the bank erosion and lateral slope parameters. As discussed above, these play a critical role in tuning the adjustment of the bed topography, and act to pivot the model response between overly diffusive behaviour (associated with low angles of repose and high lateral slope parameter values) and inhibited bank erosion (which leads to channel incision and a transition to meandering). The geotechnical model used in BASEMENT appears to provide a subtle tool to control this sensitive break-point, enabling lateral migration to continue do to the low repose angles for wet and failed material, yet maintaining bank gradients through the high critical angle for dry sediments. Ultimately, it should be recognized that identification of the effective parameters used to calibrate this response will also be a function of the spatial resolution of the model. This fixed distance determines the

local gradients that can be modelled in the near bank zone and thus we should expect a trade-off between higher effective parameters as the resolution is increased (i.e., for smaller grid sizes) and vice versa.

The lateral transport factor also serves to control the degree of bed diffusion, acting to smooth out gradients by transporting material downslope. Reductions in the lateral transport factor from 3.0 to 2.0 and 1.5 serve to reduce this effect and therefore maintain the presence of important bed waves, such as scour holes and avalanche faces that are critical features of a braided network. However, this study suggested that lateral transport alone without the use of proper bank erosion model is not sufficient to facilitate continuous evolution of braided river.

4.6.4 Evaluation of the Metrics of Model Behaviour

This study has employed a comprehensive suite of analyses to interrogate model behaviour quantitatively. This incorporates 2D planform measures such as the total braiding index, measures of 3D morphology such as bar height, channel shape informing indicator (alpha) and dynamic process characteristics such as active width, active braiding index and the pattern of erosion and deposition with respect to elevation. Individually, it is clear that some of these metrics lack effectively discriminatory power. For example, the frequency distribution of bed elevations alone, or the total braiding index fail to distinguish between simulations, despite evident qualitative differences, for example between R_5 (which evolves into a single thread channel) and R_{10} (actively braided). Given the sensitivity of diffusive adjustment of the bed, the 3D metrics, in particular the distribution of slopes (above and below mean bed level) and the channel shape exponent are much more power indicators of model performance.

However, perhaps more important still, is the need to interrogate the direct pattern of morphodynamic adjustment, neatly encapsulated by the quantifying the volumetric

pattern of erosion and deposition with respect to a priori surface elevation. This approach provides a useful simple measure to identify key processes of bed adjustment, for example, distinguishing between channel scour on one hand, and bank and bar erosion on the other. This is a novel approach that has not yet been applied in related studies of numerical morphodynamics.

4.6.5 Modelling Channel Evolution over the Long-term

An important result from this set of experiments, is the demonstrable capacity to simulate a dynamic braided river that fluctuates about a stationary condition relating to steady state inputs. Many previous studies (e.g., Doeschl-Wilson and Ashmore, 2005; Doeschl et al., 2009; Schuurman et al., 2013; Ziliani et al., 2013; Singh et al., 2017) have found it difficult to calibrate such a tuned model response, and here it is postulated that this is strongly linked to the use of the geotechnical bank erosion module. While interesting in its own right, the maintenance of steady state braiding is important as it provides a reference condition against which the response to transient boundary fluxes can be measured. This provides an opportunity to study the effects of unsteady flow regimes on the pattern of braiding as well as more catastrophic changes in flood regime or sediment supply.

4.7 Conclusions

This study provides a comprehensive analysis on the performance and parameter sensitivity of BASEMENT to model the development and maintenance of braiding processes. The synthetic channels produced by the numerical model were interrogated using broad spectrum of quantitative metrics, characterizing both the morphology and processes that reflect the form-process feedbacks driving channel adjustment. This approach has sought to use the high-quality datasets available for the prototype system, but it should be recognized that these comparisons will always be partial. The natural system incorporates processes and a complexity in terms of its

boundary conditions that cannot and were never deliberately modelled. It is difficult to determine, therefore whether key differences between the predictions and prototype such as in the distribution of gradients and channelization, are factors relating to unmodelled characteristics (e.g., vegetation and grain mixtures) or indeed are phenomena linked to the complex history of multistage flows and variable sediment supply that occur in the prototype. Nonetheless, while the model clearly involves significant simplifications, it is encouraging that the pattern of parameter sensitivity observed is logically coherent and reflected in the evolving morphology and processes predicted.

There remains also, of course, considerable scope to develop the simple experimental design used here. Key factors such as the grid resolution are likely to compensate the changes in the model parameterisation and this remains a key area for future research. Nonetheless, building on these experiments there are a number of key conclusions that can be drawn:

1. The physics based numerical model can be calibrated to develop and maintain a dynamic pattern of braiding, fluctuating about a stationary equilibrium state, driven by under steady discharge and sediment supply.
2. The emergent channel form is sensitive to the parameterisation of bank repose angles and lateral slope transport which controls the diffusivity of the bed topography.
3. The geotechnical approach to modelling bank erosion provides an effective solution to maintaining lateral channel mobility without the loss of steep local gradients that are critical to channelize flows.
4. The channel count index (a planform metric), local slope distribution (topographic metric) and most importantly, the volumes of erosion and deposition with respect to the prior surface elevation (a morphodynamic metric) were found to be most powerful measures of model response to

quantify model sensitivity and compare model behaviour to the observed prototype.

5. The multi-criterion approach to model evaluation described here, encompassing 2D and 3D metrics of channel form as well as hydrodynamic and morphodynamic processes, is vital to provide a full understanding of model behaviour.

Chapter 5: Modelling the Development and Maintenance of Braiding under Unsteady Flow Regimes

Chapter Summary

This chapter addresses the research question 3 which is: ***How do the equilibrium model forms and forces derived at a steady flow condition differ from energetically-normalised different steady and unsteady simulations that incorporate variations in the frequency and magnitude of competent floods?***

The simulations designed in Chapter 4 sought to examine the development and maintenance of braiding under conditions of steady discharge and sediment supply. This Chapter seeks to extend this analysis to examine the effects of hydrograph form on channel adjustment, specifically seeking to examine whether the range and duration of flow stages impacts significantly on the emergent channel morphology of unvegetated braided rivers. The modelling involves the design of energetically normalised boundary flows that are then used to drive the development of bed topography, taking the equilibrium channel form derived from Chapter 4 as the initial condition. Simulations are compared by interrogating the planform, topography, hydraulic and morphodynamic characteristics of the synthetic channels, using the methodology developed in Chapter 3. First, it will present some trend differences between morphodynamic evolution under steady and unsteady flow condition and different magnitude of discharge. Second, it provides some insights into morphodynamic processes during the unsteady flow condition. The steady flood determined net degradational sediment budget, while the unsteady counterpart was found to be net aggradational. This divergent behaviour reflects scour dominating during rising stages and deposition occurring during falling stages. Low magnitude flood determined shallower and complex network of channel, while high magnitude flood determined deeper anabranches.

5.1 Introduction

While early discussions of the controls on braiding widely considered flow variability, specifically flashiness, to be an requisite to maintain braided morphologies (Doeglas, 1962; Miall, 1977), more recent laboratory simulations (e.g., Ashmore, 1991; Bertoldi et al., 2009b; Redolfi et al., 2016a) have shown that this is not the case (see Ashmore, 2013 for a discussion). The simulations undertaken in Chapter 4 under steady flow, have also now demonstrated that dynamically evolving, equilibrium braided networks can be simulated using a numerical morphodynamic model.

As such, it seems, at least superficially, reasonable to reject the hypothesis that braiding is dependent on an unsteady discharge regime. However, what is far less clear, is whether there exist subtle differences in the character of braided morphologies and the suite of processes that generate them, in response to differences in their boundary flow regimes. In part, this uncertainty reflects the inevitable difficulty of addressing this question empirically. Natural river systems incorporate a latent legacy of historical adjustment to changing flow regimes and sediment supply rates, so that river forms can rarely be assumed to be in equilibrium with current conditions (Lane and Richards, 1997). As such, it is nigh impossible to unambiguously relate specific channel morphologies to their boundary conditions or, by implication, the trajectory of channel change to a unique, universal pattern of adjustment.

For this very reason, experimental modelling provides an ideal vehicle to examine how a synthetic representation of the real world responds, when subject to known adjustments in forcing controls while the system remains fully closed. Traditionally, this has only been possible using laboratory modelling and thus, at least partially, confounded by the difficulties of scaling key system characteristics such as grain-size and coherent flow structures. Even setting aside scaling problems, laboratory

modelling is both slow and costly to implement and maintain, and it remains comparatively difficult to observe the full range of system variables (see Chapter 1).

There is therefore, considerable scope to use numerical simulation models as an alternative research vehicle to examine such behaviour. By comparison with laboratory experiments, simulation models are fully transparent, relatively quick to run and while again they abstract the fundamental complexity of the natural system, they do not suffer directly from scaling problems (see Chapter 1). Moreover, there is an urgent need to understand how rivers respond to environmental changes, with increasing pressure on river systems from direct (e.g. through river regulation) and indirect (land-use and climate change) anthropogenic controls, as well as natural climatic variability.

There are comparatively few studies that have addressed the influence of unsteady flows on braiding processes directly. A notable exception is the seminal work of Mosley (1983) who examined the response of the braided Ohau River, NZ, to a range of controlled dam releases. Mosley (1983) sought to quantify the relationship between discharge and the key hydraulic variables including width, depth and velocity, in terms of the resulting hydraulic geometry relationships. As discussed in Chapter 3 and 4, as discharge increased, he observed that this was accommodated principally by increases in wetted width at a faster rate as compared to deepening and increasing velocity; contrasting strongly with the characteristics of single thread rivers (Leopold and Maddock, 1953). Laboratory and field-based experimentations have also demonstrated similar responses to varying discharge (e.g., Smith et al., 1996; Ashmore and Sauks, 2006; Bertoldi et al., 2009b; Welber et al., 2012; Ashmore, 2013). Taken together, this research suggests a typical range for width exponent of between 0.4 - 0.7, though it has been observed to exceed unity, implying that increases in discharge may actually be accompanied by decreases in average depth and/or velocity (e.g., Ashmore and Sauks, 2006).

The variability in width exponent reflects different environmental settings, broadly linked to intensity of braiding (e.g., Smith et al., 1996). However, Ashmore and Sauks (2006) suggested that the characteristic behaviour is also likely to be associated to the dominant discharge that drives river adjustment. They argue that rivers evolving within a range of low magnitude discharges (for example, responding to high frequency pro-glacial meltwater events) typically exhibit a shallow network of channels and that in this situation, bar overtopping begins with only small increases in discharge leading to a high rate of change of wetted width. By contrast, rivers that experience frequent high magnitude discharge events, are likely dominated by fewer, deeper eroded channels, and consequently a slower rate of increase of width with discharge.

Taking this hypothesis further, Egozi and Ashmore (2009) studied response of discharge variability on planform network development in an experimental braided river. They found systematic increases in the ratio of active and total braiding intensity, varying between 0.4–0.7 with step-wise increases in discharge. Again, through flume experiments, Visconti et al. (2010), examined the response of a pseudomendering channel under unsteady discharge condition, and found that low flows facilitate bar-head and thalweg erosion which increase channel capacity and thereby help to convey high flows within bank.

Takebayashi and Okabe (2009), using a two-dimensional numerical model, explored effects of steady and unsteady floods from the respect of bar and channel planform evolution of braided rivers. In their experiments, in comparison to channels networks generated under steady flow, those derived during repeated cyclical hydrographs of the same magnitude gave rise to bars of shorter wavelength. Their analysis suggested that this was due to sedimentation in small dissected channels that existed on elevated surfaces (bars) during flood peaks and the removal of riffles during low flows that caused flow to concentrate into fewer, lower stage channels during the next flood.

Noticeably, their study suggested that including the effects of vegetation under unsteady flows accelerated these processes, contributing to a further reduction of the wavelength and number of active channels.

In terms of the broad pattern of morphological response to variations in flow, three characteristic modes of channel adjustment have been recognized from field observations (Surian et al., 2009a; Bertoldi et al., 2010; Ashmore, 2013):

a) during low-magnitude formative floods, when discharge is limited to only a few anabranches, erosion and deposition are concentrated within the channel thalweg, outer-bank bends and confluences, leaving the elevated bar surfaces undisturbed;
b) during intermediate-magnitude floods, when braiding intensity peaks, many channels and bars are partially submerged and there is frequent exchange of sediment between channel bifurcations and rapid rates of lateral bank erosion.
c) At very high formative discharges, the entire braidplain may become inundated, resulting in a transient loss of apparent braiding intensity. Such conditions are associated with major reorganization of channel bifurcations, with chute cut-offs leading to frequent avulsions creating both local and far-field effects on the network structure.

Formalizing this conceptual understanding of the role of discharge on the morphodynamics of braiding is complicated by the difficulty of observing rivers in flood, so that our empirical insights are inevitably gleamed by examining channel structure before and after events, but rarely during. Moreover, scaling physical models, to account fully for the effects of variable discharge is complicated by the difficulty of representing sediment mixtures and the need to establish and maintain relationships between discharge and sediment influx. As such, there is an urgent need to evaluate alternative methods to understand these interactions and the emergent morphological responses under varying flow condition.

5.2 Aim and Objectives

The overall aim of this Chapter is to develop a step forward insight in the quantitative understanding of the response of braiding processes and forms that develop in bare sediments (unvegetated) when subject to variations in discharge magnitude, and specifically to compare braiding simulations in steady and unsteady flow regimes. This will be achieved through the lens of the numerical model BASEMENT, which has been calibrated in Chapter 4. The main objectives of the research to address this broad goal are to:

a) define a set of hypothetical boundary conditions that span a range of discharge magnitudes and durations but are normalized in terms of their total energy expenditure to afford effective comparison;
b) develop a set of simulations employing both these unsteady and reference steady hydrographs for analysis;
c) analyse model responses in terms of the planform, topography, hydraulic and morphodynamic evolution of synthetic channels; and
d) explore how the emergent channel forms respond to variations in discharge using fixed-bed hydrodynamic simulations to predict the reach-averaged hydraulic geometry and sediment transport relationships.

The remainder of the Chapter is as follows: the first section outlines the detailed experimental methodology; this is followed by a description of the key results; followed in turn by the analysis of the results. A critical discussion of the findings then places the experiment in its scientific context, before finally a set of conclusions is drawn.

5.3 Methods

Following the successful application documented in Chapter 4, this study again uses the freely available, two-dimensional morphodynamic model, BASEMENT (Vetsch et

al., 2017a). The braided reach of the river Feshie was once again used to provide the reference prototype to schematize the experiments and provide an empirical comparison. While it would be possible to use the observed topography of the natural prototype as the topographic boundary condition, there are dangers in doing so. First, this topography is represented by an empirical survey and hence incorporates data errors that may propagate into future analysis. Secondly, and more profoundly, the empirical topography reflects a set of conditions that are not represented in the version of BASEMENT used here, in particular the presence of vegetation and mixed grain sizes, as well as the effects of fully 3D flow mechanics. As such, a model configured with these initial conditions is likely to undergo a transient period of subsequent adjustment of the bed topography, slowing down the analysis and confounding a simple interpretation of the mechanics.

All simulations were therefore initialised using the numerically generated topography developed at the end of simulation Run R_9 once the channel had achieved equilibrium conditions after 96 hours (or 12 'years') of adjustment (see Figure 5.1). This self-formed braided channel is based on a steady discharge condition (70 m^3/s) representing the typical 2-year recurrence interval flood and a single grain size sediment with D_{50} = 30 mm, to match the natural prototype.

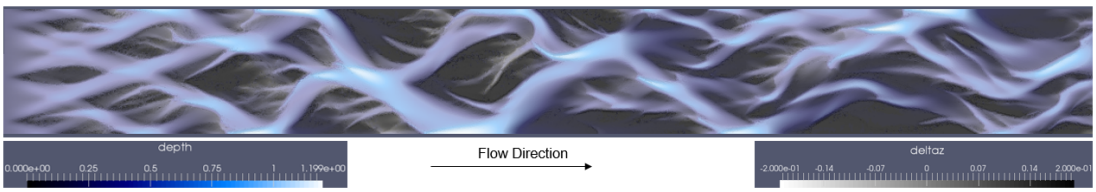

Figure 5.1 Initial topography for all simulations in this Chapter (produced by Run R_9 in Chapter 4). This equilibrium topography was generated by the numerical model itself adopting reach averaged width (175 m), longitudinal slope (0.92 %), single grain size sediment (D_{50} = 30 mm) and constant discharge (two years return period flood = 70 m^3/s), which are representative of the natural prototype Feshie.

All numerical variables and boundary condition used by the scenario R_9 in Chapter 4 were fixed except the form of discharge hydrographs. The discharge boundary

conditions were based, instead, on a set of energetically normalised hydrographs that vary in terms of their peak flow magnitude and duration, but represent same total energy expenditure, measured in terms of the integration of $Q^{1.9}$ as discussed in Chapter 4 (see Section 4.3.6 b). This approach ensures that the same total potential energy is used to drive channel adjustment in each scenario, but that the time distribution and concentration of energy varies.

The use of the discharge exponent, set to 1.9, reflects the non-linear variation of bed material flux with discharge found for the Feshie using fixed-bed hydrodynamic simulations and sediment transport calculations using the real topography (see Chapter 2). This value lies within the range found in allied laboratory experiments that quantify the discharge-sediment flux rating relationship for braided rivers (varying between 1.5 - 2.8, see (cf. Ashmore, 1988; Garcia Lugo et al., 2015).

An experimental design, incorporating three steady and four unsteady hydrographs was used to examine the effect the hydrological regime on channel evolution (Figure 5.2). These incorporated peak discharges varying between 30-110 m^3/s as shown in Figure 5.2. Each of these boundary timeseries represented the equivalent of five years of flows, in the form of either cyclical, triangular 'annual' hydrographs or as a constant discharge. The duration of each timeseries was temporally-scaled to the equivalent total energy expenditure, giving rise to a wide range of total simulation times/hydrograph durations as shown in Figure 5.2. For example, the equivalent one year of steady flows at 110 m^3/s comprised a total simulation time of just 3.3 hours, versus 7.83 hours for a steady flow of 70 m^3/s and 14.85 hours for a steady flow of 50 m^3/s. For each simulated unsteady run, the normalised energy under each flood was maintained same as these steady runs. This way, the total normalised energy under simulated five flood remains same for all runs.

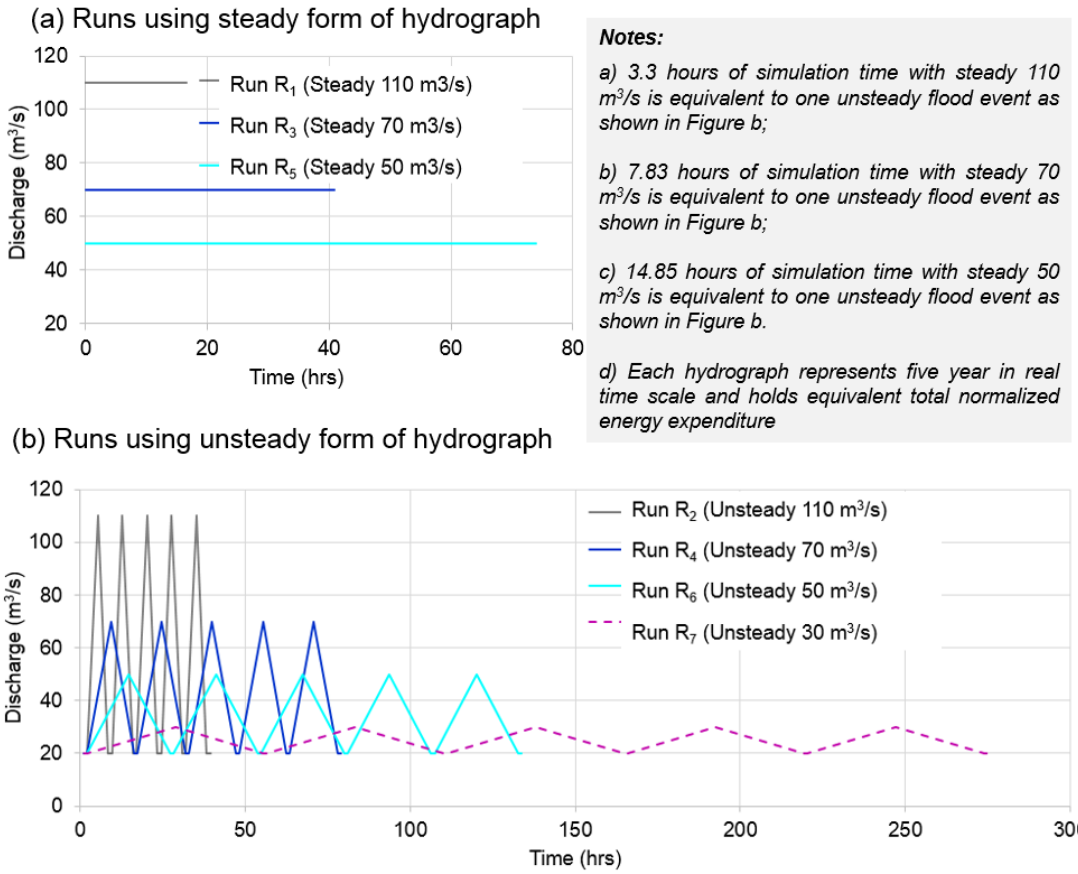

Notes:

a) 3.3 hours of simulation time with steady 110 m^3/s is equivalent to one unsteady flood event as shown in Figure b;

b) 7.83 hours of simulation time with steady 70 m^3/s is equivalent to one unsteady flood event as shown in Figure b;

c) 14.85 hours of simulation time with steady 50 m^3/s is equivalent to one unsteady flood event as shown in Figure b.

d) Each hydrograph represents five year in real time scale and holds equivalent total normalized energy expenditure

Figure 5.2 Simulated seven hydrographs. (a) Runs with steady form hydrographs; (b) Runs with unsteady form hydrographs. The normalised energy under all these hydrographs when calculated as the function of $Q^{1.9}$ remains the same.

For the cyclical unsteady form hydrographs, a one-hour of a low flow of 20 m^3/s was inserted between consecutive floods to provide a transition time between events. In the natural prototype, the peak discharges used here, 30 m^3/s, 50 m^3/s, 70 m^3/s and 110 m^3/s represent return period floods with recurrence intervals of below one year, just above one year, two years and 15 years respectively (see Chapter 2). A peak discharge of 30 m^3/s represents a low formative condition at which high-elevated bars remain largely exposed and the majority of discharge is concentrated into 1-3 principal anabranches. Peak discharges of between 50 m^3/s to 70 m^3/s represent intermediate formative conditions in which bars are partially submerged and most of anabranches are flooded. A discharge of 110 m^3/s represents a low frequency, high formative condition in which the majority of the braided fairway is flooded.

In all simulations, discharge hydrographs were imposed from the upstream boundary, and a normal water depth condition was used at the downstream boundary. The sediment input and output at the boundaries were set to the sediment transport capacity of the boundary cells. All runs were simulated using the same hydrodynamic and morphodynamic time step, without the use of a Morphological Acceleration Factor (MORFAC) to accelerate the sediment transport calculation as described in Chapters 2, 3 and 4. Outputs were saved at hourly intervals, in order to provide flexibility in data analysis given the different temporal scales of the experiments (hourly, event based and total change). All other variables such as eddy viscosity, roughness, lateral transport factor, set of repose angles are set equivalent to the run R_9 in chapter 4 (see Table 4.1 for these values).

In order to gain an insight into the stage dependent hydraulic adjustment, fixed-bed hydrodynamic simulations at different discharges were also used, taking the final topography generated from each simulation as the boundary condition. As described in previous chapters (Chapter 3, 4), the sediment transport capacity was calculated by using the shear stress predicted by the fixed-bed hydrodynamic simulation. Finally, stage dependent morphodynamic properties were determined using spatial distribution of sediment transport.

Here, simulated runs were not compared directly with the natural prototype Feshie so the data analysis hereforth will be based on the domain (1200 m x 175 m) at the middle.

5.4 Results

The experimental results were analysed using the model evaluation scheme described in Chapter 3 and used in Chapter 4. This comprised metrics describing the 2D planform, 3D topography, distributed and average hydraulics and morphodynamic processes. Planform maps showing water depths/detrended elevation and total

braiding index were used to describe planform evolution. The elevation frequency distribution, bar height and channel shape were used to describe evolution in terms of topographic signatures. Spatial distribution of erosion and deposition and related volume of sediment transport and turnover area were analysed to inform morphodynamic evolution.

Stage dependent hydrodynamic and morphdynamic properties were determined using the fixed-bed hydrodynamic simulations and sediment transport calculations for a range of discharges between 5-85 m^3/s. These calculations were carried out using the final topography obtained from each simulated run. For each run, the at-a-station hydraulic geometry relationship was derived along with the stage-dependent sediment transport capacity, active width, active braiding index and dimensionless shear stress based on the spatial distribution of sediment transport obtained from the fixed-bed hydrodynamic simulations.

To summarize the results, plots have been paired to enable simple comparison of the equivalent steady and unsteady discharges. For example, run R_1 based on a steady discharge of 110 m^3/s is paired with run R_2 which was based on the equivalent triangular hydrographs with the same peak discharge, i.e., varying between 20 m^3/s - 110 m^3/s. Similarly, Runs R_3 and R_4 with a steady and peak discharge of 70 m^3/s were paired, along with R_5 and R_6 with a steady and peak discharge of 50 m^3/s. Simulation run R_7, used an unsteady hydrograph with peak discharge 30 m^3/s and unfortunately there is no steady comparator for this discharge, due to the lack of available time on HPC resources. The results of this simulation have nonetheless been presented for the sake of completeness.

These results together provide an insight into the differences in the morphological evolution of the synthetic channel under the schematised steady and unsteady driving discharges, starting from the same initial conditions. At the same time, the differences

between the paired sets illustrate the effect of flow magnitude on the morphodynamic evolution.

5.4.1 Planform Signatures

a) Spatial Pattern of Detrended Elevation and Water Depth

Planform maps for intercomparison were constructed by overlaying the predicted water depth at peak discharge over the detrended elevation in order to facilitate visual inspection of morphodynamic evolution. The results are shown in Figure 5.3-Figure 5.6 which shows the steady-unsteady pairs of simulations for the same peak discharge, extracted annually. It should be noted, of course, that the extent of inundation varies with discharge between the sets of paired simulations.

The comparison between R_1 and R_2, representing the high stage formative flow condition is shown in Figure 5.3. Here, it is worth noting that the 110 m^3/s discharge represents the 15-year flood on the Feshie, which on average, occurs for about half an hour in a given year (see the flow duration curve in Chapter 2). Clear differences in the evolution of the two planforms are immediately evident, with a rapid divergence from the same initial condition. For example, the steady flow regime shows a strongly progressive increase in bar size and channel width, evolving rapidly in the first 1-3 years. A similar trend is evident for the unsteady flow but evolving over a longer period (upto year 5) and resulting in smaller bars and narrower channels. The final result is significantly different in terms of sharing discharges between anabranches, as such the steady flow regime dominated by a single, sinuous channel, compared to a more stable pattern of flow division around multiple bars for the unsteady simulation.

The comparison between R_3 and R_4 with a peak discharge of 70 m^3/s is shown in Figure 5.4. This discharge represents the 2 years flood on the Feshie, which occurs on average for between 0.2-20 hours in a given year (see the flow duration curve in Chapter 2). Differences in the evolution of the steady and unsteady flow regimes are

less clearly evident at this lower magnitude flow, although ultimately the steady flow regime again appears to evolve by concentrated flow into a single, lower sinuosity, dominant anabranch. Channel width and bar sizes between the two simulations are, however, superficially similar.

Figure 5.5 shows the comparison between R_5 and R_6 at the lowest reference comparison discharge of 50 m^3/s. This reveals some significant differences in terms of the broad planform evolution. This is most notable in terms of the greater channel width associated with the steady flow regime, which evolves towards a regular, high sinuosity branching pattern. By contrast, the unsteady flow condition led to a narrower series of channels and a complex set of irregular barforms.

Figure 5.6 shows the single simulation, R_7, relating to the unsteady 30 m^3/s boundary condition. At this lower flow, much of the channel bed is exposed, resulting in qualitative different planform from the previous run, although this should not necessarily be taken to imply major differences in the topographic structure. The dissected minor channels located on the high elevated bars during the early stage of evolution appear to gradually dry out, with flows progressive captured by a single, and increasingly deep main channel, which is the locus of all erosional activity. Here, it is worth noting that the 30 m^3/s discharge is slightly below the one-year flood on the Feshie, occurring on average, for about 15 - 123 hours a year (see the flow duration curve in Chapter 2).

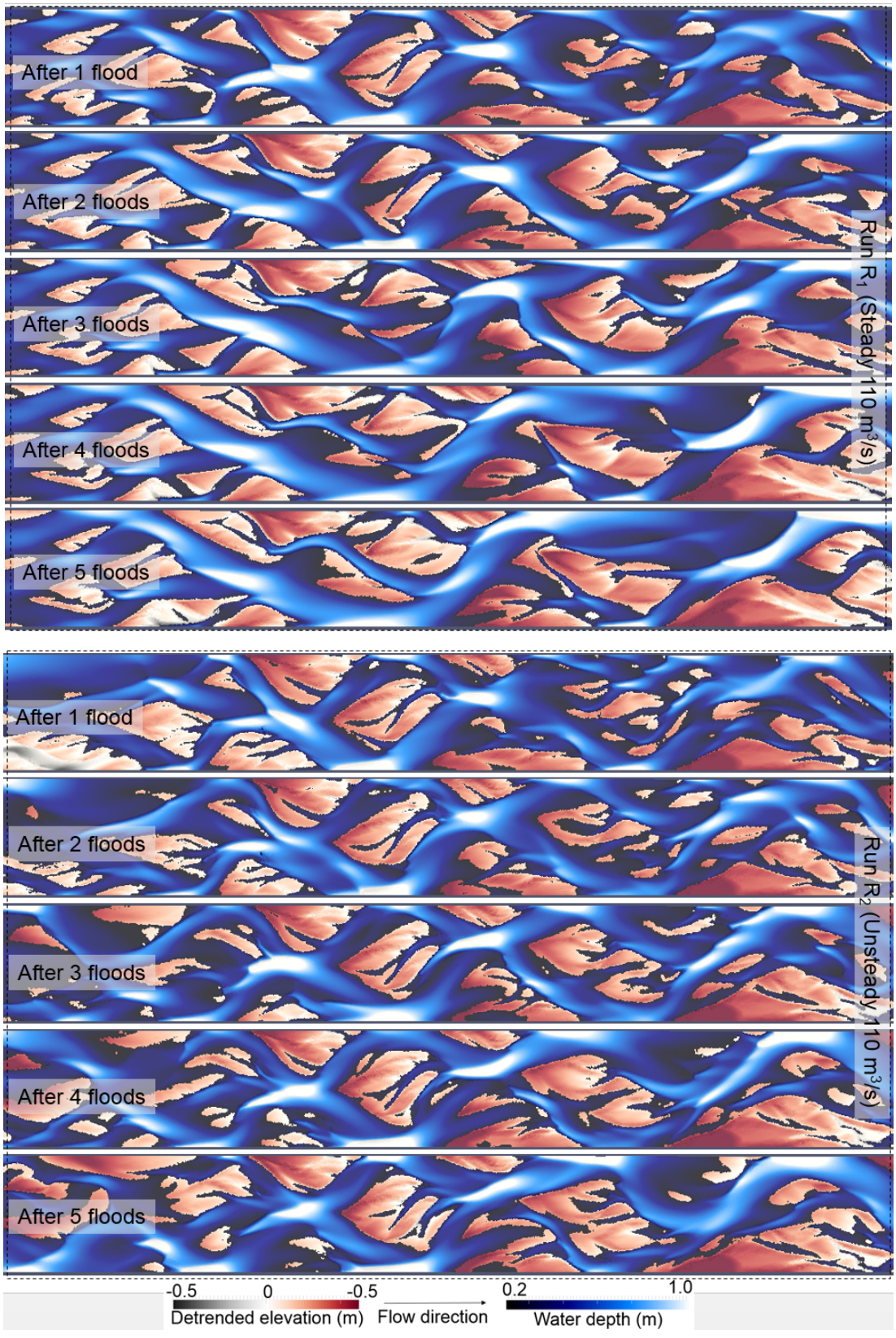

Figure 5.3 Planform dynamics (water depth and detrended elevation) obtained from Run R_1 and R_2 at discharge 110 m^3/s. These maps were prepared by considering water depth equal to and above 0.2 m for clear visualization of channels networks. Domain is 1200 m x 175 m.

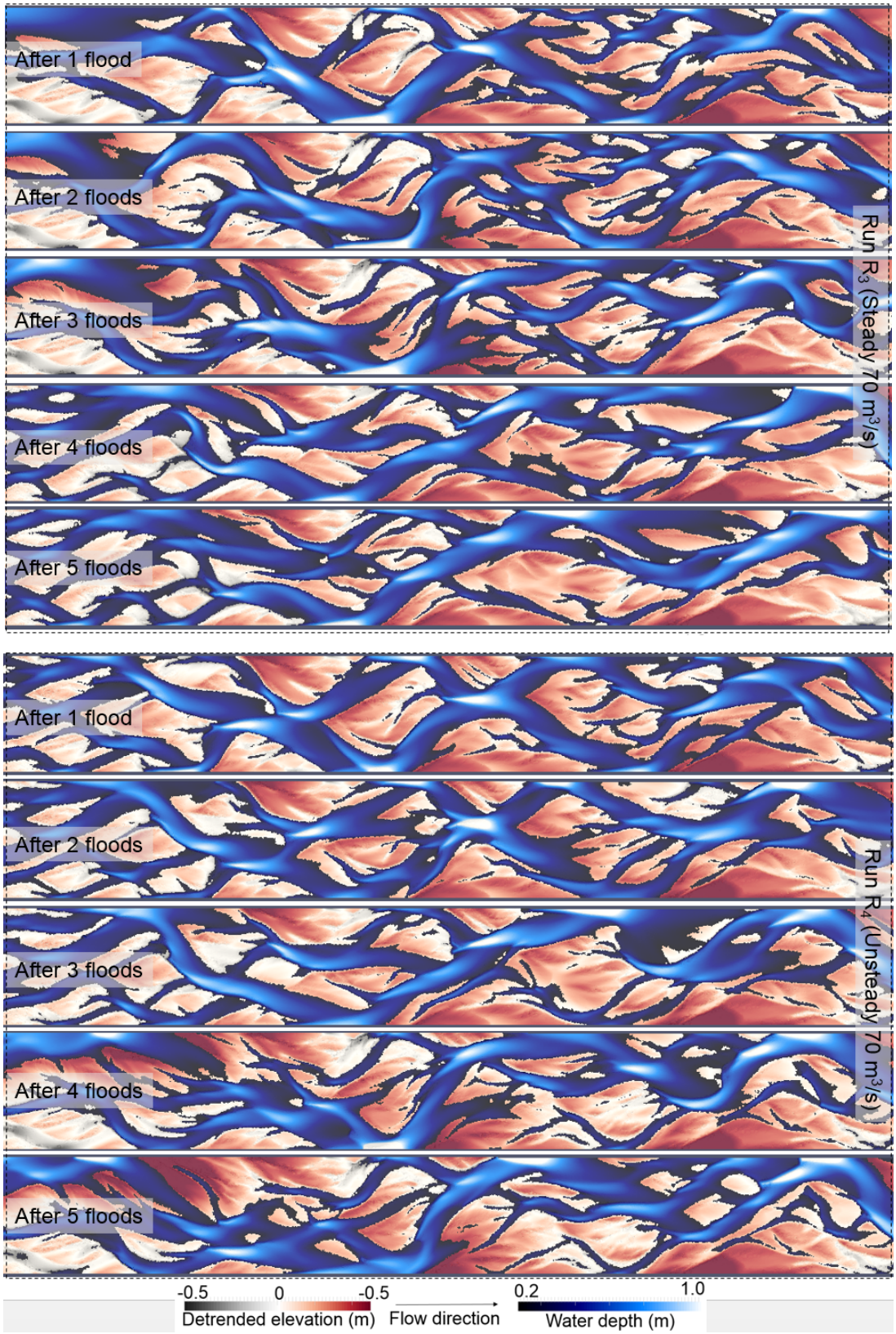

Figure 5.4 Planform dynamics (water depth and detrended elevation) obtained from Run R_3 and R_4 at discharge 70 m^3/s. These maps were prepared by considering water depth equal to and above 0.2 m for clear visualization of channels networks. Domain is 1200 m x 175 m.

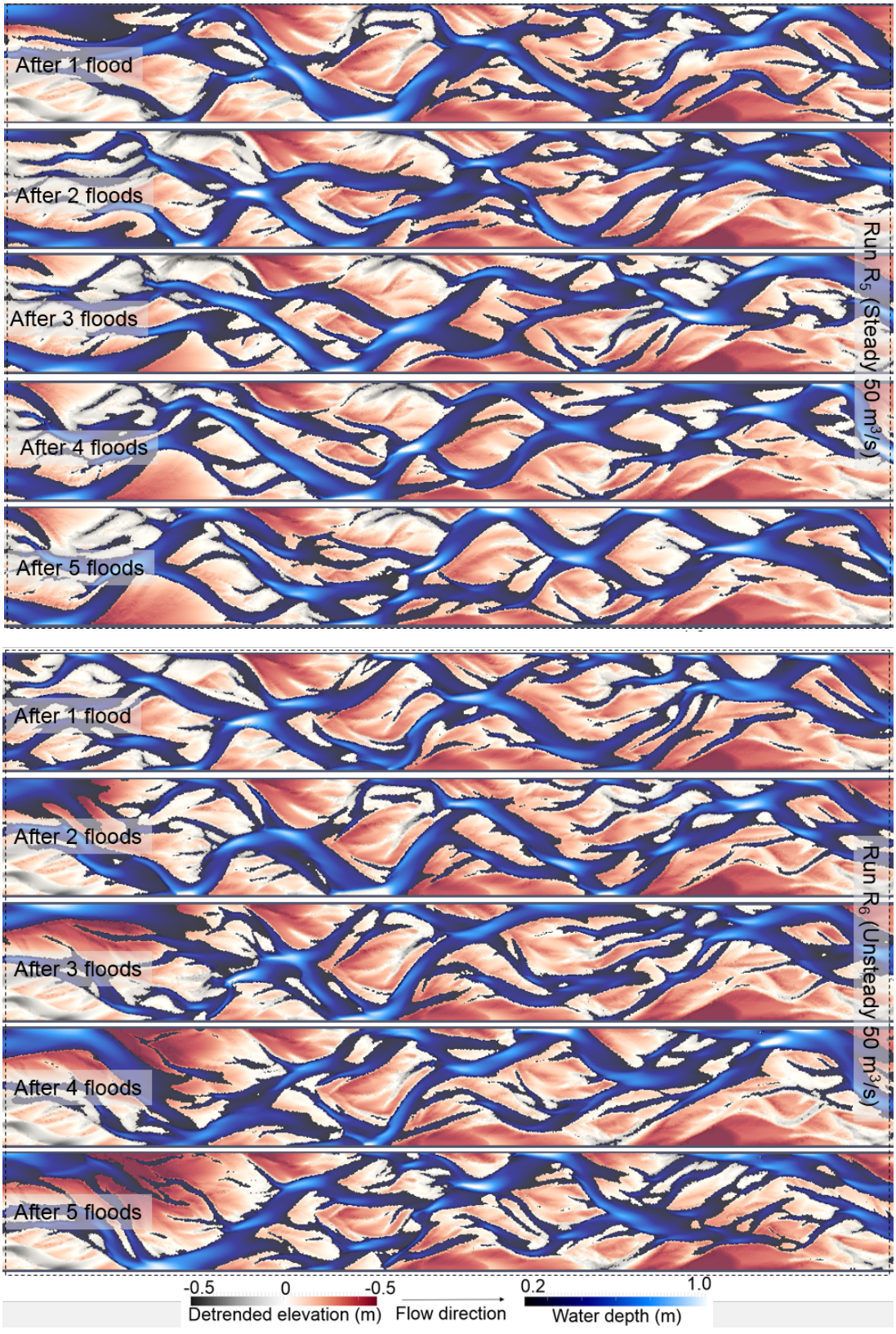

Figure 5.5 Planform dynamics (water depth and detrended elevation) obtained from Run R_5 and R_6 at discharge 50 m^3/s. These maps were prepared by considering water depth equal to and above 0.2 m for clear visualization of channels networks. Domain is 1200 m x 175 m.

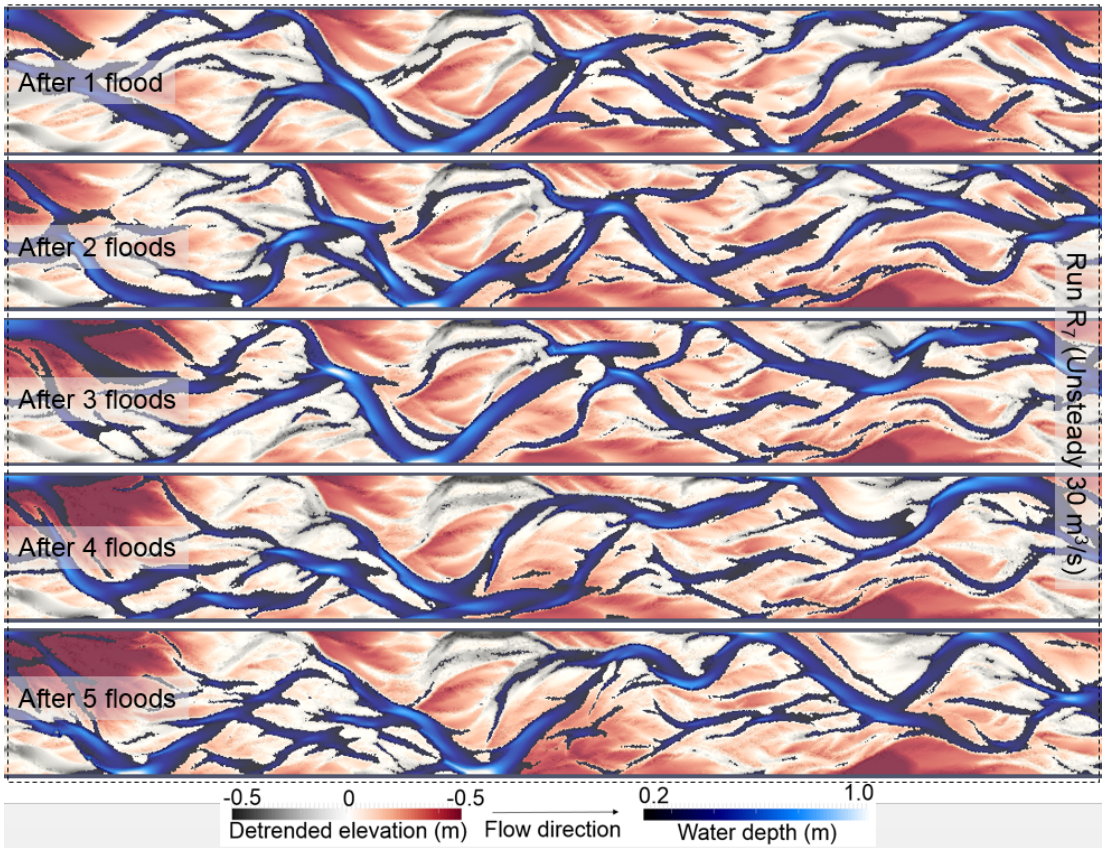

Figure 5.6 Planform dynamics (water depth and detrended elevation) obtained from Run R_7 at discharge 30 m^3/s. These maps were prepared by considering water depth equal to and above 0.2 m for clear visualization of channels networks. Domain is 1200 m x 175 m.

b) Total Braiding Index

Total Braiding Index (TBI) for each hour of each simulation was derived as per Chapter 4, by extracting cross-sections longitudinally and counting the number of channels below the mean bed level, before expressing this as a reach average (e.g., Schuurman et al., 2013; see Chapter 3 for detail). Timeseries showing the evolution of the TBI for each pair of simulations is shown in Figure 5.7 below. Some care needs to be exercised here, given the difference in the duration of the simulation, though the final condition represents the same equivalent energy expenditure.

Interestingly, despite the qualitative differences in the planforms described above, the evolution of the simulation pairs reveals little difference in the pattern of total braiding index which differs little for the steady-unsteady pairing. There is, however, an

expected difference in the TBIs associated with the driving discharges, with the highest discharge associated with the greatest pattern of inundation and hence a reduced TBI of the order of c. 2.5. This increases progressively for reductions in the boundary flow, rising to c. 3 for the 70 m^3/s discharge and up to 4.5 for the lowest 30 m^3/s scenario. There is some evidence of a trend towards progressively reduced TBIs for the two highest magnitude scenarios, 110 and 70 m^3/s, in which TBI falls from above 3 to 2.5 and from 3.5 to 3.2, respectively. The lower flows (50 and 30 m^3/s) show a stationary pattern of TBI. This difference reflects the progressive erosion that continues from the initial condition for these high flow simulations, progressively deepening the principal anabranches which in turn capture more and more of the total flow.

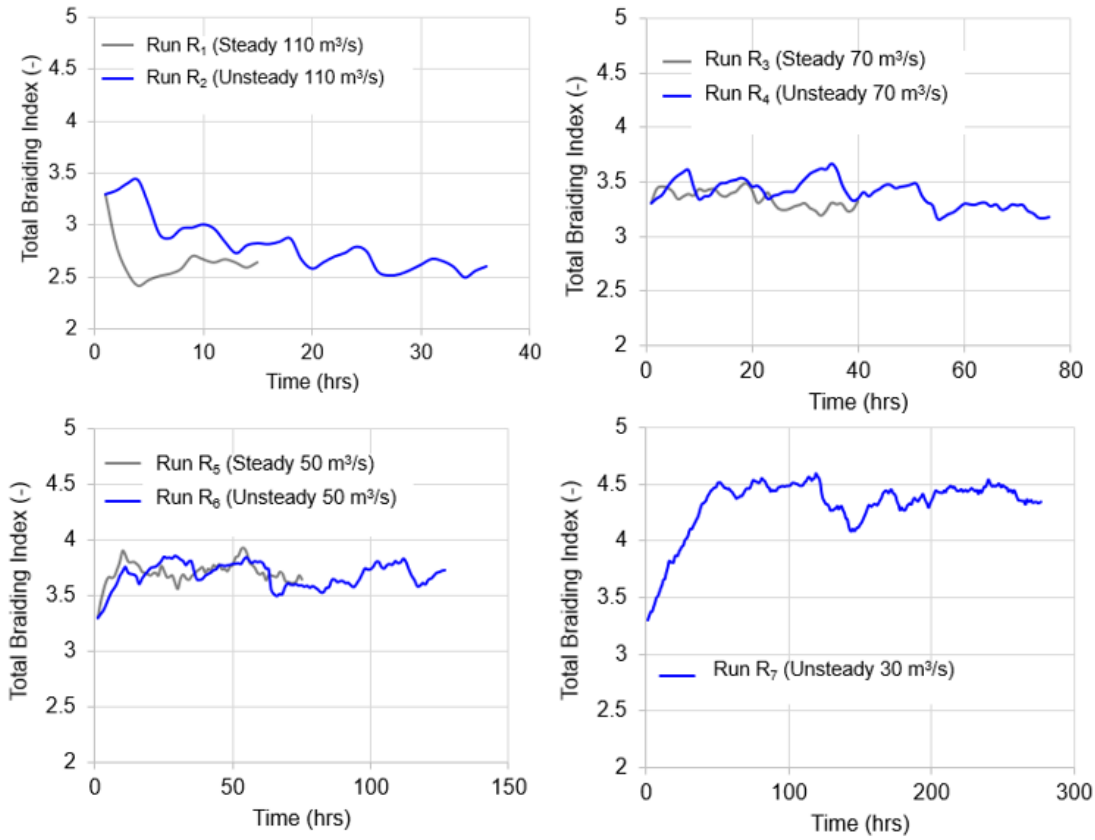

Figure 5.7 Evolution in terms of Total Braiding Index (TBI).

5.4.2 Topography Signatures

a) Elevation Distribution

The development of the 3D morphology was analysed first by comparing the trend of the 5th and 95th percentile of normalised elevation distribution, extracted for each simulation for each hour (Figure 5.8). In the Figure 5.8, the 5th percentile represents the deepest region of the topography, which, given the normalization of the surface, is likely to correspond to local scour features at confluences and outer bends. By contrast, the 95th percentile represents the high elevated areas, likely associated with older bar tops. The difference between the two is also used to provide a proxy for average bar height.

In terms of 5th percentile, the steady discharge simulations typically led to an increase in the depth relative to the unsteady simulations (i.e. an increase in the tail of the cumulative distribution function). This more notable for the high discharge scenarios (110 and 70 m^3/s) suggesting an increase in erosional trend in these simulations. Indeed, the relative difference across all the simulations shows that the higher discharge, the lower the 5th percentile elevation.

In terms of the 95th percentile, there is a significant difference between the high magnitude pair of simulations (R_1 and R_2) and the two intermediate discharge pairs (R_3/R_4 and R_5/R_6). For the high magnitude pair, the steady discharge run results in a significant increase in the relative elevation of the 95th percentile relative to a more moderate gain by the unsteady flow. By contrast both intermediate discharge runs show the unsteady flows resulting in significant increases in the elevation of the 95th percentile, rising by c. 0.1 m, while the same measure for steady flow counterpart was more or less constant.

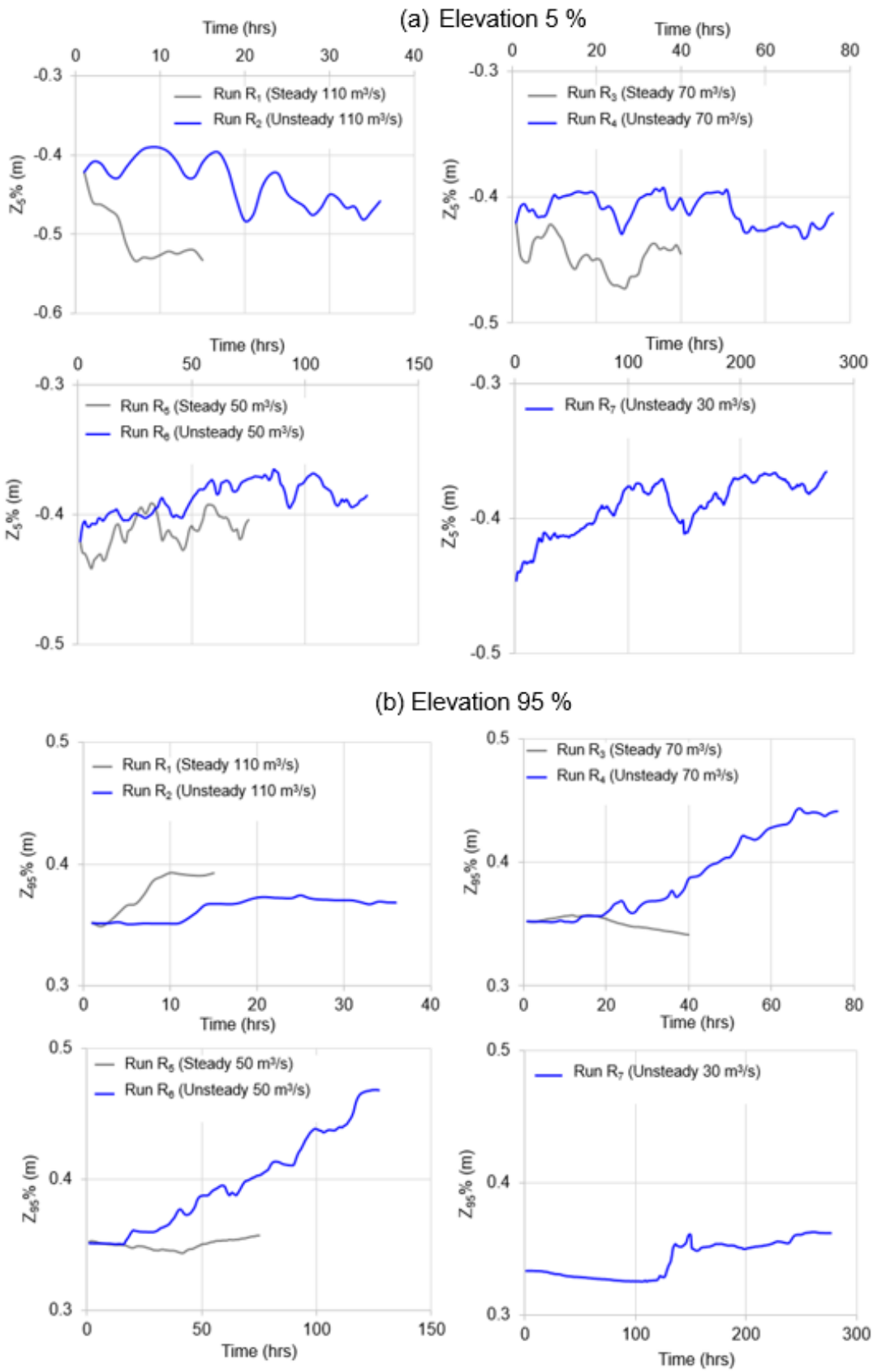

Figure 5.8 Evolution in terms of detrended elevation. (a) 5% of elevation which represents tail (deeper negative elevations) of elevation distribution curve. (b) 95% of elevation which represents head (higher positive elevations) of elevation distribution curve.

Increase in negative 5th percentile elevations imply deepening of channels, whereas gain in the elevation of the 95th percentiles is mostly likely to sedimentation on bars. Thus, bar-top deposition (higher 95% elevation) appears to be higher for the unsteady flow condition (R_2, R_4 and R_6) as compared to steady flow condition. By contrast, channel scour (lower 5th percentile elevation) was revealed to be more significant for the steady flow conditions (R_1, R_3 and R_5).

b) Bar Height

Bar height for longitudinal cross-sections was calculated as the difference between 95th and 5th percentile elevations and the averaged spatially to inform a representative value for the reach. The resulting trend over time for each of the simulation pairs is shown in Figure 5.9.

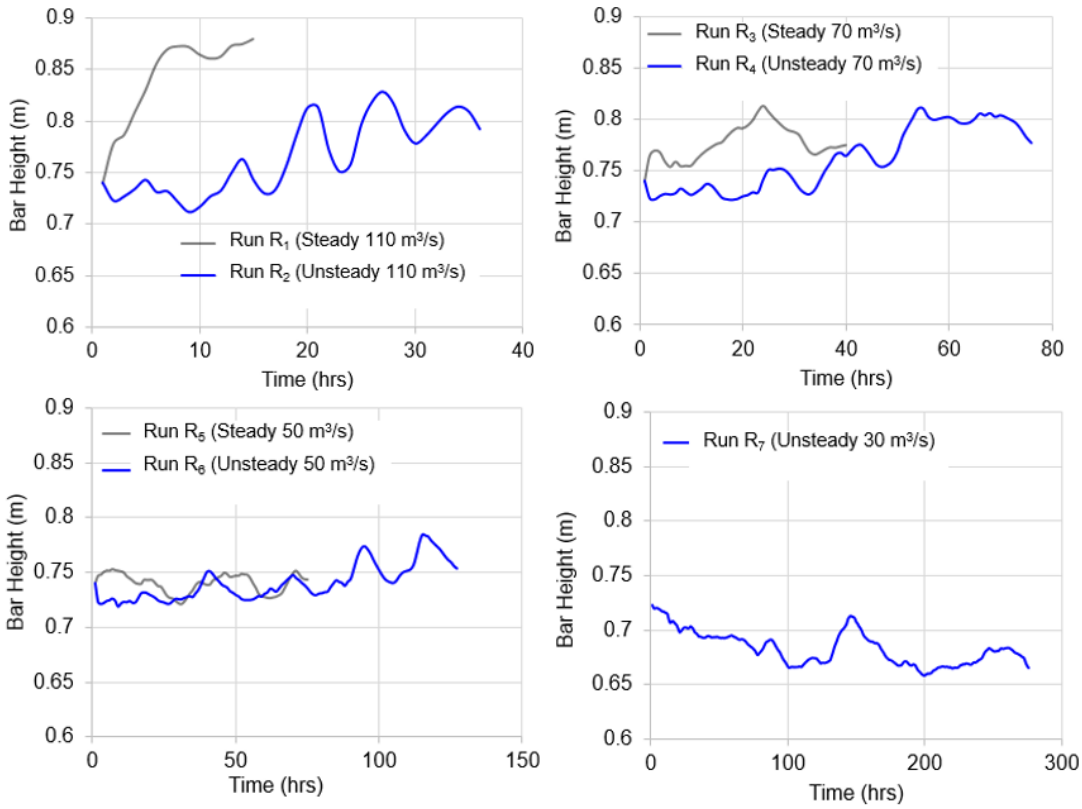

Figure 5.9 Evolution in terms of reach averaged bar height.

The two intermediate discharge pairs, R_3/R_4 and R_5/R_6 show comparatively little evidence of difference between the steady and unsteady simulations, nor any

significant trends in their evolution. However, the high magnitude pair, R_1 and R_2, reveal a significant difference between the two runs with significant increases in height found for the steady simulation, matching the results obtained for the raw percentiles discussed above. Over the '5 year' simulation period, bar height in the steady simulation increases by nearly 20 cm (4 cm per year). A similar trend is evident for the unsteady scenario but at a slower rate, rising just 10 cm over the simulation period. Analysis of the respective change in the 5th and 95th elevation percentiles described above, reveal that this increase in relief is associated primarily with bed scour rather than bar sedimentation, and reflects the concentration of flow into a smaller number of key anabranches for the steady simulation.

c) Channel Shape

Following the procedure of Redolfi et al. (2016b), the channel shape parameter, α, was determined for each topographic surface. Recalling the discussion in Chapter 3 and 4, α is the exponent of the width-depth curve and provides an effective index of the channel shape and its complexity (Figure 5.10).

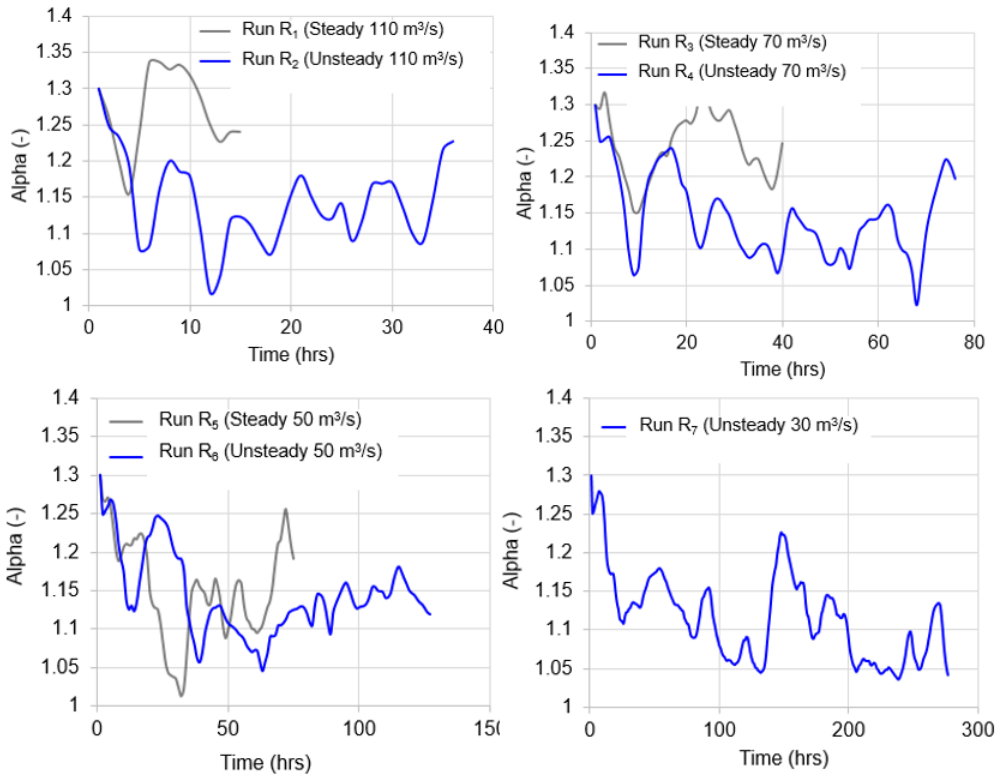

Figure 5.10 Evolution in terms of reach averaged width-depth exponent (alpha).

In all cases, the runs based on steady hydrographs generated topography characterised by higher alpha values. In terms of discharge, the highest magnitude discharge led to topography with the highest alpha values (e.g., Run R_1, R_2) and there is a clear positive relationship between the forcing discharge magnitude and the value of the exponent (e.g., R_1/R_2, cf. R_7). Overall, alpha values lie in the range 1 – 1.35.

5.4.3 Hydraulic Signatures

a) Hydraulic Geometry Relationship

The at-a-station hydraulic geometry relationships for the topography generated by each simulation was determined using fixed bed hydrodynamic simulations at different discharges. For simplicity, the final topography generated after the 5-year simulation period was used for reach run. Figure 5.11 - Figure 5.12 show the spatial distribution water depth for different discharges ranging from the average annual discharge (5 m^3/s) to the two-year recurrence interval flood (70 m^3/s).

In terms of simple discharge magnitude irrespective of the simulated hydrograph form, the runs with the highest discharge typically generate the least complex channel networks (e.g., Run R_1, R_2, c. Run R_7). This reflects the adjustment of the channel to the higher driving discharges, so that the lower flows are unfit and contained within bank. By contrast, the channel topography formed at lower discharges, evolves a narrow and comparatively shallow network of channels, which are quickly flooded in higher discharges leading to inundation of the bar surfaces, as shown clearly for the 30 m^3/s model in Figure 5.14**.**

Differences between the steady and unsteady runs at the same formative flows are less immediately apparent. On close inspection, however, it does appear (at least qualitatively) as though the channels evolved under the unsteady hydrographs have a higher wetted width and slightly higher complexity of branching network when compared to the runs using steady boundary conditions (for example, compare R_1

with R_2 (Figure 5.11); R_3 with R4 (Figure 5.12) and R_5 with R_6 (Figure 5.13). Again, this reflects the greater depth of scour observed under steady flows, as highlighted by the analysis of the elevation percentiles and bar heights above, which in turn serves to keep flows within the incised anabranches.

The Figure 5.15 summarizes the stage dependent adjustment in mean width, mean depth and mean velocity for all seven runs in the form of the at-a-station hydraulic relationship. This quantifies the observation made above, showing that the unsteady runs have higher total wetted width compared to the steady runs (although note that the pattern of individual channel width is higher for channel topographies derived under steady hydrographs; see planform maps). In general, all runs exhibit the characteristically high width exponent, compared to the depth and velocity exponents. This implies a faster rate of increase in width with discharge than depth or velocity, and is a well-established pattern of braided rivers (Mosley, 1983). However, there is no clear trend in the value of width exponent between the simulations based on steady and unsteady form hydrographs (e.g., R_1/R_2; R_3/R_4; R_5/R_6). Comparing all runs together as a set, does however demonstrate that the channel forms developed under the lower magnitude of formative discharge are associated with the highest width exponent (i.e., $R_7 = 0.43$ cf. $R_1 = 0.33$). Again, this reflects the role of the formative discharge in driving the pattern of channel form. The bed topography adjusted to the low formative discharge in R_7 comprises narrow, shallow anabranches which are quickly flooded as discharge rises above this formative level. Consequently, this leads to a rapid expansion of width as the bar tops are inundated, leading to high values of the width exponent.

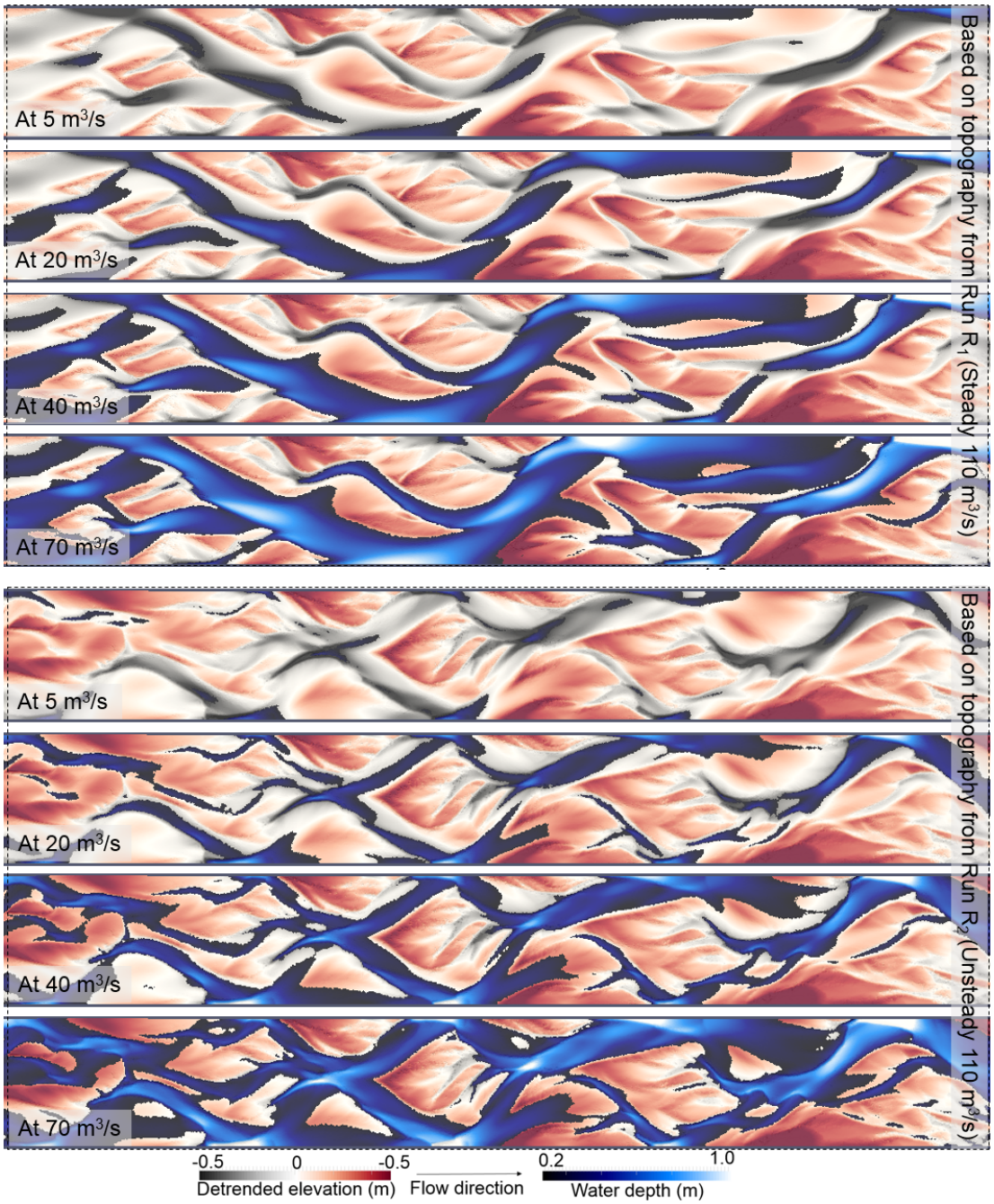

Figure 5.11 Stage-dependent planform dynamics (water depth and detrended elevation) as derived from the fix bed hydrodynamic simulation utilizing the final topography obtained from run R_1 and Run R_2. These maps were prepared by considering water depth equal to and above 0.2 m for clear visualization of channels networks. Domain is 1200 m x 175 m.

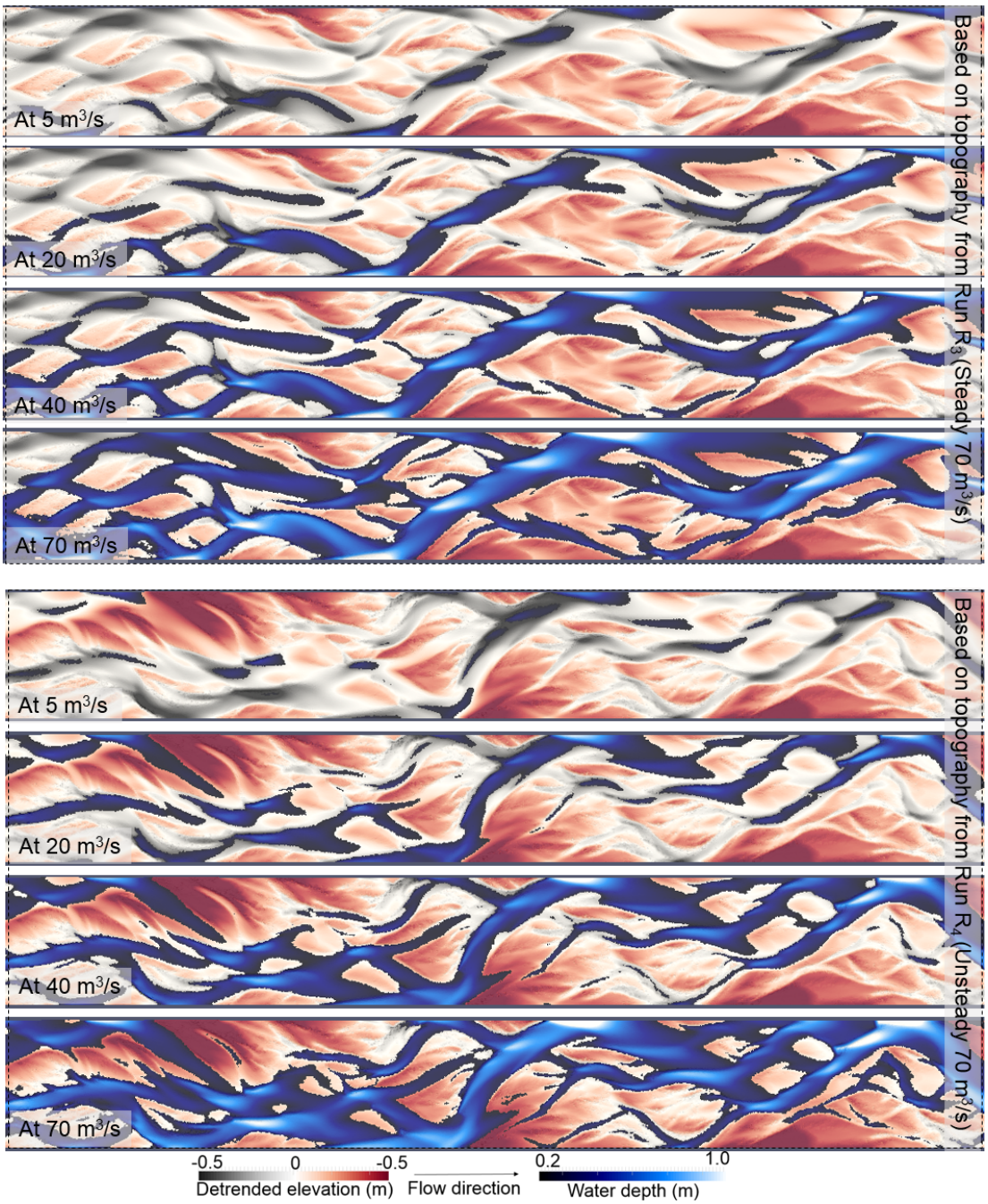

Figure 5.12 Stage-dependent planform dynamics (water depth and detrended elevation) as derived from the fix bed hydrodynamic simulation utilizing the final topography obtained from run R_3 and Run R_4. These maps were prepared by considering water depth equal to and above 0.2 m for clear visualization of channels networks. Domain is 1200 m x 175 m.

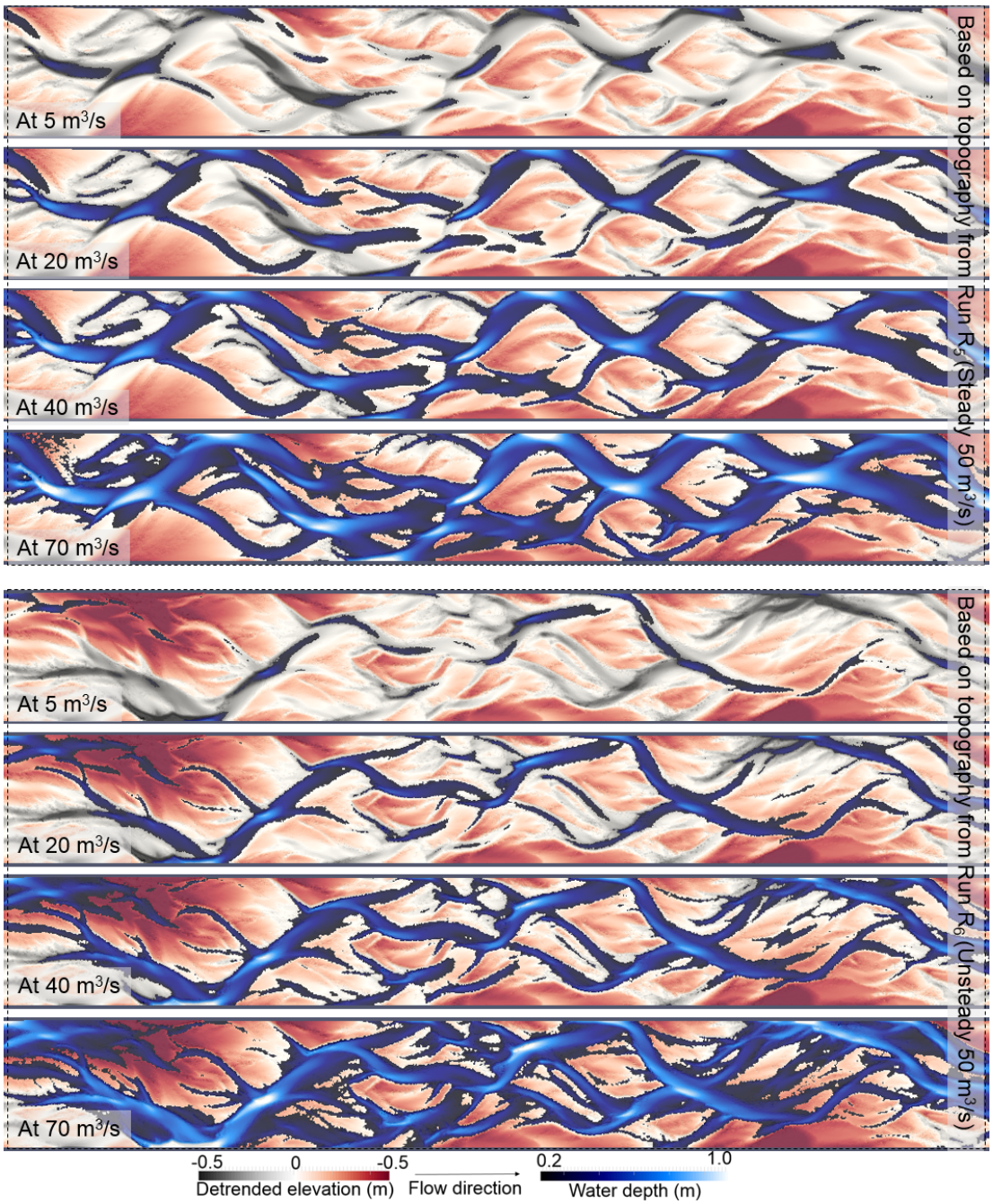

Figure 5.13 Stage-dependent planform dynamics (water depth and detrended elevation) as derived from the fix bed hydrodynamic simulation utilizing the final topography obtained from run R_5 and Run R_6. These maps were prepared by considering water depth equal to and above 0.2 m for clear visualization of channels networks. Domain is 1200 m x 175 m.

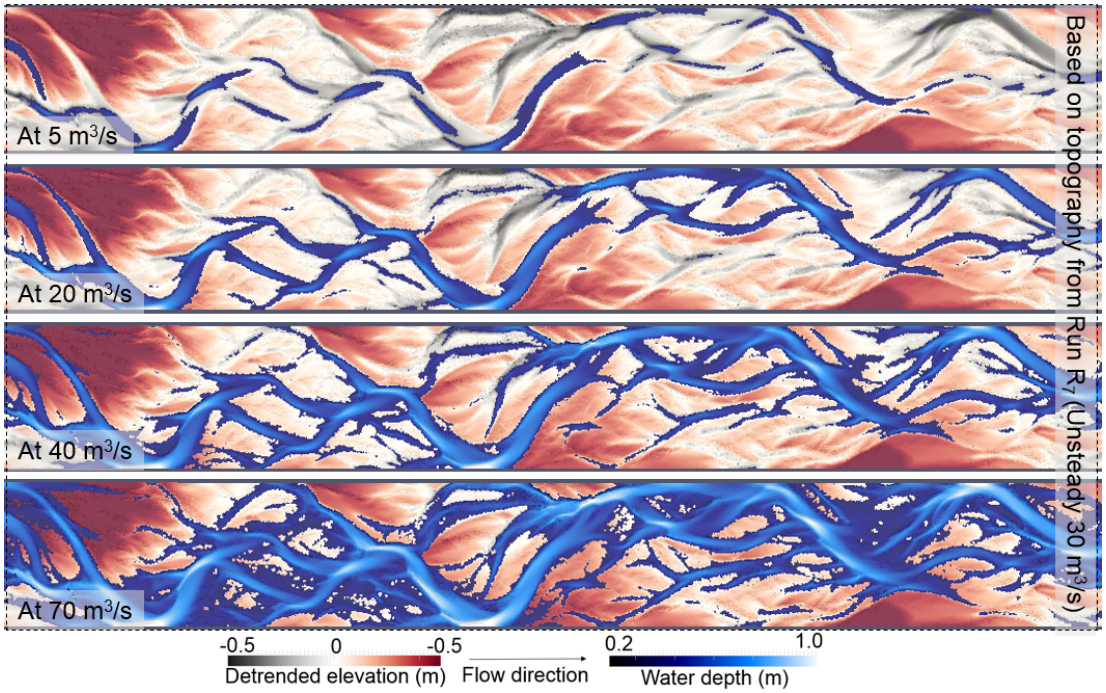

Figure 5.14 Stage-dependent planform dynamics (water depth and detrended elevation) as derived from the fix bed hydrodynamic simulation utilizing the final topography obtained from run R_7. These maps were prepared by considering water depth equal to and above 0.2 m for clear visualization of channels networks. Domain is 1200 m x 175 m.

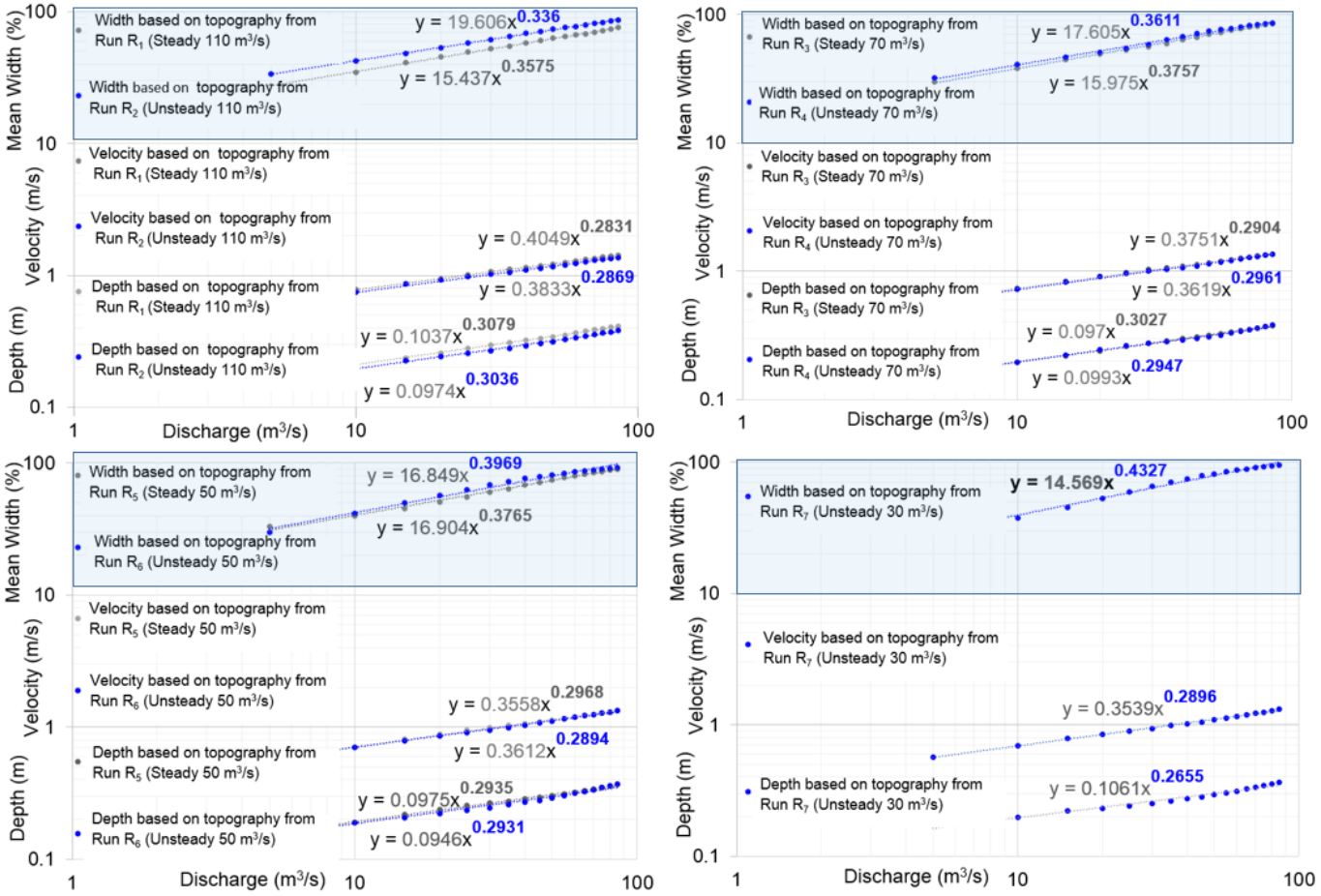

Figure 5.15 Hydraulic geometry relationship derived from fixed-bed hydrodynamic simulation based on final topography produced by all runs.

5.4.4 Morphodynamic Signatures

The morphodynamic processes characteristics of the simulations were first analysed in terms of total change, based on the differencing of final topography (after 5 years) with the initial condition. Secondly, stage dependent properties were determined using the spatial distribution of sediment transport obtained from fixed bed hydrodynamic simulations and sediment transport calculations. These calculations were based on fixed hydrodynamic simulations that were carried out at different discharges, ranging from 5-85 m^3/s. For these simulations, as for the hydraulic geometry relationships discussed above, the final topography obtained from each run were used. The subsequent sections explore the results in detail.

a) Volumetric Pattern of Erosion and Deposition

Figure 5.16 summaries the spatial pattern of erosion and deposition for each simulation and quantifies the volumetric contribution of these changes with respect to elevation of a priori topography. Additionally, the overall volumes of change and the net budget (deposition-scour) are also presented.

A clear difference between steady and unsteady runs is immediately apparent, in which the steady runs are degradational while the unsteady runs at the same discharge are aggradational. This pattern is maintained for all the formative discharges compared. While the magnitude of net change is relatively small, e.g., 2100 m^3 represents only a 1 cm of mean bed lowering (remember here the data analysis was based on the domain 1200 m x 175 m at the middle), the total difference in mean bed level (MBL) is significant when two simulations (steady and unsteady) are compared together. The resulting net differences sum to a difference of 2.2 cm in MBL at 110 m^3/s, 4.2 cm at 70 m^3/s and 4.3 cm at 50 m^3/s. The distribution of erosion and deposition by elevation is however, broadly consistent between the steady and unsteady simulations. For example, the erosion curve is centred above mean bed level, implying the dominance of high elevations by bank erosion or bar scour over

channel bed scour (Figure 5.16 middle graphs). By contrast, all runs produced peaking of deposition curve towards the negative elevation side which implies dominance of channel deposition over bar deposition (Figure 5.16 middle graphs).

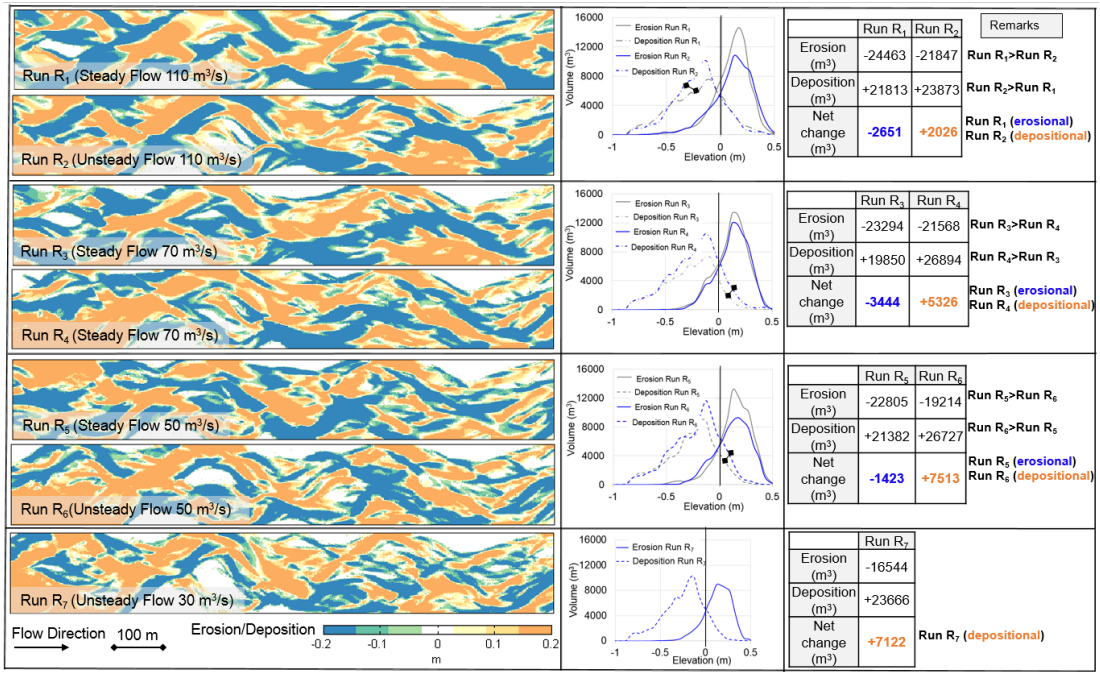

Figure 5.16 Erosion and deposition pattern based on the differencing of initial topography from the final topography (domain 1200 m x 175 m). The left block shows the spatial distribution; middle block shows the corresponding erosion and deposition pattern with respect to initial elevation, and right block shows the corresponding volumetric values.

b) Total Turnover Area

Bed turnover (percentage area of the total spatial domain) was calculated at different thresholds of vertical change (Figure 5.17) based on the DoDs showing the pattern of erosion and deposition in the Figure 5.16. The unsteady discharge simulations appear to be associated with higher turnover rates particularly, in terms of the higher magnitude changes (tail of the curve indicated by arrows in Figure 5.17; e.g., R_3-R_4). This implies a higher intensity of scour and sedimentation, while the steady hydrographs appear to be dominated by lower amplitude changes (head of the curve in Figure 5.17; e.g., R_5-R_6).

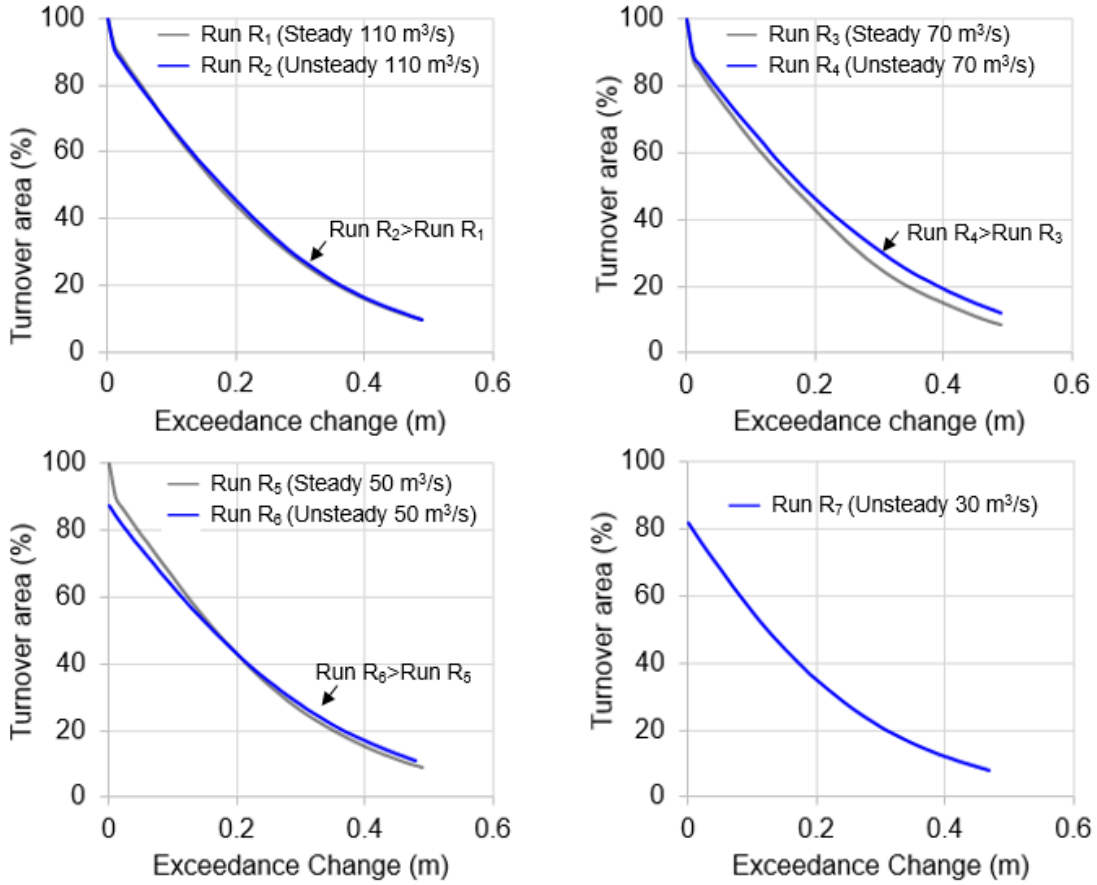

Figure 5.17 Turnover area percentage at different exceedance change.

c) Stage-dependent Sediment Transport

Sediment transport capacity of each cross-section was calculated as the sum of total transport capacity of all cells and then converted to a representative value for the reach by averaging the cross-sections. Estimates were made for range of discharge between 5 m^3/s to 85 m^3/s at an interval of 5 m^3/s to develop synthetic sediment transport rating curves (Figure 5.18).

The emergent topography from run R_1, based on the 110 m^3/s steady flow condition, is adjusted to generate significantly higher sediment transport rates across the entire range of discharges when compared to its unsteady pair, R_2. This reflects key differences in the form of the dominant anabranches which have higher sinuosity in R_1 and larger riffles or high shear stress zones, which are restricted to very local zones, principally at confluences in R_2. For the two other pairs of runs (R_3 steady, R_4

unsteady and R_5 steady, R_6 unsteady), sediment transport rate was again slightly higher for the steady boundary conditions, though rather less marked than for the high magnitude event (see top right and bottom left plot in the Figure 5.18).

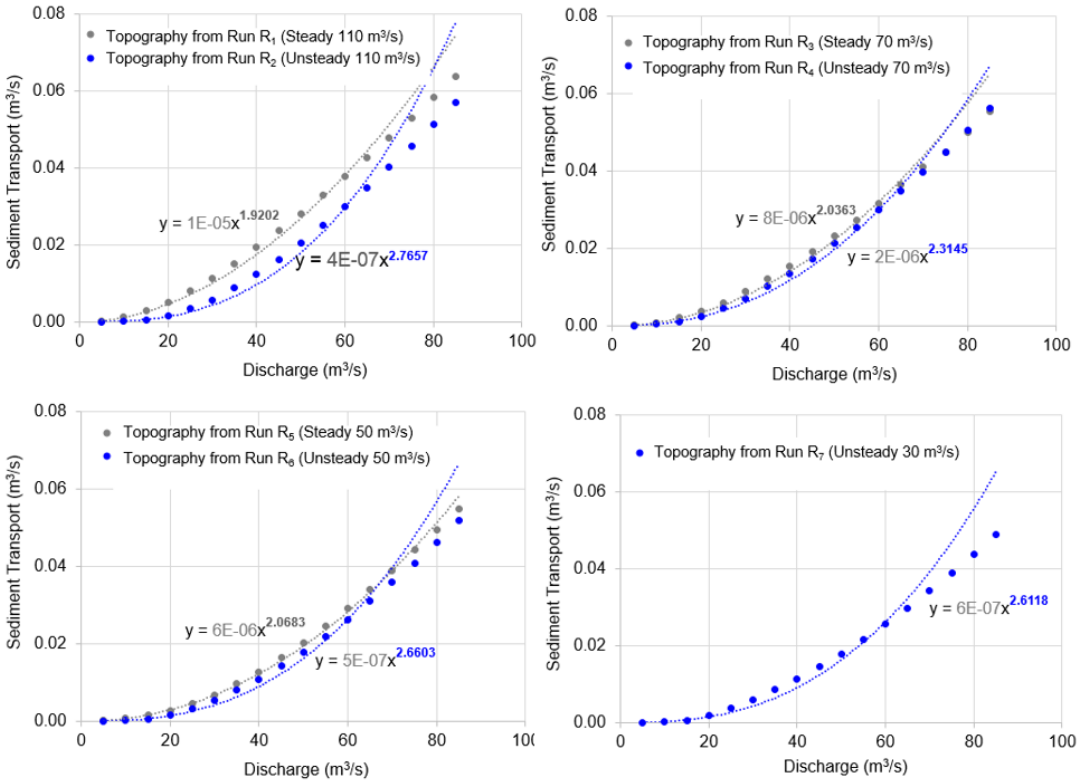

Figure 5.18 Stage dependent sediment transport capacity.

The fitted power relationships to these rating relationships also reveal some key differences. In each paired case, the unsteady runs have higher fitted exponent values (compare Run R_1 with R_2; Run R_3 with R_4 and Run R_5 with R_6 in the Figure 5.18). A higher discharge exponent implies a faster rate of increase in sediment transport capacity with discharge. The higher exponent may reflect the additional complexity evident in the unsteady topography, so that as discharge increases, a more non-linear adjustment in the transport rate ensues. This could reflect the activation of new channels as discharge increases, creating new high shear stress zones resulting progressive and steep rise in sediment transport rate. Such interpretations should, however, be treated cautiously, for the fitted power relationships shown in Figure 5.18 do not represent the rating relationship effectively at high flows, and significantly overestimate sediment flux above 60-70 m^3/s.

The Figure 5.19 shows the percentage area of the bed that experiences dimensionless shear stresses above the threshold for entrainment (0.047; cf. Meyer-Peter and Müller (1948)). For each paired case, the proportion of the bed with a dimensionless shear stress of above the critical entrainment threshold, was higher for the steady runs (see the tail of the curves in the Figure 5.19, indicated by the arrow). Similar patterns exist for all range of discharge, though only the 70 m^3/s relationship is shown here for brevity. As expected from the rating relationships show above, this difference is most significant for the high flow topography produced by the run R_1-R_2 and reflects the simplified structure of the bed which is adjusted to the higher formative flow level (110 m^3/s) so that lower discharges are largely contained within channels, concentrating flow within bank.

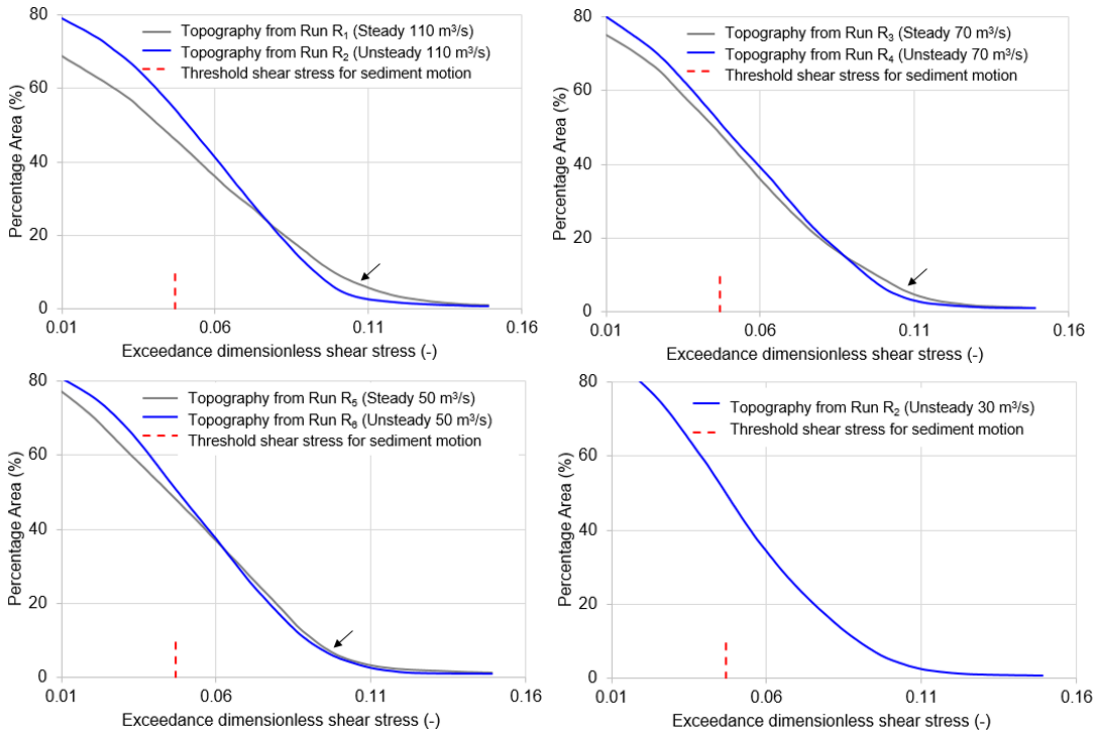

Figure 5.19 Percentage area at different exceedance dimensionless shear stress at 70 m^3/s for all the cases. Topography from the runs utilizing steady form of hydrographs showed higher percentage area particularly at higher range of shear stress (see tail side as indicted by arrow) as compared to the runs utilizing unsteady form hydrographs. Similar trend exists at all range discharges which have not shown here for brevity.

d) Stage-dependent Active Width

Active width, expressed here as the percentage of total corridor width, was calculated for each cross-section by quantifying the proportional of cells actively transporting sediment and then averaging the result. As with the results above, the most significant differences between the steady and unsteady runs appear for R_1 and R_2, reflecting the adjustment of the bed topography to the extreme 110 m^3/s flow as discussed above i.e., higher total active width at unsteady flood as compared to steady flood. For other paired runs (R_3/R_4 and R_5/R_6) there is no differences.

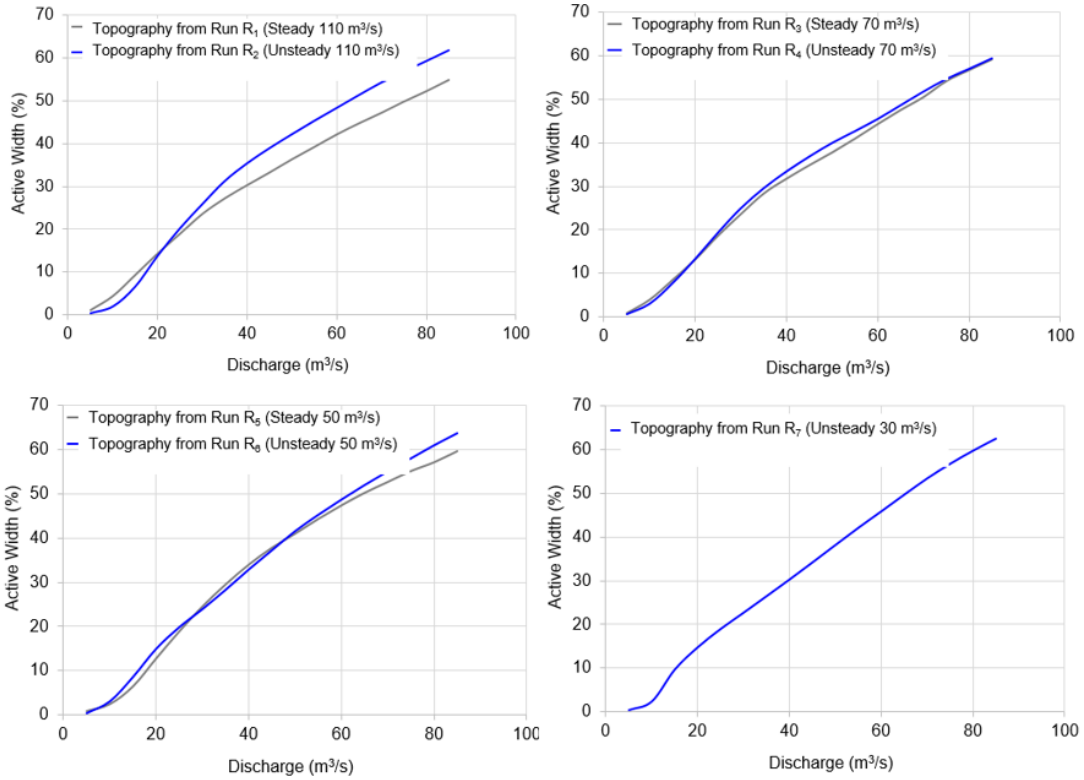

Figure 5.20 Stage-dependent active width.

e) Stage-dependent Active Braiding Index

Active braiding index was calculated by counting number of channels transporting sediment greater at a rate equal to or greater than the mean sediment transport in cross-sections extracted longitudinally, and then expressed as a reach average (e.g., Schuurman et al., 2013). Run R_2 based on the unsteady 110 m^3/s hydrograph appears to generate a significantly higher active braiding index than its simulation pair, R_1. A similar pattern was observed for the steady/unsteady pairs R_5 and R_6 as well, though

this trend was not evident for R_3 and R_4. Interestingly, while the active braiding index for the 110 m^3/s topography appears to level off with increases in discharge beyond c. 40 m^3/s, the unsteady simulations derived a lower forcing discharges in particular, appear to continue to increase across the range of simulated discharges. This again suggests that topography adjusts to the steady flow hydrographs by developing a dominant channel network which accommodates the flow within a small number of channels. By comparison, the unsteady simulation, and particularly networks developed at lower forcing flows, are more complex, so that increases in discharge lead to a great dispersion of flows into a wider range of smaller channels. This is clearly evident for the low flow simulation, R_7, which shows a progressive increase in the active braiding index up to 80 m^3/s.

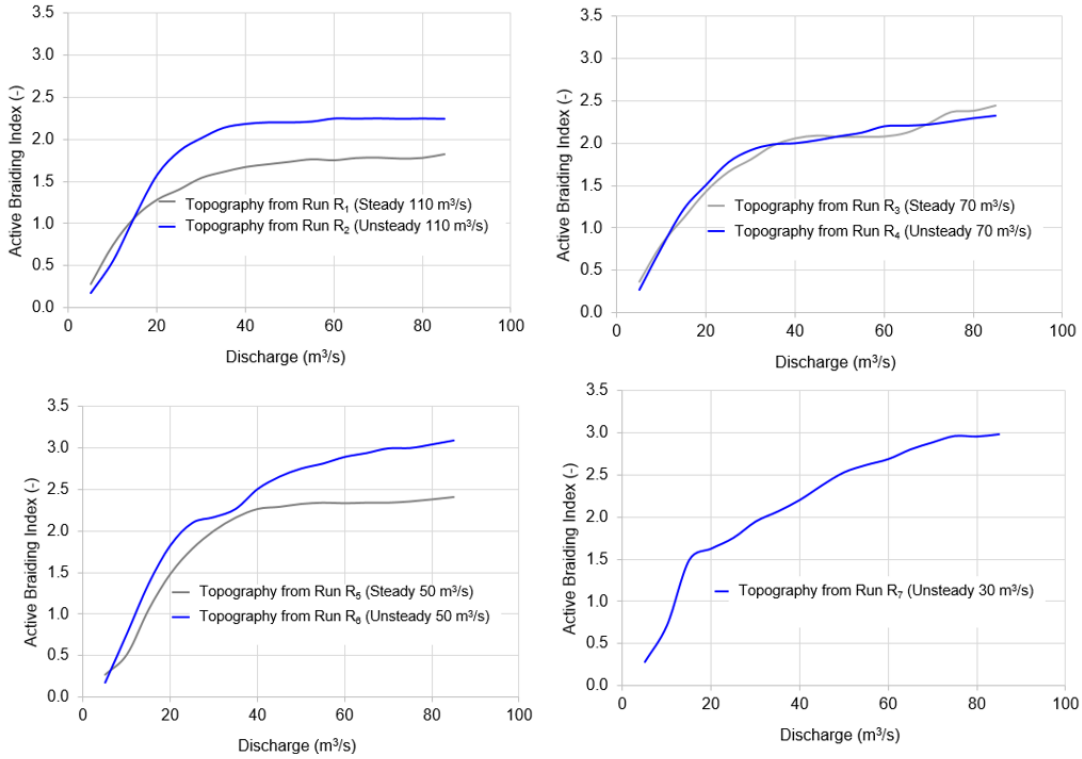

Figure 5.21 Stage-dependent Active Braiding Index. Only the runs R_1 and R_2 produced clear differences.

5.4.5 Morphodynamic Processes under Unsteady Flow

a) Nature of Simulated Unsteady Hydrographs

This section examines the dynamics of the unsteady runs by quantifying hysteresis patterns that capture the changing nature of morphodynamic processes on the rising and falling limbs of the driving hydrographs. It is helpful to first review the nature of the simulated unsteady hydrographs, which are shown below in Figure 5.22. This shows the predicted differences in the inlet and outlet discharge (ΔQ) obtained for all runs unsteady runs. Run R_2, which involves cycling discharge between 20 -110 m^3/s clearly exhibits the highest rate of change (ΔQ/t) and might therefore be expected to show the most significant intensity of hysteretic effects.

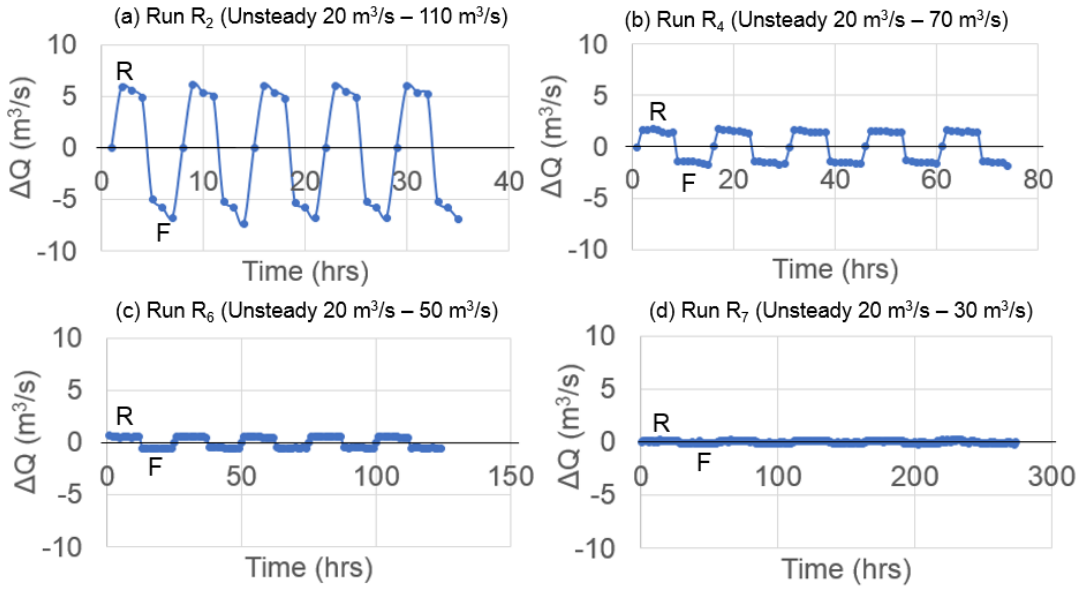

Figure 5.22 Discharge input minus discharge output (ΔQ) for four different runs utilizing unsteady flow. The Run R_2 holds highest ΔQ and Run R_7 holds lowest ΔQ.

b) Hysteresis Patters on Volumetric Changes

Hysteresis loops showing the difference in the time-dependent volumes of erosion and deposition on rising and falling limbs of the hydrographs are show in Figure 5.23. Here, the discharge is taken as the average of the influx and efflux, reflecting the lack of steady-state conditions. In general, in each of these simulated runs, the intensity of erosion and deposition was high on the rising than the falling limb. As expected this pattern was most pronounced for R_2 (Figure 5.23a), followed in turn by R_4, R_6 and R_7

respectively (Figure 5.23b, c, d). The coefficient of variation (CV) of simulated discharge series in run R_2 was highest which was then followed by the run R_4, R_6 and R_7, respectively. The intensity of hysteresis followed the similar trend. The coefficient of variation of discharge series used under a hydrograph seems to be indicating the extent to which intensity of hysteresis on work done can be expected.

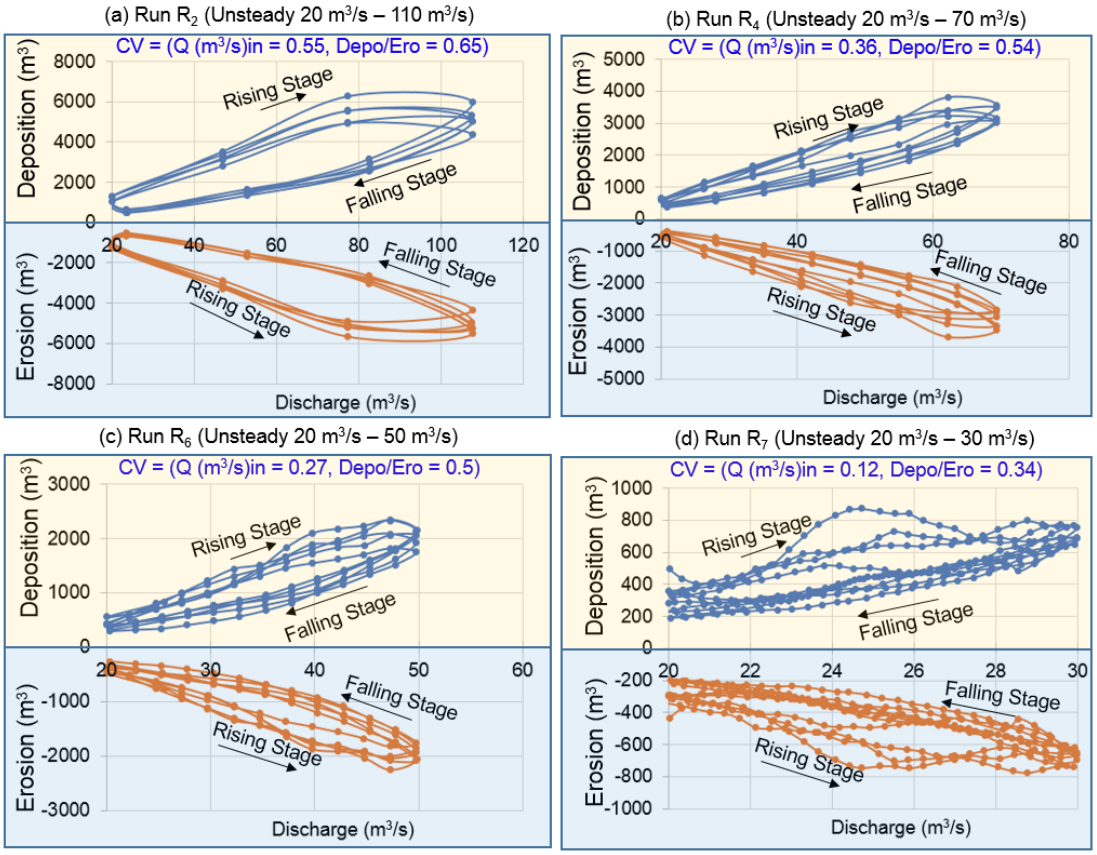

Figure 5.23 Hysteresis pattern of erosion and deposition based on the reach averaged volume in each hour interval. The coefficient of variation of the simulated discharge and the erosion/deposition volume calculated based on the hourly data have been listed under the heading CV. The form of hydrographs having higher CV resulted in higher CV of erosion/deposition.

c) Hysteresis Patterns on Sediment Transport

The sediment transport hysteresis pattern was scrutinized for each flood event (Figure 5.23). Here, it is worth noting that these are based on calculation rather than direct outgoing sediment from the model domain. Only run R_2, based on the highest magnitude discharge which exhibits the highest coefficient of variation of discharge (i.e., steepest rising and falling limb) produced a persistent pattern of clockwise

hysteresis (higher sediment transport during rising limb than falling limb). The remaining runs (Run R_4, R_6 and R_7) exhibited a more complex pattern of both clockwise and anticlockwise hysteresis, suggesting complex within reach variations in transport in response to the evolving morphological adjustment.

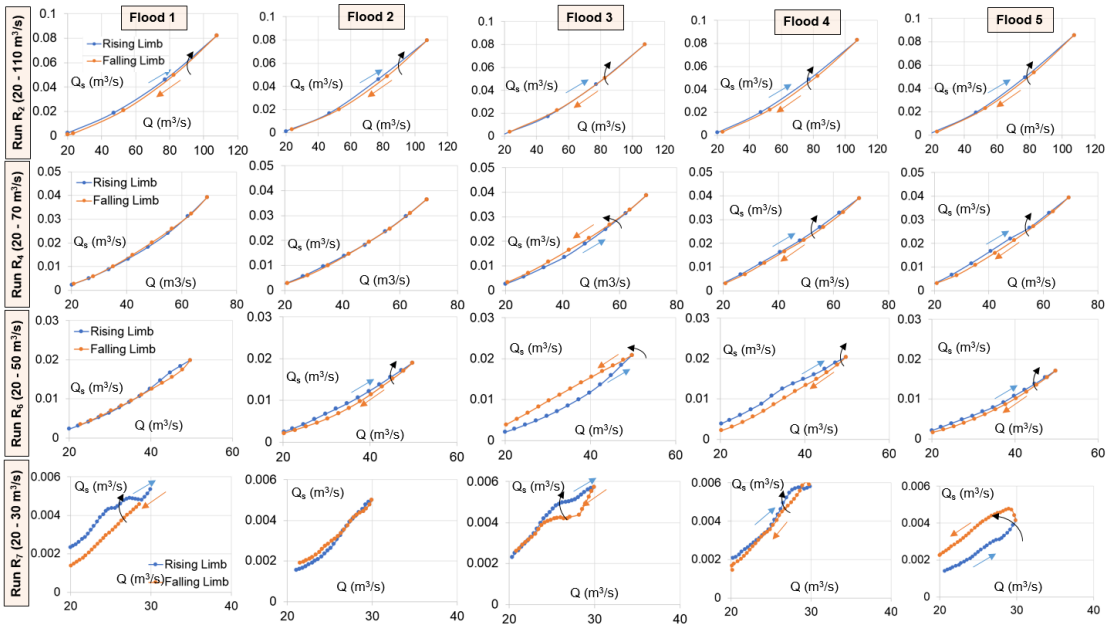

Figure 5.24 Sediment transport in each flood event, demonstrating transport hysteresis. Note: the sediment transport here is based on the calculation using the spatially distributed shear stress.

d) The Evolution of Bed Elevation

A useful way to explore the pattern of bed evolution is to track key percentiles of the detrended elevation distribution. In this context, the 5th percentile provides a useful index of the deepest areas of the channel bed corresponding to areas of localized scour while the 95th percentile provides an index of the highest bar surfaces (Figure 5.25 and Figure 5.26 respectively).

The Figure 5.25 shows the evolution of the 5th percentile elevation during rising and falling limbs for the cycle of five flood events. For each flood event, runs R_2 and R_4 show a downward elevation curve during the rising limb, corresponding to a deepening of the lowest bed topography (i.e., increased local scour) and upward tracking elevations particularly at the end of falling limb – indicating sedimentation. In

the case of R_6 and R_7, a systematic pattern of thalweg deepening was, however, rather less evident. This pattern of channel deepending is therefore associated principally with the high magnitude discharge series therefore (R_2 and R_4) again confirming the pattern of divergent scour and sedimentation on rising and fall limbs shown in Figure 5.23.

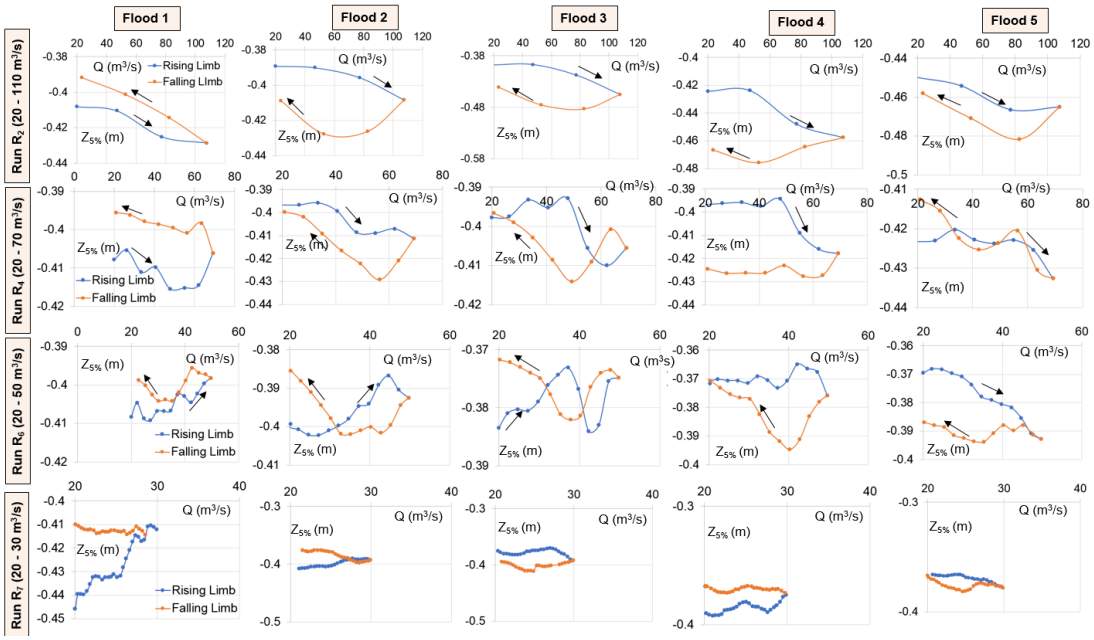

Figure 5.25 $Z_{5\%}$ elevation evolution in each flood event demonstrating relative change in elevation of deeper areas (channel thalweg).

The Figure 5.25 shows the evolution of the 95th percentile elevation corresponding to the highest bar surfaces. This analysis reveals a broadly consistent pattern of increasing elevation during the falling limbs, implies sedimentation increasing the high elevated areas of the reach.

Overall therefore, increases in the height of bars tops during the falling limb appears to be a common process at all discharges, though scour of the channel thalweg is dependent on the magnitude of simulated hydrographs. The low magnitude unsteady hydrographs, in particular, exhibited increases in elevation also during the rising limb which is possibly associated to the bar erosion processes, transforming the nature of the frequency distribution.

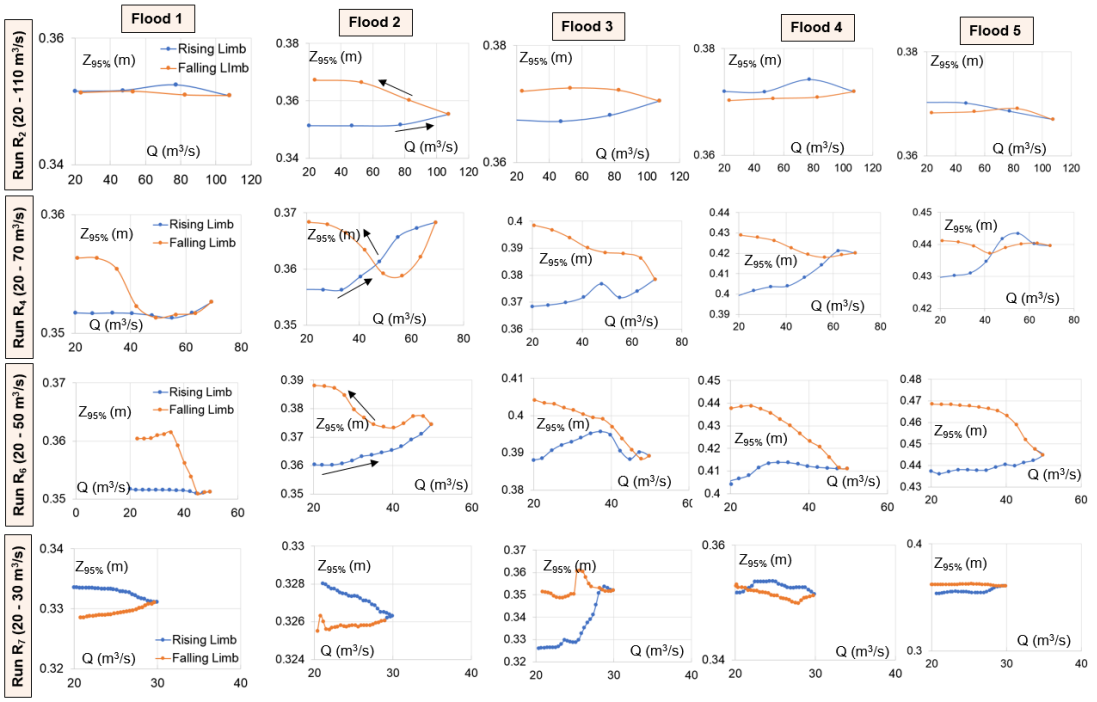

Figure 5.26 $Z_{95\%}$ elevation in each flood event demonstrating relative change in elevation of elevated areas (bars).

e) The Evolution of Bar Height

Bar height was calculated as the difference between the 5th and 95th percentiles of elevation for each cross-section and then averaging (Figure 5. 27).

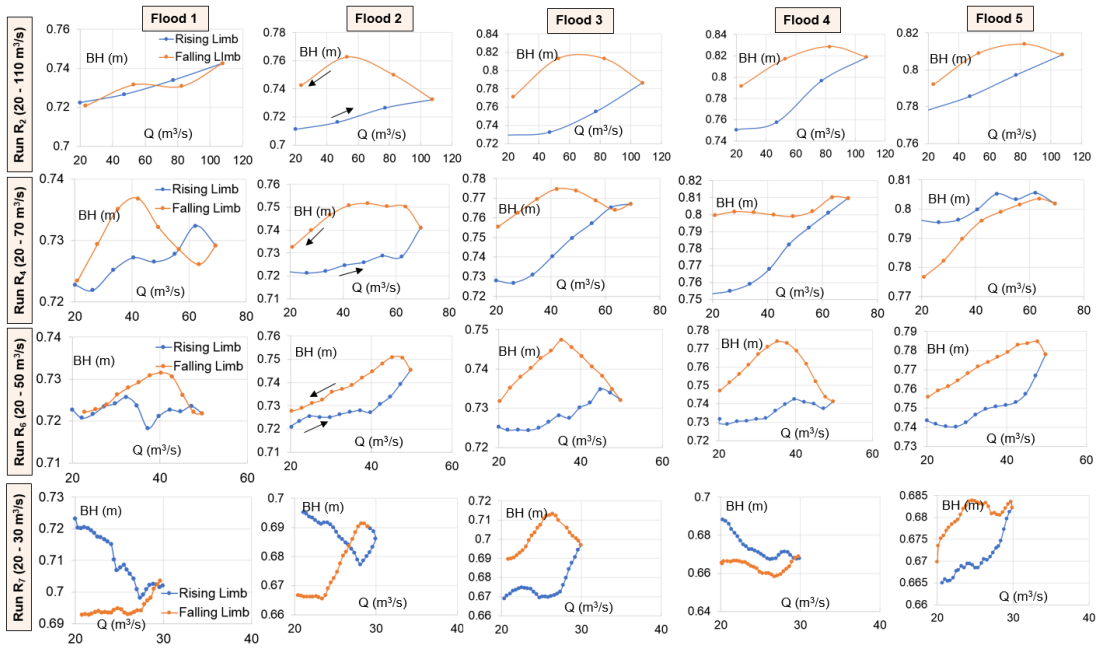

Figure 5. 27 Bar height (BH) evolution in each flood event demonstrating relative change in bar height.

As seen from the Figure 5. 27, bar height increased at higher rate during rising limb (R_2, R_4 and R_6). During falling limb, all runs showed a decreasing trend of bar height due to relatively higher rate of heightening of channel thalweg than heightening of bars tops following the decrease in flow competence during the falling limb.

5.5 Discussion

Quantifying the morphodyanmic response of braided rivers to variations in the magnitude and form of boundary fluxes is a complex problem. Empirically, it is impossible to provide sufficient experimental closure to isolate the wide range of confounding environmental effects and even then, the historical legacy and lag-times associated with the pattern of channel adjustment make the identification of cause and effect complex. Moreover, the acquisition of relevant observations of morphology and processes in large, complex braided rivers remains challenging, even if recent advances in technology have begun to address this. More significant strides in understanding have arguable been made in the laboratory. This context enables close control of the boundary conditions, detailed internal monitoring of the system state variables and emergent topography. Nonetheless, such improvements must be measured against the problems of scaling laboratory experiments and, in particular, the difficulties of using sediment mixtures and representing the effects of vegetation.

There is therefore, a growing interest in the potential to use numerical models as synthetic instruments to support such experimentation. Numerical experimentation provides an alternative tool to understand the effects and response of changing boundary conditions on the form and dynamics of channel adjustment.

In this study, a range of forcing discharge hydrographs were used to examine the effects of steady and unsteady flow regimes on unvegetated channel evolution from a common initial condition. The discharge influx scenarios were designed to create energetically normalised flow regimes to afford comparison. Three paired scenarios

were created to reflect discharges, covering return period flows ranging from 15 to 1-year recurrence intervals. Unsteady flows were represented as 5-year sequences, characterised by an annual hydrograph with a one-hour low flow period separating events. These cyclical series of hydrographs were engineered with peaks of 110, 70 and 50 m^3/s respectively, falling to low flows of 20 m^3/s. Each of these was, in turn, compared to a 'matching' steady flow input, based on the same peak discharge (110, 70, 50 m^3/s) but with a significantly shorter overall duration. The result therefore represents significant variability in the magnitude, duration and persistence of flows but that nonetheless ultimately represent the same total energy expenditure.

It should be noted, that each discharge scenario used the topography generated by simulation R_9 reported in Chapter 4 as the initial bed condition. This morphology represents the adjustment of channel form to a steady discharge of 70 m^3/s. It follows that two paired scenarios used in this chapter, R_1/R_2 and R_5/R_6 represent discharge conditions above and below this initial condition respectively, while the intermediate pair, R_3/R_4 represents a continuation of the forcing conditions (albeit in different dynamical forms). Scenarios R_1/R_2 and R_5/R_6 should, therefore, be expected to show a pattern of adjustment to higher and lower forcing conditions, while the intermediate pair, R_3/R_4 provides a control test of the difference between a steady and unsteady regime at the same discharge.

5.5.1 Planform Adjustment

The quantitative assessment of the total braiding index (TBI) revealed relatively little difference between the between the steady and unsteady paired simulations. Instead, the pattern of TBI predicted appears largely to reflect changes in the adjustment of the initial condition to the new forcing magnitude; resulting in a drop in the TBI for the higher flow scenarios R_1/R_2 and an increase in TBI for the lower flow scenarios, R_5/R_6 and R_7.

This pattern reflects the concentration of flows into a smaller number of larger anabranches for the 110 m^3/s scenarios, while the lower flow scenarios reflect the development of a network of narrower channels that bifurcating frequently around complex bars. It is important to recognize here, that the definition of the TBI used is actually *topographic* – i.e., channels are defined not by the presence/absence of flow, but by their height relative to mean bed level. This is important, the simple channel count indices based on inundation, have been shown to demonstrate a bell-shaped distribution (Bertoldi et al., 2009b), due to inundation of the entire braidplain at high flows resulting in a reduction in the complexity of the network. Here, by comparison, the TBI reflects the topographical complexity of the adjusted channel bed (e.g., Schuurman et al., 2013), and demonstrates that increases in flow lead to simplification of the bed while reductions in discharge are associated with sedimentation and scour that contributes to bed complexity.

5.5.2 Topographic Adjustment

In terms of the extremes of the elevation distribution, differences between the steady/unsteady pairs are more evident, although again the behaviour of the scenarios relates strongly to the change in the intensity of flow overall. Difference between the steady/unsteady simulations is most evident between R_1/R_2. Here the steady flow simulation (R_1) results in a rapid decrease in the 5^{th} percentile (representing an increase in bed depth or decrease in elevation), with scour contributing a -0.1 m change in the 5^{th} percentile level. While the unsteady flow scenario adjusts in the same direction, the overall change is more muted, comprising just a -0.05 m change. At the same time, steady flow simulation (R_1) also leads to a significant increase in the elevation of the 95^{th} percentile, which rises by just under 0.05 m, while again the unsteady response is less profound. Taken together, and as shown by the change in bar height (Figure 5.9) this appears to suggest the high magnitude steady simulation generates a simplification in the channel network

structure, (compared to the initial condition) but with an overall increase in the amplitude of the topography. This is consistent with DEMs of difference shown in Figure 5.16, which indicate deep scour and a net degradation of the bed for simulation R_1.

Differences in the elevation extrema and by implication bar height are also evident for the lower flow scenarios, most notably in terms of a systematic increase in the 95th percentile elevation for both the 70 and 50 m^3/s unsteady simulations. In both these cases, there was almost no change in elevation for the steady flow pair at each discharge, but a progressive increase in the elevation is observed for both unsteady simulations, generating an increase of +0.1 m in the highest bar surfaces. This points to a pattern of significant sedimentation, a pattern confirmed by the DEM difference models and it is notable that both these simulations have a strong net aggradational signal. Interestingly, this increase in bar top elevations is not mirrored by accompanying change in bar height for the unsteady 70 and 50 m^3/s simulations. This suggests that the additional bed complexity that leads to higher TBI, is driven by additional sedimentation causing flow separation, rather than processes such as cutoff and bar top dissection. This is again reflected in the net increase in bed storage and thus a higher mean bed level.

Finally, while there is no steady flow pair for the unsteady 30 m^3/s discharge scenario (R_7), it is notable that this simulation results in a net decrease in bar height, falling by 0.05 m, associated with sedimentation in the topographic lows (see the progressive increase in the 5th percentile elevation, Figure 5.8). In contrast to the high discharge magnitude simulations R_1/R_2 therefore, the adjusted low flow topography has lower relief and is associated with frequency channel division. An explanation for this reduction in relief is that the threshold angle of repose (18^o for wetted material) is sufficiently low to enable bank erosion at low flows, but that this eroded material cannot then be mobilized to create high stage (bar top) morphologies but is deposited

largely within channel (Williams et al., 2015; Rennie et al., 2017). This leads to an infilling of the channel bed and a reduction in local relief and channel capacity, which in turn promotes flow division, the creation of mid-channel bars, supporting the observed increase in the TBI.

In summary, therefore these simulations indicate a clear difference in the mode of channel adjustment from the 70 m^3/s topography initial condition. Increases in discharge lead to the production of a simplified planform network topology, but where this is characterised by high relief that constrains flows within defined banks. By contrast, reducing the forcing discharge creates a more complex network topology, where flow division is driven by low stage sedimentation that generates shallow topography and reduced channel capacity that promotes local flow switching. These patterns are consistent with field-based observations which suggest that significant bar trimming occurs at low flows, well below the one-year flood observations (e.g., Ferguson and Ashworth, 1992; Surian et al., 2009a; Bertoldi et al., 2010; Ashmore, 2013; Williams et al., 2015). Once this material is eroded from bars or bank, it is deposited within nearby channels leading to a reduction in bar height (Rennie et al., 2017). Ashmore and Sauks (2006) also suggest that the low relief associated with the Sunwapta river, reflects a quasi-regulated supply of meltwater from the Athabasca Glacier, so that the river rarely experiences a consistent regime of low diurnal flows, generating low relief topography.

The channel shape parameter (the exponent of the average width-depth curve, α), shows little difference between the steady and unsteady flow regimes. Again, the dominant signal instead relates to the change in flow magnitude, in which α falls from 1.3 to 1.05 for the low flow simulation (R_7, 30 m^3/s). Superficially, this is a surprising result given the high TBI for this simulation. However, it should be recalled that α simply defined as the exponent of a power function fitted to the width-depth relationship. This width-depth curve is produced by determining the cumulative width

of the channel in measured as a flat surface overlain on the topography of an extracted section, starting from the lowest elevation upwards (see Figure 3.8). It may be that as the bar height here is low (the difference between 95% and 5% elevation of the cross-section) the vertical step used to measure the change in height over generalizes the relationship leading to a quick levelling of the width-depth curve and subsequently a low value of α.

5.5.3 Hydraulic Response

The unsteady run of each simulation pair resulted in slightly higher predictions of wetted width. In terms of the classical width-exponent of the at-a-station hydraulic geometry relationship, there is, however, no any systematic difference between the steady and unsteady simulation pairs. Instead, the width exponent was found to be sensitive to the magnitude of discharge. For example, runs R_1 and R_2 with the highest magnitude discharge exhibited the lowest width exponent (around 0.35) which increases inversely with discharge, rising to 0.43 for the 30 m^3/s, R_7, simulation. Observations of at-a-station hydraulic geometry from natural field braided rivers have identified somewhat higher width-exponents in a range 0.4 - 0.7 (e.g., Mosley, 1983; Smith et al., 1996; Bertoldi et al., 2009b; Welber et al., 2012; Ashmore, 2013) and even as high as unity (e.g., Ashmore and Sauks, 2006). While the magnitudes of the exponent values identified here are at the low end of this spectrum, the difference between the high and low discharge simulation are coherent, with lower values for the more incised networks generated by R_1/R_2 and higher exponents for the dispersive flows associated with R_7.

5.5.4 Morphodynamic Responses

In terms of total volumetric of change, there was a clear separation between the steady and unsteady simulations, with higher volumes of erosions associated with the steady flow simulations. Indeed, the difference between these is significant, so that the steady regimes all have a net degradational budget, while the unsteady regimes

are net aggradational. It is useful to recall here that the unsteady runs (particularly the high magnitude simulations, R_1 and R_2) exhibited a pattern of thalweg scour during the rising limb of the hydrograph, followed by sedimentation in the thalweg and bar tops during the falling limbs. This switch in the dominant behaviour during unsteady flow conditions appears to be critical in creating a depositional regime.

Jerolmack and Mohrig (2007) proposed a simple conceptual model of braiding in which they suggest that in-channel sedimentation is a critical driver of avulsion. This framework quantifies the frequency of avulsion relating to the loss of channel capacity, and through the cutting of new anabranches or the reoccupation of old relict channels when flows overtax the existing channel due to sedimentation. This pattern is illustrated here, only in the unsteady simulations, during which high in-channel depositional volumes are generated during the falling limb of the hydrograph, a process less evident under steady flow. Intriguingly, this suggests the dominance of different mechanisms involved in the maintenance of braiding under the two flow regimes. Detail analysis scrutinizing the frequency of these morphological activities are needed to provide further clarification.

In terms of the sediment transport capacity, which here is modelled based on the final simulated topography of each run, the unsteady flow regimes appear to have adjusted to forms that have a lower overall transport capacity compared to their paired steady regime. Field observations by Williams et al. (2015) in braided Rees River, NZ, suggests transport pathways are often constrained to relatively narrow zones associated with locally high shear stress and can continue to transport material at relatively low flows. In the numerical simulations described here, the emergent topography developed under unsteady flows exhibited a lower proportion of the bed experiencing above critical shear stresses, reflecting the greater dispersion of flow in a larger number of shallower channels. By contrast, the concentration of erosive activity in the steady flow regime appears to create a positive feedback cycle, as the

concentration of flow creates higher shear stresses that in turn focus erosion and increase the local relief, locking the channels in place. This pattern is reflected the scour of the lower (5^{th}) percentile of the bed elevation distribution and associated increase in bank height discussed above. Rating relationships describing the increase in bedload transport rate with discharge were derived for both unsteady and steady simulation pairs. Power-law functions fitted to these relationships suggest higher exponent values for the unsteady simulation, implying faster increases in transport rate with discharge. These results should, however, be treated cautiously as the fitted functions do not represent the predicted data closely, particularly at high discharges.

In terms of active width and active braiding index, there is no clear systematic trend across the pairs of steady and unsteady runs. By contrast, both these metrics exhibit a strong sensitivity to the discharge magnitude, in which the topography derived from the low flow simulations ($R_5/R_6/R_7$) are all associated with increases in the active width and braiding index, particularly at high discharges. This again reflects the additional complexity of the bed topography generated under these lower formative flows and the influence of bar overtopping due to the shallow relief. This overtopping encourages activation of dissected channels located on the bar tops resulting higher active braiding index.

5.6 Conclusions

This study provides a comprehensive insight into the adjustment of unvegetated channel form and processes in as the bed evolves in response to changing discharge boundary conditions. Simulations were initiated using the equilibrium topography derived from experiment R_9 from Chapter 4, which was formed under a 70 m^3/s steady flow condition, which corresponds approximately to the 2-year recurrence interval flood. Here, three paired simulation sets were designed to represent five years of energetically equivalent boundary flows, but with peak discharges of 110, 70 and 50

m^3/s, representing the 15-year, 2-year and 1-year floods respectively. In so doing, the experimental design provided an examination of how the initial topography evolved in response to increasing, decreasing and maintaining (a control) the formative discharge.

The numerical simulations were interrogated to examine the evolution of planform, topographic, hydraulic and morphodynamic characteristics of the simulated channels using the framework proposed in Chapter 3. Before drawing definitive conclusions, some key simplifications of the approach used here should be recalled. Arguably the most important of these is the use of a single grainsize sediment. This significant abstraction of reality precludes textural adjustment of the channel which may, in turn, affect the sediment transport rate and could, therefore, result in a wide range of alternative simulation outcomes (Ferguson et al., 2015). Moreover, the initial condition used assumes a uniform distribution of bed material, without the likely differences between the grainsize of existing bars and channels. Furthermore, armouring of bed, a well-established phenomenon associated with selective entrainment in unsteady flows regimes cannot be effectively represented.

Nevertheless, building upon this simplified framework of numerical experiments, a number of key conclusions can be isolated.

1. Both steady and unsteady flow regimes generate channel forms that have a similar range of Total Braiding Index (TBI). The nature of the planform adjustment is, however, strongly associated with magnitude and direction of change in discharge, with the results here showing an inverse adjustment of TBI with discharge. An increasing discharge leads to the progressive dominance of flow within a smaller number of larger channels, while decreasing the formative flow appears to result in a more dispersed network of smaller channels.

2. The change in TBI reflects major differences in the relief of the emergent topographies. Higher formative flows led to an increase in average bar/bank height (by over 10 cm for the 110 m^3/s), while reductions in the forcing discharge generated smoother topography (e.g., bar height decreased by 5 cm for the 30 m^3/s). This change in relief explains the confinement of flows into a small number of channels (low TBI) for the high discharge scenario, and the greater dispersion of flow as the ratio of bar height: flow depth falls.
3. While conclusion (2) holds broadly, there are subtle differences between topographic adjustment in the unsteady and steady flow regimes. This is seen by differences in the pattern of bed adjustment during rising and falling limbs of the hydrograph, with scour dominating during rising stages and deposition occurring during falling stages. This results in increasing bar height during the rising limb which then decreases slightly during low flow stages of the falling limb, with implications for the timing of abrupt channel changes such as cutoffs and local avulsion.
4. Unsteady flow regimes are also associated with higher wetted width compared to steady flows at all discharges. However, the pattern of change in wetted width is dominated principally by the change in the driving discharge regime. Reductions in the formative flow produced channel networks that are associated with more dynamical response of wetted width to discharge, as shown by the modelled at-a-station hydraulic geometry results. This again reflects the differences in the relief of the emergent topography, with the shallower morphology produced under lower formative flows, leading to a greater frequency of flow division.
5. While the planform and morphological metrics revealed only subtle differences between the unsteady and steady flow regimes, the net sediment budget varied significantly. For all modelled discharges, the steady simulation resulted in a net degradational sediment budget, while the unsteady

counterpart was found to be net aggradational. The resulting difference in the mean bed level between the two scenarios was found to be as high as 4.3 cm (for the 50 m^3/s regimes). This divergent behaviour reflects the importance of sedimentation during falling stage conditions. In turn, the emergent topography differs, with the steady flow regime forms adjusted to generate higher rates of sediment transport due to the lack of depositional morphologies.

Chapter 6: Modelling the Interaction of Flow, Sediment Transport and Vegetation

Chapter Summary

This chapter addresses the research question 4 which is: ***How does the interaction between vegetation growth rate and discharge flow regime govern the evolutionary morphology of braided rivers?***

This chapter evaluates how the geomorphic trajectory of braided river evolution responds when vegetation is introduced into the numerical system. Experiments with different vegetation growth rates are used to represent the effects of different vegetation communities or inter arrival storm frequency and demonstrate a strong dependence of the emergent channel form on this critical interaction. In particular, simulation results from four different scenarios are presented. The first scenario is simulated without vegetation, and the second, third and fourth scenario are simulated with different non-linear growth trajectory of vegetation. Simulations reveal that, at a particular combination of vegetation growth and its parameterisation, the numerical model is able to transform an active unvegetated synthetic braided river generated by numerical model itself into vegetated single or multi-thread.

6.1 Introduction

Natural gravel-bed braided rivers are characterized by the frequent breakdown and shifting of bars and channels. This produces a spatiotemporally complex assemblage of diverse landforms and associated ecological habitats, reflecting a wide range of ages and evolutionary trajectories (Richards et al., 2002; Figure 6.1a). This mosaic of habitats furthermore, offers higher overall ecological functionality when compared to single thread rivers (Arscott et al., 2002; Ward et al., 2002; Tockner et al., 2006). However, there now exist relatively few contemporary gravel-bed braided rivers which are unaffected by anthropogenic pressures that pose a threat to their geomorphic and ecological functioning. These pressures comprise both direct interventions such as dam construction, flow regulation, gravel mining and building of embankments, but also wider catchment scale effects on flow regimes through land-use change and irrigation and unforeseen effects on climate (see Marston et al., 1995; Surian and Rinaldi, 2003; Tockner et al., 2006; Gurnell et al., 2009; Piégay et al., 2009; Surian et al., 2009b).

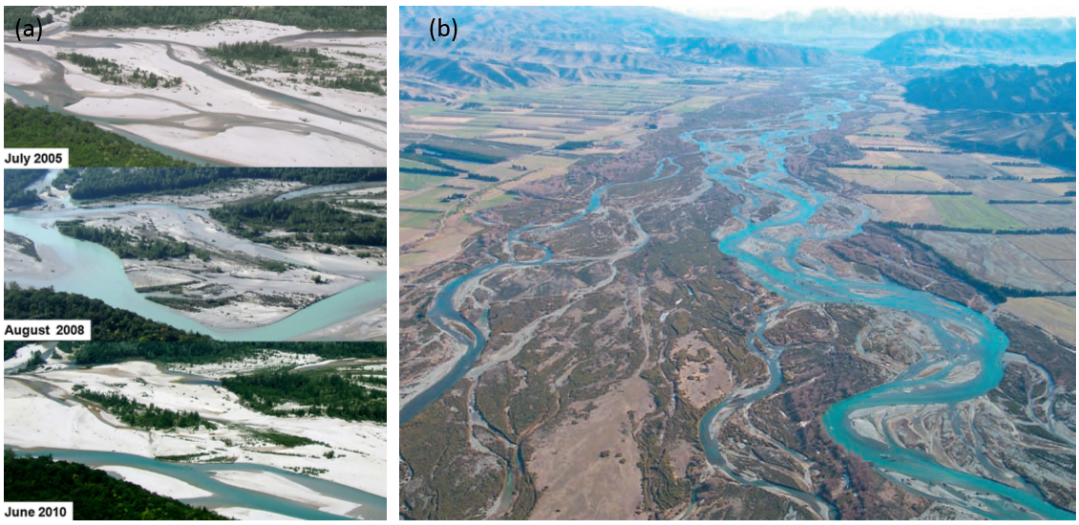

Figure 6.1: (a) Naturally maintained braided Tagliamento River, Italy in different time periods (Photo Source: Gurnell et al., 2012), where reworking of bars, channels, and vegetation patches persist. (b) Heavily managed Lower Waitaki River, NZ (Photo Source: Hicks et al., 2009) where historically highly active braiding system has transformed into vegetation control morphology due to abstraction of water for hydropower generation. Photos are not to scale.

The combined effect of these pressures has been largely to reduce sediment supply and regulate high flows, which has led to the metamorphism of channels from a braided state to less active wandering form, or in extreme cases, incised single thread rivers (e.g., the Ubaye, Ain, Fier, Arve, and Upper Rhône Rivers in France; the Platte River in the USA, and the Waitaki River in New Zealand, the latter shown in Figure 6.1b). Similar trends of change have also been reported in Italy, Austria, Japan, and other parts of the world (see Marston et al., 1995; Surian and Rinaldi, 2003; Tockner et al., 2006; Gurnell et al., 2009; Piégay et al., 2009; Surian et al., 2009b). While the transformation of braided morphologies represents a loss of key habitats, it may also have direct effects on riparian and in-stream assets and implication in contemporary problems such as the undermining of bridges and embankments (e.g., Piégay et al., 2009; Davies et al., 2013).

Conversely, there are examples of the reverse trajectory, in which single thread channels may evolve into a highly active braiding channel pattern. Such cases occur where activities such land-use change, in particular deforestation, leads to an increase in sediment supply to the river (e.g., Waiapu and the Waiapoa from New New Zealand; Piégay et al., 2009). Such scenarios again present complications for river management, and are associated with rapid losses of channel capacity, leading to avulsion of the channel belt, as well as increases in the frequency of flooding, loss of critical infrastructure such as bridges and embankments, and degradation of overall ecosystem functioning (see Piégay et al., 2009).

6.1.1 The Role of Vegetation in River Response

While many case studies are driven to assess such management pressures, there is a wealth of theoretically-inspired science that has sought to quantify the linkages between channel form, flow and sediment transport in order to provide a predictive basis for understanding such channel changes (Lane, 1957; Leopold and Wolman, 1957; Schumm and Khan, 1972; Ashmore, 1991; Germanoski and Schumm, 1993;

Bertoldi et al., 2009b; Redolfi et al., 2016a). However, much of this analysis has focused on the governing physical controls, such as flood frequency and magnitude, channel confinement, sediment supply, grainsize and slope, but largely neglected role that vegetation plays in conditioning fluvial response (Hickin, 1984). More recently however, there is increasing awareness of the critical feedback processes involving vegetation and the physical fluvial processes (see Camporeale et al., 2013; Gurnell, 2014).

The interactions between vegetation and physical fluvial processes are complex and manifold. These include direct effects on flow resistance and bank strength, indirect effects on sediment retention and groundwater dynamics and taken together these leads to emergent reach-scale dynamics that result from the modified feedback between the flow, morphology and vegetation. The direct hydraulic effects relate principally to the additional flow resistance associated with flow over and through vegetation. This incorporates the combined effects of skin drag, form drag, blocking and 3D turbulent interactions, serving in simplistic terms to reduce flow velocity and bed shear stress (Darby, 1999; Tsujimoto, 1999; Bennett et al., 2002; Baptist, 2003; Bennett, 2004; Järvelä, 2005; Ghisalberti and Nepf, 2006; Baptist et al., 2007; Nepf and Ghisalberti, 2008; Liu et al., 2010). At the same time, the below ground properties of vegetation, in particular biomass volume, rooting depth, strength and structure, serve to increase the shear strength of bulk material and decrease erodibility by both increasing the threshold for surface erosion and increasing the critical angle of repose (Smith, 1976; Thorne, 1990; Abernethy and Rutherfurd, 2001; Pollen, 2007; Docker and Hubble, 2008). The effects are not straightfoward however, and vegetation has also been implicated in accelerating mass failure due to the extra surcharge resulting from enhanced infiltration, water storage and the mass loading of the vegetation itself (Abernethy and Rutherfurd, 1998; Simon and Collison, 2002).

Indirectly, the reduction in flow strength encourages sedimentation of both the fine and coarse sediment fractions, and this effect extends to deposited living or dead vegetation which can serve to protect river banks. Such sedimentation processes make vegetated areas a nuclei for the island development, which then drives an emergent set of dynamical responses by changing the active channel width and water table levels (Gurnell et al., 2005; Welber et al., 2013).

The overall dynamical effect of vegetation depends upon the pattern of growth, decay and colonisation (Perucca et al., 2007), which is in turn tuned to the flood frequency and magnitude (Gurnell et al., 2001). Floods facilitate seed dispersal and the propagation of woody vegetation, maintain bar and island moisture content and supply nutrients critical for vegetation growth (Gurnell et al., 2001; Corenblit et al., 2014). Conversely, floods may also cause uprooting, excavation and burial of vegetation (Gurnell et al., 2001; Edmaier et al., 2011).

The preferential location for vegetation growth depends upon the channel form, flow structure and ground water availability (Camporeale et al., 2013). In braided rivers, in particular, the broad pattern of inundation can result in the widespread dispersal of plant propagules, so that recruitment of seedlings and plants, may occur irrespective of elevation. However, the overall long-term survival rate of propagules has been found to increase on higher, elevated stable bars (Francis, 2007; Francis et al., 2009b; Corenblit et al., 2014). In some cases, subsequent vegetation growth and succession may depend strongly upon upwelling of ground water (e.g., Tagliamento River, Italy; see Bertoldi et al., 2011b; Welber et al., 2012), and remains strongly conditioned by species, the method of establishment/reproduction and the hydrological conditions (Francis and Gurnell, 2006; Politti et al., 2018).

For example, in the largely pristine Tagliamento River, Italy, the trees developed from the fluvially deposited propagules of *Populus.nigra* exhibit higher growth rates than

those established from the cuttings and seedlings (Corenblit et al., 2007; Francis et al., 2009b). Indeed, due to its opportunist character, *P. nigra* facilitates rapid sprouting through its roots that results quickly in biogeomorphologically active biomass within two years (see Figure 6.2a and 6.2b; Francis and Gurnell, 2006; Corenblit et al., 2007; Francis et al., 2009b; Corenblit et al., 2014). In heavily managed rivers by contrast, new species may be introduced artificially to stabilize banks. Their characteristic behaviour adapts with the highly variable environment, facilitating abundant seedling, rapid germination and root and shoot growth (Graf, 1978; Johnson, 1994). In some cases, the impact of severe river regulation can change the ecological balance of a reach, enabling rapid and widespread - invasive - colonisation to take place. By creating the 'physical space' for such biological invasions, native species may be displaced by exotic species that are characterised by high tolerance thresholds and become hard to remove. Such effects have been well documented in some of the alpine and piedmont braided rivers in New Zealand, such as the Waitaki and Ahuriri Rivers in which dam impoundments have enabled extensive colonisation of the gravel fairway by European species of Lupins, Gorse and Pines (Tal et al., 2004; Caruso, 2006a).

6.1.2 Bed Stabilisation, Island Development and Reach-Scale Transitions

The multi-directional interaction between flow, sediment and vegetation determines the trajectory of bed stabilization, and ultimately, island building processes (Gurnell et al., 2001). A vegetated island may form through as a result of both erosional and depositional processes. For example, islands may arise from cutoff and avulsion processes, as well as the progressive degradation of anabranches and lateral channel shifting. By contrast, stable areas can develop from 'new' or 'emergent' topography, created by lee-side deposition at channel obstructions or sedimentation and tree stranding at high stage conditions (Osterkamp, 1998). Woody debris can play a critical role in this process, encouraging deposition of sediment thus serving to increase local

relief, creating new habitats for further vegetation recruitment and succession (Fetherston et al., 1995; Abbe and Montgomery, 1996).

Floodplain dissection leading to the erosion and the mobilization of living trees into the active flow may also help to accelerate island building (Gurnell et al., 2001). For example, in the braided Tagliamento River, uprooted trees that have characteristically high plasticity in their trunk and roots, are frequently found deposited downstream over bars following island or floodplain erosional events. Such deposited trees further helps to trap fine sediment, which supports moisture and nutrient retention and so facilitates further growth (Corenblit et al., 2007). Pioneer spp. with broad environmental tolerances, such a *P. nigra* may begin to reproduce vegetatively and with sprouting occurring rapidly from roots of the deposited plant propagules producing bio-geomorphologically active biomass within 1 to 2 years (Figure 6.2 a, b). In the subsequent floods, active pioneer islands have been observed to increase in length, width and thickness (e.g., Figure 6.2c) through compound sedimentation on lateral and lee sides and grow vertically through bar top deposition and concomitant channel incision (Edwards et al., 1999; Gurnell et al., 2001; Corenblit et al., 2007). Following several back and forth cycles of uprooting/burial and succession of vegetation; dissection and aggradation of islands; local avulsion of nearby channels, and coalescence with nearby islands; the bio-geomorphologically active island is transferred into established complex islands having a different mosaic of vegetation (see Edwards et al., 1999; Gurnell et al., 2001; Corenblit et al., 2007; Corenblit et al., 2014).

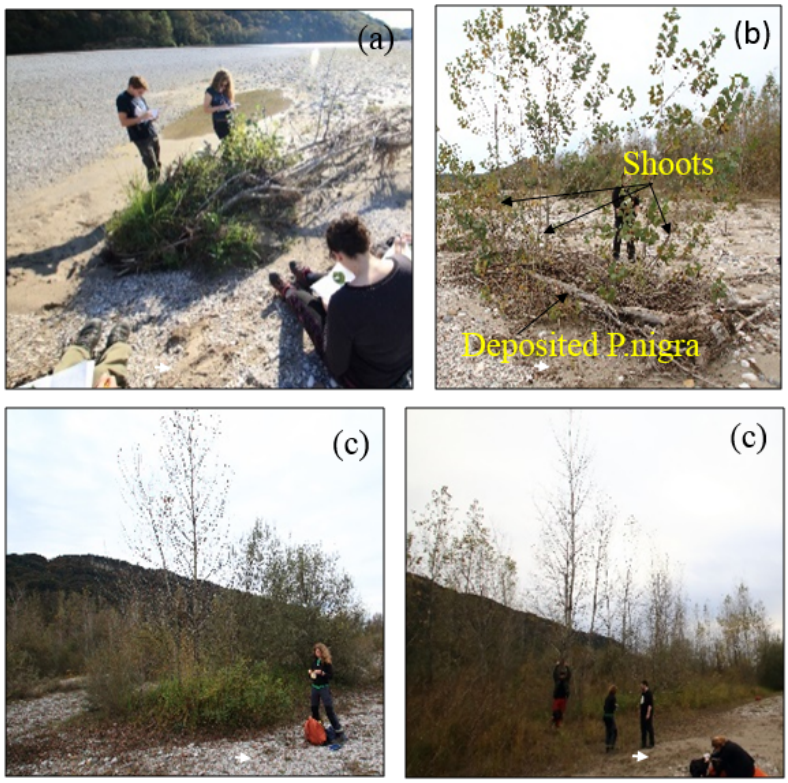

Figure 6.2: Example of islands at different stages in the braided Flaogona Reach in Tagliamento River, Italy. Photos were taken during a field visit in 2017. Figures (a) and (b) typically represent the islands at pioneer stage where shoots development and other species regeneration are taking place. At this stage, the fluvial processes dominate vegetation. Figure (c) typically represents the bio-geomorphic stage where both fluvial processes (avulsion, dissection, and erosion/deposition) and vegetation (succession and uprooting) compete with each other. Figure (d) represents a typical well-established island where vegetation dominates fluvial process, unless a relatively higher order flood arrives. Photos are not to scale.

In unregulated rivers such as the Tagliamento, established islands may ultimately become disconnected from the main flow channel over a wide range of flows (Gurnell and Petts, 2002; Corenblit et al., 2007). The majority of vegetated islands, however, are reworked within a relatively short period (2 - 5 years) and island ages rarely exceed 20 years (Surian et al., 2015). This turnover of islands and channels helps to maintains a steady state of aquatic and ecosystem diversity (Junk et al., 1989; Tockner et al., 2006).

In heavily managed rivers by contrast, particularly where peak flows are reduced, discharge may become restricted to one or two dominant anabranches. Over time,

the increased resistance to erosion of the vegetation banks reduces lateral mobility of the channel, so that the active anabranches become incised, while the minor elevated channels and bars become colonised by vegetation. Such open ecological niches also present an opportunity for invasive species that may outcompete slower growing natives, a pattern seen in systems such as the Waitaki River, NZ (Tal et al., 2004) and the Platte River, USA (Piégay et al., 2009). This results in a decrease in braiding intensity; a decrease in width:depth ratio; a decrease in the channel mobility; and an increase in depth or scour holes (Millar, 2000; Gran and Paola, 2001; Tal et al., 2004; Jang and Shimizu, 2007; Eaton et al., 2010; Tal and Paola, 2010).

6.1.3 Ecosystem Functioning

Observations in fluvial environments suggest that optimal ecosystem functioning and the provision of associated services is achieved when physical and biological processes 'compete' with each other (cf. Piégay et al., 2009; Gurnell et al., 2012). This concept has roots in the 'intermediate disturbance hypothesis' popularised in ecological theory and contends that maximum biodiversity should occur in areas subjected to frequent, but not continuous disturbance (Connell, 1978). This perspective can be used as a framework to understand the relationship between flood processes (and by implication the rate of floodplain turnover) and biomass as the drivers functioning ecosystem and channel form as shown in Figure 6.3. For example, when channel turnover rates are at their highest, vegetation cannot become established and the overall ecological functionality of the system remains limited (Zone 5 in Figure 6.3). Conversely, if fluvial activity is limited to single active channel, the floodplain may quickly be stabilized, and a relatively low-diversity habitat established (Zone 1 in Figure 6.3; see also Richards et al., 2002). In between these two extremes (Zones 2-4) lies a situation where channel activity and biomass growth compete for space, creating a mosaic of surfaces differing in age and community structure, so promoting optimal ecosystem diversity and function.

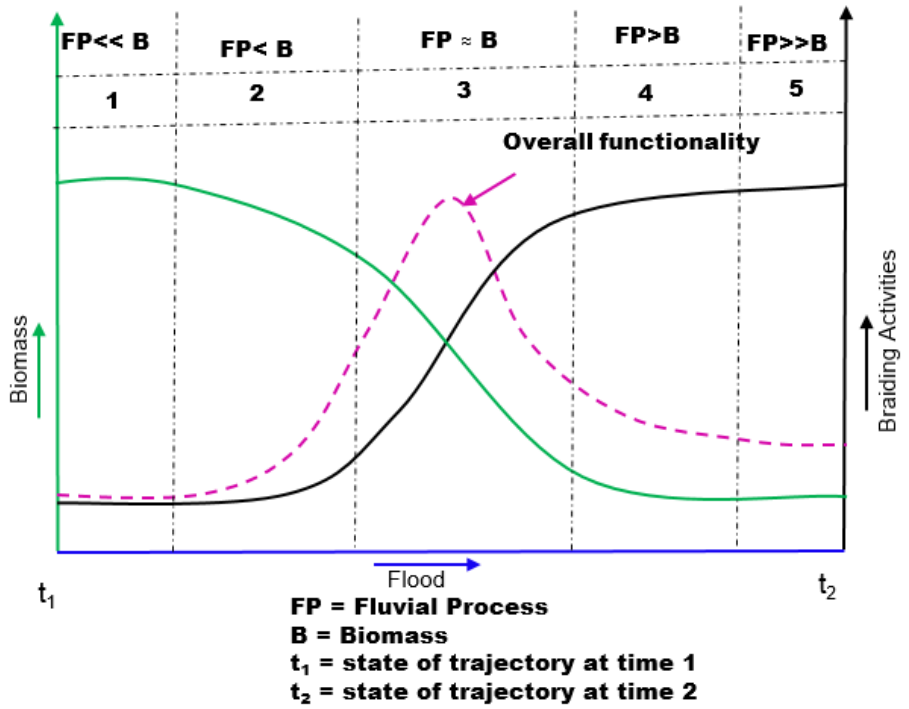

Figure 6.3 Conceptual diagram for understanding the relationship between flood, biomass, braiding activities and overall functionality in trajectory of braided rivers. Biomass (green line) increases with decrease in flood; braiding activities (erosion deposition turnover, breakdown of bars and channel, braiding intensity) (black line) increases with increase of flood, and overall socio-economic and ecosystem functioning (pink line) optimize at the stage when both biomass and floods are competitive. This diagram was prepared taking ideas from Piégay et al. (2009) and Gurnell et al. (2012).

While conceptual models such as described above, provide an insight into the feedbacks and linkages between fluvial process and vegetation, they provide only a qualitative framework to support decision making for active river management (Hicks et al., 2007; Piégay et al., 2009). For example, in the Lower Waitaki, several approaches have been trialled to address the loss of braiding and remove invasive species. This have included the removal of vegetation by mechanical and chemical means and the alteration of regulated flow regimes to include high magnitude floods (through dam releases). Such approaches are however largely based on trial and error, and ultimately these actions have proved to be ineffective (Tal et al., 2004).

6.1.4 Science-Based Frameworks to Support River Management

Field observations provide a valuable tool to gaining qualitative insights into different processes and to developing conceptual models as such of vegetation succession/regression and the development of vegetated islands (e.g., Hickin, 1984; Marston et al., 1995; Edwards et al., 1999; Gurnell et al., 2001; Gurnell et al., 2005; Francis and Gurnell, 2006; Corenblit et al., 2007; Francis et al., 2008; Francis et al., 2009a; Francis et al., 2009b; Bertoldi et al., 2011a; Corenblit et al., 2014; Surian et al., 2015). However, field programmes often lack the temporal perspective necessary to fully interpret the longer-term evolutionary trajectories and responses that lie beyond the scope of most research projects. Flume based modelling provides a useful alternative approach, creating the opportunity for system closure and detailed monitoring of within-state variables, i.e., distributed measurements of bed response and sediment transport (e.g., Gran and Paola, 2001; Tal et al., 2004; Coulthard, 2005; Jang and Shimizu, 2007; Tal and Paola, 2010). This approach provides detailed, quantitative data that can be used to test conceptual models of vegetation colonisation and island development (e.g., Welber et al., 2013). However, again, the approach suffers problems associated with the scaling of sediment and vegetation together with interrogating the long-term trajectory.

In this context, numerical models, provide a new and exciting tool to test hypotheses concerning the controls on the evolutionary trajectory of river systems, and examine scenarios that represent a range of management approaches. In this form, models are both the classic vehicles of the scientific method, but also practical frameworks to examine the feedbacks involved channel adjustment, as well as the sources of predictive uncertainty and the potential range of outcomes. Nevertheless, development of numerical models that incorporate sufficient representation of the complex process in the interplay between physical and biological forcing in rivers is still in its infancy (Gurnell et al., 2012; Camporeale et al., 2013; Gurnell, 2014).

In the past decade, a number of models and studies have attempted to examine the feedbacks between flow, sediment and vegetation (e.g., Jang and Shimizu, 2007; Takebayashi and Okabe, 2009; Crosato and Saleh, 2011; Li and Millar, 2011; Nicholas, 2013; Ziliani et al., 2013). Most of these approaches, involve significant abstraction and heavy parameterisation of the processes, for example assuming complete removal of vegetation or succession to a presumed equilibrium state. This precludes the examination of emergent phenomena that arise without pre-defining the nature of interactions, and consequently limits insights into the nonlinear trajectory of vegetation succession and retrogression and its footprint on morphodynamics.

Recently, a number of conceptual models of riparian vegetation dynamics have emerged with the aim to simulating vegetation community development, driven primitively from simple hydraulic/hydrological and topographic variables, such as flood/ground water conditions (e.g, Camporeale and Ridolfi, 2006; Perona et al., 2009; Gurnell et al., 2012). This provides a more flexible scheme to model physical-biological interactions, though to date, these models have been adapted only for schematised cross-sections and rather than into two or three dimensional morphodynamic models. More recently, Bertoldi et al. (2014), attempted such coupling, linking a simplified vegetation dynamics model with the 2d morphodynamic model used in this thesis, the BASEMENT. This ground-breaking paper sought to examine the links between vegetation and channel dynamics for a simplified single thread channel. There is, therefore, considerable scope to consider whether this framework can be applied to examine the process interactions and responses in more complex, braided rivers.

6.2 Aim and Objectives

The research presented in this Chapter aims to quantify the linkage and feedbacks between fluvial process and vegetation colonisation/die-back in braided rivers through the use of a new vegetation dynamics model integrated into BASEMENT.

The research focuses on two specific objectives:

a) to analyse the parameteric sensitivity of the vegetation dynamic model proposed by Bertoldi et al. (2014) and consider strategies to apply the model within the context of a braided river;
b) to quantify the linkage between different patterns of vegetation colonisation and evolutionary trajectory of the equilibrium-braided river.

Integrating all of these, this work lead to a level of clarification on the sensitive parameters related to the vegetation dynamic model and presents the response of different scenario of vegetation colonisation on the geomorphic trajectory.

6.3 Methods

6.3.1 Study Prototype

Early work by Werritty and Hoey (2004) suggested that spatiotemporal variation of bars and channels on the braided River Feshie, Scotland is associated principally with varying hydrological events, local bank erosion, reduced sediment supply and rapid avulsion or cut off formation. While they provide an explanation for the mechanisms involved in braiding on the Feshie, the maintenance of a braided planform remains somewhat surprising given the relatively small sediment load of the river. Wheaton et al. (2013) suggested that a key source of sediment supply to drive braiding processes originates from local reworking of the braidplain through continual lateral migration of the channels. This lateral mobility is facilitated by the low critical angle of repose of the coarse gravel bars, which lack the stabilising effect of dense vegetation

communities and in particular trees. This limited vegetation cover reflects the rapid expansion of the local deer population since the 1970s, which graze on the floodplain, supressing the development of the native populations of *Betula pendula* (birch) and *Pinus sylvestris* (Scots pine).

Local concerns over the negative impact of the rising deer population on native woodlands across Scotland, has in recent years forced a radical revision of policy, resulting in major deer cull under the auspices of the Scottish Deer Commission (Clutton-Brock et al., 2004). This controversial plan, reduced deer number on the Glenfeshie estate from an estimated 35 down to 3 animals per km^2 and has now creating the beginning of a major forest recovery on both the hillsides and valley floor (Bell, 2012). There is therefore, an interesting natural experiment taking place in Glenfeshie, and this research offers an opportunity to create a baseline of understanding that might help inform future research.

The objective of this study is not, however, to compare the model behaviour deterministically to observations in the field. Such attempts at model validation suffer from uncertainties in the initial and boundary conditions as well as an incomplete description of processes in the model as discussed earlier Chapters. Rather, the goal here is to explore how a simulation modelling framework can be used to help understand the generic interaction between flow, sediment and vegetation on morphodynamics of braided rivers more broadly.

Nevertheless, a reference case is needed to formalise the study, so simulations here take the synthetic equilibrium braided morphology generated by the run R_9 in the Chapter 4 as an initial topography that is free from vegetation (Figure 6.4). As discussed in Chapter 5, this topography is model generated, and so should avoid the introduction of transient effects associated with adjustment to new boundary conditions. For completeness, this model has a reach averaged width of 175 m, a

longitudinal slope of 0.92%, a single grain size sediment (D_{50}= 30 mm) and was formed under constant discharge over 12 years, based on a steady flow corresponding to the two-year return period flood of 70 m^3/s.

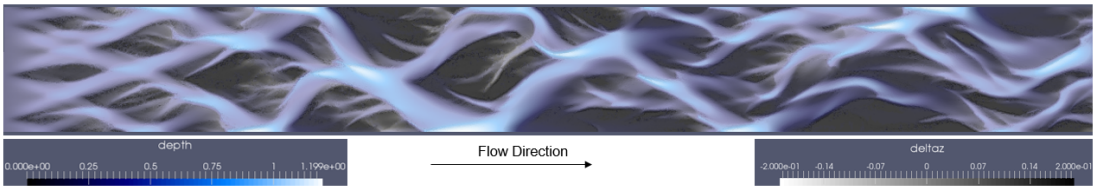

Figure 6.4: Equilibrium topography (Initial topography for simulations in this chapter) generated by the model itself adopting reach averaged width (175 m), longitudinal slope (0.92 %), single grain size sediment (D_{50} = 30 mm), and constant discharge (two years return period flood = 70 m^3/s), which are representative of the natural prototype Feshie.

6.3.2 The Vegetation Model

Bertoldi et al. (2014) described a new vegetation dynamics model introduced as a subroutine for BASEMENT. For this study, Dr. Annunziato Siviglia, ETH Zürich and Dr. Walter Bertoldi, UNITN had provided the numerical code to model vegetation dynamic that was not available in the freeware version of the BASEMENT numerical model (thanks to them). This simple framework abstracts much of the ecological complexity, seeking not to define the nature of the vegetation community itself, but rather focus on how vegetation growth and die-back influence the physical processes affecting morphodynamics. However, while simplified, the model goes beyond existing tools used in morphodynamic models which simply define fixed flow resistance terms or erodibility constants, and fail to take account of the evolution of the biological community (e.g., Jang and Shimizu, 2007; Takebayashi and Okabe, 2009; Crosato and Saleh, 2011; Li and Millar, 2011; Nicholas, 2013; Ziliani et al., 2013). By contrast, the vegetation tool within BASEMENT numerical model incorporates a non-linear growth model and distribution. Implementation of the model involves three steps, which are discussed in detail below:

a) calculation of equilibrium biomass distribution over space;

b) definition of biomass growth and decay rates; and

c) parameterisation of relationships between biomass, flow resistance (roughness) and erodibility.

a) Defining an Equilibrium Vegetation Distribution

The first step in modelling vegetation dynamics in BASEMENT involves the definition of the maximum possible distribution of bio-geomorphologically active vegetation (biomass) at equilibrium. This spatial distribution is determined here as a function of elevation and water level based on the following form posited by Marani et al. (2013), and developed for riparian areas and marshlands. This 'Marani' function is:

$$B_{eq}(z) = \frac{\phi}{\exp^{\lambda_1(z-z_o)} + \exp^{-\lambda_2(z-z_o)}} \qquad \text{Eq. 6. 1}$$

Where, B_{eq} is dimensionless equilibrium biomass (Bertoldi et al., 2014); z is elevation, ϕ is a parameter to normalize the equilibrium biomass B_{eq} to unity; λ_1 and λ_2 are parameters that control the shape of the distribution curve (the rate by which vegetation decays from its local maxima), and zo is location of maximum biomass which implicitly refers to the conditions of moisture (ground water) availability. This equation has the flexibility to model localized variations in vegetation cover by varying the shape parameters λ_1 and λ_2. The effect of these parameters on the biomass/elevation relationship is shown below in Figure 6.5.

As illustrated by this set of curves, a model using λ_1 = 0 and λ_2 = 2.5 results in an increase in the equilibrium biomass with elevation, a pattern which reflects that associated with a flood dominated river, where low lying vegetation cannot become established due to frequent inundation and erosion. By contrast, for λ_1 = 02.5 and λ_2 = 0 results in a distribution of biomass concentrated below mean bed level, better reflecting conditions associated with ground water loving plant communities in low energy rivers. The parameter set λ_1 = 2.5 and λ_2 = 2.5 concentrates biomass at mean bed level, reflecting a mixed regime river (cf. Perucca et al., 2007). By, using lower

value of λ_1 and higher value of λ_2, e.g., 2.5 and 10 respectively, results in a skewed distribution peaking above mean bed level and maintaining higher biomass at elevation. Finally, setting both parameter values to zero, results in an unselective distribution of uniform biomass (see Figure 6.5 for these dhapes).

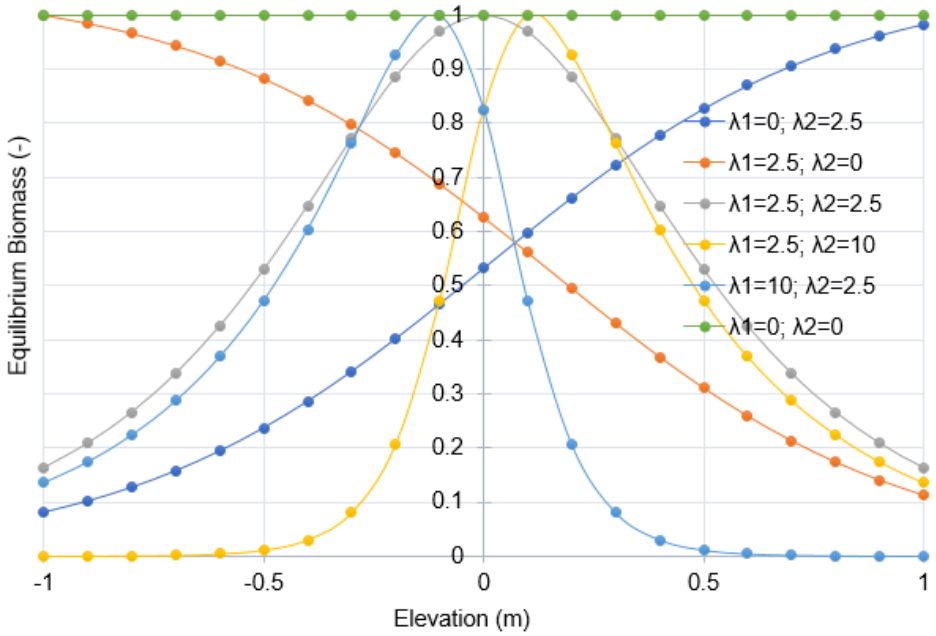

Figure 6.5: Different way of localizing equilibrium vegetation using the Marani function. These calculations were made fixing z_o at 1.15 m and varying λ1 and λ2. The case with both λ1 and λ2 equal to zero means same equilibrium biomass on all elevations, which was considered in all simulations in this study. These calculations were made for a hypothetical cross-section varying elevation between -1 and 1.

The initial plan was to scrutinize sensitiveness of these various options of vegetation localization. However, due to limited HPC facilities (here 1 simulation takes around 20 days), simulations were carried out with both λ_1 and λ_2 equal to zero (horizontal line in Figure 6.5). This means that all cells in the numerical domain consider equal equilibrium vegetation or biomass (equal opportunity to grow). This is indeed the simplest case and was needed to test before increasing complexity of the model.

b) Vegetation Growth Model

Vegetation growth towards the normalised equilibrium distribution predicted by the Marani function (discussed in preceding section) is computed using the ordinary

differential equation (e.g., Tucker and Bras, 1999; Baptist et al., 2007; Bertoldi et al., 2014; Perona et al., 2014):

$$\frac{db}{dt} = \sigma\left[B(eq) - B(t)\right] \qquad \text{Eq. 6. 2}$$

Where, σ is growth rate, which is calculated as the function $3/T_v$; where T_v here represents the time required for vegetation to attain equilibrium state starting from zero; dt is the time step; db is the change in biomass in time step dt; B(t) is the instantaneous biomass, B(eq) is the equilibrium biomass.

Solving the coupled vegetation-morphodynamic system poses computational issues due to the mismatch in the relevant timescales that control flood hydraulics (minutes to hours) and vegetation growth (years to decades). For example, within a decade during which riparian vegetation communities develop, the total time during which the channel adjusts may sum to no more than a few days, but may in turn, require a model timestep in the order of seconds or less to provide a stable solution of the driving hydrodynamic processes. Thus, slaving the coupled system to the timescale of the fastest component (the hydrodynamics) would present a major computational overhead, preventing the development of simulations over relevant durations.

A solution to this, is found by: a) limiting vegetation growth to inter-storm periods; and b) parameterizing the vegetation growth rate so that the biomass advances to an equilibrium vegetation state in a matter of hours rather than years. This approach allows the representation of full suite of processes to be simulated using a single timestep, even though in effect, time is being rescaled for the vegetation growth model (i.e., 1 hour = 2-10 years).

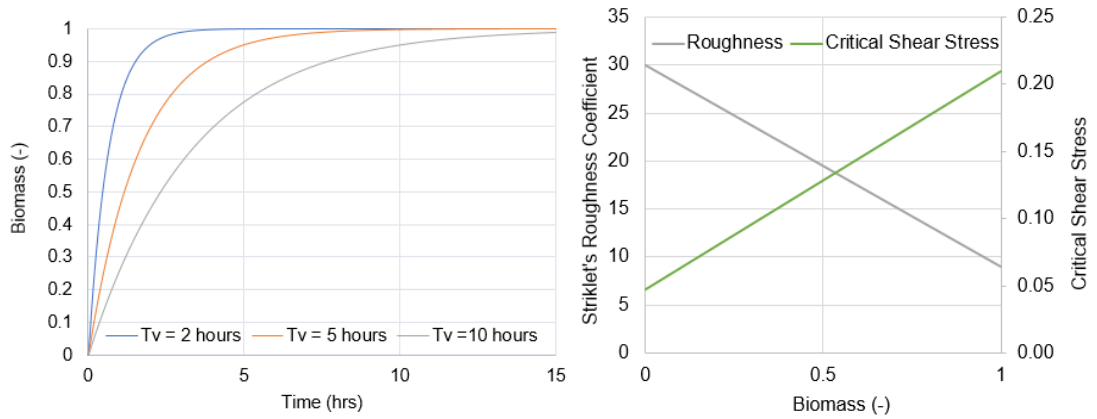

Figure 6.6: a) Three different vegetation growth rate curve; b) magnitude of biomass and corresponding roughness and critical shear stress in the vegetated area. In Figure a zero biomass refers to the bare gravel area and 1 refers to the maximum equilibrium biomass. For example, if instantaneous biomass is 0.5 (see a, b), the model takes roughness of 19 and critical shear stress 0.13 (see b).

Figure 6.6a illustrates three parameterisations of the growth rate curve, which reach the equilibrium state within 2, 5 and 10 hours (simulation time) respectively. No attempt is made here to correlate or scale these growth rates to specific natural timescales. It is useful, nonetheless, to note that the time taken for herbaceous species to colonize bar surfaces in the Feshie takes between 1-5 years and continuous cover of grass or Erica and Caluna spp. occurring typically within 10-15 years (Brasington, per commm, 2014-2017). As such, the 2, 5 and 10-hour timescales used here, are best considered as relative scales, representing *fast* (i.e., 2 hours is 5 time faster than 10 hours), *medium* (2 times faster than 10 hours) and *slow* (the 10 hour) growth rates. The biomass of a cell is removed and set to zero, if sediment entrainment is predicted to occur. For example, biomass is set to zero if the instantaneous dimensionless shear stress of a cell exceeds the critical shear stress assigned for sediment entrainment (Figure 6.6b).

c) Parameterizing Vegetation into Critical Shear stress and Roughness

To incorporate the effects of vegetation on morphodynamics, the estimated instantaneous biomass provided by (a) and (b) above, must be used to rescale estimates of the local bed roughness, as a proxy for vegetative effects on flow

resistance, and the critical shear stress for entrainment of bed particles (e.g., Jang and Shimizu, 2007; Takebayashi and Okabe, 2009; Crosato and Saleh, 2011; Li and Millar, 2011; Nicholas, 2013; Ziliani et al., 2013).

The physical processes controlling the erodibility of the bed are complex, relating to the effects of particle size and sheltering on the partitioning of bed shear stress, and the effects of particle packing on the resistance to entrainment (see Edmaier et al., 2011; Politti et al., 2018). This latter property is most often linked to an effective friction angle (ϕ') through which a particle must pivot to be entrained into the flow. This in turn, can then be related directly to critical shear stress (θ_{cr}) in conventional sediment transport calculations (see Millar and Quick, 1993; Li and Millar, 2011). This enables the critical shear stress to be expressed as a function of friction angle and an empirical scaling constant, *c* (Eq. 6.3).

$$\theta_{cr} = c \tan \phi' \qquad \text{Eq. 6. 3}$$

A range of values have been suggested for the empirical constant, *c* (see Li and Millar, 2011). Here, taking the friction angle for unconsolidated gravel to be 40^o and the critical dimensional shear stress to be 0.047 (after,Meyer-Peter and Müller, 1948) the corresponding value of c is found to be 0.056. Taking c as constant (0.056), the effects of vegetation density (biomass) can then be represented by modifying the effective friction angle alone.

Previous work by (e.g., Millar, 2000; Li and Millar, 2011) suggests indicative friction angles for bare, unconsolidated gravel and surfaces with 'moderate' and 'strong' equilibrium vegetation cover as 40^o, 60^o and 75^o respectively. The vegetation growth model described above, follows an exponential path towards equilibrium (Eq. 6.2) so that instantaneous biomass varies both spatially and temporally, between zero and the equilibrium state (i.e., 0-1), with the critical shear stress adjusting proportionally.

For this study therefore, the equilibrium state was set to reflect a 'strong' vegetation community with the friction angle of 75°. According to Eq. 6.3 therefore (and taking c = 0.056) the dimensionless critical shear stress for continuous cover (biomass = 1) is 0.21. As such, the critical shear stress varies between 0.047 for bare gravel or biomass = 0 to 0.21 for continuous vegetation cover and biomass = 1, with values in between interpolated as a function of the biomass as shown in Figure 6.6b.

To account for the effect of vegetation on the enhancement of flow resistance, a simple linear relationship between the Strickler *Ks* parameter (where *Ks* = 1/n) and the instantaneous biomass (varying between 0-1) was used. In previous work by Bertoldi et al. (2014), a Strickler *Ks* of 9 $m^{1/2}/s$ was used to account for an equilibrium coverage of 'strong' vegetation. This compares to the *Ks* = 30 $m^{1/3}/s$ used to represent bare gravel (d_{50} = 30 mm) used in Chapters 4 and 5. In common with the effect of biomass on critical shear stress, simple linear interpolation was used to determine the value of *Ks* between these two end-member states as shown in Figure 6.6b.

6.3.3 Experimental Design

a) Model Schematisation

All simulations described here were initialised using simulation R_9 (Chapter 4) to define the initial conditions, comprising a rectangular spatial domain (1550 m x 175 m), discretized into triangular cells with a maximum area of 2 m^2. A uniform sediment mixture was again used, comprising a 2.5 m thick bed of sediment with a D_{50} = 30 mm. The classical Meyer-Peter and Müller (MPM) sediment transport formula, except now, as described above, the critical dimensionless threshold for entrainment was rescaled to account for the local biomass volume (0-1). Following the results obtained in Chapter 4, the effect of gravity on sediment transport over a sloping bed was modelled using the standard Ikeda (1982) formulation, using a lateral transport factor set to 2.0. Similarly, bank erosion was modelled using the geotechnical approach in which different critical angles of repose are defined for dry, wet and deposited material

respectively, taken here to be 25°, 18° and 5° as identified in Run R_9. Sediment transport calculations were carried out at the same scale as the shallow water wave solver, so that no Morphologcial Accelaration Factor (MORFAC) was used.

b) Boundary Conditions

The relationship between channel morphodynamics and vegetation growth was examined here using an unsteady simulation framework, based on a sequence of fifteen cyclic floods, each representing one year of component flow. Following the schematisation of Chapter 4, the individual floods comprised 7.836 hours steady high flow, here set to 70 m^3/s (reflecting the two-year recurrence interval flood peak) followed by one hour of steady low flow at 20 m^3/s (half of the annual flood discharge of Feshie). The flow boundary condition is represented in Figure 6.7.

The vegetation growth model was activated only during the one-hour low flow period between hydrographs. During this time, vegetation was allowed to grow on dry surfaces, at a rate that accounted for the total time the give cell had remained dry, i.e., a memory of the prior flood condition was used to initialize the growth rate. At the end of the one-hour low-flow period, the spatial distribution of vegetation biomass was updated and cell-by-cell values of the Strickler roughness coefficient (Ks) and the dimensionless shear stress estimated.

During high flow events, vegetation growth ceases and the channel bed is reworked according to the morphodynamic subroutines. Biomass is set to zero or removed, if the instantaneous dimensionless shear stress of a cell exceeds the critical shear stress assigned for sediment entrainment accounting biomass as indicated in the Figure 6.6b. This means that the effect of root reinforcement and drag force was implicitly parameterized by increasing critical shear stress for erosion (e.g., Bertoldi et al., 2014).

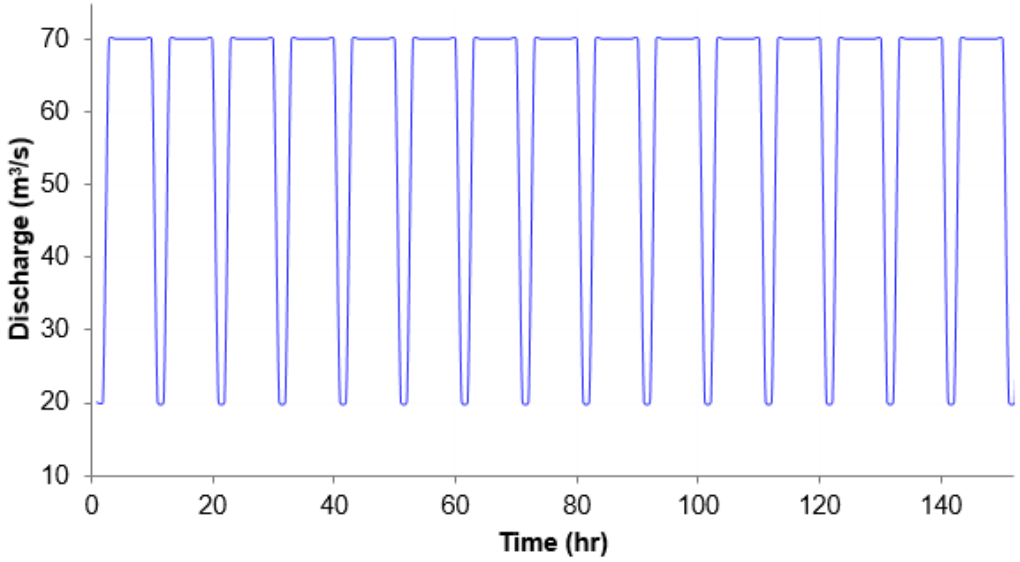

Figure 6.7 Simulation hydrographs with fifteen cyclic low flow (20 m^3/s) for one hour and subsequent high flow (70 m^3/s) for eight hours.

c) Experimental Design

The interaction between vegetation, flow and sediment transport and the consequences for the morphodynamic evolution are complex. Here, a simple experiment was designed to examine only the effect of varying vegetation growth rate towards the same equilibrium condition. Three simulations were used to examine a range of growth rates, scaled to reflect conditions of low (R_2), medium (R_3) and high (R_4) growth rates in which equilibrium conditions are achieved after 2, 5 and 10 hours respectively (Table 6.1). For each of these simulations, a uniform spatial distribution of equilibrium biomass was assumed by setting the λ parameters of the Marani function (Eq. 6.1) to zero. This represents a significant simplification of the ecogeomorphological interaction and reflects computational demands of the scale of the domain and the duration (15 years) of simulations necessary to evaluate system response. There is clearly, significant scope to extend the experimental design to incorporate a range of different parameterisations of the Marani function, but this is considered to lie out of the scope of the current experiment (e.g., Bertoldi et al., 2014 for comparision). In addition to the vegetated simulations, a further bare-gravel model, run R_1 was developed using the same physical initial and boundary conditions to

provide a control against which the ecogeomorphological models can be compared. A full list of the simulation parameters is given below in Table 6.1.

Table 6.1 Summary of simulated runs and numerical parameters

Run	*Discharge* [a] *(m^3/s)*	*Floods (nos.)*	*z_o (m)*	*λ_1 (m^{-1})*	*λ_2 (m^{-1})*	*T_v (hrs)*	*θ_{crv} (nos.)*	*K_v ($m^{1/3}/s$)*
R_1	*20 - 70*	*15*	*-*	*-*	*-*	*-*	*-*	*-*
R_2	*20 - 70*	*15*	*1.15*	*0*	*0*	*10*	*0.21*	*9*
R_3	*20 - 70*	*15*	*1.15*	*0*	*0*	*5*	*0.21*	*9*
R_4	*20 - 70*	*15*	*1.15*	*0*	*0*	*2*	*0.21*	*9*

[a] the low discharge (20 m^3/s) is simulated for one hour which is then followed by high flood of constant magnitude (70 m^3/s) for 7.836 hours.

6.4 Results

Results were analysed, following the quantitative framework proposed in Chapter 3; incorporating metrics to quantify the model response in terms of planform, topographic, hydraulic and morphodynamic characteristics. Planform maps displaying water depth and biomass and figures quantifying the total braiding index through the simulation period were used to describe the planform evolution. Elevation, distribution, bar height and channel shape were used to describe evolution in terms of topographic signatures of the synthetic channel. The percentage of area occupied by different water depths was used to provide an insight into hydraulic evolution of the system, while the spatial distribution and volumes of erosion and deposition, along with sediment transport rates, active width and active braiding index were used as to describe morphodynamic evolution. Biomass dynamics were analysed in terms of reach averaged value, the location with respect to elevation and overall frequency distribution.

It is useful to reiterate here, that the objective of this study was not to compare the model behaviour deterministically to observations from the field. Instead, the goal is

to examine the internal processes that lead to the emergence of differing channel states under differing vegetation growth rate scenarios.

6.4.1 Planform Signatures

a) Planform

The initial state for all runs was a fully developed braided river in an equilibrium state, derived at a steady formative discharge of 70 m^3/s. The resulting channel is characterized by two dominant anabranches that divide and rejoin around approximately equal size and spaced bars, which in turn have dissected bar tops reflecting a complex pattern of compound evolution (see the first image in Figure 6.8). This broad planform pattern is maintained in a qualitatively similar form throughout the full 15-year simulation period for the unvegetated model run, R_1. The bed is, however, far from fixed during this simulation, and the evolutionary planform sequence shown in Figure 6.8 illustrates frequent reworking of the bed, with shifts in the dominant channels changing as flow is unevenly divided at dynamical bar head location (this can also be visualized in erosion and deposition maps in latter section).

Figure 6.8: Planform trajectory displaying spatial distribution of water depths overlaid on elevation at high flow (70 m^3/s) (Run R_1 without vegetation). The domain width and length are 175 m and 1550 m, respectively.

In contrast, the runs with vegetation resulted in significant planform adjustment. For simulations R_2 (slow growth) and R_3 (medium growth), the dominant anabranches became more sinuous and the reach became 'anchored' by densely vegetated, bank attached alternate bars (see Figure 6.9 and Figure 6.10). The density of vegetation was, as expected, greater for the medium growth rate model, R_3. Nonetheless, it is clear that the areas of densest vegetation growth in this simulation are continuously reworked and bar patterns remain in a constant state of flux. The fast growth rate

model, R_4, is quickly colonised by vegetation (Figure 6.11), with large areas of the bed at the equilibrium vegetation cover (Biomass ~1) within 2 years as implied by the growth curve. Unlike R_2 and R_3 however, there is a clearer trajectory to the evolution characterising this simulation. While the system remains braided throughout the simulation, the width of the active anabranches appears to reduce over time, and activity becomes gradually restricted to the centre and true left of the braided fairway, while large areas of the true right appear to become stabilised and take on the form of a terrestrialised floodplain.

The vegetation dynamic pattern in the three runs can be summarized as follows. In general, during the first low flow period, the survival rate of vegetation on the elevated area (bars) was comparatively high compared to the low elevated areas (channels). The subsequent flood then largely removed vegetation in the channels but not elevated bars. Vegetation that survived in the subsequent flood begins to exert control on the processes of erosion and deposition depending upon their age and colonisation state. In the long-term, depending upon the competition between fluvial process and vegetation, succession and retrogression of vegetation take place. For example, areas not experiencing sediment transport continue to grow to reach the equilibrium state quicker. By contrast, areas experiencing episodic sediment transport pass through repeated cycles of succession and retrogression limiting the overall development of biomass. This cycling of vegetation growth and removal eventually results in a spatially and temporally variable distribution of vegetation representing surfaces of different ages and biomass. The time taken for vegetation to reach to the equilibrium state, which was parameterized externally, plays a major role in controlling overall colonisation pattern and the shifting dynamics. For example, in the run R_3, the time required for vegetation to reach the equilibrium state was defined as 10 hours, requiring therefore 10 low flow periods of undisturbed growth. By contrast, the fast

growth rate applied in run R_4 requires only 2 hours for vegetation to reach to the equilibrium state.

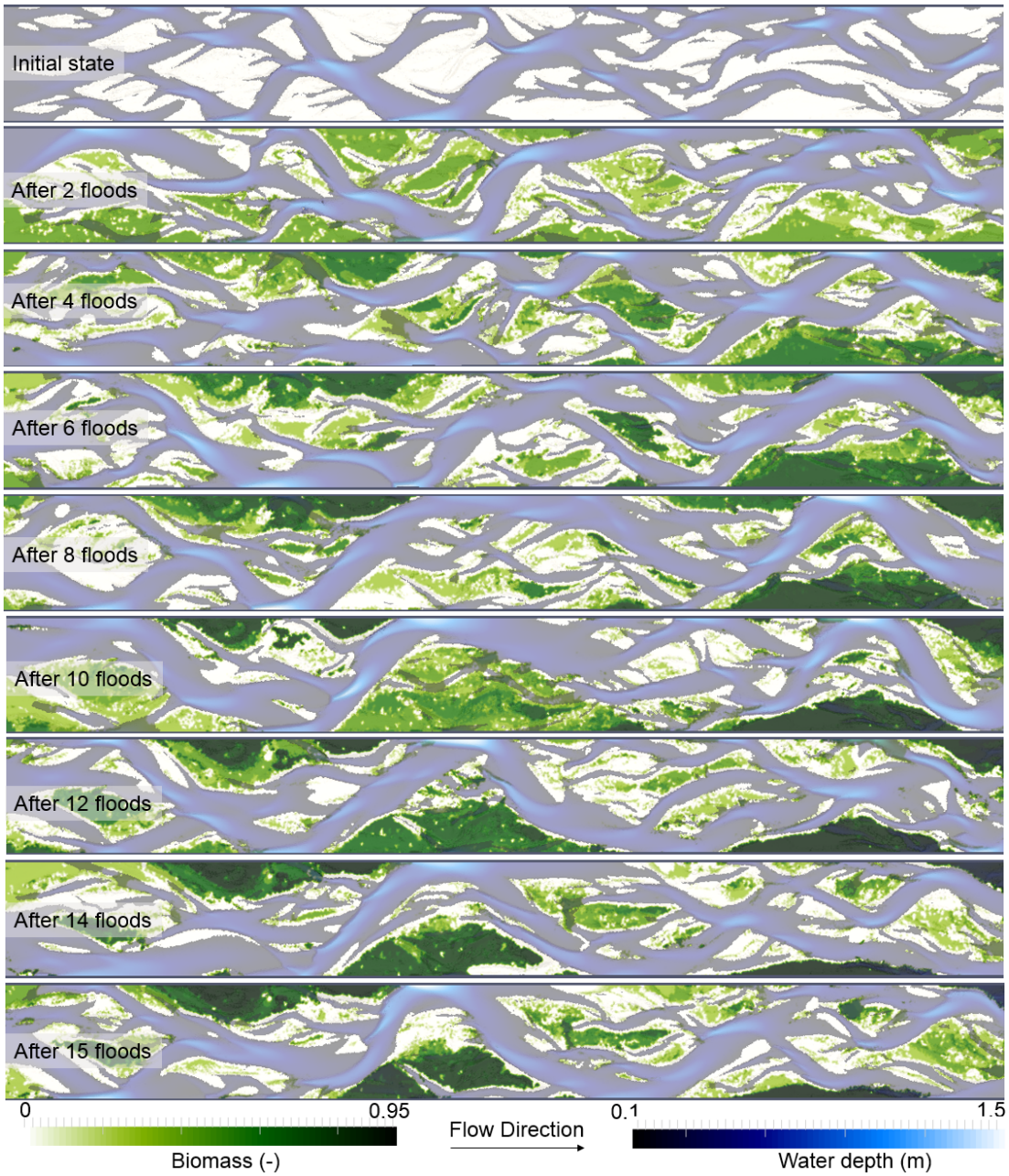

Figure 6.9: Planform trajectory displaying spatial distribution of water depths overlaid on biomass at high flow (70 m^3/s) at the end of flood (Run R_2 – slow colonisation). The domain width and length are 175 m and 1550 m, respectively.

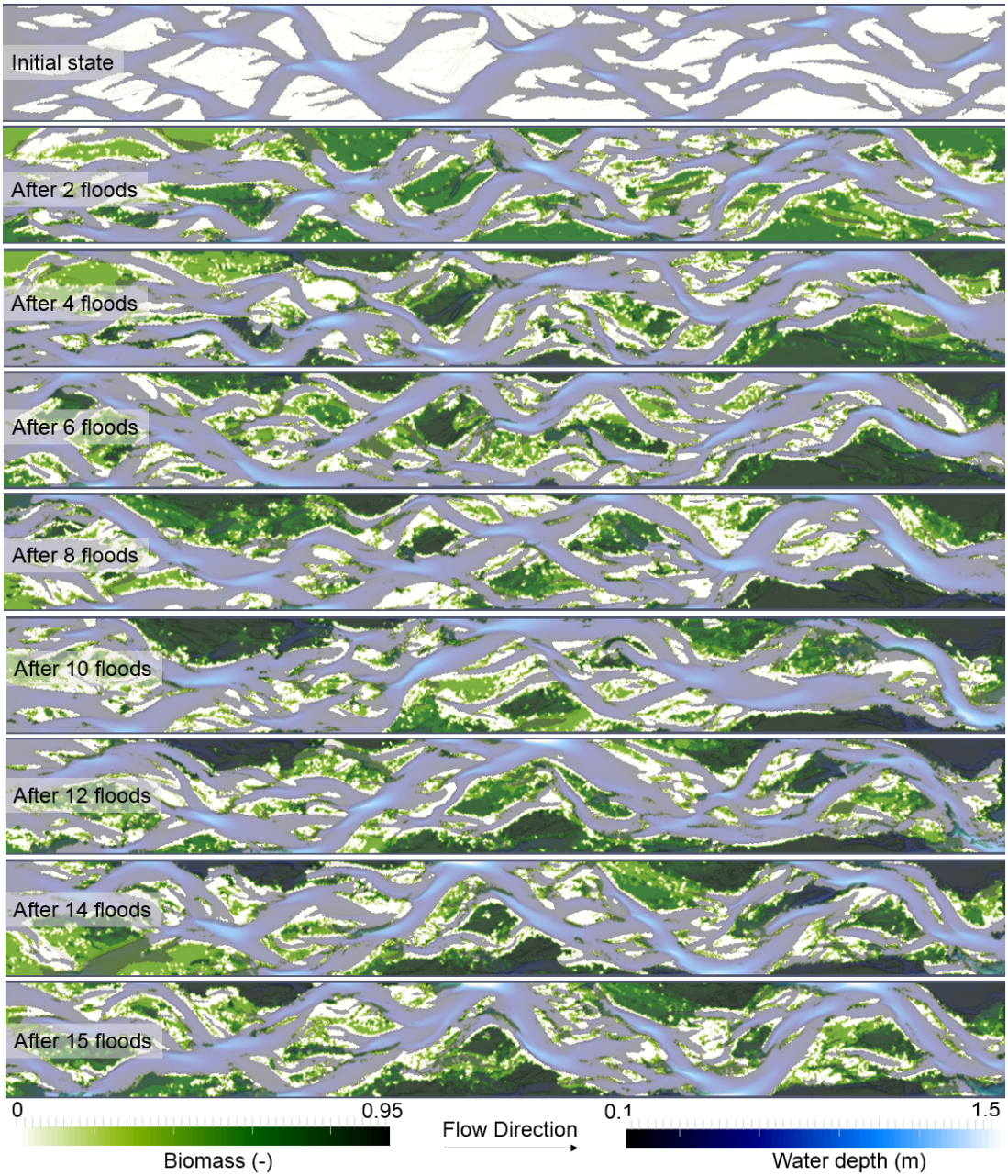

Figure 6.10: Planform trajectory displaying spatial distribution of water depths overlaid on biomass at high flow (70 m^3/s) at the end of flood (Run R_3 – medium colonisation). The domain width and length are 175 m and 1550 m, respectively.

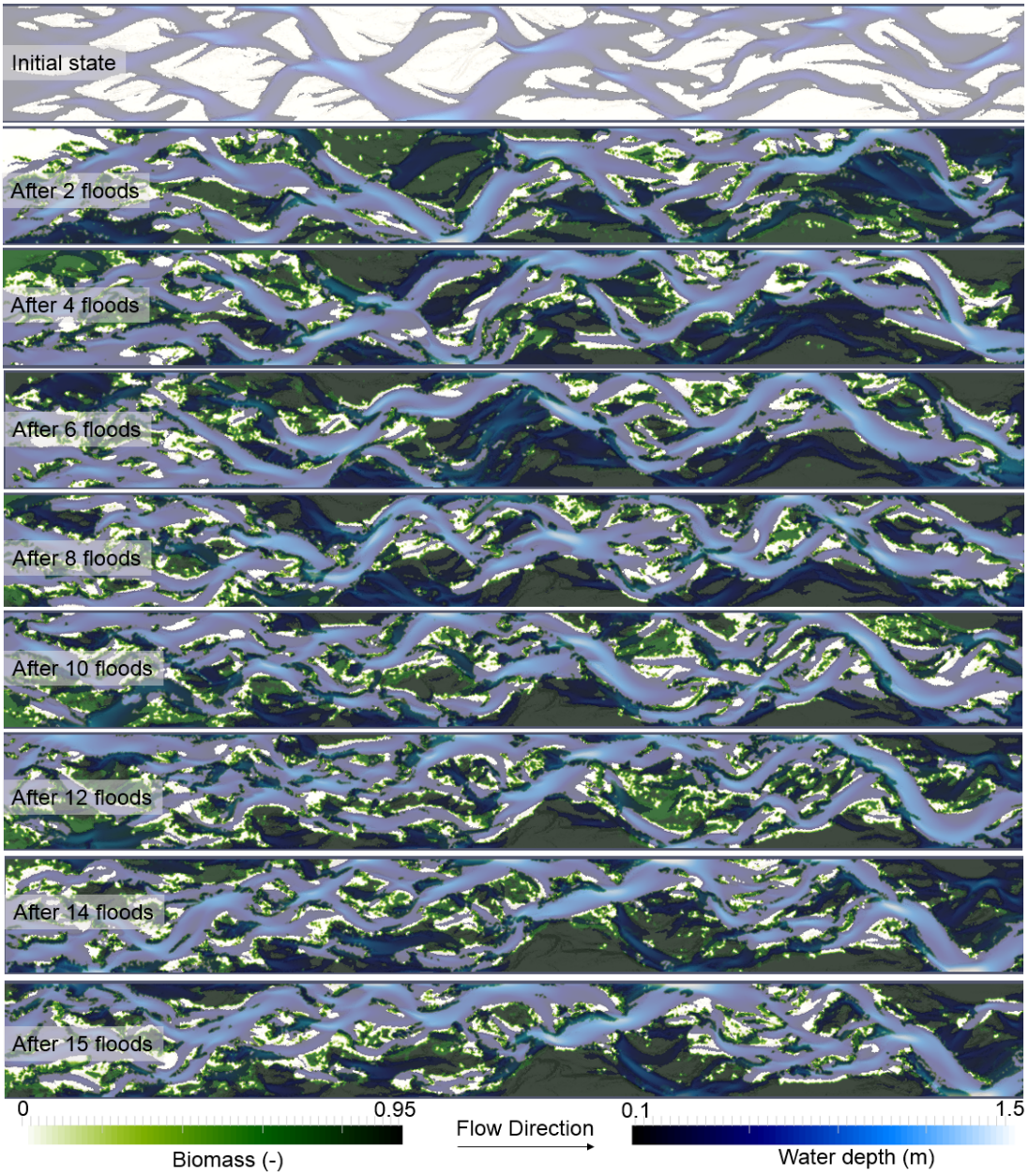

Figure 6.11: Planform trajectory displaying spatial distribution of water depths overlaid on biomass at high flow (70 m^3/s) at the end of flood (Run R_4 – fast colonisation). The domain width and length are 175 m and 1550 m, respectively.

Morphologically, the key changes during the vegetated simulations appear to the contraction of anabranch width, and while the rivers maintain multiple channels, it appears as though discharge is progressively carried by a single main channel. At the same time, the small dissected central bars gradually coalesce and are amalgamated into larger side-attached bars fixed to the outer banks. These processes occurred at the fastest pace in run R_4, followed by the run R_3 and R_2, respectively correlating to

the vegetation grown rates. As a consequence, the run R_4 is quickly transformed into an island-dominated braided system after only two floods. By contrast, the run R_2 and R_3 took a longer time to change their initial multi-thread form to sinuous form.

b) Total Braiding Index

The evolution of the Total Braiding Index (TBI) for each simulation is shown in Figure 6.12. Intriguingly, and reflecting the qualitative insights described above, the TBI actually appears to increase in the vegetated simulations, rising from a mean of 3.6 for the bare model (R_1) to 4.4 for R_4. This appears to run contrary to expectations, but it should be recalled here, that the TBI is actually defined topographically, and provides an index of local bed complexity (reflecting variations above and below mean bed level). The planform maps do indeed indicate a more complex flow network for simulations R_2 and R_3 in particular, with flows concentrated into a larger number of narrower anabranches, characterised by shorter wavelengths.

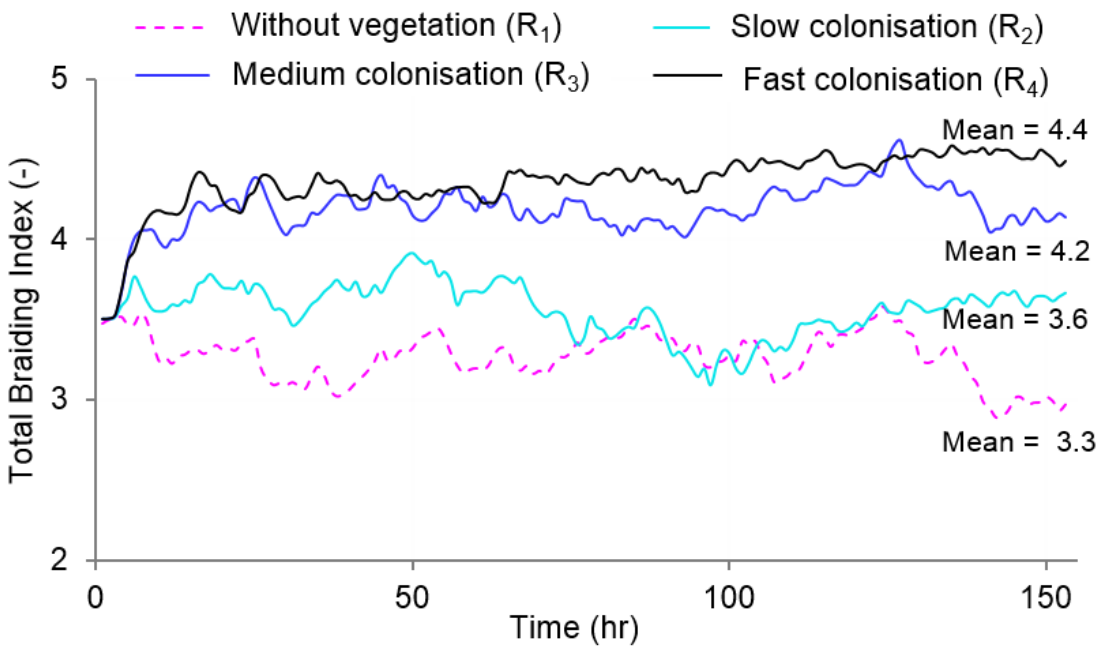

Figure 6.12 Planform evolution in terms of Total Braiding Index.

6.4.2 Topographic Signatures

a) Frequency Distribution of Elevation Relative to Mean Bed Level (MBL)

Distribution of elevation with respect to mean elevation plane of the initial topography was determined in terms of cumulative frequency distribution, shown here for the final generated topography (Figure 6.13a). All runs produced a negatively skewed distribution with a tail to low elevations (relative to the initial MBL) reflecting the presence of locally deep scour holes (e.g., Doeschl et al., 2009; Garcia Lugo et al., 2015). The run with fast colonisation (R_4), however, differs significantly from the remaining simulations, with a narrower (more kurtotic) and more strongly negatively skewed distribution, implying a larger proportion of the bed dominated by deeper channels (see Figure 6.13a).

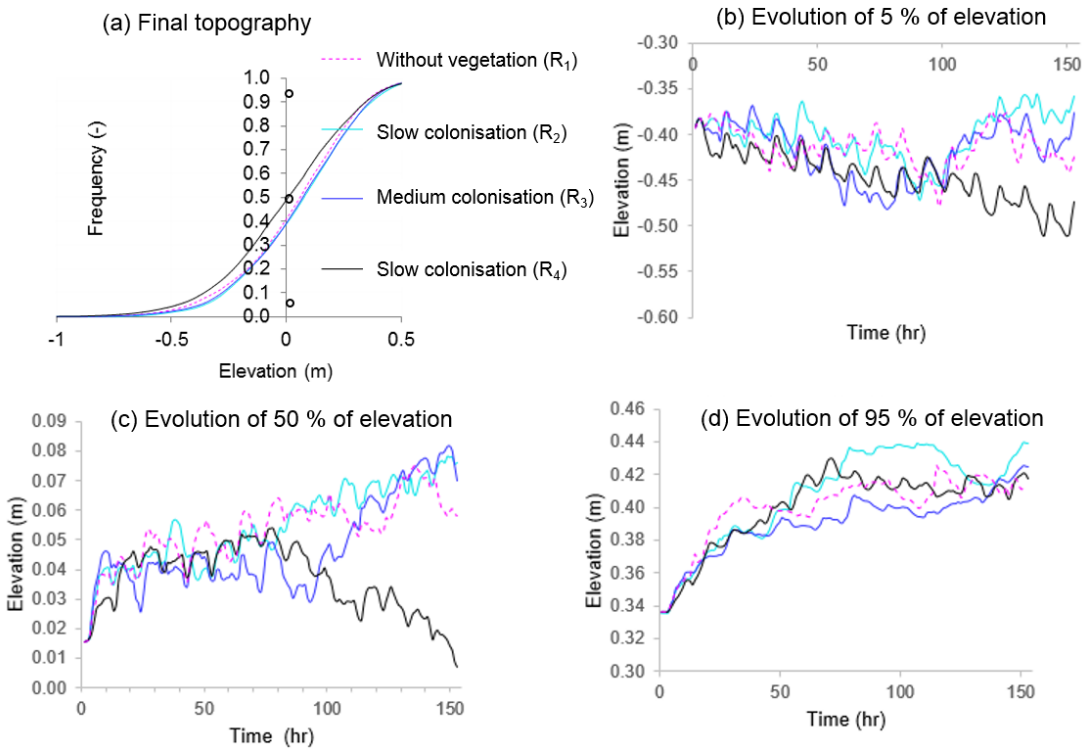

Figure 6.13 (a) Elevation distribution based on the final topography, with reference to the mean elevation plane of the initial topography. The negative and positive elevation indicates the area above and below mean elevation area, or the channel and bar area, respectively; (b) evolution of 5 % of elevation; (c) evolution of 50 % of elevation, and (d) evolution of 95 % of elevation.

This difference is illustrated by quantifying the evolution of 5th, 50th and 95th percentile values of the elevation distribution through time, shown in Figure 6.13b-d. Taking the median (50th percentile) elevation first, the departure of R_4 from the remaining simulations is clearly evident at between 60-80 hrs, with a rapid drop in the median bed level, while at this point the median elevation systematically increases in the other simulations. By 150 hours, there is a 0.06-0.07 m difference in median elevation, which represents a volumetric difference of ~16-19,000 m^3, equivalent to 50-100% (varying from 15,000 for R_3 to 35,000 for R_1) of the total sediment exported by the simulations over the entire modelled period. The channel degradation associated with R_4 is further illustrated by the systematic decline in the 5th percentile elevation, which drops by over 10 cm during the evolution, while the 95th percentile appears to follow a similar trajectory to R_1, R_2 and R_3. In combination, this indicates a pattern of progressive, localized channel incision occurring in R_4.

b) Bar Height

Bar height was calculated as the difference between the 95th and 5th percentile elevation on a cross-sectional basis and then averaged. The temporal evolution of this measure of bed relief is plotted in Figure 6.14.

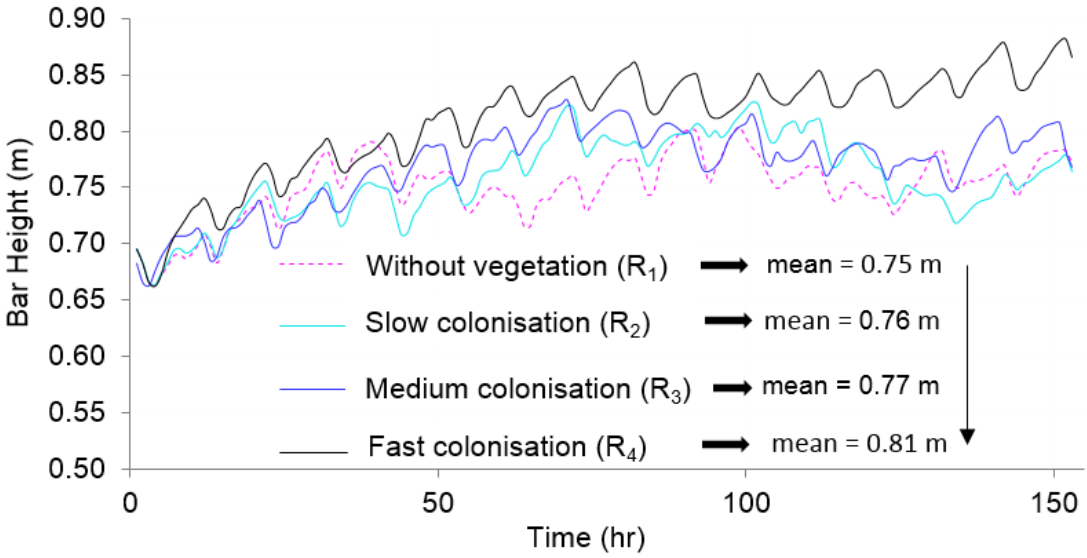

Figure 6.14 Evolutionary trajectory in terms of bar height.

All simulations demonstrate a period of adjustment to the new hydrological boundary condition, with increases in bar height from the initial (0.7 m) condition. However, there is then a clear systematic difference between the runs, with the final bar height achieved reflecting the speed vegetation colonisation; so that the average bar height varies from 0.75 m in R_1 to 0.76 m for R_2 through to 0.77 m and 0.81 m for R_3 and R_4 respectively. As expected given the differences in the elevation percentiles observed above, this difference is most pronounced for R_4 and is again indicative of channel incision in this scenario.

c) Channel Shape

Following the procedure of Redolfi et al. (2016b) the channel shape reflecting parameter, α, the exponent of the width-depth curve (see chapter 3 for details), was computed as a measure of channel complexity (Figure 6.15).

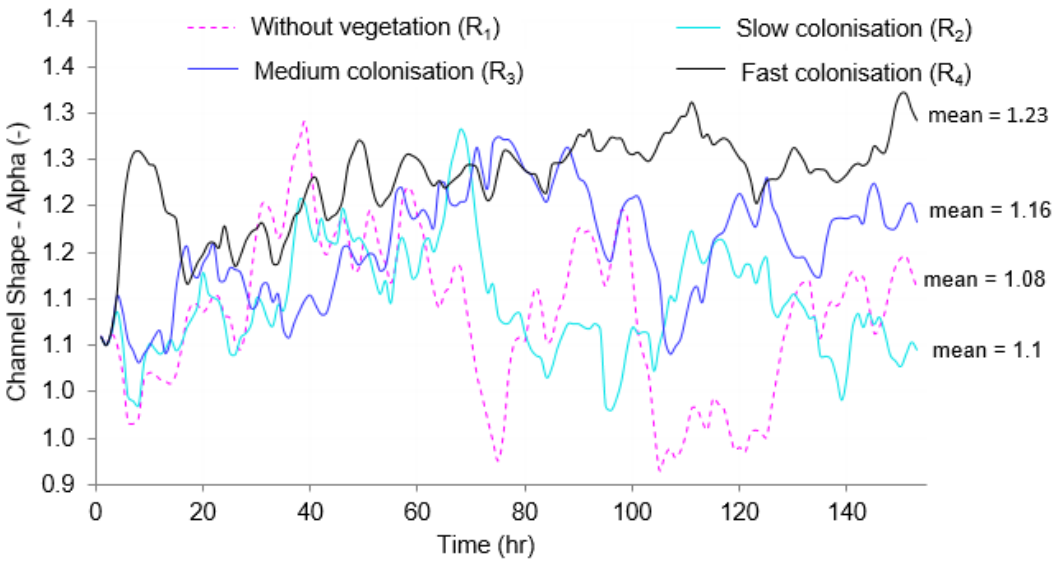

Figure 6.15 Evolutionary trajectory in terms of channel shape reflecting parameter (Alpha). The alpha value is the exponent of the reach averaged width - depth curve as used by Redolfi et al. (2016b).

Separation between the simulations is again evidence from c. 60 hours, with R_4 exhibiting the highest α value, fluctuating around a mean value 1.26. This was then followed R_3, R_2 and R_1 reflecting the pace of vegetation growth, with α fluctuating

around 1.16, 1.1 and 1.08 respectively. Values higher than one, indicate a 'Y-shaped' width-depth curve typical of multi-thread rivers (Redolfi et al., 2016b) with higher values implying the greater complexity of morphology (Redolfi et al., 2016b). This pattern appears to indicate the important role of vegetation in increasing the relief of individual anabranches (as highlighted by the bar height results).

6.4.3 Hydraulic Signatures

In order to understand the pattern of water allocation, a comparison was undertaken to examine a binary classification of predicted water depths; 0-0.5 m and > 0.5 m, as shown in Figure 6.16.

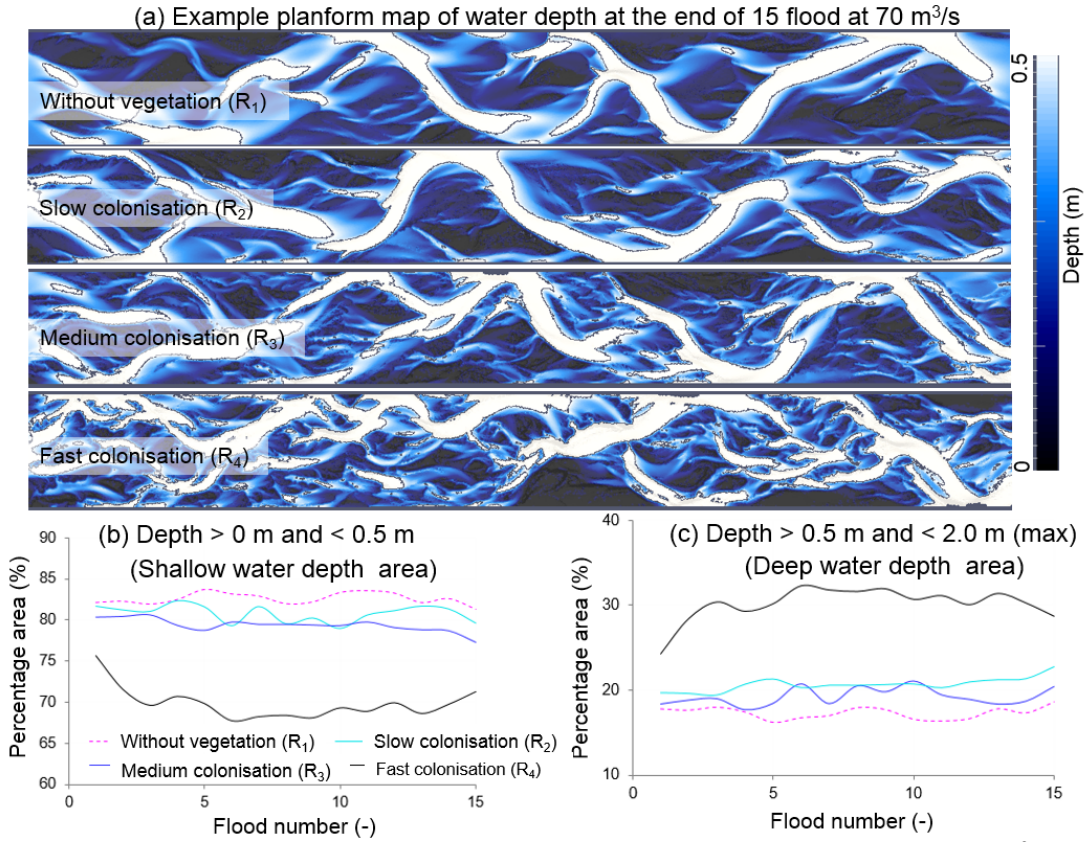

Figure 6.16 (a) An example spatial distribution of water depth at high flow (70 m^3/s) at the end of 15th flood produced by four different runs. The whitest patches surrounded by line are the areas with water depths higher than 0.5 m (deeper water area); (b) Evolution in terms of percentage area occupied by water depths less than 0.5 m (shallow water depth area) at high flow (70 m^3/s) at the end of each flood; (c) Evolution in terms of percentage area occupied by water depths greater than 0.5 m (deeper water depth area) at high flow (70 m^3/s) at the end each flood.

In these planform maps, deep water is shaded as white, while depths between 0-0.5 m are in shades of black-blue-white. Clear differences are evident in the pattern of inundation. Simulation R_1 exhibits a single deep-water channel, with shallow water inundation over bar tops, with localized flow concentration in chutes and dissection channels. There is a progressive change to this pattern with the speed of vegetation colonisation. Simulations R_2-R_3, exhibit a larger areal coverage of deep water, but where this is increasingly discontinuous and confined to a larger number of narrower channels. This trend accelerates with the colonisation speed, with over 30% inundated area in the deep-water class for R_4 compared to less than 20% for R_1. Timeseries of the inundation classes suggests that this pattern is established rapidly during the simulation and is largely stable through time.

6.4.4 Morphodynamic Signatures

a) Erosion and Deposition

The distribution of modelled erosion and deposition was derived by constructing a timeseries of DoDs based on the topography before and after each event. These are shown for each simulation in Figure 6.17 - Figure 6.20. The run without vegetation (R_1) exhibits a shifting pattern of erosion and deposition patches, both in space and in time, dominated by exchanges between the two principal anabranches (Figure 6.17). The DoDs reveal the key role of lateral migration, illustrated by side-to-side patterns of scour and fill, during the lead into a sudden shift in the dominance of one anabranch over another.

The simulations based on the slow (R_2) and medium (R_3) colonisation rates exhibit a more localized pattern of the erosion and deposition which is concentrated within a sinuous active belt (see for example Figure 6.18, floods 10, 12; Figure 6.19, floods 10, 15). This pattern is exaggerated further in R_4, which has a much narrower active belt which still exhibits switching behaviour associated with avulsions (e.g., see Figure 6.20, floods 4 and 6). In this case, the units of scour and fill and not just the active belt

are significantly narrower than the broad channels of adjustment illustrated for R_1 in Figure 6.17.

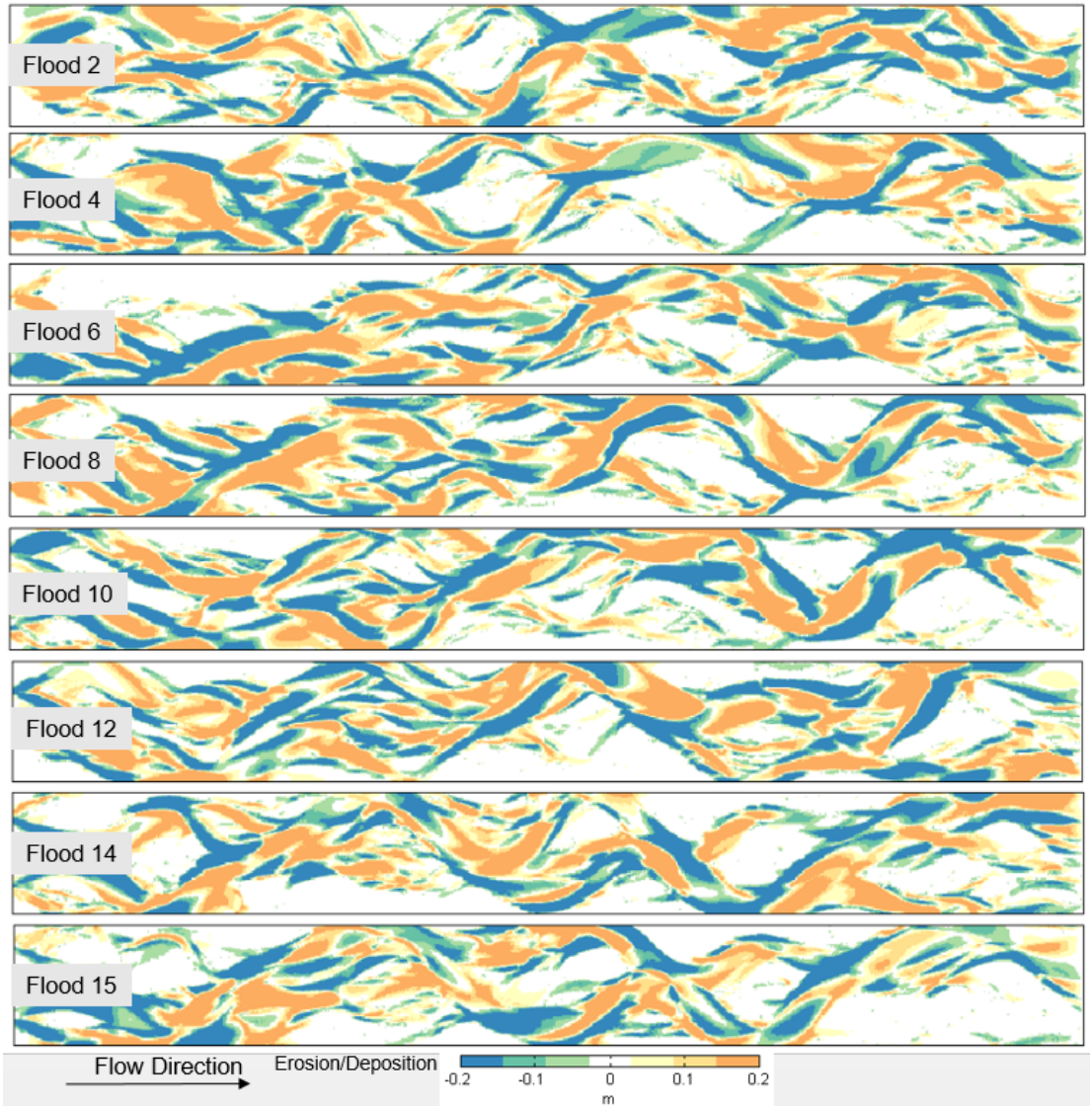

Figure 6.17 Planform trajectory displaying spatial distribution of erosion and deposition in the case without vegetation (Run R_1). The domain width and length are 175 m and 1550 m, respectively. Flow is from left to right. These maps represent changes in the corresponding flood as indicated in the figure.

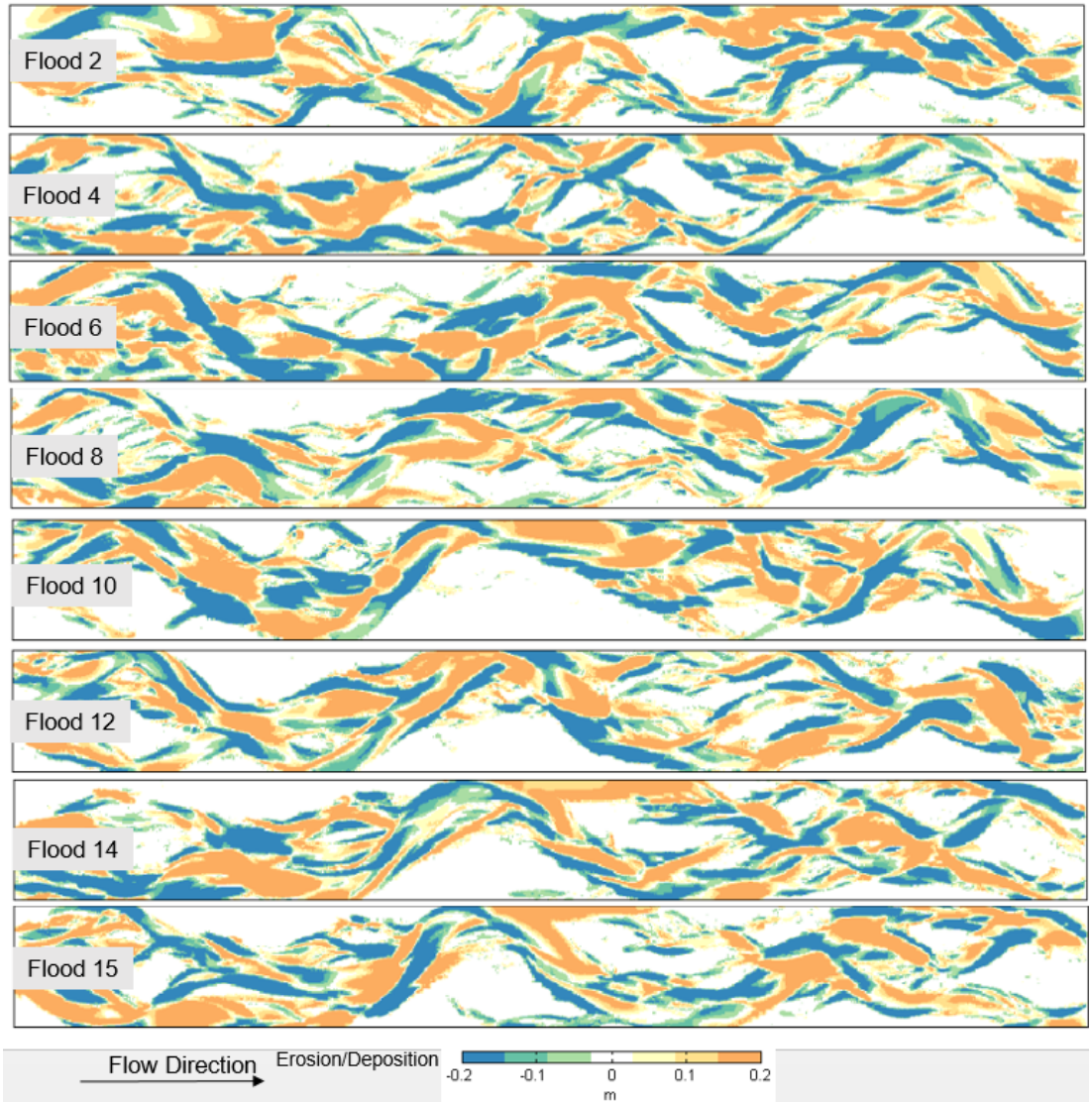

Figure 6.18 Planform trajectory displaying spatial distribution of erosion and deposition in the case with slow colonisation (Run R_2). The domain width and length are 175 m and 1550 m, respectively. These maps represent changes in the corresponding flood as indicated in the figure.

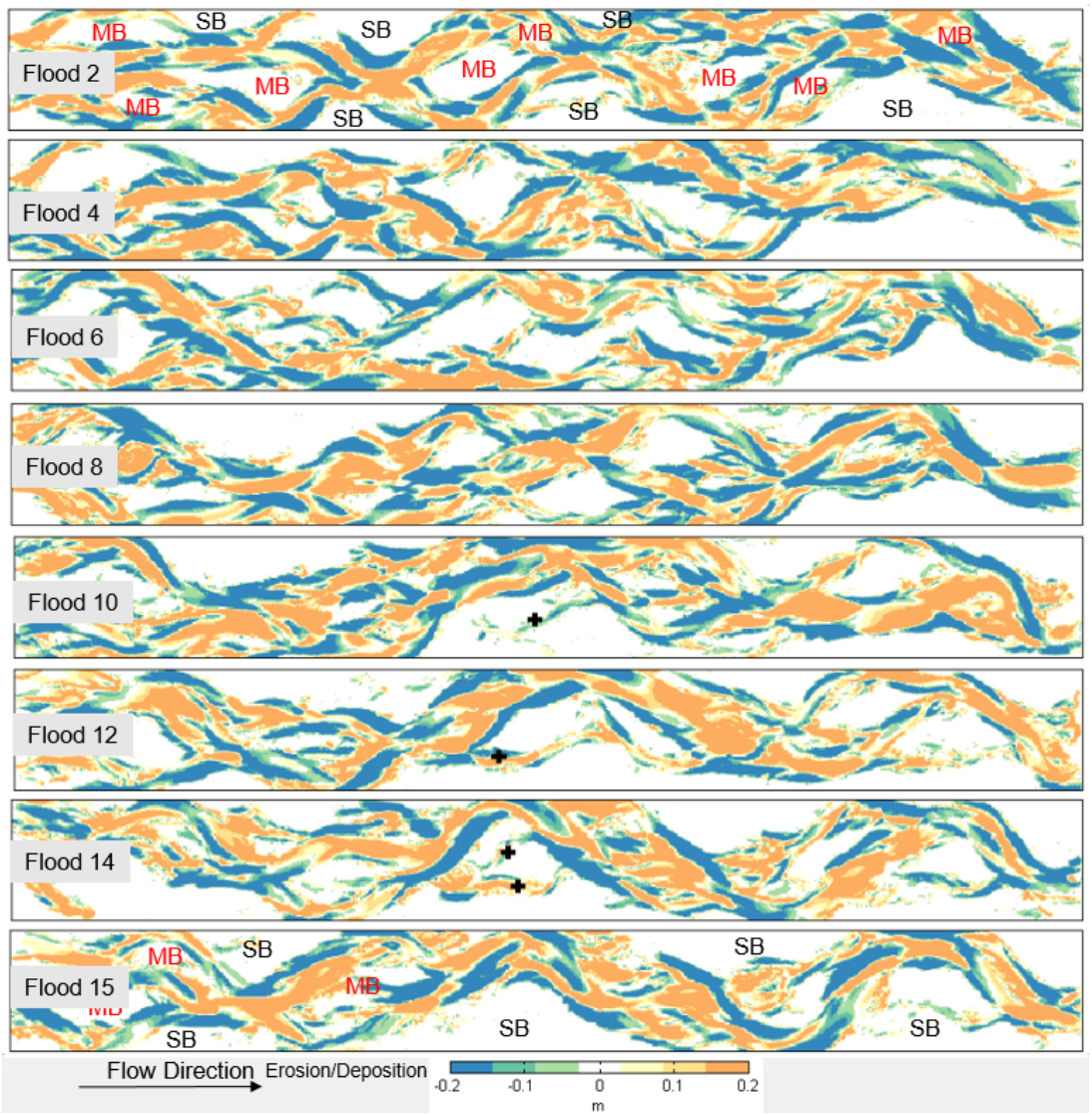

Figure 6.19 Planform trajectory displaying spatial distribution of erosion and deposition in the case with medium colonisation (Run R_3). The notations MB and SB stand for Mid Bar and Side Bar, respectively. The black spotted mark depicts the reactivation of minor channels located on the elevated area. These maps represent changes by the corresponding flood as indicated in the figure.

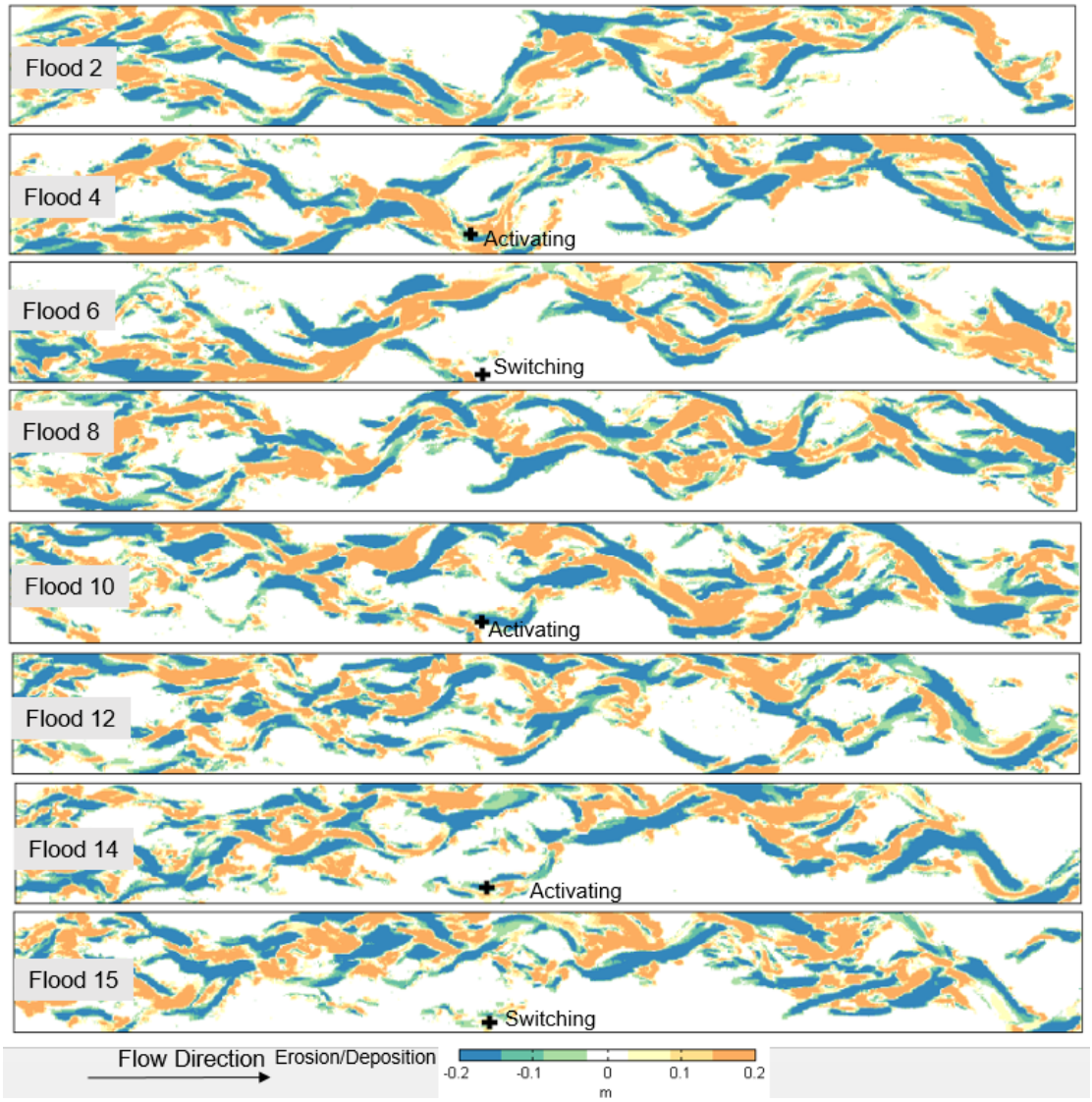

Figure 6.20 Planform trajectory displaying spatial distribution of erosion and deposition in the case with fast growing vegetation (Run R_4). The domain width and length are 175 m and 1550 m, respectively. Flow is from left to right. These maps represent changes in the corresponding flood as indicated in the figure.

Some general observations can be deduced that link the vegetation controls on the pattern of channel adjustment. As vegetation colonisation and biomass density increases, a sequence of changes ensues: a) the vegetation moderates bar edge erosion and flow are increasingly confined into smaller, deeper channels; b) undisturbed areas (i.e. high bars) gradually coalesce; c) central and bank attached bars merge to create large areas of undisturbed 'floodplain'. For the runs with slow colonisation (R_2) and medium colonisation (R_3), these changes become evident by

after flood 10, however for the faster colonising simulation (R_4) this change is more or less accomplished within 5 floods.

b) Turnover Area

The pattern of braidplain turnover was calculated for a range of vertical change thresholds ranging from 0.05 – 0.5 m, reflecting the intensity of vertical adjustment. In this case, the area refers to the total change based on the final DoD for each simulation, is plotted in Figure 6.21. This shows a significant difference between R_4 and the remaining slower or non-vegetated simulations, with a significantly lower proportion of shallow changes (0.05-0.2 m). This pattern reflects the dominance of the deeper, increasingly confined flows in R_4, that give rise to a greater proportion of higher magnitude vertical changes.

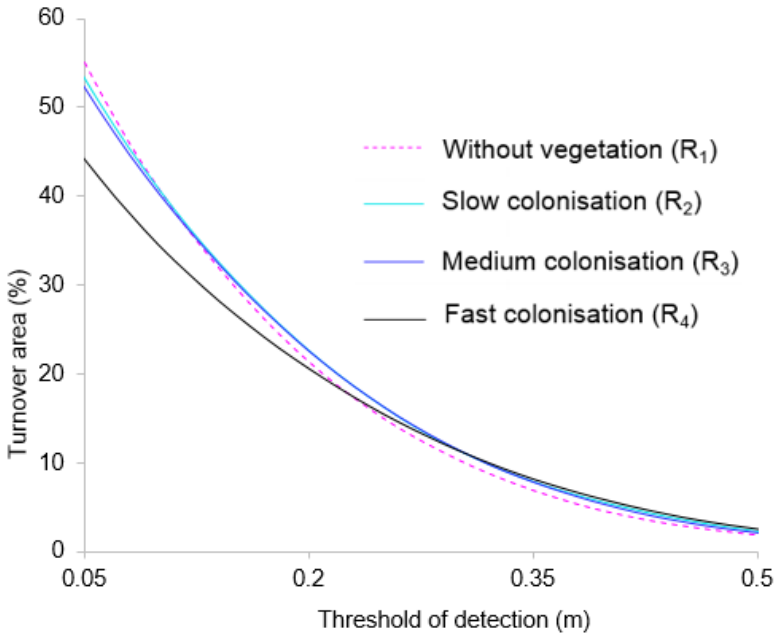

Figure 6.21 Turnover area based on the erosion and deposition maps of Figure 6.17-20 after averaging all of them, at different threshold of detection. The percentage area was calculated as the percentage of total domain (1500 m x 175 m) in each case.

c) Volumetric Erosion and Deposition Pattern

In addition to the spatial pattern of changes, the cumulative volumes of erosion and deposition were examined to investigate the temporal evolution of each simulation (Figure 6.22a). This provides an insight into the total geomorphic work accomplished.

The runs without vegetation (R_1) and the slowest colonisation rate (R_2) generated the highest cumulative volumes of erosion and deposition, followed closely by R_3. These all differ significantly from R_4 for which the cumulative volumes were reduced by ~25%.

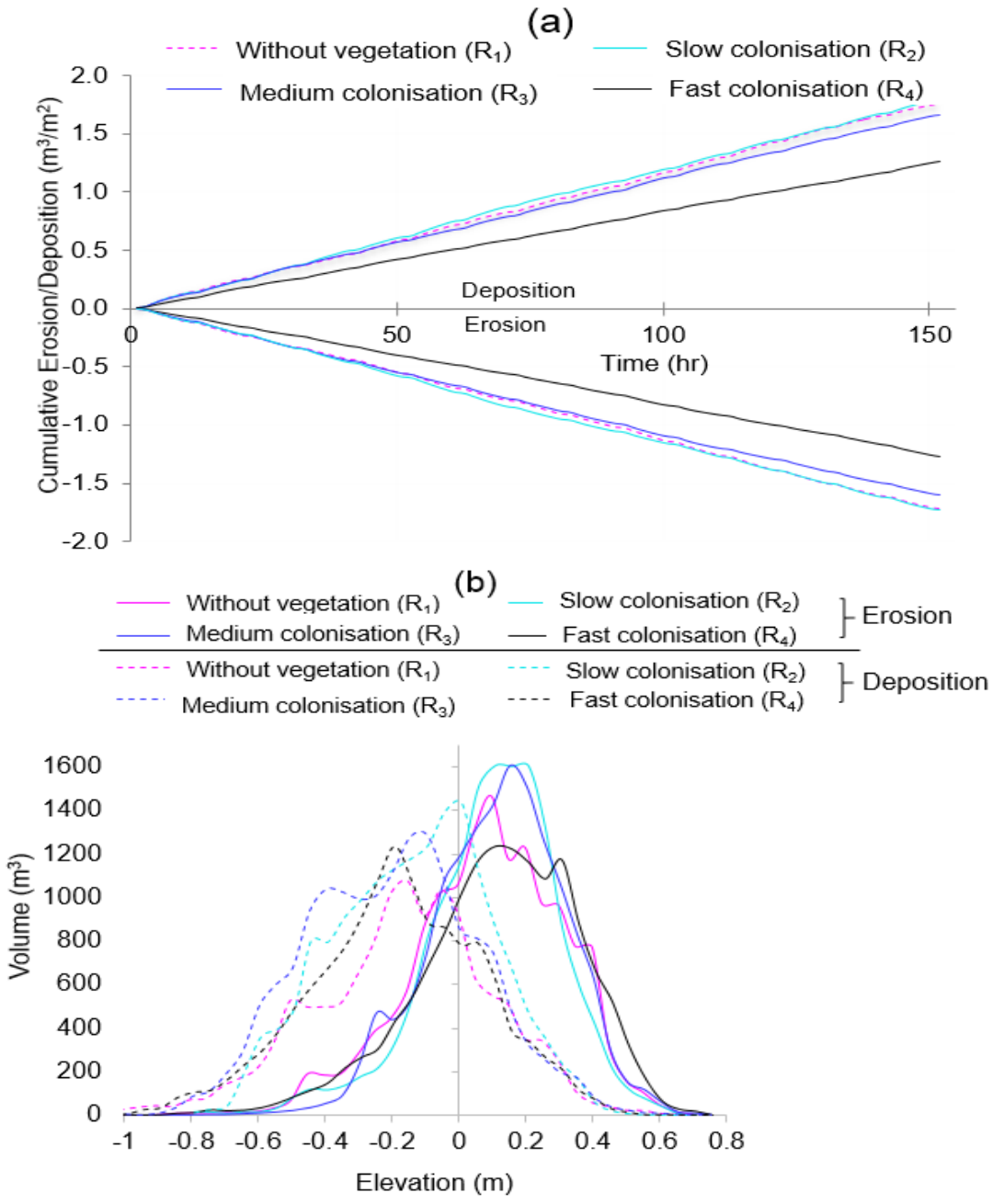

Figure 6.22 a) Cumulative erosion and deposition based on the changes in one hour interval; b) Distribution of erosion and deposition volume by the last flood (flood 15) with respect to elevation of preceding topography used in DEM differencing.

The Figure 6.22b shows a typical distribution of erosion and deposition volume with respect to prior DEM based on changes by the flood 15 only. The distribution of erosion and deposition by elevation is, however, broadly consistent between simulated runs. For example, the erosion curve is centred above mean bed level, implying the dominance of high elevations by bank erosion or bar scour over channel bed scour. By contrast, all runs produced peaking of deposition curve towards the negative elevation side which implies dominance of channel deposition over bar deposition.

d) Sediment Transport

While catchment sediment supply, sediment calibre and the hydrological regime provide the broad scale context for sediment transport rates, vegetation can play an important role in modifying the local pattern of adjustment and net flux. As discussed previously, the biogeomorphological effects are complex, as vegetation may serve to enhance sediment retention or trapping (Ghisalberti and Nepf, 2006; Baptist et al., 2007) while the below mass structure (roots) provides additional resistance to bar or bank erosion (Smith, 1976; Thorne, 1990). At the same time, the enhanced stability of banks, helps to confines flows and may result in an additional local incision of the channel bed.

A measure of the system behaviour associated with each simulation is provided by the cumulative efflux of bed material, which is plotted in Figure 6.23. This illustrates strong differences between the simulations, with significantly higher net sediment export from the unvegetated simulation (R_1), which reduces, in turn, with the rate of biomass production in vegetated runs (R_2-R_4). This cumulative sum is not entirely linear, and simulations R_3 and R_4 in particular exhibit a step change in the rate of efflux at c. 70 hours. The exact cause of this is not clear, but likely reflects a change in the configuration of the downstream boundary condition, resulting in either a reduction (R_3) or enhancement of the flux (R_4).

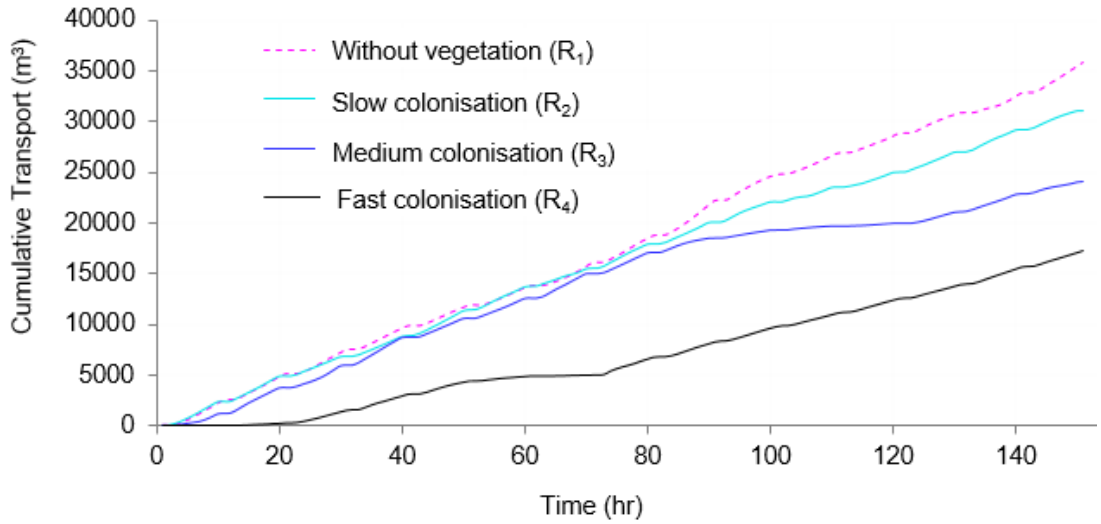

Figure 6.23 Cumulative sediment transport from the outlet of the model domain.

e) Active Width

Significant changes in active width have previously been observed in physical experiments associated with vegetation colonisation of braided channels (Ashmore et al., 2011). Such experiments have demonstrated that bio-geomorphologically active vegetation serves to reduce the active width, confining sediment transfer pathways to narrow, incised channels (e.g., Gran and Paola, 2001; Tal et al., 2004; Jang and Shimizu, 2007; Tal and Paola, 2010). Here, the active width was calculated as a percentage of the bed area, using a 0.05 m threshold for significant vertical changes using the DoDs presented earlier. The trend for each simulation is shown in Figure 6.24, based on a flood-by-flood interval. The run without vegetation (R_1), as expected, exhibited the highest width, fluctuating around a mean value of 56%. This was followed in turn, by R_2, R_3 and R_4 with means of 54 %, 53% and 44 % respectively. Again, therefore, there is a clear step-change in behaviour associated with the fast colonising simulation R_4, with the active belt heavily constrained as suggested by the DoDs discussed above.

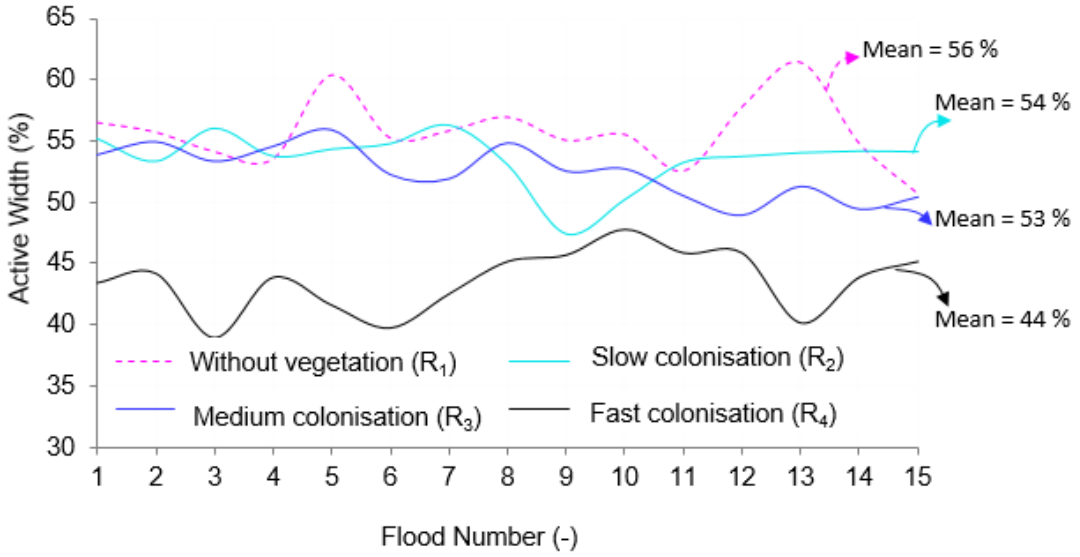

Figure 6.24 Evolutionary trajectory in terms of active width. The active width was determined based on the erosion and deposition map at one flood interval.

6.4.5 Vegetation Dynamic

The distribution of simulated biomass was analysed in terms of overall reach averaged density (0-1), spatial frequency distribution and location with respect to the mean elevation. The reach averaged biomass density is synchronized with the sequencing of low and high flows as shown in Figure 6.25. During the one-hour low flow periods, biomass grows rapidly on dry surfaces, reflecting the accelerated growth curve, but is then subsequently removed from active areas during the next flood event, with the retrogression following a sharp, exponential trajectory. Superimposed on this high-frequency signal, the low and medium growth rate simulations, R_2 and R_3, show a gradual increase average biomass density, rising by approximately 5% over the simulation period (with post-flood densities in R_2 rising from c. 0.1 to 0.15 and R_3 from 0.15-0.2). By contrast, the fast colonising simulation, R_4, reaches a constant average density of approximately 0.4 after just two floods.

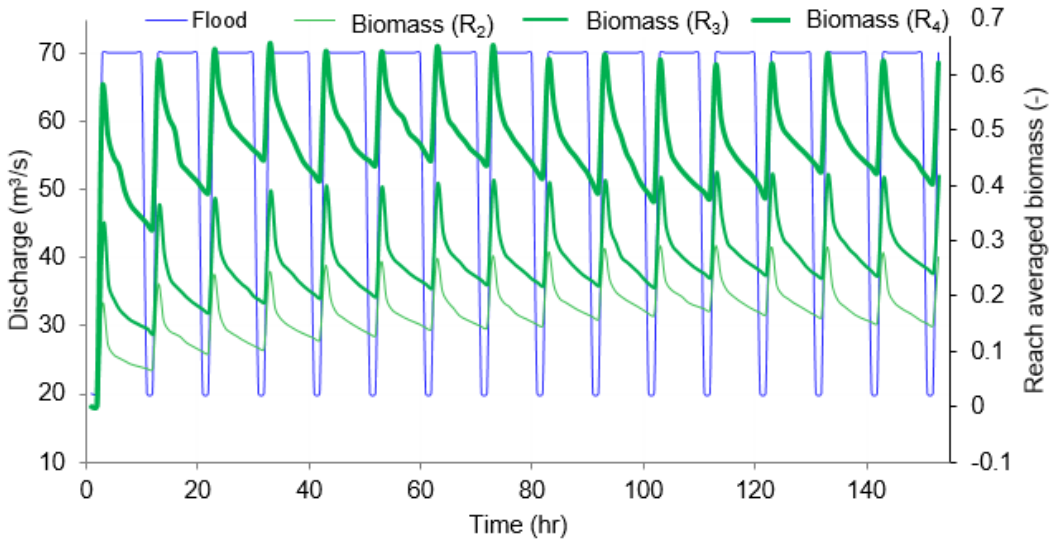

Figure 6.25 Competition between biomass (reach averaged) and flood during the fifteen-cyclic low and high flows.

In order to provide quantitative insights into the spatial distribution of the modelling biomass, the pattern of colonisation was analysed with respect to mean bed level. Figure 6.26 shows pairs of images of biomass on areas above (i.e., 'bars') and below (i.e., 'channels') mean bed level, both before and after the last flood (event 15) in order to illustrate the growth and subsequent regression of vegetation cover. This approach provides a quick visual assessment of areas of vegetation preservation following this final event. Run R_4 exhibits the largest area of vegetation colonisation of both bars and channels and at both at low and high flows (Figure 6.26c), followed by the runs R_3 (Figure 6.26c) and R_2 (Figure 6.26a), respectively. Notably, simulation R_4 exhibits significantly denser biomass coverage on both the central but in particular the large bank-attached floodplain areas on the true right (Figure 6.26c). At these high densities, the critical dimensionless threshold for entrainment is such that these areas become resistant to erosion and persist between events and provide nuclei for further island coalescence. By contrast, while R_2 and R_3 generate a broad vegetation cover, biomass densities rarely exceed 0.7 and are, therefore, associated with lower thresholds for entrainment. Consequently, while colonized by vegetation, islands and

floodplain areas in these simulations are readily reworked and the characteristics behaviour of the channel differs little from an unvegetated model.

The distribution of biomass density was also analysed with respect to the mean bed level. Figure 6.27 summarizes the spatial biomass distribution in terms of the elevation of the colonized surfaces, with biomass classified into two groups, low (0-0.5) and high (0.5-1) densities. These plots show the distribution before and after an event (flood 15) and thus provide an indication of the 'survival' of vegetation in areas of differing elevation. From this, it is clear that for all simulations, the highest density biomass is associated with elevated bar surfaces (negative (left) skewed distributions), which remain largely free from inundation and disturbance, enabling flood-on-flood vegetation growth. The trend is apparent for all simulations, though distribution of surviving dense biomass is progressively skewed to higher and higher elevations as the rate of colonisation decreases (i.e., R_4 to R_2). The critical shear stress for entrainment is linearly correlated to biomass density, so it is likely that the principal agent of erosion to remove vegetation from such elevated bar surfaces is bank erosion. The areas of less dense biomass have a more generalist distribution, colonising a wide range of surface elevations. This vegetation class dominates for the slower colonising simulations (R_2 and R_3), reflecting for these parameterisations to reach maturity.

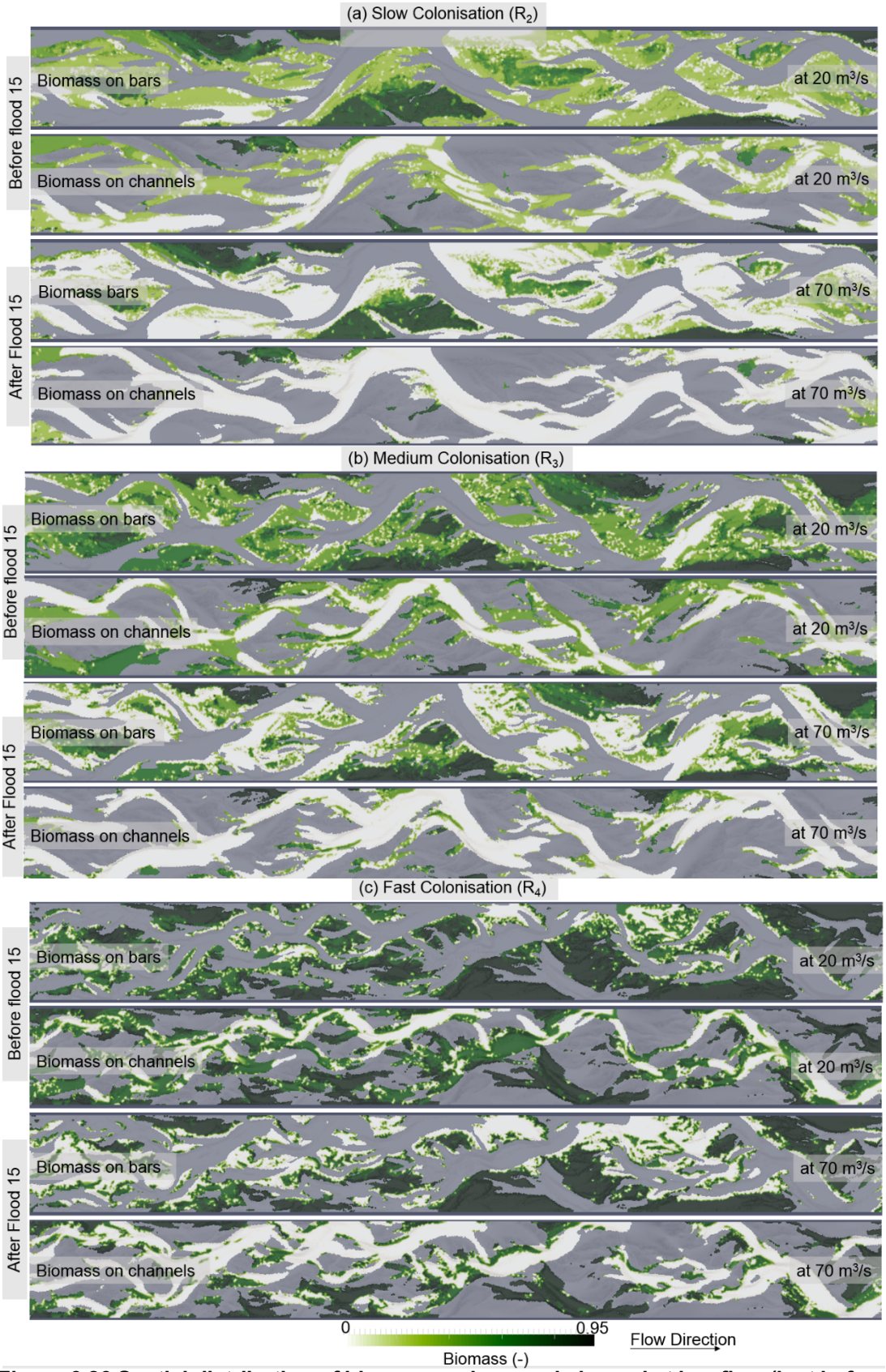

Figure 6.26 Spatial distribution of biomass on bars and channel at low flow (just before flood 15) and high flow (just after the flood 15). Bars and channel here means areas above and below mean elevation, respectively. Biomass in each case has been overlapped on the white backgrounds.

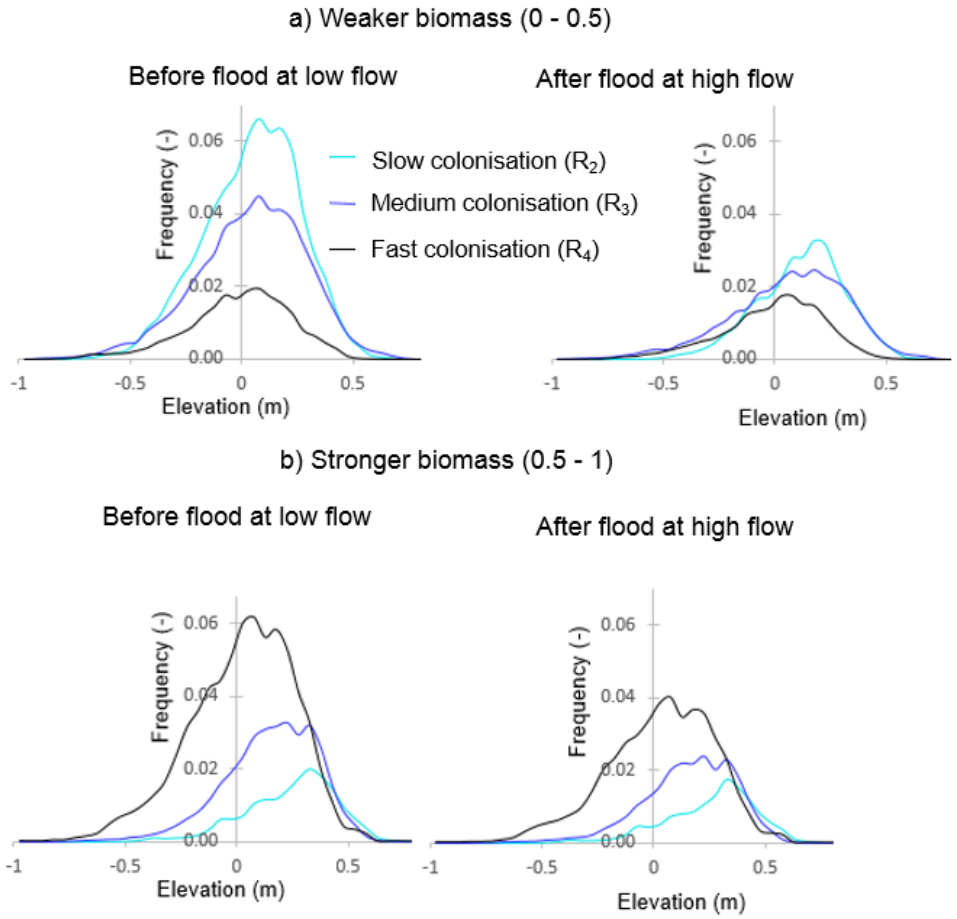

Figure 6.27 Relative position of biomass with respect to mean elevation just before the flood 15 at low flow and just after the last flood 15 at high flow. Here frequency distribution of two clusters of biomasses namely 0-0.5 (weaker-milder) and 0.5-1 (stronger) in each case have been presented.

Lastly, in order to provide an insight into the evolutionary trajectory of biomass throughout the simulations, the reach-scale frequency distribution of biomass was calculated on a flood-by-flood interval. This pattern reflects the mosaic of surfaces defined by their 'time-since-last-disturbance' and is plotted for each growth rate scenario in Figure 6.28. These plots summarize the distribution of biomass before and after flood, at selected intervals through the 15-year simulation period.

Unsurprisingly, the simplest pattern of the evolutionary trajectory is associated with R_4, the fast colonisation scenario. Given the 2-year period to reach equilibrium, this simulation is limited to only three vegetated end-states, with biomass densities of 0, 0.7 and 1 respectively. This evolutionary trajectory shows a progressive increase in

the proportion of the bed covered by the climax distribution (biomass ≃ 1), reflecting the increasing area of stabilised high surfaces through time. By contrast, the slow and intermediate growth rate scenarios (R_2 and R_3) generate more complex statistical and spatial distributions, resulting from the longer time to reach equilibrium (5 and 10 years respectively). For the slow growth rate (R_2), the post-flood biomass exhibits a multi-modal distribution, with equal magnitude peaks, that shift progressively towards higher values through the simulation as a small set of undisturbed sites continue to develop mature vegetation communities. By year 15, a broad range of vegetation densities (and surface) ages is apparent, with densities varying between 0.3-0.9. By contrast, the intermediate growth rate (R_3), while exhibiting a similar multi-modal distribution, achieves a statistically similar state with peaks at 0.4, 0.7 and 0.9 more rapidly, after just over 5 years. In this case, the older (and denser) surfaces predominate post-flood, but a diverse mosaic of surface coverage is maintained.

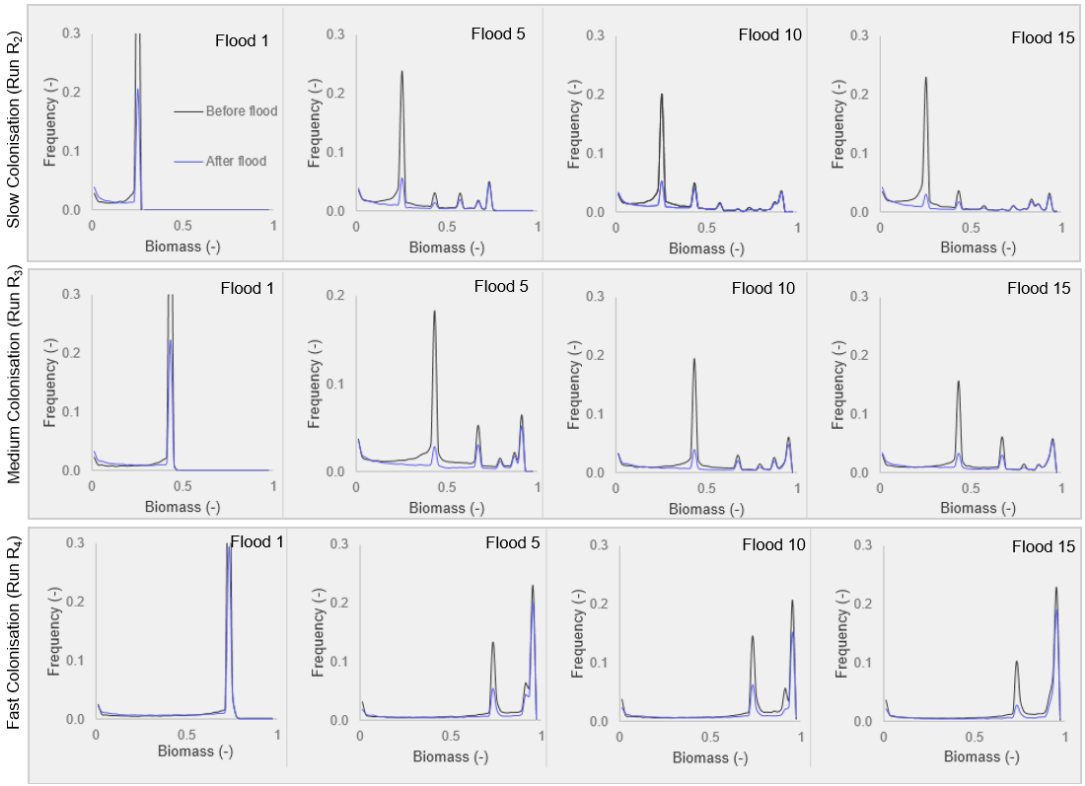

Figure 6.28 Overall frequency distribution of biomass from flood 1 to flood 15 from left to right and top to bottom. The black line represents the biomass distribution before flood (at low flow) and the blue line represents the biomass distribution after flood (at the end of high flow).

6.5 Discussion

The simple experiment described above provides a useful insight into the role of vegetation in modifying fluvial processes and the capacity of a parsimoniously parameterized numerical framework to simulate these interactions. The results indicate the major influence of vegetation on planform dynamics, and through the use of a simulation tool, such as BASEMENT, it is possible to interrogate the process mechanisms that drive the differing evolutionary trajectories.

6.5.1 Effect of Vegetation on Planform

The unvegetated simulation, R_1, was used as a reference control, a baseline against which the three-growth rate parameterisation models could be compared. It also provides a test to ensure that no unforeseen transient effects arose from initiating these simulations from the topographic boundary condition developed by R_9 from Chapter 4.

The planform evolution of R_1 follows the trends established in Chapters 4 and 5 with the 70 m^3/s steady regimes, leading to a planform dominated by two, wide and relatively sinuous anabranches separated by mid-channel bars. This planform continuously adjusts, with the frequent switching of the primary and secondary channel. This evolution appears to capture many of the processes observed in natural braided rivers, including lateral channel mobility driven by bar trimming and localized bar head deposition (e.g., Wheaton et al., 2010; Wheaton et al., 2013; Williams et al., 2015). This localized reworking of bed material plays an important role in conditioning the morphology (reducing flow capacity) in the lead up to an avulsion during which switches in the dominant channel occur (e.g., Slingerland and Smith, 2004; Ashworth et al., 2007; Jerolmack and Mohrig, 2007). The long-term result of this reworking is a set of time-transgressive or diachronous bars, that are formed through a complex sequence of depositional and erosional phases (Egozi and Ashmore, 2009).

The introduction of simulated biomass serves to impact these dynamics through the twin axes of: a) increasing the local flow resistance; and b) increasing the critical shear stress for entrainment. This is a highly simplified representation of the complex set of interactions relating to vegetation and importantly, the formulation used here neglects the role of the root reinforcement on bank stability. Despite this streamlined process representation, the introduction of the vegetation growth model has a profound effect on the simulated channel planform.

The run with slow colonisation (R_2) and medium colonisation (R_3) quickly evolve into a sinuous active channel belt, dominated by a single channel that meanders around large bank attached, alternate, vegetated bars. The transformation from active braiding state to this narrowed, sinuous form followed a sequence of changes: a) reduced lateral mobility leading to discharge confinement and subsequent local deepening of channels; b) gradual loss of secondary branching or chute channels located on the elevated bars; c) the coalescence of smaller mid-channel and lateral bars leading to the formation of large alternate bars, a pattern also observed in flume based experiments (e.g., Gran and Paola, 2001; Tal et al., 2004; Jang and Shimizu, 2007; Tal and Paola, 2010). Thereafter, the main flow is constrained within a sinuous, narrowed active belt around the alternate (floodplain) bars. There is some evidence of periodic re-activation of the dry, chute channels located on the top of the vegetated bars. These excursions were facilitated by bank erosion leading to localized deposition and a loss of channel capacity, promoting localized avulsions that preferentially occupied the locally low, chute channels (Jerolmack and Mohrig, 2007). In natural single thread rivers, major cutoffs are developed once the sinuosity of channel reaches a threshold value (Perucca et al., 2007; Crosato, 2008). Such behaviour is not observed here, though this may reflect the use of hard outer boundary walls that prevent the amplification of meanders and thus the potential for belt-scale cutoffs. Furthermore, the driver of bend amplification is now well understood to be

linked to secondary, helical flow circulation patterns arising from centrifugal effects on the outer bends (Powell, 1998; Mosselman and Le, 2016). In curvatures, helical flow is developed due to the dominance of centrifugal force acting towards the outer bend at the surface over the inward acting pressure force and vice versa at the bottom (Powell, 1998). This alters the direction of depth-averaged flow and sediment transport so that the secondary flow model is important to mimic this strong 3D processes of bends and confluences particularly in the depth-averaged model (Mosselman and Le, 2016). These secondary flows serve to encourage outer bend erosion and inner bend deposition (Crosato, 2008). Importantly, the 2D SWW solver used in BASEMENT does not account for variations in the vertical pressure gradient that would be needed to represent such circulations, and nor does it incorporate any secondary parameterisation of these effects. It is, therefore, unclear whether the lack of such process representation inhibits the development of critical sinuosity.

The run with fast colonising simulation, R_4, evolved rapidly into multi-thread form, comprising narrow, lower sinuosity anabranches. In this case, the rate of local channel confinement, deepening and bar amalgamation was so rapid that it facilitated quick succession of vegetation to the equilibrium state both on bars and on the elevated channels. Due to the rapid succession of vegetation, elevated secondary channels ceased to supply sediment and failed to further evolve morphologically. The speed of vegetation succession is crucial to understanding the behaviour of this simulation, for only once vegetation reaches a mature state, with biomass densities above 0.7 does the increase in the critical shear stress become a significant inhibitor of bed mobility. For this simulation, such succession occurs within just one to two years, so that areas of vegetation growth on the channel margins quickly become infilled, constraining the channel further and narrowing the size of anabranches effectively. Furthermore, the development of small but biogeomorphologcially ‘strong’ patches of vegetation in the main flow channel encourages flow division, leading to the development of

streamlined bars that separate comparatively incompetent narrow channels, driving the system towards an anastomosing state. This trajectory mirrors similar behaviour seen in flume experiment of Coulthard (2005) using small but strong patches of vegetation. In the long-term, these processes lead to the development of a large, continuous vegetated floodplain attached (in this case) to the true right bank, narrowing not just the individual channels, but the entire active channel belt significantly. The sporadic channel switching and activation as such observed in the case of R_2 and R_3 nonetheless remains evident.

6.5.2 Effect of Vegetation on Topography

Flume based experiments have indicated that the introduction of vegetation into a braided channel results in discharge confinement and a tendency to deepen local scour holes (e.g., Gran and Paola, 2001; Tal et al., 2004; Jang and Shimizu, 2007; Tal and Paola, 2010) and enhance the overall topographic relief and complexity (e.g., Redolfi et al., 2016b). In the numerical experiments described here, the topographic effects on channel form are strongly related to the rate of vegetation growth. The slow and intermediate growth scenarios (R_2 and R_3) reveal frequency distributions along with 5^{th}, 50^{th} and 95^{th} percentiles of the elevation distribution that follow a similar trajectory to the unvegetated model. However, the fast colonising model, R_4, exhibits significant local scouring, deepening the 5^{th} percentile elevation significantly, and lowering the overall median elevation. As a result, the bar height develops rapidly, resulting in a 6 cm increase in average relief compared to the unvegetated scenario. This increase in relief is captured by the channel shape parameter, α (e.g., Redolfi et al., 2016b), which is consistently higher for the vegetated models.

6.5.3 Effect of Vegetation on the Flow Field and Hydrodynamics

Surface structure of vegetation increases the local flow resistance, resulting in greater water depths and reduced velocity/shear stress (Darby, 1999; Tsujimoto, 1999; Bennett et al., 2002; Baptist, 2003; Bennett, 2004; Järvelä, 2005; Ghisalberti and

Nepf, 2006; Baptist et al., 2007; Nepf and Ghisalberti, 2008; Liu et al., 2010). Additionally, the below mass properties of vegetation, such as root structure increases shear strength and decreases erodibility (Smith, 1976; Thorne, 1990; Abernethy and Rutherfurd, 2001; Pollen, 2007; Docker and Hubble, 2008). Previous studies have suggested that vegetated braided rivers have proportionally deeper scour at confluences and bends (e.g., Gran and Paola, 2001; Tal et al., 2004; Jang and Shimizu, 2007; Tal and Paola, 2010). The results of this study also show similar changes in the flow field associated with the vegetated scenarios, in particular, an increase in water depth.

However, while all vegetated simulations resulted in a greater proportion of deep areas of water (classified here as > 0.5 m), there is a notable step-change between the slow/intermediate and the fast colonising scenarios, i.e., R_2/R_3 vs R_4. As discussed above, this difference relates to the linked hydraulic roughness and critical shear stress models that are, in turn, a function of the biomass density. In the parameterisation used here, both these key properties are made linear functions of biomass density. Over the full scale of biomass densities (0-1), the Strickler *Ks* varies from 30 to 9 $m^{1/3}/s$ (or more familiarly in terms of Manning's n, 0.033 to 1.111 $s/m^{1/3}$), while the critical dimensionless threshold for entrainment raises from 0.047 to 0.21 (Figure 6.6).

The key to understanding the interaction is the scale at which these changes become limiting factors on the system processes. For example, as predicted dimensionless shear stresses rarely exceed 0.15, but noting that bed material transport varies as an exponential function of the excess shear stress, the effective range of dimensionless shear stresses that account for intense sediment transport in the unvegetated simulations reported in Chapters 4 and 5, lie in the range 0.1-0.15 (see Section 5.4.4. and Figure 5.19). For vegetation to inhibit entrainment over this range requires biomass densities of 0.4-0.7. The fast growth rate scenario R_4 achieves biomass

densities of 0.7 after just one year without disturbance, however, at the slower growth rate of R_3, succession to even low densities of 0.4 requires three years without disturbance and seven years to reach densities of 0.7.

The net result of this is that the slow rates of colonization present a large proportion of sparsely vegetated surfaces that are readily reworked before they become limiting controls on erosion. As a consequence, the channel morphology and related flow fields differ comparatively little from the unvegetated scenario. By comparison, within just a year, surfaces that are undisturbed in R_4 become 'erosionally-limiting'. This serves to further constrain discharge within existing banks, in turn deepening the flow, enhancing the shear stress locally within the channel and so accelerating incision which continues this cycle of feedback. It should also be noted, that the full effects of vegetation on this chain of processes are probably not effectively realized, as the biomass density here does not link to the bank stability model.

6.5.4 Effect of Vegetation on Morphodynamics

The similarity between R_1, R_2 and R_3 and the distinction between these scenarios as R_4 is again illustrated when considering the pattern of channel adjustment through time. The DEMs of Difference presented in Figure 6.17- Figure 6.20, illustrate the dramatic contraction of the actively reworked channel belt in R_4 compared to the remaining three scenarios. What is less clear from this sequence, is that the DoDs also provide evidence of a significant difference in the net sediment budget between the simulations. Comparing the final modelled topography with the initial condition provides a quick assessment of the net change in volume through the simulation, as described in Figure 6.29. The analysis reveals that for R_1, R_2 and R_3, all simulations resulted in a net increase in sediment storage, with volumetric increases equating to average bed level increases 0.035, 0.058 and 0.053 m respectively. By contrast, the sediment budget for R_4 was net degradational, resulting in a total bed level change of -0.004 m over the 15-year simulated period. Total volumes (erosion + deposition) of

mobilized bed material are similar across the simulations (~69,000-73,000 m^3), and the highest volumes of erosion occur in R_4. This reversal of the trajectory of bed level change between the scenarios, therefore relates to significantly lower rates of deposition in R_4, indicating the more efficient transfer of sediment downstream through the reach.

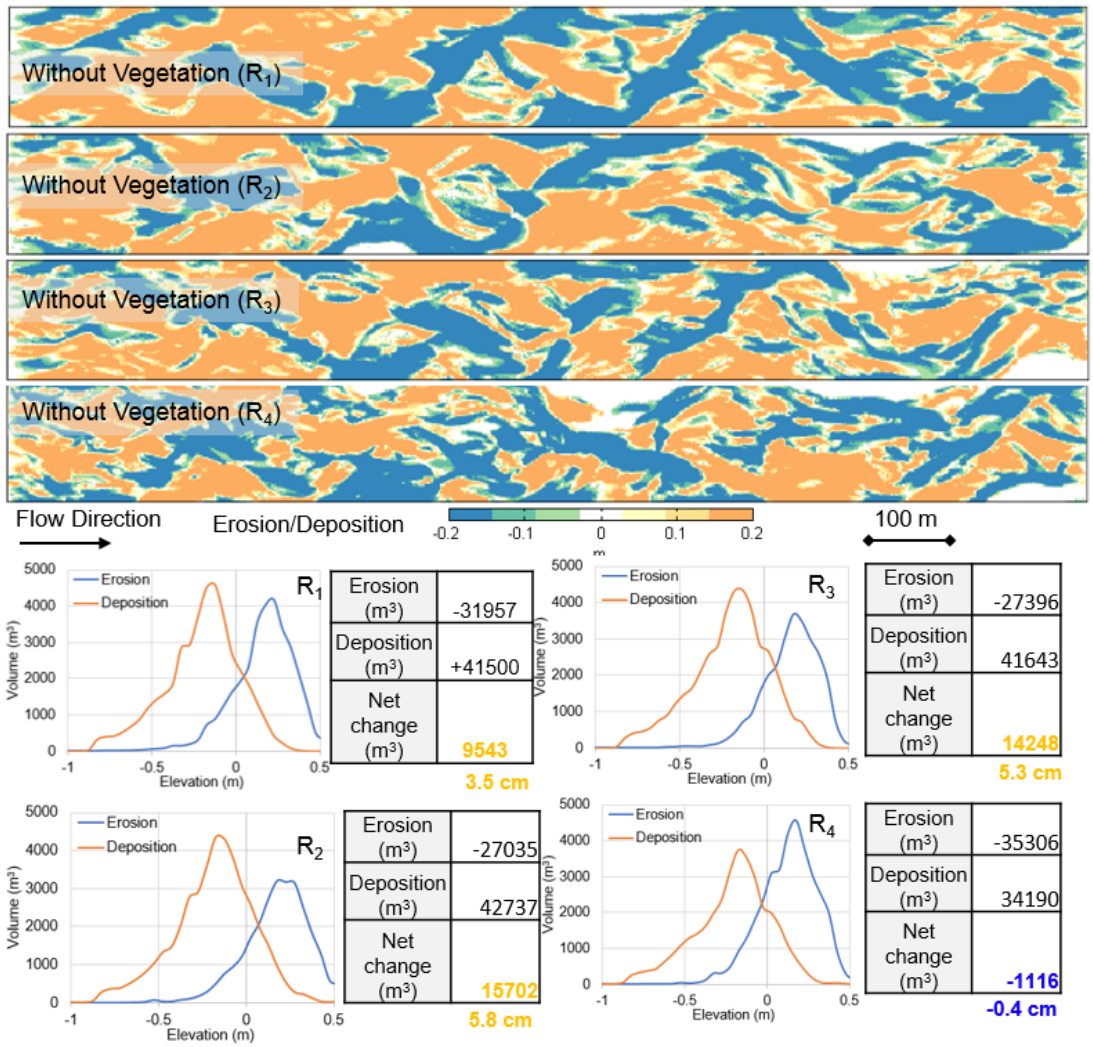

Figure 6.29 Total volumetric change pattern with respect to initial topography. The top maps show spatial distribution; the graphs below show distribution with respect to initial topography, and the table shows total erosion and deposition volume and the net change.

This pattern, in turn, relates to differences in the frequency modelled shear stress distribution between the scenarios, which are shown in Figure 6.30 below, extracted at the peak discharge of the final flood.

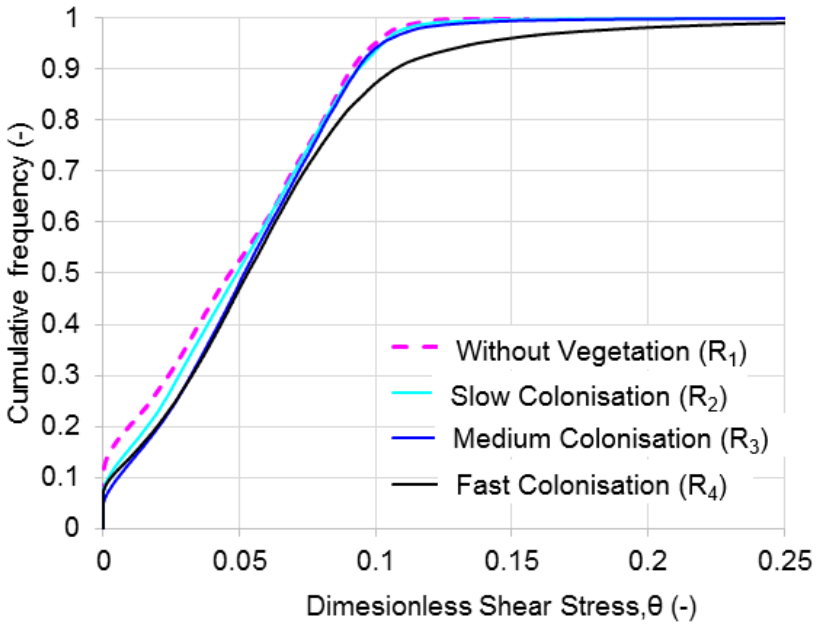

Figure 6.30 Frequency distribution of dimensionless shear stress (θ) for four simulated scenarios extracted at the peak discharge (70 m^3/s) of the final flood.

While median dimensionless shear stresses between the vegetated scenarios differ only marginally, 0.0492, 0.051 and 0.053 for R_2, R_3 and R_4 respectively, the tail of the distribution contrasts strongly as illustrated by the 95th percentiles of 0.102, 0.101 and 0.137 respectively. This pattern reflects the confinement of discharge into the reduced active belt (only 44 % of the total reach width for R_4 vs 56-53 % for R_1-R_3; Figure 6.24), within which the flow is further channelled into anabranches that are narrowed by vegetation encroachment. The higher erosional power of the resulting flows increases the rate of bed scour, incising the active channels as discussed above in 6.5.3, and in so doing reinforcing the feedback between flow and form that accentuates further bed scour and disconnection of the channel and bar topography.

6.5.5 Simulated Vegetation Dynamics

The vegetation model used in this version of BASEMENT does not seek to represent the complexities of community structure and autogenic controls such as competition on growth and development. Rather, the focus is on establishing a simplified succession framework that is 'fit-for-purpose' in representing the effects of vegetation on the physical hydrodynamic and sedimentological character of the system. These

processes, in turn, shape the morphology, creating opportunities and constraints for biomass growth. Together, this approach thereby represents the feedbacks that control the emergent properties of the simulation reach as a biogeomorphological system.

This vegetation model is based on a standard limiting growth curve, which predicts normalised biomass density based on time and single growth rate parameter. There is the capacity to control the final equilibrium (climax) distribution of vegetation according to mean bed level (after Marani et al., 2013), though in this case, a uniform potential biomass distribution was used for simplicity. In the simulations used here, a further decision was taken *a priori* to represent vegetation as woody species, here termed 'strong' vegetation after (e.g., Millar, 2000; Li and Millar, 2011; Bertoldi et al., 2014)). A simple linear function correlating the change in dimensionless critical shear stress to the biomass density was then applied to model the effects of root reinforcement.

Despite the gross simplification of the ecological processes, the scenarios modelled here illustrate the complexity of the interaction between fluvial processes and vegetation. The three differing parameterisations give rise to statistically distinctive emergent distributions of biomass density as shown in Figure 6.28. These patterns are principally linked to the time taken to reach equilibrium biomass, which sets the rate on vegetation growth and hence the morphological feedback to become established through the linked parameterisation of the critical shear stress.

The simplest simulated vegetation structure arises in R_4, which given the short time to equilibrium (2 years) has only three modal vegetation states: biomass = 0; 0.7; or 1.0. There is only a minor overall shift between the proportions of the bed in these three states through time, with the climax vegetation state dominating quickly after 2 years. The dominance of vegetation quickly leads to 'terrestrialisation' of the channel

margins, creating homogeneous floodplain environments. By contrast, the slower growth rate models, R_2 and R_3, generate more spatially (and therefore, statistically) diverse distributions of vegetation states, with pioneer communities persisting in R_2, while the faster rate of succession leads to the dominance of climax communities in R_3 after the full 15-year period. Again, the channel margins, as the least disturbed areas of the reach, develop the most mature communities, in for R_3 present the only areas reaching the climax state. By contrast, a number of mature mid-fairway islands develop in R_4 and play a key role as nuclei around which bars coalesce. However, unlike R_4, these larger units are still subject to reworking over the longer term, and there are very limited persistent stable areas of the floodplain that develop. A more sophisticated ecological model would be required to interpret these biomass distributions from the perspective of biodiversity or broader ecosystem services. However, the maximum diversity of vegetative states here is associated with the intermediate growth rate model, R_3.

6.5.6 **Model Parameterisation and Equifinality**

The experiments described here provide a highly constrained review of the full parameter space of the system. Decisions were made to simplify key aspects of the parameterisation a priori, for example assuming a uniform distribution of equilibrium vegetation states (by fixing the Marani et al. (2013) function), and only examining single roughness and critical shear stress functions with biomass. Within the context of a single thread system, Bertoldi et al. (2014) provide a more comprehensive analysis of the vegetation model, considering multiple parameterisations of the Marani et al. (2013) function and representations three ‘strengths’ of vegetation class, associated with differing curves for the Strickler Ks and critical dimensionless shear stress. Their experiments suggested a threshold in the system behaviour, resulting in only two possible stable end states for bars, vegetated and unvegetated. They argued that the incorporation of further effects, such as including the effects of rooting on

slope stability, or more complex (i.e., logistic) vegetation growth models may be required to simulate a smoother transition between vegetation states.

It should be noted, however, that there exists the potential for significant parameter compensation to occur as the complexity of the range of functions used increases. For example, by using a range of different vegetation strength models, it becomes possible to generate equivalent predictions of the critical shear stress after a given period without disturbance, with very different growth rate models. Figure 6.31 below illustrates the potentially overlapping relationships between the estimated critical shear stress and time-since-last-disturbance based on three different growth models and three different models of root reinforcement. This clearly highlights the chance for equivalent outcomes to emerge in terms of the morphodynamic forcing with widely varying representations of the vegetation structure and growth.

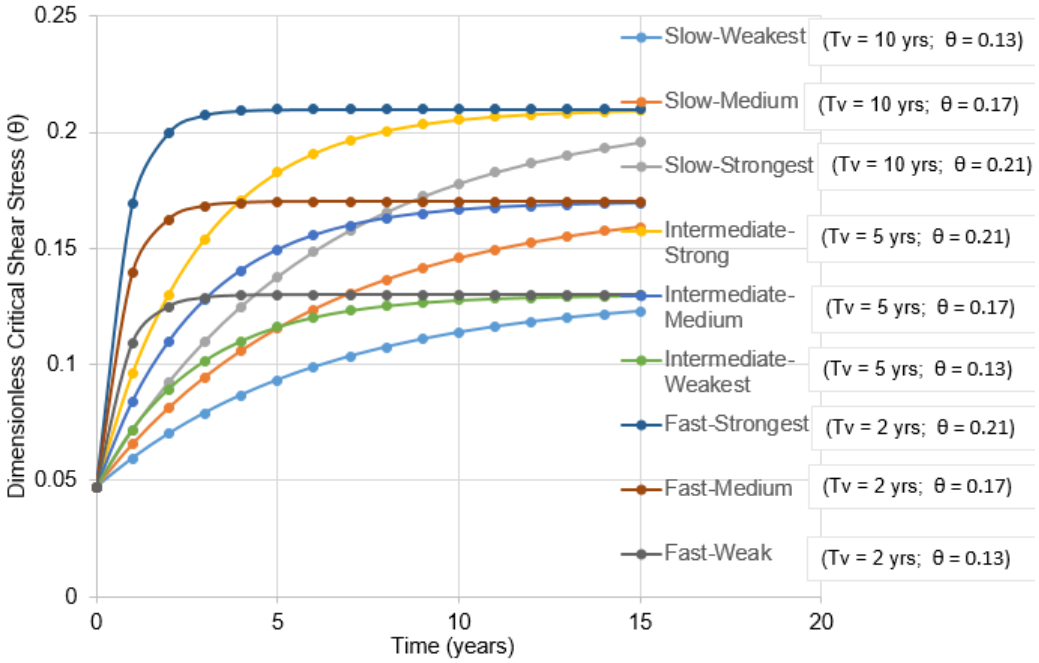

Figure 6.31 Growth rate curves at different combination of vegetation showing estimated critical shear stress and time-since-last-disturbance.

6.6 Conclusions

Scientific explanations of the feedback and linkage between flow, sediment transport and vegetation dynamics in braided rivers have most often inferred from the short-

term field and highly abstracted laboratory experiments. Although these approaches have been useful in providing an insight, nature the feedback processes, quantifying the long-term trajectory of river systems remains a challenge.

The application of numerical modelling offers a useful alternate vehicle to explore these interactions. The approach used here, incorporates a highly abstracted model of the ecological processes, focusing principally on the impact of vegetation on hydraulic roughness and entrainment. By coupling these effects within a morphodynamics model, it becomes possible to explore the different scenario of vegetation type and growth that may impact directly on the geomorphic trajectory of braided rivers. Key conclusions to arise from this study include:

1. Simulated vegetation colonisation may limit lateral channel mobility, while encroachment of vegetation further serves to confine flows, resulting in narrowing of individual channels and the entire active channel belt.
2. The extension of (1) may lead to the metamorphism of the active braided channel to wandering channel planform, with terrestrialisation of the once active floodplain.
3. Confinement of flows accelerates the loss of active width, as shear stresses increase in the narrowly confined anabranches, causing them to incise and driving an increase in bed relief and disconnection of the wetted and sub-aerial areas of the bed.
4. The modelled effects are sensitive to the combination of growth rate and the linked functions for the critical shear stress and hydraulic roughness. There is, furthermore, the possibility for significant parameter interaction between these functions in the current model structure. Such compensation may make it difficult to deterministically isolate potential effects to a given timescale or vegetation type, so that interpretation of the timescales of modelled responses should be approached critically.

Chapter 7: Thesis Discussion

7.1 The Research Context

The concept of 'equilibrium' dominated geomorphology for over half a century, fed by the thermodynamic paradigm imported into the discipline in the 1960s. This provided a systems-framework to explain how form-process interactions and the associated forces and energy transformations drive landscapes to a given (equilibrium) steady form (Thorn and Welford, 1994; Huggett, 2007; Church, 2010). There is now, however, a growing understanding that the transient dynamics of the natural and anthropogenic drivers of the environment and the associated complex patterns of environmental response, implies that very few open natural environmental systems ever reach a steady equilibrium condition. There is now an emerging interest in landscapes that lie far from such perceived equilibria, associated with recent and/or high magnitude changes in the driving forces or boundary conditions (Phillips, 2011). Gaining an understanding of how rivers, in particular, behave in the face of such environmental stresses, their resilience to change, the presence of non-linear response or thresholds in their behaviour, is now seen as essential to help manage the hazards, assets and services they provide (Brierley and Fryirs, 2016).

The evolutionary trajectory of rivers responds to broad-scale (catchment) boundary conditions that parameterize the hydroclimatological regime and sediment supply, but also internal, reach-scale feedbacks between river morphology, discharge, sediment transport and vegetation. At both scales, these dynamics may be influenced by direct human intervention through mining, water abstraction, impoundment, resectioning, realignment and indirectly through climate and land use change. There is, therefore, an ever more pressing need to develop a robust science basis to help inform river

management strategies, offering insight into the short- and long-term the consequences of such anthropogenic interventions.

Developing understanding through large-scale natural experiments in real rivers is rare, reflecting the high costs, risks and natural societal scepticism of intervention as well as the methodological concerns associated with the difficulty of maintaining controls. Historically, therefore, our insight into river behaviour has been gleamed through empirical monitoring, albeit strategically designed, and scaled laboratory investigations. These approaches offer a means to derive the reductionist physical principles that link flow, sediment transport and vegetation, but provide only a limited basis to predict the longer term, and larger scale dynamics of natural systems.

This difficulty of generalizing site-specific field and scaled-laboratory experiments while well-recognized (e.g., Williams et al., 2016b), is not easily resolved with an alternative methodology. However, in the last decade, numerical simulation modelling has emerged as a synthetic tool to interrogate theories of river response and interpret the sensitivity of system dynamics to key physical parameters and process-representations (Siviglia and Crosato, 2016; Escauriaza et al., 2017).

Numerical models enable comprehensive quantification of system behaviour across all relevant time and space scales, so that the constitutive mechanisms that control the pattern of morphodynamics in simulations are fully transparent. However, while considerable progress has been achieved using morphodynamic models over the last decade, key challenges still remain. At the heart of these, is a framework for model evaluation that provides a robust examination of model performance to prevent run-away conclusions being achieved hurriedly without due criticality. This is particularly important now, as the technological advances mean that morphodynamic models may increasingly be developed and used as black-box tools. Mosselman and Le (2016)

caution against the risks that the community now faces, with an extreme example of the dangers that these developments may lead to:

Fast technological developments have fuelled impressive advances in two-dimensional depth-averaged (2DH) numerical models of river morphodynamics over the past eighty years. Bendegom (1947) numerical code was solved by hand in the 1930s, when a calculator was still a profession instead of a machine. Today, river engineers visit a river in a far-away country, collect elementary data on the spot, set up a computational grid based on Google Earth in their Wi-Fi-equipped hotel room in the evening, run a morphodynamic simulation, and present plots and animations of the morphodynamic evolution to the client or stakeholders the next morning.

Mosselman and Le (2016), p. 1.

In this thesis, the popular numerical framework model BASEMENT was used as a vehicle to explore the processes and controls that influence the development, maintenance and evolutionary trajectories of active, gravel-bed braided rivers. This thesis focused on four principle themes, exposed in four interlinked chapters, each targeting (a) specific research question(s). A discursive review of the finding of each research theme was integrated within each chapter, so that this discussion seeks to synthesize these results and highlight the key contributions of the thesis, and most importantly, indicate the direction of future travel.

7.1.1 Research Question 1

What characteristics of the structure and dynamics of braided rivers can be quantified as a hierarchical set of metrics and used to evaluate the performance of numerical models of braiding?

Chapter 3 was formulated directly to address the need for a consistent, multi-criterion, multi-scale and multi-dimensional framework to evaluate the performance of morphodynamic models applied to study the form and dynamics of braided rivers. Building on opportunities presented by new datasets and methods of geospatial analysis, this chapter proposed a quantitative framework emphasising four sets of

criteria: a) metrics of planform and network structure; b) metrics describing the 3D morphology; c) process descriptions of the hydrodynamic processes; and finally, d) metrics describing the morphodynamics behaviour. While many of the methods proposed in this framework rest on the availability of new high-resolution topographic data, the approach can be generalized to focus on well-established (universal) properties of braided rivers (see, Section 3.7.1).

For this thesis, an unparalleled dataset comprising multi-annual high-resolution surveys of a braided reach of the River Feshie was used to parameterize and evaluate model behaviour. A 700 m reach was taken to provide the natural prototype for future modelling, and metrics defining the system extracted using DEM data from 2003-2007. These data were also used to provide the boundary conditions for fixed-bed hydrodynamic simulations which were used to characterize stage-dependent hydraulic characteristics, such as the reach averaged at-a-station hydraulic geometry and sediment transport rating curves.

Importantly, it becomes clear from the wide-ranging metrics used to characterise the structure, form and kinematics of this system that no single measure provides a robust signature against which performance can be measured. Classical metrics, such as the frequency distribution of elevations (and their accompanying moments or percentiles) often obscure key differences in the deterministic form that are clearly abehavioural. New approaches, such as the use of DEMs of Difference, and quantifying the structure and form of modelled and observed changes, provides a higher-level assessment of model behaviour.

While there is relatively little literature describing common approaches to the validation of morphodynamic models in the river science community, there has been a more concerted effort to consolidate practice in coastal engineering. A common approach in this context is a single-number metric to quantify the relative accuracy of

simulations using a mean-squared error skill score (MSESS) often referred to as the Brier Skill Score or BSS (Sutherland et al., 2004). This measures the improvement in the accuracy of a prediction over that provided by a reference model, usually taken to be the initial bed condition. In effect, the approach tests the information gained by using the model over that provided by the original data. In essence, the measure is similar to the Nash Efficiency Statistic or NES (Nash and Sutcliffe, 1970) beloved of rainfall-runoff modellers, that assesses the improvement in model fit relative to a stationary mean.

Application of such model skill assessments for the specific context at hand is complicated. First, it is clear that the behaviour of the natural system inevitably incorporates phenomena that are not represented in the model (e.g., sediment size mixtures), so deviations between the model and reality should, therefore, be expected. Moreover, there is a latent danger in targeting skill measures as the incomplete process representation could lead the modeller to over-calibrate their 'tool', resulting in unforeseen parameter and process compensation effects which yield 'apparently better' predictions but for the wrong reasons.

Second, it should be recognized that our observational framework is also uncertain, and often in error. While models of the topographic form of rivers have improved dramatically, estimates of cut-and-fill derived from uncertain DEMs have been shown to have wide estimates of uncertainty that often dwarf the net sediment budget (see, Wheaton et al., 2010). Finally, we should expect a well-behaved model to yield similar sensitive dependence to initial conditions that we observe in natural prototype braided rivers. This implies that small uncertainties in our observed data and generated by the model discretisation, are likely to lead to a rapid divergence between simulations and reality.

It could be argued, therefore, that the goal of modelling in this context should be to focus on understanding the physical controls on system behaviour rather than predicting the future. While laudable, it is likely, however, that commercial (and practical) drivers will always create a desire to use morphodynamic models for forecast unknown futures as illustrated by the quotation from Mosselman and Le (2016) above.

The research undertaken here, at a minimum clearly points to the need for multiple metrics of model behaviour to be used in combination. With the spread of evaluation criteria defined here, it was possible to identify key differences between the simulations developed in later chapters, and this approach provides a template for future work.

There are interesting potential avenues to explore in refining this approach. For example, it may be possible to formalise a multi-criterion measure, which combines individual metrics, weighted to account for the desired user goals. Alternative strategies could involve the use of decision trees to refine the calibration process, allowing the use of binary or categorical evaluations of model performance to guide parameter and process identification.

Beyond, this, perhaps the most valuable application of the framework, would be to evaluate similarities and differences between the growing ranges of natural systems for which high-quality data are available. This incorporates a wide range of rivers encompasses different energy states (e.g., the sand-bed South Saskatchewan (e.g., Lane et al., 2010) to the higher energy gravel piedmont rivers such as the Tagliamento, Italy (e.g., Bertoldi et al., 2011b) and the Rees, NZ (e.g., Williams et al., 2016a), through to high energy mountain braided systems such as the Veneon River, France (e.g., Piegay et al., 2009). Such comparison of braided rivers from different physiographic setting could provide a clear insight into the spectrum of forms and

processes that are shared universally by braided rivers, and those that are case dependent.

7.1.2 Research Question 2

To what extent can the physics based numerical model BASEMENT reproduce the characteristic behaviour of a natural prototype braided river under steady flow, equilibrium conditions?

Chapter 4 focused on a sensitivity analysis designed to assess the capability of BASEMENT to simulate the development and maintenance of a braided channel from a plane bed initial condition. The experimental design involved parameterisation of the model, using the braided reach of the River Feshie as a prototype to define key system characteristics (width, slope, grain-size) and a formative steady flow condition based on the 2-year return period discharge (70 m^3/s). The sensitivity analysis focused on two key aspects of the process representation of the model; a) the effect of gravity on the vector of bed material transport, as parameterized by a 'lateral slope factor'; b) the approach to modelling bank erosion using repose angles of varying magnitude and vertical variation. It should also be noted, that the code used for the simulations involve further generalizations that could be significant. For example, there is no representation of helical fluid motion that arises from the interplay of centrifugal and pressure gradients in curved channels (see Powell, 1998; Mosselman and Le, 2016), and a single, uniform grain size was used in all calculations, precluding grain sorting effects and the potential development of any bed armouring (see Powell, 1998; Church, 1999; Hunziker and Jaeggi, 2002; Vericat et al., 2006; Mao and Surian, 2010). Furthermore, a fixed cell size was used for the spatial discretisation which places further constraints on the maximum slope angles that can be represented in the bank erosion model, and the hydraulic roughness and eddy viscosity were spatially 'lumped'.

Despite these simplifications, the experiments demonstrated the capacity of the model to develop and maintain braided conditions across a wide range of formulations. This was evaluated using the four-fold model validation framework, illustrating the importance of incorporating 3D morphological perspectives, as well as process-based measures to discriminate between simulations effectively. Importantly, the results highlighted the importance of incorporating representations of both lateral (gravitational) transport and vertical variations in bank stability in order to achieve steady equilibrium conditions. The sensitivity analysis suggests parameterisation of the lateral transport factor in a range 1.5 – 2, while for the grid size of 2 m^2 used here, critical angles of repose for dry = 25°, wet = 18° and deposited material = 5° should be used. Vertically varying the critical angle of repose in this way enables the removal of deposited and wet material at comparatively low threshold angles, while maintaining steep bank slopes through the use of a higher angle for dry conditions. Without this variation, globally low repose angles quickly diffuse slopes resulting in a lack of surface relief and channelization, while globally high repose angles limit lateral bank erosion causing the existing anabranches to incise in response and disconnect bar and channel topography.

The development of an effective bank erosion model has been a limiting step in the progress of morphodynamic models. This reflects the combined difficulties of modelling near bank flows in 2D depth-averaged models and representing steep gradients that require a fine scale of spatial discretisation or separate sub-grid model (Siviglia and Crosato, 2016). As a result, angles of repose are often calibrated, yielding unrepresentatively low parameter values that undermine the physicality of the process representation (Williams et al., 2016b). While alternative solutions, such as irregular adaptive gridding and sub-grid parameterisation schemes offer more sophisticated solutions to this conundrum, it appears that the simple framework used here provides an effective compromise.

Interestingly, the lack of a scheme to represent secondary circulation does not appear to have prevented the development of representative modelled topography and processes. The presence of such flows can cause the direction of sediment flux to deviate from the depth-average flow direction and which has been found important in studies using other morphodynamic models (see Schuurman et al., 2013). However, while there is no representation of this processes in BASEMENT, the code does account for the gravitational pull on particles through the lateral slope model described in Chapter 2. The incorporation of this force serves to dampen the evolving topography (Mosselman and Le, 2016), effectively reducing the tendency for exaggerated local scour to develop, a key problem associated with morphodynamic evolution in rule-based, reduced complexity models (e.g., Doeschl-Wilson and Ashmore, 2005).

There is clear potential to extend the scope of the current sensitivity analysis. All simulations here were conducted using spatially fixed values for the flow resistance parameters (hydraulic roughness and eddy viscosity). While Schuurman et al. (2013) found the pattern of bed and bar development modelled with Delft3D to be relatively insensitive to these parameters, detailed validation of the hydraulic predictions of Delft3D using distributed aDcp velocimetry by Williams et al. (2013) found the eddy viscosity parameterisation to be critical for the predicted distribution of bed shear stresses.

There are also aspects of the numerical solution that require further investigation, both in terms of the solver used and the resolution of the spatial discretisation. Mosselman and Le (2016) illustrate how grid truncation errors in the numerical discretisation can introduce diffusive effects, similar to those deliberately generated by secondary circulation and gravitational effects. There exists, therefore, scopes for compensation effects between these choices that may compromise calibration and validation of the model.

Perhaps the most significant area for future research, however, lies in the development and application of mixed grain-size models of sediment transport (Parker et al., 2000; Blom, 2008). Singh et al. (2017), examined the influence of multi-grain size sediment on the numerical evolution of gravel-bed braided river using Delft3D. In this, they observed lower bar heights for formulations with uniform sediment when compared to simulations with sediment mixtures. Such responses are likely to arise from by simulating bed armouring that leads to spatial variations in the threshold for motion and concomitant increases in flux once the armour is disrupted.

Finally, the validation framework used here could also be extended effectively to model other prototype systems and as a basis for benchmarking the growing range of morphodynamic models (e.g., Delft3D, TELEMAC-MASCARET, iRIC). This multi-criterion approach incorporated new metrics, such as the vertical distribution of erosion and deposition volumes, which proved to be particularly effective in distinguishing between simulations and have broad applicability.

7.1.3 Research Question 3

How do the equilibrium model forms and forces derived at a steady flow condition differ from energetically-normalised different steady and unsteady simulations that incorporate variations in the frequency and magnitude of competent floods?

At its heart, this research question sought to examine a historical conundrum – specifically – whether braiding is dependent on the existence of an unsteady, flashy flow regime. To some extent, this question has been resolved by laboratory experiments that have demonstrated the emergence of braided planforms under steady flow regimes. However, it is less clear whether subtle differences in the nature of braiding and the key hydraulic and sedimentological processes involved differ under steady and unsteady flow regimes.

A simple numerical experiment was designed to evaluate this question in Chapter 5. This involved the development of paired steady-unsteady energetically normalised flow regimes, across a range of discharges spanning annual to 15-year return period discharges. Vegetation was excluded in all simulations so that the results of simulations represents the case of unvegetated braided rivers. Simulations were initialised using the synthetic topography from the 70 m^3/s steady flow experiments in Chapter 4 as the initial condition. This design, therefore, enabled at insight into how channel form and processes respond as the discharge regime is increased (up to 110 m^3/s) and decreased (down to 50 m^3/s) in magnitude and maintained at 70 m^3/s as a control. Moreover, this also provided insights into difference between channel evolution under steady and unsteady form of hydrographs.

A qualitative examination of the difference in response between the steady and unsteady models revealed few significant findings, with the overall planform and topographic adjustment similar under these two types of regime. However, the analysis of morphological change, conducted using DEM differencing, revealed some striking differences in the system behaviour under these flow regimes. This is illustrated by the net sediment budget, which for all unsteady simulations was found to be aggradational, while all steady simulations were found to be degradational. This pattern was interpreted to reflect hysteresis effects on bed mobilization, with scour dominating the rising limbs of the hydrographs and deposition dominant during falling limbs. The reduction in discharge during the hydrograph cycles was found to be essential in promoting deposition and bar formation, which in turn promotes further channel complexity and sedimentation in the future. By contrast, the steady flow regimes were found to be much more effective conveyors of sediment, essentially transferring all internally mobilized sediment, generating a series of streamlined, simple anabranches.

The pattern of channel adjustment to the change in discharge magnitude was, however, the most significant effect observed, regardless of whether the flow regime was steady or unsteady. Increasing the flood magnitude served to evolve less complex channel networks with higher amplitude bars (see evolution in terms of TBI and bar height in Section 5.4.2). This reflects the progressive dominance of flow within a smaller number of larger channels. By contrast, lowering the flood magnitude appeared to lead to a more complex and shallower network of anabranches. At these lower discharges, with flows are largely contained within the capacity of the principal anabranches, erosional and depositional processes are concentrated within the channels, leaving the elevated bars intact. The locally available high shear stresses here then promote bar (bank) edge erosion, particularly near bends and confluences. The eroded mass is then deposited locally downstream due to the limited competence of the flows. This leads to progressively reduce the amplitude of bars, and in turn then facilitates overtopping of discharge on previously elevated areas, resulting in the shallow but complex network of smaller channels. This pattern of adjustment is captured by the change in the at-a-station hydraulic geometry relationship, with higher width exponents associated with the lower discharge scenario (Section 5.4.3).

7.1.4 Research Question 4

How does the interaction between vegetation growth rate and discharge flow regime govern the evolutionary morphology of braided rivers?

In Chapter 6, a new code to simulate vegetation dynamics and feedbacks (Bertoldi et al., 2014) was used to investigate the interaction between flow, sediment and vegetation on the emerging river form and ecosystem structure. Historically, controlled simulation of these feedbacks has only been possible through scaled physical modelling (e.g., Gran and Paola, 2001; Tal et al., 2004; Tal and Paola, 2010). While these experiments have provided useful insights into the mechanisms controlling the interrelationship between vegetation and physical processes, they are

confounded by the difficulties of scaling the properties of vegetation and the difficulty of representing cohesive sediments. Numerical modelling does not offer a comprehensive panacea to these issues but does provide a framework in which interactions can be modelled relatively quickly and flexibly.

In the experimental design used here, simulations were initiated using the 'equilibrium' topography generated in Chapter 4 (Run R_9). The model realizations were then based on a hypothetical 15-year period, in which flows oscillated between 70 m^3/s (for 8 hours) and 20 m^3/s (for one hour) to represent, an annual high flow event. The one hour of low flow conditions was introduced to allow vegetation growth, which was accelerated to represent one-year of intervening growth within this period, confined to areas above the inundation level associated with this intermediate frequency discharge. Decoupling the vegetation growth and morphodynamic models in this way provided a ready means to optimize simulation times, enabling a comprehensive evaluation of dynamics over a 'synthetic' 15-year period. The experiment sought to examine the interaction between the evolving morphodynamics and vegetation based on three different hypothetical growth rates. A further simulation without vegetation was used to provide a reference control.

In the absence of vegetation (Run R_1), the structure and dynamics of bars, channels, confluences and bifurcations of the active river remain intact throughout the simulation. By contrast, introducing slow (Run R_3) to medium (Run R_4) growing vegetation causes the channel to evolve into a narrowed, wandering form, comprising a dominant sinuous channel with a bank attached, vegetated alternate bars. After 15 years, at quasi-equilibrium, the active channel follows a stable sinuous tract, albeit with dissection of chute channels on the bar tops occurring episodically. Simulations based on fast growing vegetation (Run R_4) resulted in a vegetated multithread channel, confined close to the left bank, while a large and continuous floodplain evolved on the right bank. This pattern is heavily linked to the associated

parameterisation of the critical bed shear stress for entrainment which is made a function of the normalised local biomass density (varying between 0-1). In the scenarios modelled here, a linear relationship is assumed, in which densities of over 0.7 were associated with rarely predicted dimensionless shear stress (i.e., 0.15). This parameterisation implied that need for extensive biomass development to impact directly on the pattern of erosion, and only the fast-growing vegetation scenario provided a sufficient speed of colonization to impact strongly on the morphodynamics.

The results nonetheless, broadly appears to replicate some key features observed in previous flume experiments (e.g., Gran and Paola, 2001; Tal et al., 2004; Jang and Shimizu, 2007; Tal and Paola, 2010). In particular, the numerical simulations with vegetation show: a) a tendency to increase the depth of scour holes; b) a reduction in erosion and deposition volumes; c) a reduction in the turnover rate of the channel bed; and d) a reduction in the active width.

The structure of the evolving vegetation communities was also found to be strongly linked to pattern of emerging morphodynamics. The relatively low rates of turnover associated with the fast vegetation scenario led quickly to a monoculture of vegetation stands of similar age. By contrast, the slower growing scenarios developed a more complex structure of surface cover, reflecting the time-transgressive nature of bar formation and disruption. Such results provide a useful first step towards testing key ecological concepts such as the 'intermediate disturbance hypothesis' (Connell, 1978).

Nonetheless, the numerical simulations conducted here are relatively simplistic and there is a pressing need to consolidate these insights, in particular through a more comprehensive sensitivity analysis of the vegetation model. A number of clear avenues for further research are evident. First, a uniform distribution of equilibrium vegetation (biomass) density was assumed. The Marani function used within the

model does, however, provide a basis to explore more complex scenarios, reflecting the of bed level of water availability and plant growth explicitly. Further avenues for research involve the assessment of more complex parameterisations of the effect of biomass on flow resistance and the critical threshold for entrainment. Here, data from existing studies was used to parameterize these relationships (e.g., Millar, 2000; Li and Millar, 2011; Bertoldi et al., 2014). However, such relationships depend strongly on the hydrology, species and climatic conditions, and there remains significant scope to examine the range of potential responses.

Third, there remains vital work to be done in terms of time scaling of vegetation growth and decay. The growth and decay rate used in this study is strongly accelerated in order to provide a model effective run-time. As discussed in Chapter 6, the simple design of the feedback functions implies the potential for considerable compensation effects to emerge that run the risk of confusing the interpretation of the model results (Section 6.6.6). Simulating hydraulic, morphodynamic and vegetation dynamics at a 1:1:1 scale, using the actual hydrographs of the natural prototype could provide a useful approach to clarify some of the time scaling issues (e.g., the time required to achieve optimal biomass density) and the two-way flow-form-vegetation feedbacks. It is important to note that the present version of vegetation model permits for morphological evolution even during the low flows. This creates an unnecessary computational burden, adding to simulation time (as the CFL condition is relatively resilient to the flow magnitude). Consequently, it would be advantageous to modify the existing code to explicitly restrict the morphodynamic evolution to high flow events only.

Chapter 8: Thesis Conclusion

Braided rivers are highly prized landscapes, both in terms of their geographical, geological and ecological diversity and the valuable economic resources they provide. However, direct and indirect human interventions in the past century have led to loss of these environments, through an apparent combination of flow regulation, invasive species colonisations and land management. As we are an integral component of this landscape, the services that these rivers provide in the future depends upon the sustainable management of their naturally occurring processes in the face of these increasing anthropogenic stresses.

Developing an understanding of the form and processes in braided rivers is a prerequisite to support both ecosystem assessments and the sustainable utilization of the resources that these rivers provide. This thesis provided novel perspective on the functioning of braided rivers, derived through numerical simulation using an existing coupled flow, sediment and vegetation numerical model. In particular, the thesis provided four key contributions to the current state of knowledge, which are:

1. Firstly, the thesis developed a quantitative framework to measure the multi-dimensional form and processes of braided rivers, designed with the validation of numerical models in mind. This framework provides a multi-criteria assessment of model performance, incorporating planform, topographic, hydraulic and morphodynamic properties of the modelled system. Additionally, the framework offers a means to quantify the river environment of existing prototype systems to support model testing directly on empirically rich case studies.
2. Secondly, the thesis provided a comprehensive evaluation of the capability of the numerical model to simulate the development and maintenance of braiding processes. The simple experimental design under steady flow and sediment

supply demonstrated possibility to generate a continuously evolving dynamic model of braiding from plane bed initial conditions. The incorporation of a complex bank erosion model and representation of gravitational effects of the vector of sediment transport were revealed to be crucial to determine such behaviour. Together these representations enable the development of a sensitive model balance between too much and too little diffusivity which is crucial to prevent exaggerated channel incision on one hand, or the failure to maintain defined channels on the other.

3. Thirdly, this thesis provided a step forward in understanding how the form and processes of unvegetated braided rivers change with respect to the magnitude of discharge and under steady and unsteady discharge condition. The numerical experiments suggested that reductions in discharge led to the evolution of a shallow network of complex channels, while increases in discharge led to the opposite, with dominant anabraches conveying the principle sediment load. Differences between the steady and unsteady flow regimes appeared secondary to the overall adjustment to changes in discharge. However, key differences were observed in the net sediment balance, which identified strong differences between the aggradation and degradation nature of steady and unsteady flow regimes. The unsteady flow regimes were dominantly aggradational whereas the steady flow regimes were degradational. The aggradation nature of bed morphology under unsteady flow was revealed to be associated with the hysteresis effect in bed-reworking (e.g., dominance of scour activities during rising limbs and bar deposition during the falling limbs) that avoid local erosion of channels as in the case of steady flow. Such insights are useful in river management programs as there is increasing pressure on rivers from direct (e.g. through river regulation) and indirect (land-use and climate change) anthropogenic controls, as well as natural climatic variability.

4. Finally, this thesis provided an advance in our understanding of the two-way interactions between flow, sediment, and nonlinear vegetation colonisation/die-back. The numerical modelling experiments suggest that at specific combinations of flood flows and vegetation, it may be possible to transform the active braided river into wandering or single thread rivers.

To sum, the study therefore opens a way forward to simulate the long-term geomorphic response of braided rivers to different anticipated flow, sediment supply and vegetation providing critical support in river management strategies.

References:

ABBE, T. B. & MONTGOMERY, D. R. 1996. Large woody debris jams, channel hydraulics and habitat formation in large rivers. Regulated Rivers Research & Management, 12, 201-221.

ABERNETHY, B. & RUTHERFURD, I. D. 1998. Where along a river's length will vegetation most effectively stabilise stream banks? Geomorphology, 23, 55-75.

ABERNETHY, B. & RUTHERFURD, I. D. 2001. The distribution and strength of riparian tree roots in relation to riverbank reinforcement. Hydrological processes, 15, 63-79.

ANDERSON, M. G. & BATES, P. D. 2001. Model validation: perspectives in hydrological science, John Wiley & Sons Ltd.

ARCEMENT, G. & SCHNEIDER, V. 1989. United States Geological Survey Water Supply Paper 2339. Guide for Selecting Manning's Roughness Coefiicients for Natural Channels and Floodplains.

ARSCOTT, D. B., TOCKNER, K., VAN DER NAT, D. & WARD, J. 2002. Aquatic habitat dynamics along a braided alpine river ecosystem (Tagliamento River, Northeast Italy). Ecosystems, 5, 0802-0814.

ARULANANDAN, K., GILLOGLEY, E. & TULLY, R. 1980. Development of a Quantitative Method to Predict Critical Shear Stress and Rate of Erosion of Natural Undisturbed Cohesive Soils. CALIFORNIA UNIV DAVIS DEPT OF CIVIL ENGINEERING.

ASHIDA, K. An investigation of river bed degradation downstream of a dam. Proceedings of 14th Congress of the IAHR, 1971, 1971.

ASHMORE, P. 2001. Braiding phenomena: statics and kinetics. Gravel Bed Rivers V, 95-121.

ASHMORE, P., BERTOLDI, W. & TOBIAS GARDNER, J. 2011. Active width of gravel-bed braided rivers. Earth Surface Processes and Landforms, 36, 1510-1521.

ASHMORE, P. & CHURCH, M. 1998. Sediment transport and river morphology: a paradigm for study. Water Resources Publications LLC, Highlands Ranch, Colorado, 115-148.

ASHMORE, P. & SAUKS, E. 2006. Prediction of discharge from water surface width in a braided river with implications for at-a-station hydraulic geometry. Water Resources Research, 42.

ASHMORE, P. E. 1982. Laboratory modelling of gravel braided stream morphology. Earth Surface Processes and Landforms, 7, 201-225.

ASHMORE, P. E. 1987. Bed load transfer and channel morphology in braided streams. Erosion and Sedimentation on the Pacific Rim. IAHS Publication, 165, 333-341.

ASHMORE, P. E. 1988. Bed load transport in braided gravel-bed stream models. Earth Surface Processes and Landforms, 13, 677-695.

ASHMORE, P. E. 1991. How do gravel-bed rivers braid? Canadian journal of earth sciences, 28, 326-341.

ASHMORE, P. E. 2013. Morphology and dynamics of braided rivers. Treatise on geomorphology, 9, 289-312.

ASHWORTH, P. J., BEST, J. L. & JONES, M. A. 2007. The relationship between channel avulsion, flow occupancy and aggradation in braided rivers: insights from an experimental model. Sedimentology, 54, 497-513.

BAPTIST, M., BABOVIC, V., RODRÍGUEZ UTHURBURU, J., KEIJZER, M., UITTENBOGAARD, R., MYNETT, A. & VERWEY, A. 2007. On inducing equations for vegetation resistance. Journal of Hydraulic Research, 45, 435-450.

BAPTIST, M. J. A flume experiment on sediment transport with flexible, submerged vegetation. International workshop on riparian forest vegetated channels: hydraulic, morphological and ecological aspects, RIPFOR, Trento, Italy, 2003.

BEESON, C. & DOYLE, P. 1995. Comparison of bank erosion at vegetated and non-vegetated channel bends. JAWRA Journal of the American Water Resources Association, 31, 983-990.

BELL, S. 2012. Landscape: pattern, perception and process, Routledge.

BENDEGOM, L. V. 1947. Some considerations on river morphology and river improvement, De Ingenieur vol. 59–4, pp. B1–11. Dutch. English translation: Nat. Res. Council of Canada, Tech. Transi, 1054, 1963.

BENNETT, S. J. 2004. Effects of emergent riparian vegetation on spatially averaged and turbulent flow within an experimental channel. Riparian vegetation and fluvial geomorphology, 29-41.

BENNETT, S. J., PIRIM, T. & BARKDOLL, B. D. 2002. Using simulated emergent vegetation to alter stream flow direction within a straight experimental channel. Geomorphology, 44, 115-126.

BERTOLDI, W., ASHMORE, P. & TUBINO, M. 2009a. A method for estimating the mean bed load flux in braided rivers. Geomorphology, 103, 330-340.

BERTOLDI, W., DRAKE, N. A. & GURNELL, A. M. 2011a. Interactions between river flows and colonizing vegetation on a braided river: exploring spatial and temporal dynamics in riparian vegetation cover using satellite data. Earth Surface Processes and Landforms, 36, 1474-1486.

BERTOLDI, W., GURNELL, A. & DRAKE, N. 2011b. The topographic signature of vegetation development along a braided river: results of a combined analysis of airborne lidar, color air photographs, and ground measurements. Water Resources Research, 47.

BERTOLDI, W., SIVIGLIA, A., TETTAMANTI, S., TOFFOLON, M., VETSCH, D. & FRANCALANCI, S. 2014. Modeling vegetation controls on fluvial morphological trajectories. Geophysical Research Letters, 41, 7167-7175.

BERTOLDI, W. & TUBINO, M. 2007. River bifurcations: Experimental observations on equilibrium configurations. Water Resources Research, 43.

BERTOLDI, W., ZANONI, L. & TUBINO, M. 2009b. Planform dynamics of braided streams. Earth Surface Processes and Landforms, 34, 547-557.

BERTOLDI, W., ZANONI, L. & TUBINO, M. 2010. Assessment of morphological changes induced by flow and flood pulses in a gravel bed braided river: The Tagliamento River (Italy). Geomorphology, 114, 348-360.

BEVEN, K. 1993. Prophecy, reality and uncertainty in distributed hydrological modelling. Advances in water resources, 16, 41-51.

BEVEN, K. 2006. A manifesto for the equifinality thesis. Journal of hydrology, 320, 18-36.

BEVEN, K. J. 2011. Rainfall-runoff modelling: the primer, John Wiley & Sons.

BIGGS, B. J. F., IBBITT, R. P. & JOWETT, I. G. 2008. Determination of flow regimes for protection of in-river values in New Zealand: an overview. Ecohydrology & Hydrobiology, 8, 17-29.

BLOM, A. (2003). A vertical sorting model for rivers with non-uniform sediment and dunes. PROEFSCHRIFT ter verkrijging van de graad van doctor aan de Universiteit Twente, op gezag van de rector magnificus, prof. dr. FA van Vught, volgens besluit van het College voor Promoties in het openbaar te verdedigen op donderdag 6 maart 2003 om 15: 00 uur.

BLOM, A. 2008. Different approaches to handling vertical and streamwise sorting in modeling river morphodynamics. Water resources research, 44.

BOGEN, J. 1980. The hysteresis effect of sediment transport systems.

BOLLA PITTALUGA, M., REPETTO, R. & TUBINO, M. 2003. Channel bifurcation in braided rivers: equilibrium configurations and stability. Water Resources Research, 39.

BRASINGTON, J., LANGHAM, J. & RUMSBY, B. 2003. Methodological sensitivity of morphometric estimates of coarse fluvial sediment transport. Geomorphology, 53, 299-316.

BRASINGTON, J. & RICHARDS, K. 2007. Reduced-complexity, physically-based geomorphological modelling for catchment and river management. Elsevier.

BRASINGTON, J., RUMSBY, B. & MCVEY, R. 2000. Monitoring and modelling morphological change in a braided gravel-bed river using high resolution GPS-based survey. Earth Surface Processes and Landforms, 25, 973-990.

BRASINGTON, J., VERICAT, D. & RYCHKOV, I. 2012. Modeling river bed morphology, roughness, and surface sedimentology using high resolution terrestrial laser scanning. Water Resources Research, 48.

BRESTOLANI, F., SOLARI, L., RINALDI, M. & LOLLINO, G. 2015. On the morphological impacts of gravel mining: The case of the Orco River. Engineering Geology for Society and Territory-Volume 3. Springer.

BRIERLEY, G. & FRYIRS, K. 2016. The use of evolutionary trajectories to guide 'moving targets' in the management of river futures. River Research and Applications, 32, 823-835.

BRIERLEY, G., FRYIRS, K., CULLUM, C., TADAKI, M., HUANG, H. Q. & BLUE, B. 2013. Reading the landscape: Integrating the theory and practice of geomorphology to develop place-based understandings of river systems. Progress in Physical Geography, 37, 601-621.

BRIERLEY, G. J. & FRYIRS, K. A. 2013. Geomorphology and river management: applications of the river styles framework, John Wiley & Sons.

BRISTOW, C. & BEST, J. 1993. Braided rivers: perspectives and problems. Geological Society, London, Special Publications, 75, 1-11.

CAMPOREALE, C., PERUCCA, E., RIDOLFI, L. & GURNELL, A. 2013. Modeling the interactions between river morphodynamics and riparian vegetation. Reviews of Geophysics, 51, 379-414.

CAMPOREALE, C. & RIDOLFI, L. 2006. Riparian vegetation distribution induced by river flow variability: A stochastic approach. Water Resources Research, 42.

CARUSO, B. S. 2006a. Effectiveness of braided, gravel-bed river restoration in the Upper Waitaki Basin, New Zealand. River Research and Applications, 22, 905-922.

CARUSO, B. S. 2006b. Project river recovery: restoration of braided gravel-bed river habitat in New Zealand's high country. Environ Manage, 37, 840-61.

CHURCH, M. 1999. Sediment sorting in gravel-bed rivers. Journal of sedimentary research, 69.

CHURCH, M. 2006. Bed material transport and the morphology of alluvial river channels. Annu. Rev. Earth Planet. Sci., 34, 325-354.

CHURCH, M. 2010. The trajectory of geomorphology. Progress in Physical Geography, 34, 265-286.

CHURCH, M. & FERGUSON, R. 2015. Morphodynamics: Rivers beyond steady state. Water Resources Research, 51, 1883-1897.

CLUTTON-BROCK, T., COULSON, T. & MILNER, J. 2004. Red deer stocks in the Highlands of Scotland. Nature, 429, 261-262.

CONNELL, J. H. 1978. Diversity in tropical rain forests and coral reefs. Science, 199, 1302-1310.

CORENBLIT, D., STEIGER, J., GONZÁLEZ, E., GURNELL, A. M., CHARRIER, G., DARROZES, J., DOUSSEAU, J., JULIEN, F., LAMBS, L. & LARRUE, S. 2014. The biogeomorphological life cycle of poplars during the fluvial biogeomorphological succession: a special focus on Populus nigra L. Earth Surface Processes and Landforms, 39, 546-563.

CORENBLIT, D., TABACCHI, E., STEIGER, J. & GURNELL, A. M. 2007. Reciprocal interactions and adjustments between fluvial landforms and vegetation dynamics in river corridors: a review of complementary approaches. Earth-Science Reviews, 84, 56-86.

COULTHARD, T., KIRKBY, M. & MACKLIN, M. 2000. Modelling geomorphic response to environmental change in an upland catchment. Hydrological Processes, 14, 2031-2045.

COULTHARD, T., MACKLIN, M. & KIRKBY, M. 2002. A cellular model of Holocene upland river basin and alluvial fan evolution. Earth Surface Processes and Landforms, 27, 269-288.

COULTHARD, T. J. 2005. Effects of vegetation on braided stream pattern and dynamics. Water Resources Research, 41.

COUPER, P. R. & MADDOCK, I. P. 2001. Subaerial river bank erosion processes and their interaction with other bank erosion mechanisms on the River Arrow, Warwickshire, UK. Earth Surface Processes and Landforms, 26, 631-646.

COWAN, W. L. 1956. Estimating hydraulic roughness coefficients. Agricultural Engineering, 37, 473-475.

CROSATO, A. 2008. Analysis and modelling of river meandering.

CROSATO, A. & MOSSELMAN, E. 2009. Simple physics-based predictor for the number of river bars and the transition between meandering and braiding. Water Resources Research, 45.

CROSATO, A. & SALEH, M. S. 2011. Numerical study on the effects of floodplain vegetation on river planform style. Earth Surface Processes and Landforms, 36, 711-720.

DARBY, S. E. 1999. Effect of riparian vegetation on flow resistance and flood potential. Journal of Hydraulic Engineering, 125, 443-454.

DAVIES, T., CAMPBELL, B., HALL, B. & GOMEZ, C. 2013. Recent behaviour and sustainable future management of the Waiho River, Westland, New Zealand. Journal of Hydrology (New Zealand), 41-56.

DOCKER, B. & HUBBLE, T. 2008. Quantifying root-reinforcement of river bank soils by four Australian tree species. Geomorphology, 100, 401-418.

DOEGLAS, D. 1962. The structure of sedimentary deposits of braided rivers. Sedimentology, 1, 167-190.

DOESCHL, A. B., ASHMORE, P. E. & DAVISON, M. 2009. Methods for assessing exploratory computational models of braided rivers. Braided Rivers: Process, Deposits, Ecology and Management, International Association of Sedimentologists Special Publication, 36, 177-197.

DOESCHL-WILSON, A. B. & ASHMORE, P. E. 2005. Assessing a numerical cellular braided-stream model with a physical model. Earth Surface Processes and Landforms, 30, 519-540.

EATON, B. C., MILLAR, R. G. & DAVIDSON, S. 2010. Channel patterns: braided, anabranching, and single-thread. Geomorphology, 120, 353-364.

EDMAIER, K., BURLANDO, P. & PERONA, P. 2011. Mechanisms of vegetation uprooting by flow in alluvial non-cohesive sediment. Hydrology and Earth System Sciences, 15, 1615-1627.

EDWARDS, P., KOLLMANN, J., GURNELL, A., PETTS, G., TOCKNER, K. & WARD, J. 1999. A conceptual model of vegetation dynamics on gravel bars of a large Alpine river. Wetlands Ecology and Management, 7, 141-153.

EGOZI, R. & ASHMORE, P. 2008. Defining and measuring braiding intensity. Earth Surface Processes and Landforms, 33, 2121-2138.

EGOZI, R. & ASHMORE, P. 2009. Experimental analysis of braided channel pattern response to increased discharge. Journal of Geophysical Research: Earth Surface, 114.

ENGELUND, F. 1974. Flow and bed topography in channel bends. Journal of the Hydraulics Division, 100.

ENGELUND, F. & SKOVGAARD, O. 1973. On the origin of meandering and braiding in alluvial streams. Journal of Fluid Mechanics, 57, 289-302.

ENGGROB, H. G. & TJERRY, S. 1999. Simulation of morphological characteristics of a braided river. Proceedings of the IAHR Symposium on River, Coastal and Estuarine Morphodynamics, Vol. I. Genova, pp. 585–594. 6-10 Sept.

ESCAURIAZA, C., PAOLA, C. & VOLLER, V. R. 2017. Computational Models of Flow, Sediment Transport and Morphodynamics in Rivers. Gravel-Bed Rivers: Process and Disasters, 1.

ESCHNER, T. R. 1983. Hydraulic geometry of the Platte River near Overton, south-central Nebraska, US Department of the Interior, Geological Survey.

EXNER, F. M. 1925. Uber die wechselwirkung zwischen wasser und geschiebe in flussen. Akad. Wiss. Wien Math. Naturwiss. Klasse, 134, 165-204.

FAEH, R. 2007. Numerical modeling of breach erosion of river embankments. Journal of Hydraulic Engineering, 133, 1000-1009.

FEDERICI, B. & PAOLA, C. 2003. Dynamics of channel bifurcations in noncohesive sediments. Water Resources Research, 39.

FERGUSON, R. 1984. Magnitude and modelling of snowmelt runoff in the Cairngorm Mountains, Scotland. Hydrological Sciences Journal, 29, 49-62.

FERGUSON, R. 1993. Understanding braiding processes in gravel-bed rivers: progress and unsolved problems. Geological Society, London, Special Publications, 75, 73-87.

FERGUSON, R. 2003. The missing dimension: effects of lateral variation on 1-D calculations of fluvial bedload transport. Geomorphology, 56, 1-14.

FERGUSON, R., ASHMORE, P., ASHWORTH, P., PAOLA, C. & PRESTEGAARD, K. 1992. Measurements in a braided river chute and lobe: 1. Flow pattern, sediment transport, and channel change. Water Resources Research, 28, 1877-1886.

FERGUSON, R. & ASHWORTH, P. 1992. Spatial patterns of bedload transport and channel change in braided and near braided rivers. Dynamics of Gravel-Bed Rivers; Billi, P., Hey, RD, Thorne, CR, Tacconi, P., Eds.

FERGUSON, R., CHURCH, M., RENNIE, C. & VENDITTI, J. 2015. Reconstructing a sediment pulse: Modeling the effect of placer mining on Fraser River, Canada. Journal of Geophysical Research: Earth Surface, 120, 1436-1454.

FERGUSON, R. I. & WERRITTY, A. 1983. Bar development and channel changes in the gravelly River Feshie, Scotland. Modern and ancient fluvial systems, 181-193.

FETHERSTON, K. L., NAIMAN, R. J. & BILBY, R. E. 1995. Large woody debris, physical process, and riparian forest development in montane river networks of the Pacific Northwest. Geomorphology, 13, 133-144.

FRANCIS, R. A. 2007. Size and position matter: riparian plant establishment from fluvially deposited trees. Earth Surface Processes and Landforms, 32, 1239-1243.

FRANCIS, R. A., CORENBLIT, D. & EDWARDS, P. J. 2009a. Perspectives on biogeomorphology, ecosystem engineering and self-organisation in island-braided fluvial ecosystems. Aquatic sciences, 71, 290.

FRANCIS, R. A. & GURNELL, A. M. 2006. Initial establishment of vegetative fragments within the active zone of a braided gravel-bed river (River Tagliamento, NE Italy). Wetlands, 26, 641-648.

FRANCIS, R. A., GURNELL, A. M., PETTS, G. E. & EDWARDS, P. J. 2009b. Riparian tree establishment on gravel bars: interactions between plant growth strategy and the physical environment. Braided Rivers: Process, Deposits, Ecology and Management, 361-380.

FRANCIS, R. A., PETTS, G. E. & GURNELL, A. M. 2008. Wood as a driver of past landscape change along river corridors. Earth Surface Processes and Landforms, 33, 1622-1626.

FREDSØE, J. 1978. Meandering and braiding of rivers. Journal of Fluid Mechanics, 84, 609-624.

FRYIRS, K., BRIERLEY, G. J. & ERSKINE, W. D. 2012. Use of ergodic reasoning to reconstruct the historical range of variability and evolutionary trajectory of rivers. Earth Surface Processes and Landforms, 37, 763-773.

GARCIA LUGO, G., BERTOLDI, W., HENSHAW, A. & GURNELL, A. 2015. The effect of lateral confinement on gravel bed river morphology. Water Resources Research, 51, 7145-7158.

GERMANOSKI, D. & SCHUMM, S. 1993. Changes in braided river morphology resulting from aggradation and degradation. The Journal of Geology, 101, 451-466.

GHISALBERTI, M. & NEPF, H. 2006. The structure of the shear layer in flows over rigid and flexible canopies. Environmental Fluid Mechanics, 6, 277-301.

GODUNOV, S. K. 1983. Difference method of numerical computations of discontinuous solutions in hydrodynamic equations, US Army Foreigh Science and Technology Center.

GRAF, W. L. 1978. Fluvial adjustments to the spread of tamarisk in the Colorado Plateau region. Geological Society of America Bulletin, 89, 1491-1501.

GRAN, K. & PAOLA, C. 2001. Riparian vegetation controls on braided stream dynamics. Water Resources Research, 37, 3275-3283.

GURNELL, A. 2014. Plants as river system engineers. Earth Surface Processes and Landforms, 39, 4-25.

GURNELL, A., SURIAN, N. & ZANONI, L. 2009. Multi-thread river channels: A perspective on changing European alpine river systems. Aquatic Sciences, 71, 253-265.

GURNELL, A., TOCKNER, K., EDWARDS, P. & PETTS, G. 2005. Effects of deposited wood on biocomplexity of river corridors. Frontiers in Ecology and the Environment, 3, 377-382.

GURNELL, A. M., BERTOLDI, W. & CORENBLIT, D. 2012. Changing river channels: The roles of hydrological processes, plants and pioneer fluvial landforms in humid temperate, mixed load, gravel bed rivers. Earth-Science Reviews, 111, 129-141.

GURNELL, A. M. & PETTS, G. E. 2002. Island-dominated landscapes of large floodplain rivers, a European perspective. Freshwater Biology, 47, 581-600.

GURNELL, A. M., PETTS, G. E., HANNAH, D. M., SMITH, B. P., EDWARDS, P. J., KOLLMANN, J., WARD, J. V. & TOCKNER, K. 2001. Riparian vegetation and island formation along the gravel-bed Fiume Tagliamento, Italy. Earth Surface Processes and Landforms, 26, 31-62.

HARTEN, A. 1983. High resolution schemes for hyperbolic conservation laws. Journal of computational physics, 49, 357-393.

HARVEY, A. 1969. Channel capacity and the adjustment of streams to hydrologic regime. Journal of Hydrology, 8, 82-98.

HENDERSON, F. M. 1963. Stability of alluvial channels. . Transactions of the ASCE 128, 657–686, 46 p.

HENSHAW, A. J., GURNELL, A. M., BERTOLDI, W. & DRAKE, N. A. 2013. An assessment of the degree to which Landsat TM data can support the assessment of fluvial dynamics, as revealed by changes in vegetation extent and channel position, along a large river. Geomorphology, 202, 74-85.

HICKIN, E. 1984. Vegetation and river channel dynamics. Canadian Geography 28: 111–126.

HICKS, D. M., DUNCAN, M. J., LANE, S. N., TAL, M. & WESTAWAY, R. 2007. 21 Contemporary morphological change in braided gravel-bed rivers: new developments from field and laboratory studies, with particular reference to the influence of riparian vegetation. Developments in Earth Surface Processes, 11, 557-584.

HICKS, D. M., SHANKAR, U., DUNCAN, M., REBUFFÉ, M. & ABERLE, J. 2009. Use of remote-sensing with two-dimensional hydrodynamic models to assess impacts of hydro-operations on a large, braided, gravel-bed river: Waitaki River, New Zealand. Braided Rivers, 311-326.

HODGE, R., BRASINGTON, J. & RICHARDS, K. 2009a. Analysing laser-scanned digital terrain models of gravel bed surfaces: linking morphology to sediment transport processes and hydraulics. Sedimentology, 56, 2024-2043.

HODGE, R., BRASINGTON, J. & RICHARDS, K. 2009b. In situ characterization of grain-scale fluvial morphology using Terrestrial Laser Scanning. Earth Surface Processes and Landforms, 34, 954-968.

HODGE, R., RICHARDS, K. & BRASINGTON, J. 2007. A physically-based bedload transport model developed for 3-D reach-scale cellular modelling. Geomorphology, 90, 244-262.

HONG, L. B. & DAVIES, T. 1979. A study of stream braiding. Geological Society of America Bulletin, 90, 1839-1859.

HUGGETT, R. 2007. A history of the systems approach in geomorphology. Géomorphologie: relief, processus, environnement, 13, 145-158.

HUNDEY, E. & ASHMORE, P. 2009. Length scale of braided river morphology. Water Resources Research, 45.

HUNZIKER, R. P. & JAEGGI, M. N. 2002. Grain sorting processes. Journal of Hydraulic Engineering, 128, 1060-1068.

IKEDA, S. 1982. Lateral bed load transport on side slopes. Journal of the Hydraulics Division, 108, 1369-1373.

IKEDA, S., PARKER, G. & SAWAI, K. 1981. Bend theory of river meanders. Part 1. Linear development. Journal of Fluid Mechanics, 112, 363-377.

JAMES, L. A. 1991. Incision and morphologic evolution of an alluvial channel recovering from hydraulic mining sediment. GSA Bulletin, 103, 723-736.

JANG, C.-L. & SHIMIZU, Y. 2005. Numerical simulation of relatively wide, shallow channels with erodible banks. Journal of Hydraulic Engineering, 131, 565-575.

JANG, C.-L. & SHIMIZU, Y. 2007. Vegetation effects on the morphological behavior of alluvial channels. Journal of Hydraulic Research, 45, 763-772.

JÄRVELÄ, J. 2005. Effect of submerged flexible vegetation on flow structure and resistance. Journal of Hydrology, 307, 233-241.

JAVERNICK, L., BRASINGTON, J. & CARUSO, B. 2014. Modeling the topography of shallow braided rivers using Structure-from-Motion photogrammetry. Geomorphology, 213, 166-182.

JAVERNICK, L., HICKS, D., MEASURES, R., CARUSO, B. & BRASINGTON, J. 2016. Numerical Modelling of Braided Rivers with Structure-from-Motion-Derived Terrain Models. River Research and Applications, 32, 1071-1081.

JEROLMACK, D. J. & MOHRIG, D. 2007. Conditions for branching in depositional rivers. Geology, 35, 463-466.

JOHNSON, W. C. 1994. Woodland expansions in the Platte River, Nebraska: patterns and causes. Ecological monographs, 64, 45-84.

JOWETT, I. 1998. Hydraulic geometry of New Zealand rivers and its use as a preliminary method of habitat assessment. Regulated Rivers: Research & Management, 14, 451-466.

JUNK, W. J., BAYLEY, P. B. & SPARKS, R. E. The flood pulse concept in river-floodplain systems. Proceedings of the International Large River Symposium. , 1989 Dodge, DP (Ed). Can. Spec. Publ. Fish. Aquat. Sci.

KASPRAK, A., WHEATON, J. M., ASHMORE, P. E., HENSLEIGH, J. W. & PEIRCE, S. 2015. The relationship between particle travel distance and channel morphology: Results from physical models of braided rivers. Journal of Geophysical Research: Earth Surface, 120, 55-74.

KELLY, S. 2006. Scaling and hierarchy in braided rivers and their deposits: examples and implications for reservoir modelling. Braided Rivers: Process, Deposits, Ecology and Management, 75-106.

KLEINHANS, M. G. 2010. Sorting out river channel patterns. Progress in Physical Geography, 34, 287-326.

KLEINHANS, M. G., FERGUSON, R. I., LANE, S. N. & HARDY, R. J. 2013. Splitting rivers at their seams: bifurcations and avulsion. Earth Surface Processes and Landforms, 38, 47-61.

KLEINHANS, M. G. & VAN DEN BERG, J. H. 2011. River channel and bar patterns explained and predicted by an empirical and a physics-based method. Earth Surface Processes and Landforms, 36, 721-738.

KONDOLF, G. M., SALE, M. J. & WOLMAN, M. G. 1993. Modification of fluvial gravel size by spawning salmonids. Water Resources Research, 29, 2265-2274.

LANE, E. W. 1957. A study of the shape of channels formed by natural streams flowing in erodible material, US Army Engineer Division, Missouri River.

LANE, S., RICHARDS, K. & CHANDLER, J. 1993. Developments in photogrammetry; the geomorphological potential. Progress in Physical Geography, 17, 306-328.

LANE, S., WIDDISON, P., THOMAS, R., ASHWORTH, P., BEST, J., LUNT, I., SAMBROOK SMITH, G. & SIMPSON, C. 2010. Quantification of braided river channel change using archival digital image analysis. Earth Surface Processes and Landforms, 35, 971-985.

LANE, S. N. & RICHARDS, K. S. 1997. Linking river channel form and process: time, space and causality revisited. Earth Surface Processes and Landforms, 22, 249-260.

LANE, S. N. & RICHARDS, K. S. 2001. The 'validation'of hydrodynamic models: some critical perspectives. Model validation: perspectives in hydrological science, 413, 439.

LANE, S. N., WESTAWAY, R. M. & MURRAY HICKS, D. 2003. Estimation of erosion and deposition volumes in a large, gravel-bed, braided river using synoptic remote sensing. Earth Surface Processes and Landforms, 28, 249-271.

LANGBEIN, W. B. 1947. Topographic characteristics of drainage basins, US Government Printing Office USA.

LEOPOLD, L. B. & MADDOCK, T. 1953. The hydraulic geometry of stream channels and some physiographic implications, US Government Printing Office.

LEOPOLD, L. B. & WOLMAN, M. G. 1957. River channel patterns: braided, meandering, and straight. US Government Printing Office.

LESSER, G., ROELVINK, J., VAN KESTER, J. & STELLING, G. 2004. Development and validation of a three-dimensional morphological model. Coastal engineering, 51, 883-915.

LI, S. & MILLAR, R. 2011. A two-dimensional morphodynamic model of gravel-bed river with floodplain vegetation. Earth Surface Processes and Landforms, 36, 190-202.

LIÉBAULT, F. & PIÉGAY, H. 2002. Causes of 20th century channel narrowing in mountain and piedmont rivers of southeastern France. Earth surface processes and landforms, 27, 425-444.

LIU, D., DIPLAS, P., HODGES, C. & FAIRBANKS, J. 2010. Hydrodynamics of flow through double layer rigid vegetation. Geomorphology, 116, 286-296.

MACKIN, J. H. 1948. Concept of the graded river. GSA Bulletin, 59, 463-512.

MADEJ, M. A., SUTHERLAND, D. G., LISLE, T. E. & PRYOR, B. 2009. Channel responses to varying sediment input: A flume experiment modeled after Redwood Creek, California. Geomorphology, 103, 507-519.

MAO, L., DELL'AGNESE, A., HUINCACHE, C., PENNA, D., ENGEL, M., NIEDRIST, G. & COMITI, F. 2014. Bedload hysteresis in a glacier-fed mountain river. Earth Surface Processes and Landforms, 39, 964-976.

MAO, L. & SURIAN, N. 2010. Observations on sediment mobility in a large gravel-bed river. Geomorphology, 114, 326-337.

MARANI, M., DA LIO, C. & D'ALPAOS, A. 2013. Vegetation engineers marsh morphology through multiple competing stable states. Proceedings of the National Academy of Sciences, 110, 3259-3263.

MARCUS, W. A. & FONSTAD, M. A. 2010. Remote sensing of rivers: the emergence of a subdiscipline in the river sciences. Earth Surface Processes and Landforms, 35, 1867-1872.

MARSTON, R. A., GIREL, J., PAUTOU, G., PIEGAY, H., BRAVARD, J.-P. & ARNESON, C. 1995. Channel metamorphosis, floodplain disturbance, and vegetation development: Ain River, France. Geomorphology, 13, 121-131.

MARTI, C. & BEZZOLA, G. R. 2009. Bed load transport in braided gravel-bed rivers. Braided Rivers: Process, Deposits, Ecology and Management. Special Publication, 36, 199-215.

MEYER-PETER, E. & MÜLLER, R. Formulas for bed-load transport. IAHSR 2nd meeting, Stockholm, appendix 2, 1948. IAHR.

MIALL, A. D. 1977. A review of the braided-river depositional environment. Earth-Science Reviews, 13, 1-62.

MIALL, A. D. 2013. The geology of fluvial deposits: sedimentary facies, basin analysis, and petroleum geology, Springer.

MILLAR, R. G. 2000. Influence of bank vegetation on alluvial channel patterns. Water Resources Research, 36, 1109-1118.

MILLAR, R. G. & QUICK, M. C. 1993. Effect of bank stability on geometry of gravel rivers. Journal of Hydraulic Engineering, 119, 1343-1363.

MOSLEY, M. 1982. Analysis of the effect of changing discharge on channel morphology and instream uses in a braided river, Ohau River, New Zealand. Water resources research, 18, 800-812.

MOSLEY, M. 1983. Response of braided rivers to changing discharge. Journal of Hydrology (New Zealand), 18-67.

MOSSELMAN, E. 2005. Basic equations for sediment transport in CFD for fluvial morphodynamics. Computational fluid dynamics: applications in environmental hydraulics, 71-89.

MOSSELMAN, E. 2012. Modelling sediment transport and morphodynamics of gravel-bed rivers. Gravel-Bed Rivers: Processes, Tools, Environments, 101-115.

MOSSELMAN, E. & LE, T. B. 2016. Five common mistakes in fluvial morphodynamic modeling. Advances in Water Resources, 93, 15-20.

MURRAY, A. 2013. Which Models Are Good (Enough), and When? Treatise on geomorphology, 9, 50-57.

MURRAY, A. B. & PAOLA, C. 1994. A cellular model of braided rivers. Nature, 371, 54-57.

MURRAY, A. B. & PAOLA, C. 1997. Properties of a cellular braided-stream model. Earth Surface Processes and Landforms, 22, 1001-1025.

NAGATA, N., HOSODA, T. & MURAMOTO, Y. 2000. Numerical analysis of river channel processes with bank erosion. Journal of Hydraulic Engineering, 126, 243-252.

NASH, J. E. & SUTCLIFFE, J. V. 1970. River flow forecasting through conceptual models part I—A discussion of principles. Journal of hydrology, 10, 282-290.

NELSON, J. M., BENNETT, J. P. & WIELE, S. M. 2003. Flow and sediment-transport modeling. Tools in fluvial geomorphology, 18, 539-576.

NELSON, J. M., MCDONALD, R. R., SHIMIZU, Y., KIMURA, I., NABI, M. & ASAHI, K. 2016. Modelling flow, sediment transport and morphodynamics in rivers. Tools in Fluvial Geomorphology, 412-441.

NEPF, H. & GHISALBERTI, M. 2008. Flow and transport in channels with submerged vegetation. Acta Geophysica, 56, 753-777.

NICHOLAS, A. 2000. Modelling bedload yield in braided gravel bed rivers. Geomorphology, 36, 89-106.

NICHOLAS, A., THOMAS, R. & QUINE, T. 2009. Cellular modelling of braided river form and process. Braided Rivers: Process, Deposits, Ecology and Management (Special Publication 36 of the IAS), 21, 137.

NICHOLAS, A. P. 2013. Modelling the continuum of river channel patterns. Earth Surface Processes and Landforms, 38, 1187-1196.

O'DONNELL, C. F. J., SANDERS, M., WOOLMORE, C. & MALONEY, R. F. 2016. Management and research priorities for conserving biodiversity on New Zealand's braided rivers. Department of Conservation, Wellington, New Zealand, 46 p.

ORESKES, N. & BELITZ, K. 2001. Philosophical issues in model assessment. Model validation: Perspectives in hydrological science, 23.

OSTERKAMP, W. 1998. Processes of fluvial island formation, with examples from Plum Creek, Colorado and Snake River, Idaho. Wetlands, 18, 530-545.

PAOLA, C. 2001. Modelling stream braiding over a range of scales.

PARKER, G. 1976. On the cause and characteristic scales of meandering and braiding in rivers. Journal of fluid mechanics, 76, 457-480.

PARKER, G. 1979. Hydraulic geometry of active gravel rivers. Journal of the Hydraulics Division, 105, 1185-1201.

PARKER, G., PAOLA, C. & LECLAIR, S. 2000. Probabilistic Exner sediment continuity equation for mixtures with no active layer. Journal of Hydraulic Engineering, 126, 818-826.

PARTHENIADES, E. 1965. Erosion and deposition of cohesive soils. Journal of the Hydraulics Division, 91, 105-139.

PERONA, P., CROUZY, B., MCLELLAND, S., MOLNAR, P. & CAMPOREALE, C. 2014. Ecomorphodynamics of rivers with converging boundaries. Earth Surface Processes and Landforms, 39, 1651-1662.

PERONA, P., MOLNAR, P., SAVINA, M. & BURLANDO, P. 2009. An observation-based stochastic model for sediment and vegetation dynamics in the floodplain of an Alpine braided river. Water Resources Research, 45.

PERUCCA, E., CAMPOREALE, C. & RIDOLFI, L. 2007. Significance of the riparian vegetation dynamics on meandering river morphodynamics. Water Resources Research, 43.

PHILLIPS, J. D. 2011. Emergence and pseudo-equilibrium in geomorphology. Geomorphology, 132, 319-326.

PIEGAY, H., ALBER, A., SLATER, L. & BOURDIN, L. 2009. Census and typology of braided rivers in the French Alps. Aquatic Sciences-Research Across Boundaries, 71, 371-388.

PIÉGAY, H., GRANT, G., NAKAMURA, F. & TRUSTRUM, N. 2009. Braided river management: from assessment of river behaviour to improved sustainable development. Braided Rivers: Process, Deposits, Ecology and Management, Sambrook Smith GH, Best, JL, Bristow, CS, & Petts, GE (Eds), 257-276.

POLITTI. E,. BERTOLDI, W., GURNELL, A. & HENSHAW, A. 2018. Feedbacks between the riparian Salicaceae and hydrogeomorphic processes: A quantitative review. Earth-Science Reviews, 176, 147-165.

POLLEN, N. 2007. Temporal and spatial variability in root reinforcement of streambanks: accounting for soil shear strength and moisture. Catena, 69, 197-205.

POWELL, D. M. 1998. Patterns and processes of sediment sorting in gravel-bed rivers. Progress in Physical Geography, 22, 1-32.

PROSSER, I. P., HUGHES, A. O. & RUTHERFURD, I. D. 2000. Bank erosion of an incised upland channel by subaerial processes: Tasmania, Australia. Earth Surface Processes and Landforms, 25, 1085-1101.

RADICE, A., GIORGETTI, E., BRAMBILLA, D., LONGONI, L. & PAPINI, M. 2012. On integrated sediment transport modelling for flash events in mountain environments. Acta Geophysica, 60, 191-213.

REDOLFI, M. 2014. Morphological changes and sediment transport: The Rees River (New Zeland). Doctoral thesis in Science for MAnagement of Rivers and their Tidal System, Chapter 2.

REDOLFI, M., BERTOLDI, W. & TUBINO, M. Analysis of the spatiotemporal planform dynamics of braided rivers: a novel laboratory investigation. EGU General Assembly Conference Abstracts, 2016a. 16540.

REDOLFI, M., TUBINO, M., BERTOLDI, W. & BRASINGTON, J. 2016b. Analysis of reach-scale elevation distribution in braided rivers: Definition of a new morphologic indicator and estimation of mean quantities. Water Resources Research, 52, 5951-5970.

REID, I., FROSTICK, L. E. & LAYMAN, J. T. 1985. The incidence and nature of bedload transport during flood flows in coarse-grained alluvial channels. Earth Surface Processes and Landforms, 10, 33-44.

RENNIE, C. D., VERICAT, D., WILLIAMS, R. D., BRASINGTON, J. & HICKS, M. 2017. Calibration of Acoustic Doppler Current Profiler Apparent Bedload Velocity to Bedload Transport Rate. Gravel-Bed Rivers: Process and Disasters, 209.

RIBBERINK, J. S. 1987. Mathematical modelling of one-dimensional morphological changes in rivers with non-uniform sediment.

Rice, S. P., & Church, M. (2010). Grain-size sorting within river bars in relation to downstream fining along a wandering channel. Sedimentology, 57(1), 232-251.

RICHARDS, K., BRASINGTON, J. & HUGHES, F. 2002. Geomorphic dynamics of floodplains: ecological implications and a potential modelling strategy. Freshwater Biology, 47, 559-579.

RINALDI, M. & DARBY, S. E. 2007. 9 Modelling river-bank-erosion processes and mass failure mechanisms: progress towards fully coupled simulations. Developments in Earth Surface Processes, 11, 213-239.

RINALDI, M., MENGONI, B., LUPPI, L., DARBY, S. E. & MOSSELMAN, E. 2008. Numerical simulation of hydrodynamics and bank erosion in a river bend. Water Resources Research, 44.

RODI, W. 1993. Turbulence models and their application in hydraulics, CRC Press.

ROUŠAR, L., ZACHOVAL, Z. & JULIEN, P. 2016. Incipient motion of coarse uniform gravel. Journal of Hydraulic Research, 54, 615-630.

RÜEDLINGER, C. 2010. Sediment dynamics and morphological change in the braided Pfynwald reach of the Rhone River. Master Thesis, Institute of Environmental Engineering (IfU), Institute for Atmospheric and Climate Science (IAC), ETH Zürich.

RUMSBY, B., BRASINGTON, J., LANGHAM, J., MCLELLAND, S., MIDDLETON, R. & ROLLINSON, G. 2008. Monitoring and modelling particle and reach-scale morphological change in gravel-bed rivers: Applications and challenges. Geomorphology, 93, 40-54.

SALTELLI, A., CHAN, K., & SCOTT, E. M. (2000). Sensitivity analysis (Vol. 1): Wiley New York.

SAMBROOK SMITH, G., BEST, J., BRISTOW, C. & PETTS, G. 2006. Braided rivers: where have we come in 10 years? Progress and future needs. Braided Rivers: Process, Deposits, Ecology and Management, 1-10.

SANYAL, N. Effect of embankment of River Kosi. Proceedings of the international workshop on 'Alluvial Rivers' organisation by University of Roorkee, March, 1980. 18-20.

SAPOZHNIKOV, V. B., MURRAY, A. B., PAOLA, C. & FOUFOULA-GEORGIOU, E. 1998. Validation of Braided-Stream Models: Spatial state-space plots, self-affine scaling, and island shapes. Water Resources Research, 34, 2353-2364.

SCHUMM, S. & KHAN, H. 1972. Experimental study of channel patterns. Geological Society of America Bulletin, 83, 1755-1770.

SCHUMM, S. A. 1988. Variability of the fluvial system in space and time. Scales and global change, 225-250.

SCHUURMAN, F., MARRA, W. A. & KLEINHANS, M. G. 2013. Physics-based modeling of large braided sand-bed rivers: Bar pattern formation, dynamics, and sensitivity. Journal of geophysical research: Earth Surface, 118, 2509-2527.

SCORPIO, V., ZEN, S., BERTOLDI, W., SURIAN, N., MASTRONUNZIO, M., DAI PRÁ, E., ZOLEZZI, G. & COMITI, F. 2018. Channelization of a large Alpine river: what is left of its original morphodynamics? Earth Surface Processes and Landforms, 43, 1044-1062.

SIMON, A. & COLLISON, A. J. 2002. Quantifying the mechanical and hydrologic effects of riparian vegetation on streambank stability. Earth Surface Processes and Landforms, 27, 527-546.

SINGH, U., CROSATO, A., GIRI, S. & HICKS, M. 2017. Sediment heterogeneity and mobility in the morphodynamic modelling of gravel-bed braided rivers. Advances in Water Resources, 104, 127-144.

SIVIGLIA, A. & CROSATO, A. 2016. Numerical modelling of river morphodynamics: Latest developments and remaining challenges. Advances in Water Resources, 93, 1-3.

SIVIGLIA, A., STECCA, G., VANZO, D., ZOLEZZI, G., TORO, E. F. & TUBINO, M. 2013. Numerical modelling of two-dimensional morphodynamics with applications to river bars and bifurcations. Advances in Water Resources, 52, 243-260.

SLINGERLAND, R. & SMITH, N. D. 2004. River avulsions and their deposits. Annu. Rev. Earth Planet. Sci., 32, 257-285.

SLOFF, K. & MOSSELMAN, E. 2012. Bifurcation modelling in a meandering gravel–sand bed river. Earth Surface Processes and Landforms, 37, 1556-1566.

SLOFF C., & OTTEVANGER, W. (2008). Multiple-layer graded-sediment approach: Improvement and implications. Altinakar, Kokpinar, Gogus, Tayfur, Kumcu & Yildirim (eds) River Flow, 1447.

SMITH, D. G. 1976. Effect of vegetation on lateral migration of anastomosed channels of a glacier meltwater river. Geological Society of America Bulletin, 87, 857-860.

SMITH, L. C., ISACKS, B. L., BLOOM, A. L. & MURRAY, A. B. 1996. Estimation of discharge from three braided rivers using synthetic aperture radar satellite imagery: Potential application to ungaged basins. Water Resources Research, 32, 2021-2034.

SOULSBY, C., TETZLAFF, D., DUNN, S. & WALDRON, S. 2006. Scaling up and out in runoff process understanding: insights from nested experimental catchment studies. Hydrological Processes, 20, 2461-2465.

STRUIKSMA, N. 1985. Prediction of 2-D bed topography in rivers. Journal of Hydraulic Engineering, 111, 1169-1182.

SUN, J., LIN, B. & YANG, H. 2015. Development and application of a braided river model with non-uniform sediment transport. Advances in Water Resources, 81, 62-74.

SURIAN, N. 2006. Effects of human impact on braided river morphology: examples from Northern Italy. Braided Rivers: Process, Deposits, Ecology and Management, edited by: Sambrook Smith, GH, Best, JL, Bristow, C., and Petts, GE, International Association of Sedimentologists Special Publication, 36, 327-338.

SURIAN, N. 2015. Fluvial processes in braided rivers. Rivers–Physical, Fluvial and Environmental Processes. Springer International Publishing.

SURIAN, N., BARBAN, M., ZILIANI, L., MONEGATO, G., BERTOLDI, W. & COMITI, F. 2015. Vegetation turnover in a braided river: frequency and effectiveness of floods of different magnitude. Earth Surface Processes and Landforms, 40, 542-558.

SURIAN, N., MAO, L., GIACOMIN, M. & ZILIANI, L. 2009a. Morphological effects of different channel-forming discharges in a gravel-bed river. Earth Surface Processes and Landforms, 34, 1093-1107.

SURIAN, N. & RINALDI, M. 2003. Morphological response to river engineering and management in alluvial channels in Italy. Geomorphology, 50, 307-326.

SURIAN, N., RINALDI, M., PELLEGRINI, L., AUDISIO, C., MARAGA, F., TERUGGI, L., TURITTO, O. & ZILIANI, L. 2009b. Channel adjustments in northern and central Italy over the last 200 years. Geological Society of America Special Papers, 451, 83-95.

SUTHERLAND, J., PEET, A. & SOULSBY, R. 2004. Evaluating the performance of morphological models. Coastal engineering, 51, 917-939.

TAKEBAYASHI, H. & OKABE, T. Numerical modelling of braided streams in unsteady flow. Proceedings of the Institution of Civil Engineers-Water Management, 2009. Thomas Telford Ltd, 189-198.

TAL, M., GRAN, K., MURRAY, A. B., PAOLA, C. & HICKS, D. M. 2004. Riparian vegetation as a primary control on channel characteristics in multi-thread rivers. Riparian vegetation and fluvial geomorphology, 43-58.

TAL, M. & PAOLA, C. 2010. Effects of vegetation on channel morphodynamics: results and insights from laboratory experiments. Earth Surface Processes and Landforms, 35, 1014-1028.

TALMON, A., STRUIKSMA, N. & VAN MIERLO, M. 1995. Laboratory measurements of the direction of sediment transport on transverse alluvial-bed slopes. Journal of hydraulic research, 33, 495-517.

TETTAMANTI, S. 2013. Study of the effects of vegetation on river plan-form style with the numerical model BASEMENT. Master Thesis, Dipartimento di Ingegneria Civile, Ambientale e Meccanica Corso di Laurea Magistrale in Ingegneria per l'Ambiente e il Territorio.

THOMAS, R. & NICHOLAS, A. 2002. Simulation of braided river flow using a new cellular routing scheme. Geomorphology, 43, 179-195.

THOMAS, R., NICHOLAS, A. & QUINE, T. 2007. Cellular modelling as a tool for interpreting historic braided river evolution. Geomorphology, 90, 302-317.

THORN, C. E. & WELFORD, M. R. 1994. The equilibrium concept in geomorphology. Annals of the Association of American Geographers, 84, 666-696.

THORNE, C. 1990. Effects of vegetation on river bank erosion and stability.

THORNE, C. R. & TOVEY, N. K. 1981. Stability of composite river banks. Earth Surface Processes and Landforms, 6, 469-484.

TOCKNER, K., PAETZOLD, A., KARAUS, U., CLARET, C. & ZETTEL, J. 2006. Ecology of Braided Rivers. 339-359.

TOFFOLON, M. & CROSATO, A. 2007. Developing macroscale indicators for estuarine morphology: The case of the Scheldt estuary. Journal of Coastal Research, 195-212.

TORO, E. F. 2001. Shock-capturing methods for free-surface shallow flows, John Wiley.

TSUJIMOTO, T. 1999. Fluvial processes in streams with vegetation. Journal of hydraulic research, 37, 789-803.

TUCKER, G. E. & BRAS, R. 1999. Dynamics of vegetation and runoff erosion. A 3D Computer Simulation Model of Drainage Basin and Floodplain Evolution: Theory and Applications. Tech. report US Army Corps. of Eng. Const. Eng. Res. Lab., Champaign, IL.

VAN DE WIEL, M. J., COULTHARD, T. J., MACKLIN, M. G. & LEWIN, J. 2007. Embedding reach-scale fluvial dynamics within the CAESAR cellular automaton landscape evolution model. Geomorphology, 90, 283-301.

VAN DEN BERG, J. H. 1995. Prediction of alluvial channel pattern of perennial rivers. Geomorphology, 12, 259-279.

VAN RIJN, L. C. 1984. Sediment transport, part I: bed load transport. Journal of hydraulic engineering, 110, 1431-1456.

VAN RIJN, L. C. 1993. Principles of sediment transport in rivers, estuaries and coastal seas, Aqua publications Amsterdam.

VERICAT, D., BATALLA, R. J. & GARCIA, C. 2006. Breakup and reestablishment of the armour layer in a large gravel-bed river below dams: The lower Ebro. Geomorphology, 76, 122-136.

VERICAT, D., WHEATON, J. M. & BRASINGTON, J. 2017. Revisiting the Morphological Approach: Opportunities and Challenges with Repeat High-Resolution Topography. Gravel-Bed Rivers: Process and Disasters, 121.

VETSCH, D., SIVIGLIA, A., EHRBAR D., FACCHINI M., KAMMERER S., KOCH A., PETER S., VONWILLER L., GERBER M., VOLZ C., FARSHI D., MUELLER R., ROUSSELOT P., VEPREK R., FAEH R. 2017a. BASEMENT Basic Simulation Environment for computation of environmental flow and natural hazard simulation (System Manual), Version 2.7. VAW, ETH Zurich.

VETSCH, D., SIVIGLIA, A., EHRBAR D., FACCHINI M., KAMMERER S., KOCH A., PETER S., VONWILLER L., GERBER M., VOLZ C., FARSHI D., MUELLER R., ROUSSELOT P., VEPREK R., FAEH R. 2017b. BASEMENT Basic Simulation Environment for computation of environmental flow and natural hazard simulation (User Manual), Version 2.7. VAW, ETH Zurich.

VISCONTI, F., CAMPOREALE, C. & RIDOLFI, L. 2010. Role of discharge variability on pseudomeandering channel morphodynamics: Results from laboratory experiments. Journal of Geophysical Research: Earth Surface, 115.

VOLZ, C., ROUSSELOT, P., VETSCH, D. & FAEH, R. 2012. Numerical modelling of non-cohesive embankment breach with the dual-mesh approach. Journal of Hydraulic Research, 50, 587-598.

WARBURTON, J. 1996. Active braidplain width, bed load transport and channel morphology in a model braided river. Journal of Hydrology (New Zealand), 259-285.

WARBURTON, J., DAVIES, T. & MANDL, M. 1993. A meso-scale field investigation of channel change and floodplain characteristics in an upland braided gravel-bed river, New Zealand. Geological Society, London, Special Publications, 75, 241-255.

WARD, J., TOCKNER, K., ARSCOTT, D. & CLARET, C. 2002. Riverine landscape diversity. Freshwater Biology, 47, 517-539.

WARREN, I. & BACH, H. K. 1992. MIKE 21: a modelling system for estuaries, coastal waters and seas. Environmental Software, 7, 229-240.

WELBER, M., BERTOLDI, W. & TUBINO, M. 2012. The response of braided planform configuration to flow variations, bed reworking and vegetation: the case of the Tagliamento River, Italy. Earth Surface Processes and Landforms, 37, 572-582.

WELBER, M., BERTOLDI, W. & TUBINO, M. 2013. Wood dispersal in braided streams: results from physical modeling. Water Resources Research, 49, 7388-7400.

WERNER, B. 1999. Complexity in natural landform patterns. Science, 284, 102-104.

WERRITTY, A. & BRAZIER, V. 1991. The geomorphology, conservation and management of the River Feshie SSSI. Peterborough: Nature Conservancy Council Report, 1.

WERRITTY, A. & HOEY, T. 2004. Geomorphological changes and trends in Scotland: river channels and processes, Scottish Natural Heritage.

WESTOBY, M., BRASINGTON, J., GLASSER, N., HAMBREY, M. & REYNOLDS, J. 2012. 'Structure-from-Motion'photogrammetry: A low-cost, effective tool for geoscience applications. Geomorphology, 179, 300-314.

WHEATON, J. M., BRASINGTON, J., DARBY, S. E., KASPRAK, A., SEAR, D. & VERICAT, D. 2013. Morphodynamic signatures of braiding mechanisms as expressed through change in sediment storage in a gravel-bed river. Journal of Geophysical Research: Earth Surface, 118, 759-779.

WHEATON, J. M., BRASINGTON, J., DARBY, S. E. & SEAR, D. A. 2010. Accounting for uncertainty in DEMs from repeat topographic surveys: improved sediment budgets. Earth Surface Processes and Landforms, 35, 136-156.

WILLGOOSE, G. & HANCOCK, G. 1998. Revisiting the hypsometric curve as an indicator of form and process in transport-limited catchment. Earth Surface Processes and Landforms, 23, 611-623.

WILLIAMS, R., BRASINGTON, J., HICKS, M., MEASURES, R., RENNIE, C. & VERICAT, D. 2013. Hydraulic validation of two-dimensional simulations of braided river flow with spatially continuous aDcp data. Water Resources Research, 49, 5183-5205.

WILLIAMS, R., BRASINGTON, J., VERICAT, D. & HICKS, D. 2014. Hyperscale terrain modelling of braided rivers: fusing mobile terrestrial laser scanning and optical bathymetric mapping. Earth Surface Processes and Landforms, 39, 167-183.

WILLIAMS, R., BRASINGTON, J., VERICAT, D., HICKS, M., LABROSSE, F. & NEAL, M. 2011. Chapter twenty-monitoring braided river change using terrestrial laser scanning and optical bathymetric mapping. Developments in Earth Surface Processes, 15, 507-532.

WILLIAMS, R., MEASURES, R., HICKS, D. & BRASINGTON, J. 2016a. Assessment of a numerical model to reproduce event-scale erosion and deposition distributions in a braided river. Water resources research, 52, 6621-6642.

WILLIAMS, R., RENNIE, C., BRASINGTON, J., HICKS, D. & VERICAT, D. 2015. Linking the spatial distribution of bed load transport to morphological change during high-flow events in a shallow braided river. Journal of Geophysical Research: Earth Surface, 120, 604-622.

WILLIAMS, R. D., BRASINGTON, J. & HICKS, D. M. 2016b. Numerical modelling of braided river morphodynamics: Review and future challenges. Geography Compass, 10, 102-127.

WORNI, R., STOFFEL, M., HUGGEL, C., VOLZ, C., CASTELLER, A. & LUCKMAN, B. 2012. Analysis and dynamic modeling of a moraine failure and glacier lake outburst flood at Ventisquero Negro, Patagonian Andes (Argentina). Journal of Hydrology, 444, 134-145.

WRIGHT, N. & CROSATO, A. 2011. The hydrodynamics and morphodynamics of rivers.

WU, W., SHIELDS, F. D., BENNETT, S. J. & WANG, S. S. 2005. A depth-averaged two-dimensional model for flow, sediment transport, and bed topography in curved channels with riparian vegetation. Water Resources Research, 41.

YOSSEF, M. F., JAGERS, H., VAN VUREN, S. & SIEBEN, J. Innovative techniques in modelling large-scale river morphology. River flow 2008, Proc. of the intern. conf. on fluvial hydraulics, Cesme, Izmir, Turkey, 2008. 1065-1074.

YOUNG, W. & DAVIES, T. 1990. Prediction of bedload transport rates in braided rivers: a hydraulic model study. Journal of Hydrology (New Zealand), 75-92.

ZILIANI, L. & SURIAN, N. 2012. Evolutionary trajectory of channel morphology and controlling factors in a large gravel-bed river. Geomorphology, 173, 104-117.

ZILIANI, L., SURIAN, N., COULTHARD, T. & TARANTOLA, S. 2013. Reduced-complexity modeling of braided rivers: Assessing model performance by sensitivity analysis, calibration, and validation. Journal of Geophysical Research: Earth Surface, 118, 2243-2262.

ZOLEZZI, G., BERTOLDI, W. & TUBINO, M. 2009. Morphological analysis and prediction of river bifurcations. Braided rivers: Processes, Deposits, Ecology and Management. Blackwell Publishing Ltd Oxford, UK.